Strong-Field Physics with a High Energy Waveform Synthesizer

Dissertation
zur Erlangung des Doktorgrades
an der Fakultät für Mathematik, Informatik und Naturwissenschaften
Fachbereich Physik
der Universität Hamburg

vorgelegt von

Fabian Scheiba

Hamburg

2023

Gutachter der Dissertation:	Prof. Dr. Franz X. Kärtner Prof. Dr. Markus Drescher
Zusammensetzung der Prüfungskommission:	Prof. Dr. Franz X. Kärtner Prof. Dr. Markus Drescher Prof. Dr. Jochen Küpper Prof. Dr. Francesca Calegari Prof. Dr. Daniela Pfannkuche
Vorsitzende/r der Prüfungskommission:	Prof. Dr. Daniela Pfannkuche
Datum der Disputation:	13.03.2023
Vorsitzender Fach-Promotionsausschusses PHYSIK:	Prof. Dr. Günter H. W. Sigl
Leiter des Fachbereichs PHYSIK:	Prof. Dr. Wolfgang Parak
Dekan der Fakultät MIN:	Prof. Dr.-Ing. Norbert Ritter

Abstract

The motivation to control and temporarily isolate a single quantum mechanical event like an electronic transition has driven the quest for ever shorter light pulses. Controlling a highly intense electric field in the visible to infrared wavelength range on a sub-cycle time scale becomes feasible with the concept of the parametric waveform synthesizer. High harmonic generation (HHG) is explored as a primary application with the aim to generate isolated attosecond pulses and high photon energies in the "Water Window" spectral region from 284 eV to 533 eV.
The tight synchronization of pulses from optical parametric amplifiers (OPAs) spanning from 650 nm to 2200 nm is achieved with long-term synthesized waveform stability. To work out and monitor the ideal synthesis parameters, a set of characterization methods are developed in the time and spatial domain.
The ability to control sub-cycle fields is displayed via the large variety of XUV and soft X-ray continua as generated via HHG covering photon energies starting from 30 eV all the way up entering the "Water Window". The peculiarity of sub-cycle infrared driving pulses allows to generate isolated attosecond pulses a priori without further gating techniques. The phase-stable control of the driver pulse allows to shape the harmonic continua in bandwidth and central energy.
Characterization of both the generated isolated attosecond pulses and the synthesized infrared driving field is performed in an attosecond streaking experiment yielding reproducible and compressed XUV pulses down to 80 as FWHM, including the retrieval of an ≈ 2 octaves spanning driver pulse.
A partial redesign of the vacuum apparatus to aim for high-pressure phase-matching conditions inside the HHG gas nozzle enabled the generation of soft X-ray continua up to 450 eV. The continuous spectra in neon and helium are investigated as a function of the driving waveform and macroscopic parameters. A comparison of the pulse energies at soft X-ray bandwidths once generated with the infrared OPA (two-cycle pulse) and once generated with the synthesized pulse (sub-cycle), shows an up to 5-fold flux increase. The absolute maximum pulse energy is measured to 1 pJ integrated from 200 eV onwards.
Finally, the design of an experimental chamber, an updated toroidal mirror and a soft X-Ray spectrometer prepare for future attosecond transient absorption experiments.

Zusammenfassung

Die Entwicklung ultrakurzer Laserpulse ermöglicht die natürlichen Zeitskalen einzelner quantenmechanischer Zustände wie beispielsweise elektronischer Übergänge abzubilden. Die kohärente Synthese von ultrakurzen Laserpulsen mit Spektren vom optisch sichtbaren Bereich bis in das Infrarot ermöglicht es, die elektrischen Felder innerhalb einer Wellenlänge zu manipulieren und zeitlich bis auf weniger als eine Periode zu begrenzen. Die stabile Synchronisation und Abstimmung von optisch parametrischen Verstärkern (OPA) im Wellenlängenbereich 650 nm bis 2200 nm zu einem synthetisierten Puls wird langfristig als stabil gezeigt. Die dafür notwendigen Methoden und entsprechenden Charakterisierungen werden in der vorliegenden Arbeit entwickelt.

Ihre primäre Anwendung finden die Pulse in der Erzeugung Höherer Harmonischer (HHG). Die Möglichkeit der Manipulation solcher Sub-Zyklus-Pulse wird durch die große Anzahl der erzeugten und kontinuierlichen Spektren im XUV- und weichen Röntgenbereich demonstriert. Dabei werden Photonenenergien von 30 eV bis in das "Wasserfenster" bei $284 - 533$ eV erreicht. Die Besonderheit der Sub-Zyklus-Infrarotpulse zeigt sich in der direkten Erzeugung isolierter Attosekundenpulse ohne Verwendung von Gating-Methoden. Durch eine phasenstabile Manipulation des Treiberpulses kann das erzeugte harmonische Spektrum geziehlt in Bandbreite und mittlerer Photonenenergie beinflusst werden.

Die Charakterisierung der erzeugten Attosekundenpulse und der synthetisierten Infrarotpulse erfolgt in einem Streak-Kamera-Experiment. Die Messungen zeigen Attosekundenpulse bis zu einer minimalen Dauer von 80 as. Auch das annähernd zwei Oktaven umfassende Feld des Treiberpulses kann bestimmt werden.

Die Ergänzung und Neuausrichtung der Vakuumapparatur ermöglicht durch eine Hochdruck-Gaszelle die Phasenanpassung hin zu höheren Photonenenergien, wobei bis zu 450 eV im weichen Röntgenspektrum erreicht werden. In diesem Spektrum wird die Erzeugung weicher Röntgenstrahlung als Funktion des elektrischen Feldes des treibenden Laserpulses und der makroskopischen Parameter im Prozess der HHG untersucht. Im Falle eines Infrarot OPA (zwei optische Zyklen) und eines synthetisierten Pulses (Sub-Zyklus) zeigen die durch HHG erzeugten Pulsenergien im weichen Röntgenbereich eine bis zu 5-fach gesteigerte Konversionseffizienz für den synthetisierten Treiberpuls bei ausgewählten Photonenergien. Die maximale Pulsenergie im weichen Röntgenbereich oberhalb von 200 eV beträgt 1 pJ.

Schlussendlich bereitet die Entwicklung einer neuen Experimentierkammer, des Spektrometers und die Erneuerung der Röntgenoptiken den Einsatz der parametrischen Synthese von ultrakurzen Lichtpulsen in zukünftigen Attosekunden-Pump-Probe-Experimenten vor.

Acknowledgement

In the course of the Ph.D. at DESY, I have met many remarkable and motivated people who are always ready to discuss, help and support each other.
First of all, I would like to thank Professor Franz X. Kärtner for the long-term level of trust in the project itself and me as a Ph.D. student. His confidence in the idea of a next generation of attosecond light source despite a sometimes tedious development of experimental infrastructure, technology and data acquisition made the results presented in this thesis possible.
Furthermore, I would like to express how amazing the "synthesizer team" runs the lab. Here, especially Dr. Giulio Maria Rossi and Dr. Roland Mainz formed a very stable team with very broad competence and the ability to find the golden center between friendship and collegiality in the lab.
I was lucky to find a good partner and friend from the other side of the world, Miguel Angel Silva Toledo and me went most of the path towards our Ph.D. together. Sharing the same office has led to sharing the same thoughts and the interpretation of all the work and measurements we have done is very much a common effort.
Also big thanks to Dr. Yudong Yang, as he prepared and introduced me to the attosecond beamline and stayed with us for the first attosecond streaking experiments of an infrared waveform synthesizer. Dr. Phillip "Donnie" Keathley has greatly supported the evaluation of the streaking measurements and I would like to thank him for the few but very fruitful discussions. Not to forget Dr. Guanjin Ma when he joined us over a period of time and invested in theoretical modeling of waveform-driven HHG, as well as Maximilian Kubullek that joined our efforts recently.
The XUV photodiode calibration measurements were done at PETRA III P04 beamline with Dr. Moritz Hoesch, whom I would like to thank for those data and for his advice and knowledge regarding XUV/SXR optics for the HHG beamline.
Apart from the "synthesizer team", I like to thank Dr. Nicolai Klemke (cheers mate) for the nice chats about common interests and joint work we published. Also thanks to my colleagues Dr. Giovanni Cirmi, Dr. Halil Olgun and Dr. Huseyin Cankaya for the friendly collaboaration and support.
Furthermore, the travel to conferences, group gatherings and probably the thesis itself would not have been possible without Uta Freydank - many thanks.
I would not have continued in the field of physics without the great support of my parents and family. Their motivation, backing and trust were and are most important for me. The freedom to do what I like and the encouragement to continue going on new paths is unbelievable. Also the (rare) time I spend with my sister, the telephone calls with my mother and the multiple support from my grandparents − thank you. Finally, my life with Louisa gave us so many moments, friends and fun that I do not want to miss. You gave me the feeling to always feel at home even though my head was still in the lab.

Contents

List of Abbreviations . . . .

1 Broadband Coherent Light Fields **1**
1.1 Broadband Laser Sources 1
1.2 Nonlinear Broadband Frequency Conversion 2
1.3 Control of the Electric Field 4

2 Synthesized Light Fields **7**
2.1 Synthesized Sub-cycle Light Fields 8
2.2 Presentation of the High-Energy Parametric Waveform Synthesizer 9
2.2.1 Ti:Sapphire Pump Laser 10
2.2.2 Broadband CEP stable Seed and Parametric Amplification 13
2.2.3 Spectral Phase Control and Characterization 18
2.2.4 Coherent Synthesis 28
2.2.5 Spatial Characterization and Stabilization 32

3 High Harmonic Generation with Synthesized Infrared Fields **37**
3.1 Introduction to High Harmonic Generation 37
3.1.1 Theory of High Harmonic Generation 38
3.1.2 Multicolor driven HHG 46
3.1.3 The Isolated Attosecond Pulse 47
3.2 Waveform Dependent Strong-Field Control and Attosecond Science 49
3.3 The Attosecond Beamline 50
3.3.1 Experimental Setup 50
3.3.2 High-Pressure Gas Cell 53
3.3.3 Beamline Modification 54
3.3.4 Experimental Data Recording and Processing 58
3.3.5 XUV Photodiode 63
3.3.6 Electron Time-of-Flight Spectrometer 66
3.4 Waveform-Controlled HHG in Argon and Neon 67
3.5 Attosecond Streaking 74
3.5.1 The Attosecond Streaking Experiment 76
3.5.2 Shaping the Attosecond Pulse 82
3.6 Waveform Controlled HHG in Neon and Helium 84
3.6.1 Generation of “Water Window” Soft X-Rays 84

4 A Beamline for Future Pump-Probe Experiments **95**

5 Summary **99**

6 List of Publications **121**

7 Appendix **123**
7.1 Feedback Synchronization 123
7.2 RP-CEP Scan for f=400 mm 126
7.3 XUV grating 127
7.4 Toroidal Mirror 128

List of Figures

1.1 A few-cycle pulse given with electric field envelope and electric field for different values of the carrier-envelope phase (CEP). 2

2.1 Synthesis of short pulse electric fields at central wavelength λ and $2 \cdot \lambda$ and at different relative time delays. The fundamental fields are defined with CEP $= 0$ except for the field with a CEP flip equals to CEP $= \pi$ 8

2.2 Capture of the monitoring display as developed for constant beam profile recording and visual feedback. The Screenshot was taken on October 27, 2022 and thus displays the beam deviations over a period of $\approx$ two months with respect to the defined reference day. The top row displays a live view, the second row is the daily average and the third row is the average of the reference day. The last two rows display the deviations with the daily deviations (subtraction of live frame - today's average) in the fourth row and long-term deviations (live frame - reference day average) in the bottom row. The three columns represent three different cameras positioned at the compressed laser output, the uncompressed output and after the external compressor. The positions are indicated in figure 2.5 as (CAM1-3). 12

2.3 Relative log of the Laser intensity. The permanent log is recorded single shot and shown for a period of ≈ 2 months. The data is shown with a moving average over 100 samples. A deactivated beam-pointing stabilization explains the drops in intensity between October 6, 2022 and October 16, 2022. The long-term decreasing slope shows the effect of freeze over on the crystal due to the accumulation of water in the vacuum chamber. The recovery (temperature cycling) shows the intensity increase on November 8, 2022. 12

2.4 Scheme of dispersion and spectral management of the first-generation synthesizer. A CEP stable 1.06μm pulse drives an initial white light (WL) in 3 mm YAG. The WL is split and partially recompressed by intermediate double-chirped mirrors (DCMs). Three channels are shown with three amplification stages each. A final beam combination via dichroic mirror (DM) optics and synchronization via a balanced optical cross-correlator (BOC) is shown on the right side. The feedback signal is derived from DM leakage with the main beam ending at a vacuum chamber, indicating the intended application for HHG. From [43] 15

2.5 Scheme of the current implementation of the PWS adapted from [44]. The pump laser is shown on the top left with Compressor C1 located closely and compressor C2 located to the right side. The CEP-stab. seeder to the bottom left with the first f-2f characterization on the 1040 nm seed beam. Delay management of pump and seed prior to the OPA channels is located in the center. The VIS-Channel is grayed out as it is currently not integrated. Beam combination via dichroic mirrors (DM) and feedbacks are located on the right side. Pointing stabilization (PS), including position-sensitive detectors (PSD) for each spectral channel. Second f-2f and integrated f-f spectrometer and 2DSI setup for temporal and spectral phase control. Spatial f-2f setup with CCD camera and beam profile characterization right before the HHG chamber on top. The camera positions (CAM1-3) indicate the beam profile monitoring system. 17

2.6 Spectra of the PWS. WL generated seed, first, second and third amplification stage for NIR and IR channel. Spectra taken with Ocean Optics Flame (Si detector) and Ocean Optics NirQuest (InGaAs detector). The first and second stage is measured via fiber coupling (FG105LCA, Thorlabs). 18

2.7 Group delay (GD) characteristics of optical elements as transmitted in the PWS (red-ish colors) and group delay of custom double-chirped mirror (DCM 1-3) and dichroic mirror (DM 1,2) (blue-ish colors). The DCM group delay is plotted as the average of a DCM pair. The GD of the DMs is given for the reflection. The transmission mainly exhibits a linear phase and is not plotted. The linear delay offset is removed for better overlap and visibility. The spectral location of the synthesizer channels are indicated. DCM and DM Data from [60], other data from [61] and references therein. 19

2.8 Comparison of dielectric chirped coating design for ultrabroadband optics. The newly developed DAM structure on the lower panel as used for the PWS. Adapted from [60] 21

2.9 Scheme of a Two-dimensional spectral shearing interferometry (2DSI) setup for pulse characterization. The pulse under test is only reflected by silver mirrors before the focus in the BBO crystal exploits the $\chi^{(2)}$ nonlinearity. A second "ancillae" pulse pair is prepared in a Michelson interferometer equipped with two narrowband bandpass interference filters (IF) slightly sheared in frequency. The combination of narrowband IF allows for ≈ 1 nm bandwidth. The central wavelength of the ancillae are separated by ≈ 5 nm. One arm of the interferometer is modulated as indicated by the arrow to introduce a time delay. The signal from the 2DSI is collimated and focused in a spectrometer. The control of delay and synchronized recording of the spectra is computer controlled. . . . 22

2.10 Characterization of the NIR and IR pulse by means of 2DSI. (a1,b1) shows the recorded spectrogram with the time delay between the ancillae pulses τ_{CW}. (a2,b2) displays the measured spectral phase and the spectrum. (a3,b3) shows the pulses in time domain measured to 6 fs FWHM (6 fs TL) for the NIR and 8.1 fs FWHM (7.2 fs TL) for the IR channel. 24

2.11 Characterization of the NIR and IR pulse simultaneously by 2DSI. The bandwidth in a single measurement spans from 670 nm to 2200 nm. The measurement is taken with the ancillae at 804 nm and 808 nm and a BBO of 10 μm in type II phase-matching. 25

2.12 Numerical delay scan based on 2DSI measurements of NIR and IR channel. The electric fields of the synthesizer, depending on the delay are plotted as a colormap (a). The location of the zero nodes ($E(t) = 0$) with respect to the peak for left and right first node is indicated by cyan and magenta dots is plotted in panel (b) with the average in black. The average temporal distance of the first zero nodes (left to right zero crossing) is taken as a half-cycle duration and the wavelength scale is plotted accordingly to estimate the central wavelength locally for the central cycle. Out of time zero, the central wavelength corresponds to the single IR channel one (1.6 μm) whereas around time zero, the calculated half-cycle durations dynamically modulate the central wavelength of the synthesized pulse. CEP variation of the field at $t = 0$ shown in panel (c) and lineouts from the delay scan around time zero given in panel (d). In panel (d) the nodes are marked exemplarily. 27

2.13 In-line multi-phase meter as developed for the measurement of relative phase (RP) and CEP in a PWS. The individual pulses are combined at the dichroic mirror (DM1) and a leakage of the mirrors drives the phase meter. A first delay (DL1) between the pulses via chromatic dispersion is introduced before the long wavelength pulse (IR) undergoes SPM in a bulk crystal. A second delay (DL1) rearranges the pulses in time before the SHG of the broadened IR channel. A polarizer (Pol.) projects the polarizations on the same plane. Panel (b) plots the measured signal of the optical multichannel analyzer (OMA) vs. time. The retrieved measured CEP and RP is plotted in (c) with the feedback signal controlling the piezo (PZT) delay stages in (d). The measured RMS noise (d) reads 70 mrad RMS for the RP and of 233 mrad RMS for the CEP (both single-shot every-shot, calculated over 900,000 consecutive pulses). From [44] 29

2.14 Experimental setup (a) of a spatially resolved f-2f measurement. A weak copy of the main beam is guided to a spherical mirror. The second harmonic generation (SHG) in BBO is tuned for the IR channel. The resulting spectra are shown in (b). A spectral overlap of fundamental NIR and second harmonic IR is selected by a bandpass filter and projected on the same polarization by a wire grid polarizer (Pol.) The second spherical mirror images the focus on a CCD camera. 31

2.15 Measurement and control of CEP and RP parallel to the recording of the spatial interference between the NIR channel and second harmonic of the IR channel at focus. A measure of the interference is given as integral of a detector signal. The insets display the signal for constructive (left) and deconstructive (right) interference. First, the phases are stabilized and a constant constructive interference is observed. The zoomed region shows the modulated signal. First, the CEP is modulated at low and high frequencies and second, the RP is modulated at low and high frequencies. The interference signals follow the modulated phases. 32

2.16 Beam profile of the seed beam (a) NIR channel (b) and IR channel (c). The diameters are measured to 5.8 mm for the seed, 4.7 mm for NIR and 10.9 mm for IR at 4σ $(1/e^2)$. 33

2.17 Analysis of the focus for NIR and IR channel with a PCB board CCD camera mounted on the stage of the HHG gas cell. The gas cell is removed from the focus positions and seen to the left. The beam profile characterization happens in-situ in the vacuum chamber but at atmospheric conditions. 34

2.18 Comparison of focus measurements of the IR channel. Panel (a) plots the waist along the focus as measured by the two-photon CCD absorption $\sqrt{2}$ corrected compared to a knife edge measurements. The knife edge data at two positions are displayed by the insets. Gaussian fits are plotted for CCD and knife edge data. Panel (b) and (c) display a measurement of the focus with an pyroelectric-based detector (Pyrocam 4, Spiricon, pixel pitch 80 μm) which pixel pitch is too large for precise detection. At least an upper limit can be given. 35

2.19 Beam profile scan along the laser focus for NIR channel (left) and IR channel (right). The waist at focus is measured to 44 μm and 47 μm, respectively defined at $4\sigma = 1/e^2$. The insets display the beam profiles at selected positions as marked by the arrows. The laser direction is from right to left, given by the positioning of the stage. The x axis "distance" are absolute positions. 36

3.1 Multiphoton (left) vs. tunnel ionization (right). In multiphoton ionization, the potential is reached by absorbing several photons ob energy $h\nu$. Tunnel ionization describes the passage through the Coulomb barrier that is lowered in the field of an intense laser. from [109] 39

3.2 Electron trajectories for 800 nm driving laser (left) and 1600 nm driving laser (right). The driving field is plotted in black, and the electron trajectories in color. Note the drastically increased electron excursion for the 1600 nm driving laser. 40

3.3 Kinetic energy of the returning electrons. Separated in short (green) and long (red) trajectories. Note the increased kinetic energy by almost an order of magnitude for a two-fold increase of the driving laser wavelength. Based on calculations for laser wavelength of 800 nm (left) and 1600 nm (right). 41

3.4 Ionization vs. recombination time of the tunnel ionized electrons in the classical trajectory picture of HHG. 42

3.5 Kinetic energy of the electrons with respect to their recombination time. Short trajectories in red, long trajectories in green. Driving laser wavelength of 800 nm (left) and 1600 nm (right) 45

3.6 Effect of plasma defocusing on the HHG yield. Plotted is the enhancement factor that is proportional to the HH energy and comprises the propagation effects of HHG. The dotted line is calculated without propagation effects. The solid line includes propagation effects. From [133] 46

3.7 Transmission properties of metal filters (top) and GDD properties (bottom) with a thickness of 200 nm. For greater visibility, the low dispersion at high energies is multiplied by $\times 100$. The XUV/soft X-ray data is downloaded from [164] . . 48

3.8 Attosecond beamline in the initial state as used for attosecond streaking measurements. The PWS pulse enters on the left and undergoes a final reflection on a pair of DCM (SDCM0) before the pulse is split in the vertically arranged CaF_2 splitting unit. The reflection of the CaF_2 window is guided to the second chamber while the transmission is focused with a spherical mirror ($f = 500/375$ mm) on the HHG gas target. The lower energy pulse copy, the "streaking field" is recombined with the HHG beam in the second chamber by means of a holey mirror and focussed at the TOF spectrometer while the harmonics are imaged with a toroidal mirror at the TOF. The driver beam is observed after passing through the beamline with a kick-out mirror as sketched by the dashed lines. The inset shows a camera image as used for geometrical alignment of the beams and TOF. To the right, a grating spectrometer (251MX, McPherson) with XUV CCD (Newton CCD, Andor, 13.5 μm pixel pitch) is placed. The frame and floating table is indicated with the breadboards in the first two big chambers connected to the floating table. 52

3.9 Semi-infinite gas nozzles for the generation of HHG. Glass capillaries from hollow core fibers are glued to metallic tubes (a). Tapering of the thick walls (c) allowed for well-shaped conical holes. A metal gas cell (d) is shown in detail and mounted with the Luer-lock system in the high-pressure gas cell (e). 54

3.10 Attosecond beamline modified for the generation and efficient detection of SXR harmonics. After final compression on a pair of DCM (SDCM0), the PWS pulse is focussed with an $f = 4$ inch 45° degree OAP mirror on the HHG gas target. An additional motorized wheel to hold SXR metal filter foils and the XUV photodiode is mounted in the second chamber. The toroidal mirror installed is specified with an imaging distance of $S = 746.39$mm. The input slit of the XUV spectrometer is placed as close as possible to the image point of the toroidal mirror. 56

3.11 Measurements of the movement between TOF spectrometer as mounted on a solid frame and the floating optical table. Data retrieved by analyzing the beam position on a CCD camera with a temporal resolution of 1 s. The positioning of laser diode and CCD camera is shown in figure 3.12. The left plot shows some manual excitation of the table. The position in vertical and horizontal direction does not recover. Four exemplary frames of the CCD camera recorded beam profile at characteristic times. The right panel shows the measurement while the vacuum chambers are evacuated (pumped) repeatedly two times. Again, especially the vertical positions stay with an offset. 57

3.12 Infrastructure of the laser system and attosecond beamline with a special focus between ground floor referenced and floating optical tables referenced setups as marked by the colors (see legend) Left panel displays the initial setup with the "T" connected optical tables and floating breadboards. The force raised by the vacuum leads to a vertical tilting (indicated by α). The right setup shows the disconnected tables and the optical table of the beamline fixed to the frame. . . 57

3.13 Geometry of the gratings as used in the grating spectrometer. The high photon energy grating (2400 gr/mm) requires different angles compared to the low photon energy gratings (300 gr/mm, 1200 gr/mm) 59

3.14 Calibration procedure of HHG spectra based on harmonic peaks. The raw data are background corrected (a) and a pair of neighboring harmonic peaks in first and second diffraction order are manually selected as indicated by dashed lines (b). Based on the grating equation and known grating geometry, the calibrating spectra including the Jacobi correction is plotted in (c). 60

3.15 Calibration procedure for HHG spectra based on absorption edges of metallic filters for broadband continuous spectra. The raw data are background corrected (a) and two spectra transmitted through different metallic filters are overlayed. The absorption edges are identified as indicated by dashed lines (b). Based on the known energy from literature of the absorption edges, the calibrating spectra, including the Jacobian correction, is plotted in (c). Filters used in this calibration are Boron (188 eV) and Mylar (C-edge, 284 eV). 61

3.16 The reflectivity of XUV optics and quantum efficiency (QE) of XUV CCD camera as used in the beamline and applied for intensity calibrations. The reflectivity of the gratings is plotted for the 1^{st} diffraction order. The reflectivity of gold (Au) at given incident angle of 4° degree is taken for the toroidal mirror. The reflectivity of Nickel (Ni) plotted for comparison. 61

3.17 The representation of a synchronized RP-CEP scan. The top panel (a) plots the measured RP and CEP data. The two curves for the CEP correspond to the measured CEP at the CEP stable front-end "CEP seed" (blue) and to the CEP measured with the multi-phase meter at the PWS output (green). The central panel (b) shows the spectrogram of the recorded HHG spectra in argon and the bottom panel (c) plots the integral of the spectra in arb. units. The plots show several sections of CEP and/or RP sawtooth like modulation and short sections of stabilized conditions. A tight dependence of the HH spectra on the phase values is observed. 63

3.18 Calibration measurements of an XUV photodiode (SXUV100, Opto Diode) at P04, PETRA III beamline. The responsitivity curve (a) as provided by the manufacturer for the photodiode of 10×10 mm active area. The measurements of our photodiode "UFOX" compared to the calibrated photodiode from P04 beamline ón the undulator beam (c) and calculated power (d). The resulting photon flux (e) is plotted including the photon flux as displayed by the beamline software. 65

3.19 HHG spectra generated with the PWS. Signal generated with the NIR channel only (red) and XUV continua as generated with NIR and IR channel at different phase settings. All spectra generated with argon. 67

3.20 Generation of HH continua in argon with the PWS as function of the RP and CEP. The spectra are recorded in the low energy range with the 300 gr/mm grating (a,c,d,g,h) and in the higher energy range with the 1200 gr/mm grating. The top panels (a,b) display a RP scan at a fixed CEP showing the formation of various broadband spectra. The higher energy spectra indicate an increase of yield and cut-off energy around the time zero interaction region. The direction of the RP is given with the IR channel advancing towards negative RP values. A $\pi/2$ CEP shift changes the spectra across the RP axis (c,e). The RP-CEP maps are plotted as a function of the CEP in (d,f,g,h,i,j) for fixed RP values as indicated at the plots. All continua show a CEP dependence with an increased contrast close to RP ≈ 0 and a moderate slope outside the time overlap. The spectra are recorded with 200 ms integration time and a 500 nm Beryllium filter is applied to block the driving laser beam. Taken from [45] 69

3.21 Record of the HHG spectra for a RP-CEP scan in neon. The PWS waveform is focused by an $f = 375$ mm spherical mirrors on a 300 mbar backing pressure neon gas nozzle of 2 mm length. The spectra are resolved with the mid-energy (1200 gr/mm) grating. According to an RP $= 0.7$ rad, the CEP scan is plotted on the right panel. 70

3.22 Long-term stability measurements of generated HHG continua by the PWS waveform. From top to bottom: Plots (a)-(c) show HHG generated in argon at 300 mbar backing pressure and plot (d) showing HHG generated in neon at 550 mbar backing pressure, all with $f = 375$ mm focusing. 72

3.23 HHG spatial profiles recorded with the XUV CCD camera. Panel (a,b) is measured spectrally resolved from the 1^{st} diffraction order and vertically resolved in spatial dimension. (a) shows distinct harmonics when driven with the single NIR channel, while (b) shows a continuous spectrum when driven with the synthesized PWS as input pulse. The XUV continuum conserves a single coherent profile of the HHG continuum. On the path from the source to the spectrometer apparatus, the HHG beam is deflected from a flat gold mirror at 4° grazing incidence. Panel (c,d) show the adjacent zero-order reflection from the grating, therefore imaging the x and y spatial dimension on the XUV CCD camera for single NIR channel (c) and synthesized PWS (d). The hard cuts on the imaging is the limitation by the entrance slit opening, that the HHG at the given distance of 1.7 m from the source is clipping. Measurements are taken at 0.2 s and with the 300 gr/mm grating installed. 74

3.24 Schematic of an attosecond streaking experiment. The laser ((N)IR) overlaps with the attosecond pulse (XUV) in a noble gas. The photoionized electrons are streaked by the laser field and recorded by a time-of-flight (TOF) spectrometer. The modulated electron momenta as shown in the simulated streaking spectrograms resemble the vector potential $A(t)$ of the laser pulse recorded as a function of τ (+T). The polarization of the laser field in the simple case is linear, so that the electric field and the TOF apparatus are in plane. 76

3.25 Reflectivity of a CaF_2 plate as function of incident angle for S- and P-polarization for the central wavelength of 1.4 μm (a) and reflectivity as function of wavelength for incident angles as given in the legend (a). The beam splitting assembly is shown in (s) with the dotted line being the reflection for the pulse copy. 77

3.26 Energy calibration of the TOF apparatus. The TOF data is calibrated by matching the XUV comb peaks (b) to a calibrated spectrum from the XUV CCD camera(a). The dipole moment of the streaking gas (neon) is given in the right scale of (a). Cross sections taken from [188]. The energy calibrated spectra is compared in (c) with the XUV spectrum shifted by the ionization potential and corrected by the dipole moment. 78

3.27 First attosecond streaking measurement with a PWS. Measured (a) and calibrated (b) streaking spectrogram and retrieved, calculated spectrogram as with VTGPA (c). 79

3.28 Retrieved streaking field E(t) and corresponding instantaneous intensity I(t) and intensity envelope A(t) (left panel). Spectral intensity of the retrieved streaking field (right panel) as calculated directly from E(t) via FFT. 81

3.29 Retrieved attosecond pulse from streaking measurement (figure 3.27). Plotted is the intensity and phase in time domain. The FWHM duration is measured as $\tau_{FWHM} = 240$as 82

3.30 Consecutive streaking measurements over a time span of ≈ 2 hours to demonstrate a long-term stable operation of the synthesizer phase-locked waveform and HHG beamline. First two rows show streaking traces at constant phase settings of the waveform. Bottom left plot shows the CEP flipped waveform and bottom right panel plots the evaluated electric field of the IR waveform. 82

3.31 Attosecond streaking measurements of various HH continua as generated with the PWS. The XUV continua are tuned in bandwidth and central photon energy. XUV continua are generated from argon (a,b) and neon (c,d). The measured photoelectron spectra as measured (i) and reconstructed (ii) with the retrieved attosecond pulse in time (iii) and photon energy (iv) domain. The transform-limited pulse envelope and FWHM duration is given in black. The XUV spectrum is measured independently from the XUV CCD camera and plotted in black for comparison. from [45] 83

3.32 Backing pressure scan for neon (a) and helium (b) gas target. The spectra are generated in a metallic gas nozzle with ≈ 0.5 mm inner diameter and the single IR channel. The position of the nozzle is optimized with a difference of 250 μm between the neon and helium measurements. A 200 nm Ti filter blocks the IR light. The beams are focussed with $f = 6$ inch leading to a peak intensity of $I_{peak} \approx 2.5 \times 10^{14}$ for the IR channel. 85

3.33 Gas nozzle scan for neon (left) and helium (right) gas target. The spectra are generated in a metallic gas nozzle with ≈ 0.5 mm inner diameter and the single IR channel as driving pulse. A 200nm Ti filter blocks the IR light. Both measurements are taken with a backing pressure of 4 bar. The beams are focussed with $f = 6$ inch leading to a peak intensity of $I_{peak} \approx 2.5 \times 10^{14}$ W/cm^2 for the IR channel. 86

3.34 HHG results of RP scans of the PWS waveform in neon and helium. The CEP is optimized qualitatively for highest cut-off HHG for the spectra around time zero and stabilized during a scan. The IR channel is advancing to the left side of the x-axis. Scan (a) is recorded with neon at 4 bar backing pressure. Due du ionization at time zero and onwards, the harmonic emission is suppressed. Panels (b-d) are recorded with helium as generation gas at a backing pressure of 10 bar. To the right, the adjacent lineouts are plotted for two spectra from the scan and for case with transfer function (W/ tr. func.) including XUV CCD QE, grating response, filter transmission and for the case without transfer function (w/o tr. func.). Mainly due to the high slope of the XUV CCD in the range from $100-200$ eV, the spectra are heavily altered. The colormap plots show the spectra without transfer function. The scans in helium are taken at various positions of the gas nozzle as indicated by Δz. A 300 μm Ti filter is used to block the residual IR light with exception to panel (d) where 2×100 μm Al is used. 87

3.35 HHG dependency on the CEP of single IR channel (a) and PWS waveform (b). The RP of the PWS is fixed around time zero. The measurements are taken with helium at 10 bar backing pressure and the residual IR light is blocked by 2×100 nm Al filter. 88

3.36 Optimization of the gas cell position for the single IR driven HHG in helium at 8 bar (a) and neon at 2 bar (b) backing pressure. The spectrogram displays the data without transfer function. Panel (a2,b2) plot the lineouts in dotted lines and the transfer function corrected spectra in solid lines. The residual IR light is filtered by 100 nm Al and 100 nm Cu filter. 89

3.37 Presentation of the RP-CEP scan in helium at 8 bar backing pressure and a focusing condition of $f = 400$ mm. The recorded XUV spectra are presented as a function of the RP (a1) and a single CEP. (b,c) correspond to CEP scans at a specific RP indicated by the solid markers in (a1). (d) corresponds to a CEP scan measurement of the single IR channel. All measurements are taken with the same position of the gas nozzle. The spectrograms do not contain the transfer function while the pulse energies and photon flux given in rows 2 and 3 include the transfer function and correspond to photon numbers at the source. The photon flux is given in a 1% bandwidth (BW) given by the legend. The lineouts indicated by the dotted lines and marked (1-4) are plotted in (e), showcasing various continua as generated with the PWS compared to the single IR channel in red color (5). 91

4.1 Extension of the beamline for attosecond transient absorption experiments and photo electron measurements. A powerful pumping system is added for the high-pressure gas cell. XUV optics with longer imaging distances allows for additional differential pumping. The newly designed experimental chamber is located between the toroidal mirror (TM) chamber and spectrometer. 97

7.1 Procedure in synching the RP and CEP as stabilized and recorded with the feedback system at 1 kHz (FB data) with the HHG spectra. The lower resolution data (UDP stream) are exchanged between FB system process and XUV CCD recording by means of the User Datagram Protocol (UDP). For details, see main text. 125

7.2 Data of figure 3.37 plotted with an extended RP axes. Out of time zero, the single IR channel contribution becomes visible. 126
7.3 Specification of XUV to SXR gratings as mounted in the grating spectrometer (251MX, McPherson). 127
7.4 Specification of the toroidal mirror #2 with $S = 746$ mm. 128

List of Tables

2.1 A listing of optical elements as propagated by NIR and IR channel starting from the white-light generation (WLG) to the point of HHG in the vacuum chamber. SAP:sapphire, FS: fused silica, SDCM#: custom double-chirped mirror, BBO: β-Bariumborat, BC: beam combiner, BS: beam splitter, DM#: custom dichroic mirror 20

2.2 Peak intensity and rayleigh range for NIR, IR channel and synthesized pulse as calculated for the focus measurements with a $f = 6$ inch off-axis parabola mirror. 36

3.1 Parameters of toroidal mirrors as used in the beamline 51

3.2 Details of XUV/SXR gratings as used with the McPherson 251MX spectrometer. The gratings are blazed aberration-corrected concave gratings for a flat-field image plane. See figure 7.3 in appendix. 58

3.3 Ionization potential I_P of noble gases 75

3.4 Summary of the photon numbers at source for the single IR channel and synthesized waveform (Synth) driven conditions. The macroscopic parameters such as focal length, gas type and nozzle diameter are given. The HH yield is given in pulse energy (pJ) and flux (photons/s). For high photon energy HHG, the flux is given in the water window (WW) spectrum and at 1 % bandwidth (BW). A couple of published sources with flux measurements in the WW regime are added for reference. The pulse energy and central wavelength of the driver pulse are given in the comments. 93

List of Abbreviations

Abbreviation	Description
PWS	parametric waveform synthesizer
HHG	High Harmonic Generation
WW	Water Window (photon energy range 284-530 eV)
ATI	above threshold ionization
IAP	isolated attosecond pulse
OAP	off-axis parabolic (mirror)
TOF	time-of-flight
BBO	beta barium borate
KDP	Potassium Dideuterium Phosphate
BS	beam splitter
BC	beam combiner
CEP	carrier-envelope phase
RP	relative phase
DCM	double chirped mirror
DAM	dual-adiabatic-matching
SFG	sum frequency generation
DFG	difference frequency generation
OPA	optical parametric amplifier
OPCPA	optical parametric chirped pulse amplifier
DOPA	degenerate optical parametric amplifier
NOPA	noncollinear optical parametric amplifier
fps	frames per second
FT	Fourier transform
FFT	fast Fourier transform
FWHM	full width at half maximum
GD	group delay
GDD	group delay dispersion
GTI	Gires-Tournois interferometer
GUI	graphical user interface
GVM	group velocity mismatch
HCF	hollow core fibre
NIR	near-infrared (here mostly related to spectral range 600 nm – 1000 nm)
IR	infrared (here mostly related to spectral range 1000 nm – 2500 nm)
XUV	extreme ultra-violet (here mostly related to photon energy range $<$ 100 eV and $>$ 10 eV)
SXR	soft X-ray (here mostly related to photon energy range $>$ 200 eV)
PUT	pulse under test
SHG	second harmonic generation
THG	third harmonic generation
2DSI	Two-dimensional spectral shearing interferometry
FROG	frequency-resolved optical gating
SPIDER	spectral phase interferometry for direct electric-field reconstruction
SPM	self-phase modulation
TL	transform limit
WLC	white light continuum
FPGA	Field Programmable Gate Array

1 Broadband Coherent Light Fields

The high peak intensity and broad bandwidth of modern laser sources significantly expanded scientific applications. Starting from nonlinear spectroscopy [1], as historically pioneered with dye lasers, the possibilities for light-matter interaction using ultrafast Ti:Sapphire lasers [2] became manifold.
The short duration of such laser pulses enables unpreceded time-resolved light-matter interaction. Early experiments with a laser pulse intensity of 10^{13} W/cm^2 at the interaction with xenon atoms have demonstrated nonlinear above six-photon ionization (ATI) [3] and with the existence of few- to single-cycle laser pulses Paulus *et al.* have shown the carrier-envelope phase (CEP) dependent photoionization as measured in a stereo ATI setup [4] due to the asymmetry in the electron yield. The attosecond time domain is entered with the generation of high harmonics (HHG) from a laser and the subsequent isolation of a single isolated attosecond pulse (IAP). The HHG process is discussed in section 3.1. Broadband laser pulses and subsequently generated attosecond pulses enable control and observation of ultrafast light-matter interactions demonstrated in photoionization in molecules [5], atomic relaxation dynamics [6], charge migration in molecules [7], real-time observation of electronic motion in krypton [8], [9], exciton dynamics [10], the dynamic AC-Stark effect [11] and even ionization dynamics on a sub-cycle time scale [12].

1.1 Broadband Laser Sources

From the time when Theodore Maiman confirmed experimentally in 1960 the light amplification by stimulated emission of radiation (LASER) [13], a major interest of research remained to this day: How to shorten the laser pulse duration? Maiman's first laser, a flashlight-pumped Ruby laser, even was a pulsed laser as defined by the lifetime of the excited state. The motivation to generate pulses versus continuous-wave (cw) operation stems from (1) the ability to generate very high peak intensities and (2) the ability to generate the shortest and best-defined man-made event. Pulses in the time domain require a certain minimum bandwidth in frequency

domain, since the summation of phase-locked frequencies leads to the isolation of a defined pulse according to Fourier synthesis.

After the birth of the LASER as a solid-state laser, gas and dye lasers became more popular in the first decades due to their capabilities in energy and tunable bandwidth [14]. In 1986, P. Moulton *et al.* demonstrated the capabilities of the Ti:Sapphire laser [15] as a broadband solid-state laser with a gain bandwidth from 660 nm to 1180 nm established the Ti:Sapphire laser as a very popular laser to this day. The concept of mode-locking in a Ti:Sapphire laser oscillator enabled the generation of sub 10 fs pulses [16]. Incorporating the effect of intracavity nonlinear broadening while maintaining the dispersion control enabled ≈ 5 fs pulses from a Ti:Sapphire oscillator [17].

The description of a laser pulse in terms of pulse envelope and carrier electric field oscillating at the period of the laser frequency and a spatial dependent amplitude $A(z)$ and phase usually as radial coordinate z. The shorter the pulse, the closer the envelope follows the carrier field in terms of duration. The carrier-envelope phase (CEP) defines the phase and thus the maxima of the carrier field with respect to the maximum of the envelope, as shown in figure 1.1

$$\vec{E}(z,t) = A(z,t) \cdot e^{i(kz-\omega t+\phi_{CE})}\hat{x} \tag{1.1}$$

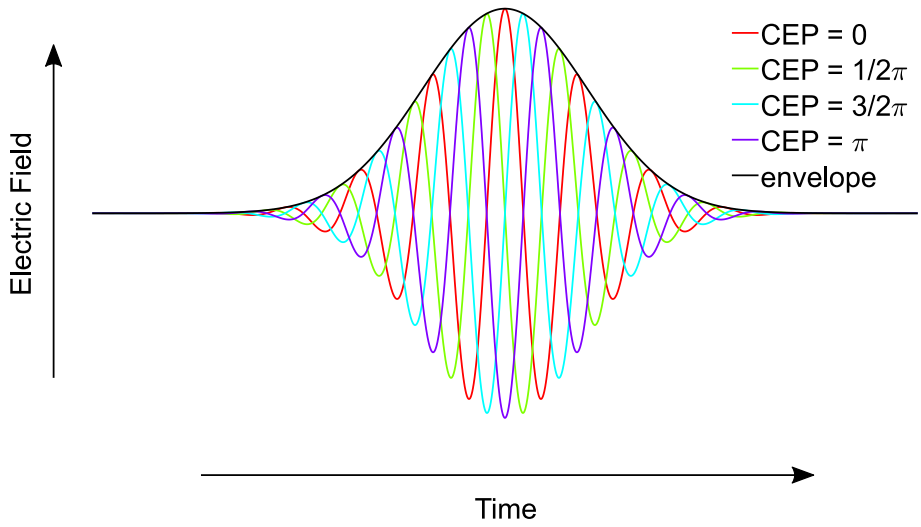

Figure 1.1: A few-cycle pulse given with electric field envelope and electric field for different values of the carrier-envelope phase (CEP).

1.2 Nonlinear Broadband Frequency Conversion

Ultrabroadband, few-cycle Ti:Sapphire oscillators are limited to a pulse energy of a few nJ. The application of Ti:Sapphire as a laser amplifier at higher energies limits the pulse duration to ≈ 20 fs due to the gain narrowing effect during amplification. Therefore, it is not possible to

obtain pulses with few or single cycles at mJ energies directly from the laser gain medium. The high peak intensities $> 10^{14}$ W/cm^2 of such lasers, however, allow to drive nonlinear polarizations in various media from solids to gases and thus to generate new frequency components almost independently of the fundamental laser gain spectrum.

The second-order nonlinear process is exploited for amplification in the Optical Parametric Amplification (OPA). Common solid media with high nonlinear index are e.g., Lithiumniobat ($LiNbO_3$), β-Bariumborat (BBO) or potassium dihydrogen phosphate (KDP). Those materials allow efficient energy conversion from an intense "pump" pulse to a weaker "signal" or "seed" pulse that gets amplified. The residual energy between pump and signal photon remains as an "idler" pulse. Depending on the phase matching between the constituent pulses, the process can be tuned for the parametric amplification of a longer wavelength signal, an up-conversion or sum frequency generation (SFG) of two photons and a down-conversion or difference frequency generation (DFG) between two photons. Since the nonlinear crystal does not store any energy, the achievable energy with the chirped pulse amplification (OPCPA) technique can be in the range of several 100 mJ before thermal limits are reached. The bandwidth of the parametric amplification process is limited by the group velocity mismatch between the constituent pulses as defined by the refractive index and polarization. OPAs that exploit the good match of Ti:Sapphire wavelength and the group velocities in BBO have an amplification bandwidth close to an octave in the near- and infrared ((N)IR) spectrum [18], [19]. Ultrafast sources in the far-infrared have been realized via DFG [20]. During the amplification process in an OPA, the CEP is preserved, allowing the generation of CEP-stable pulses with few cycles. Since OPAs are a central unit of the parametric waveform synthesizer, they are discussed in detail in chapter 2.2.2

Nonlinear third-order processes such as self-phase modulation (SPM) lead to modulation of the temporal phase of the pulses during propagation, generating new frequencies. At relatively low energies below the damage threshold, this behavior enables the generation of multi-octave spanning spectra, so-called white light continua (WLC) when focussing a laser pulse in a solid media such as Sapphire (SAP) or Yttrium-Aluminium-Garnet (YAG). Depending on the intensity, the Kerr effect as a third-order nonlinearity gives rise to self-focusing, which further increases the intensity until a plasma forms, which is counteracted by the plasma-induced change in the refractive index. This interplay of various nonlinear effects is discussed in the context of filamentation [21]. The WLC generation in YAG/Sapphire is a well-established method to generate broadband seed spectra for the subsequent amplification in an OPA and since the process conserves the CEP phase [22]–[24], it is well suited for phase stable ultrashort pulse generation. Apart from low energy spectral broadening, the technique of SPM spectral broadening is employed in Hollow Core Fiber (HCF) setups [25]. A fiber filled with a noble gas guides the coupled laser pulse, which undergoes SPM during propagation. A manifold compression of the initial pulse duration has been demonstrated and technological improvements have driven the pulse compression and energy scalability [26]. Due to the limited ionization threshold of the

noble gas, the pulse energy is limited and very high pulse energies (> 0.5 mJ) require very long (> 1m) fiber setups with well-controlled peak intensities along the propagation.
Recent interest in SPM-based broadening schemes has revived solid-state based broadening. Precise tuning of the solid material thickness and a manifold propagation through the nonlinear medium, hence called multiplate continuum (MPC), have shown the generation of octave-spanning spectra at very high conversion rates even for input pulses of ps duration. [27]–[29].

1.3 Control of the Electric Field

To exploit the full potential of broadband light fields, techniques are being developed to precisely control the frequencies they contain. In the femtosecond regime, the temporal structure of a light field is controlled via the spectral phase in the frequency domain. Due to the extremely short time scales, direct access in time domain is technically very limited. The devices to control the spectral phase are to a large extent targeted to ensure a single arriving time for all frequency components to compress the pulse in the time domain. The chromatic dispersion of the optical elements alters the temporal structure of the pulse in the time domain. At optical and NIR wavelengths, most optical elements i.e. substrates, laser and OPA crystals, exhibit positive dispersion, with the longer wavelength traveling faster than the shorter wavelength. To counteract the positive dispersion, grating and prism compressors are used to shorten the geometric path for the shorter wavelength. Higher order dispersion compensation and a custom dispersion design for large bandwidth is realized with double-chirped mirrors (DCMs) [30]. The DCMs as the core of the parametric waveform synthesizer dispersion scheme are discussed in section 2.2.3. Adaptive control of the light field is given via pulse shapers. The spatial light modulator (SLM) modulates the spectral phase in a liquid crystal array that transmits the spectrally dispersed pulse in, for example, a grating configuration to disperse the colors on the SLM pixels. The index of refraction at each liquid crystal pixel is controlled by an applied electric field. The spectral control with light modulators in a synthesis approach is presented in [31] for a close to single-cycle pulse.
For very short pulses, the property of CEP defines the amplitudes of the electric field in the time domain and is the central control parameter for single color few- to single-cycle sources. Characterization of the CEP via beating of the short wavelength and frequency doubled long wavelength component was first used in [32] to stabilize the CEP of a broadband Ti:Sapphire oscillator by controlling of a wedged glass to stabilize the relation between phase and group delay in the cavity. The measurement of the CEP as a beat signal in frequency, the so-called f-2f setup, is explained in detail in *phase meter* in section 2.2.4. In laser amplifiers, the pump laser intensity can be modulated by the feedback or the phase of the seed pulse to stabilize the CEP at the output of the laser amplifier. Recently, acousto-optic programmable dispersive filters (AOPDFs) are employed to control the individual CEPs of spectrally distinct portions in broadband short-wave-infrared (SWIR) OPA, leading to sub-cycle field control. [33]

Polarization control adds to the temporal control and allows for shaped ultrashort electric fields in time and space [34] as applied e.g. for single atom control and the generation of circular polarized HHG [35]. Due to the construction of pulse shapers, the bandwidth and/or pulse energy is limited and the losses are not negligible. Complex single-pulse manipulation is still limited to sub-octave pulses.

2 Synthesized Light Fields

The concept of synthesis is the most versatile approach to sub-cycle optical waveform control. The idea of synthesizing several pulses can overcome numerous limitations of today's ultrashort pulse technologies, not by replacing them, but by coherently combining them. The coherent synthesis of individual laser sources is demonstrated experimentally for a variety of sources targeting even more different applications from fiber laser coupling reaching kW powers[36], for gravitational wave detection [37], or on-chip photonics for frequency metrology [38]. Here, the subject of pulse synthesis are ultrabroadband sub-cycle pulses with precise control of the electric field approaching mJ level energies and peak intensities of 10^{15} W/cm^2. The underlying single pulses are designed with a sub-octave bandwidth that allows for efficient generation and compression. Subsequent synthesis forms multi-octave spanning spectra and allows the generation of sub-cycle pulses at high pulse energy. The primary application of the synthesized laser field are strong field processes such as e.g. HHG and the ability to shape the process by the driving waveform. As shown in figure 2.1, a combination of two short pulses with different central wavelengths deviates the electric waveform drastically from a sinusoidal modulation. Two pulses with amplitudes $A_1(t)$ and $A_2(t)$ with central frequency ω_{0_1} and ω_{0_2} respectively are synthesized. The CEPs ϕ_{CE_1} and ϕ_{CE_2} can be individually controlled or, as in our experimental case, jointly. The relative phase ϕ_{RP} between the adjacent fields is the additional control parameter in synthesized fields.

$$E(t) = A_1(t)\cos(\omega_{0_1}t + \phi_{CE_1}) + A_2(t)\cos(\omega_{0_2}t + \phi_{CE_2} + \phi_{RP}) \tag{2.1}$$

This chapter starts with an overview of the published ideas and realizations of ultrashort synthesized sources before the parallel parametric waveform synthesizer that has been finalized for long-term stable operation within the frame of this thesis is described in detail.

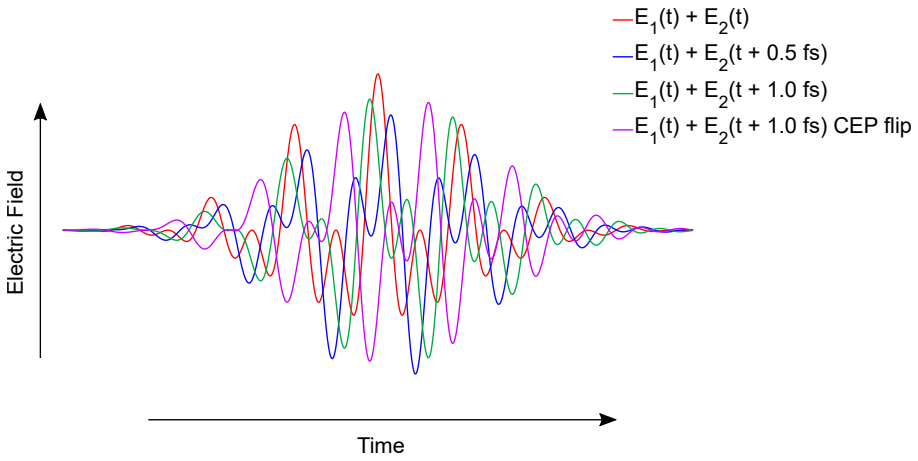

Figure 2.1: Synthesis of short pulse electric fields at central wavelength λ and $2 \cdot \lambda$ and at different relative time delays. The fundamental fields are defined with CEP = 0 except for the field with a CEP flip equals to CEP = π

2.1 Synthesized Sub-cycle Light Fields

Broadband coherent pulses, as described in earlier chapters, are the basis for sub-cycle synthesized light fields. In addition, a precise temporal lock must be maintained to a few 100 as between the electric fields. One of the first working waveform synthesizers with a pulse energy high enough to drive HHG is based on a very broadband hollow-core fiber compressor [8]. The Ti:Sapphire driven HCF generates a bandwidth from $270 - 1130$ nm [39]. For the temporal compression and manipulation of the pulse, the bandwidth is split into four spectral channels, each of which is individually compressed by DCMs and is finally recombined. During the split and recombination, the source can be seen as a fully parallel synthesizer where the relative phases can be adjusted independently. The electric field of this four-channel synthesizer has been measured in an attosecond streaking experiment, demonstrating the stability and control over the electric waveform. With the recent extension to the fourth channel in the ultraviolet (UV), the central wavelength is given at $\lambda_0 = 530$ nm. The advantages of geometrically small path differences between the point of spectral splitting and recombination are traded off against the limitations of the HCF in terms of energy at a few ≈ 100 μJ at the output of the HCF synthesizer. The sub-cycle pulse in the visible domain and generated attosecond pulses via HHG are applied to ultrafast time-resolved measurements [10], [39] giving sub-fs resolution. As a driver for HHG reaching photon energies in the water window ($284 - 533$ eV), an HCF waveform synthesizer with a longer central wavelength is an interesting approach. Recently, a $\lambda_0 = 1.7$ μm HCF synthesizer was demonstrated by Ridente *et al.* [40], albeit with a rather modest energy of 5 μJ.

Based on broadband OPAs, early ideas have considered the parallel amplification of a super octave spanning WL seed and final combination of such multicolor sources [41]–[43] for sub-cycle synthesis. The extended geometrical setup and non-common beam path of several meters,

including amplification stages, has required severe technological development to make this approach a stable and viable source. Motivated by the recent interest in the water window HHG by ultrashort infrared laser pulses, the utilization of infrared OPAs is suggested. As presented in this thesis, we have shown the long-term stable operation of sub-cycle synthesized waveforms at $\lambda_0 = 1.4$ μm for the control of HHG and subsequent streaking measurements in [44], [45]. The interest in waveform synthesis for high-energy applications has been likewise followed in the group of Midorikawa and co-workers in Japan [46]. This group presented a high-energy multi-cycle synthesizer with a total pulse energy of 50 mJ that consists of phase stabilized combination of pump (800 nm), signal (1350 nm) and idler (2050 nm) of an OPCPA. HHG with that source yielded a 0.2 μJ XUV pulse at a central photon energy of 60 eV. The authors report an increase of the efficiency by an order of magnitude compared to single channel (800 nm) driven HHG. The synthesizer is designed for high-energy but not sub-cycle pulse duration with a pump of 30 fs, signal 44 fs and idler 88 fs at FWHM. The same group shows a sub-cycle time duration in [33], [47] with µJ energies combining the techniques of pulse shapers (AOPDFs) and parametric amplification, including spectral splitting and recombination of the bandwidth. As a result, they obtain a 0.7-cycle pulse at 1.8 μm with 32 μJ of energy. The additional freedom in shaping the electric field by AOPDFs currently appears to limit the maximum pulse energy.
In order to mitigate the experimental difficulties when splitting, combining and phase-locking the constituent spectral channels, the concept of a serial synthesizer maintains a common optical beam path. Several OPA stages in series are tuned and pumped at different wavelengths. Such concepts are demonstrated in [48] for < 3 fs pulses of 1 μJ energy at 200 kHz repetition rate. Rivas *et al.* [49] published a serial synthesis approach intended to generate high peak intensities 10^{20} W/cm^2. The consecutive noncollinear (N)OPA stages are pumped with second and third harmonic of an Nd:YAG pump laser and span the bandwidth from $600 - 1000$ nm. With the development of broadband OPA schemes for Ytterbium pumped systems, the transfer from Ti:Sapphire pumped waveform synthesizer becomes feasible. This would increase the overall power drastically and experiments would benefit from a higher repetition rate [50], [51].

2.2 Presentation of the High-Energy Parametric Waveform Synthesizer

The parametric waveform synthesizer as currently operated in our lab can be considered as the second iteration of the Ti:Sapphire driven waveform synthesizer, where to a large extend Dr. Giulio Maria Rossi and Dr. Roland Mainz implemented various new conceptual, hardware and electronic developments. The final version of this apparatus has been built and continuously improved during the course of this work and adapted as a driver for HHG and attosecond experiments, while the previous first version and thus the pump laser was installed back in 2012. In order to operate the parametric waveform synthesizer as a drive source for HHG at high photon

energies, the parameters and design criteria are justified in the following.
For the generation of high-energy photons in the process of HHG, the electric field of the laser must transfer a significant amount of energy to the ionized electron. According to the scaling laws for HHG [52], the photon energy scales with the driving laser wavelength as $E_{cutoff} \sim \lambda^2$. Experiments with OP(CP)As at ≈ 1.8 μm have shown that a mid-infrared pulse is ideal for the generation of high-energy photons in the water window spectral region [53]–[55].
In order to limit the HH emission to a single event, the bandwidth of the PWS supports nearly two octaves to ensure a sub-cycle temporal duration. These parameters allow, for the first time, the exploration of the water window soft X-ray generation and isolated attosecond pulse generation without any further gating techniques. Finally, the central wavelength is located at 1.6 μm $\pm$ 200 nm, depending on the relative channels contributions.
The peak intensity necessary to drive HHG is approximately 10^{13-15} W/cm^2 depending on the gas type and desired cut-off energy, so a pulse energy of a couple of 100 μJ is required if we assume moderate focusing conditions and very short pulse durations of $3-5$ fs as possible with the PWS.

2.2.1 Ti:Sapphire Pump Laser

The PWS is a large coupled optical system with temporal and spatial dependencies. Any underperforming element of the system drastically affects the overall performance. Since the pump laser of the entire system is the first element in the chain (with the exception of the laboratory infrastructure and environment), a failure or change in laser parameters usually entails a cumbersome realignment of the full setup.
A commercial cryogenically cooled Ti:Sapphire laser system serves as pump laser for the PWS. The Ti:Sapphire laser perfectly suits as a pump laser for white light generation [21], as well as for pumping OPAs since the pump duration of ≈ 150 fs gives the right balance of peak intensity vs. energy to drive such nonlinear processes. The energy stability of our laser system is measured to be around 0.15% RMS on a daily and long-term basis. The beam profile turns out to be a very critical factor for the stability of all subsequent nonlinear processes. Any deviation from a reference beam profile changes the nonlinear interaction and beam propagation and would lead to an undetermined state of the synthesizer. Due to the rhombic geometrical shape of the Ti:Sapphire crystals and a longitudinal pumping scheme, the beam profile of our laser is close to a Gaussian mode and ideal for a stable operation of the PWS.
Lastly, the total power that a Ti:Sapphire crystal can handle limits the output energy of Ti:Sapphire laser systems compared to Yb-based systems. The broad gain bandwidth demand for a certain quantum defect between the pump photon and the emitted photon. In the case of Ti:Sapphire, the absorption at around 500 nm and the emission at around 800 nm leads to a quantum defect of ≈ 0.93 eV and thus a heat load on the crystal of around 35 % of the pump power is unavoid-

able. With the advantages but also the limitations of a Ti:Sapphire laser system that has to run in a stable and reliable regime, the total power capabilities are distributed to a pulse repetition rate of 1 kHz and a pulse energy of ≈ 20 mJ.

The laser system consists of a fully sealed Ti:Sapphire oscillator (Vitesse 800, Coherent) which has been proven to run for several years without a touch. The central wavelength is around 805 nm, with a pulse duration < 100 fs and a repetition rate of 80 MHz. Subsequent amplification of the pulses at 1 kHz repetition rate is happening in the first Ti:Sapphire amplifier (Legend Elite Duo HE+, Coherent), which consists of a regenerative amplifier and a single-pass amplifier. In both amplification stages, the Ti:Sapphire crystal is cooled down to -10 °C by means of a Peltier element. The pulse energy after amplification reaches ≈ 10 mJ. In a final amplification stage, the pulse is amplified to ≈ 20 mJ. The last amplifier (Legend Elite Cryo PA, Coherent) consists of a closed-loop helium cooling system that cools down the Ti:Sapphire crystal to ≈ 80 K as mounted on a copper cold finger in a 10^{-8} mbar vacuum environment. The cryogenic apparatus adds complexity, but the Ti:Sapphire crystal has a better thermal conductivity at lower temperatures, allowing higher pump power to be used.

The commercial laser system was optimized and equipped with anti-vibration measures, temperature and humidity monitoring and a beam-pointing stabilization system (Aligna, TEM Messtechnik). Details can be found in the theses of R. E. Mainz [56] and G. M. Rossi [57].

During the course of this thesis a couple of anomalies occured in the laser that led to a downtime of the PWS and that were initially difficult to identify. A system of CCD cameras (Ethernet CCD and CMOS, Basler) is used and a python script automatically takes and logs beam profile images. A graphical user interface displays the beam profiles as live shots, averages and historic beam profiles. The system currently consists of three cameras distributed at specific points in the optical setup and mainly serves as a qualitative and long-term observation tool. The signal on the CCD is derived from mirror leakages. Lenses reduce the beam size to fit the beam onto cost-effective CCDs with small sensors. These measurements do not intend for absolute beam characterization but for convenient tracking of relative changes in beam position or beam profile. Figure 2.2 shows a capture of a typical monitoring display from the laboratory. One can see how the beam profile has changed, possibly due to some diffraction (left panel) and offset (right panel), even though the active beam-pointing stabilization is active. In addition to the beam profile, a large area photodiode serves as a relative intensity log with high temporal data density.

A history of the relative pulse intensity is shown in figure 2.3. The beam profile logging has shown that in most cases where the PWS pulses are out of reference, the reason is the laser itself. Slow aging effects in the laser system have occurred over the 6 to 10 year lifetime of the laser and manifest as slow drifts and slowly decreasing performance.

The deterioration of the beam profile due to freeze over on the cryogenically cooled crystal was attributed to faster contamination of the cryo chamber with moisture due to porous rubber gaskets at the entrance and exit windows and flanges. The amount of water in the vacuum

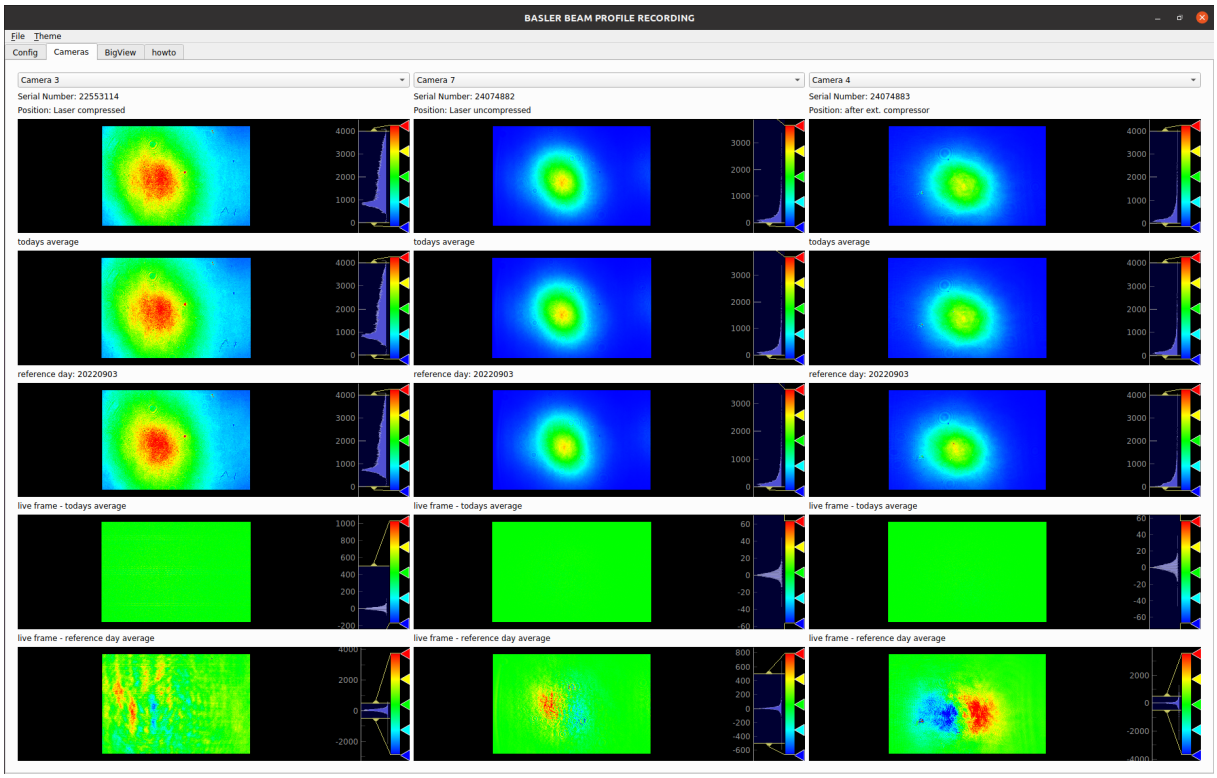

Figure 2.2: Capture of the monitoring display as developed for constant beam profile recording and visual feedback. The Screenshot was taken on October 27, 2022 and thus displays the beam deviations over a period of ≈ two months with respect to the defined reference day. The top row displays a live view, the second row is the daily average and the third row is the average of the reference day. The last two rows display the deviations with the daily deviations (subtraction of live frame - today's average) in the fourth row and long-term deviations (live frame - reference day average) in the bottom row. The three columns represent three different cameras positioned at the compressed laser output, the uncompressed output and after the external compressor. The positions are indicated in figure 2.5 as (CAM1-3).

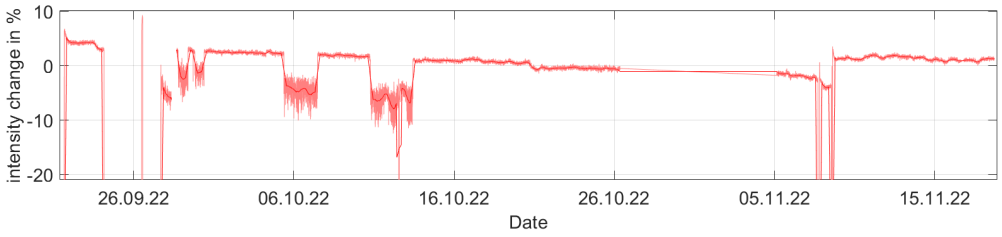

Figure 2.3: Relative log of the Laser intensity. The permanent log is recorded single shot and shown for a period of ≈ 2 months. The data is shown with a moving average over 100 samples. A deactivated beam-pointing stabilization explains the drops in intensity between October 6, 2022 and October 16, 2022. The long-term decreasing slope shows the effect of freeze over on the crystal due to the accumulation of water in the vacuum chamber. The recovery (temperature cycling) shows the intensity increase on November 8, 2022.

chamber can be observed when temperature cycling the chamber. At around 210 K, the sublimation point is reached and the pressure increases drastically up to the mbar regime. The more water has accumulated in the chamber, the more the pressure increases. Even with new sealings on the cryo chamber, a regular temperature cycling $\approx$ once a month is necessary to guarantee long-term stable pulse energy and beam profile. Figure 2.3 shows the effect of a temperature cycle on November 8, 2022, where the laser intensity had previously decreased by ≈ 7 % over ≈ 1.5 month.

In addition, the diodes of the Coherent Evolution Nd:YLF pump lasers had to be replaced, the Pockels cell and high-voltage driver of the regenerative amplifier were replaced, and the membrane of the dry air pump (ECU unit, Coherent) caused problems that led to freeze over and water accumulation in the Peltier cooled crystal containers of the Coherent Legend Elite Duo HE+.

The pump laser is designed with two output channels realized by splitting the amplified ≈ 20 mJ beam by means of a thin film polarizer (TFP). One beam ≈ 4 mJ is compressed right at the laser and used to pump the seeding front end and the first two OPA stages of the PWS, while the second beam ≈ 16 mJ is guided and imaged with an evacuated $1:1$ lens telescope to an external compressor located close to the third stages of the OPAs. The pulse splitting, beam routing and pulse compressors are included in figure 2.5.

2.2.2 Broadband CEP stable Seed and Parametric Amplification

The generation of multi-octave spanning pulses by means of parametric amplification in one or multiple OP(CP)A relies on the existence of a same-wise multi-octave spanning seed spectrum. The characteristics of the amplified pulse in terms of bandwidth, energy fluctuation, and well behaved compressible spectral phase depend on the initial seed pulse. Furthermore, as the nonlinear processes preserve the CEP, the final CEP and pulse-to-pulse CEP fluctuation of the ultrashort amplified pulses are inherited and can be controlled by the initial seed pulse. Starting from a non phase-stable multi-cycle laser, the following section covers in detail the generation and amplification of few-cycle CEP stable pulses.

At first, a CEP stable seed is generated in a parametric process. First experimentally demonstrated in [58], the so-called self-referenced or passive CEP stabilization relies on the difference frequency generation between two coherent pulses that originate from the same pulse and having a fixed absolute phase relation. The subtraction of the phases in the DFG process cancels the variation of the CEP. It should be emphasized that this method allows to cancel out the CEP shot-to-shot fluctuations, but not to define the CEP precisely to zero. Similar to the measurement of the (relative) CEP with an interferometric setup between fundamental and second harmonic as will be described later, only the phases of the electric fields are referenced to each other. The electric field is not referenced against the pulse envelope, which would give an absolute measurement of the CEP in the spirit of the CEP definition.

The third-order SPM effect as a case of four-wave mixing is described for the generation of new frequency component ω_4 and adjacent phase ϕ_4 out of existing frequency components $\omega_1, \omega_2, \omega_3$ in the laser pulse.

$$\begin{aligned} \omega_4 &= \omega_1 + \omega_2 - \omega_3 \\ \phi_4 &= \pi/2 + \phi_1 + \phi_2 - \phi_3 \end{aligned} \tag{2.2}$$

In the process of DFG, the frequency and phases are linked as

$$\begin{aligned} \omega_i &= \omega_p - \omega_s \\ \phi_i &= -\pi/2 + \phi_p - \phi_s \end{aligned} \tag{2.3}$$

Once the signal pulse inherited the phase from the pump pulse (ϕ_P) up to a constant factor ($-\pi/2$), the idler pulse phase ϕ_I is constant and leaves only with a phase shift of $-\pi$. The passive CEP stabilization method relies on the seed and pump pulses having equal and stable path lengths. Any jitter due to beam-pointing of air fluctuations results in a imperfect phase subtraction and according pulse-to-pulse CEP jitter.

As one of the first system components, the CEP stable seed generation benefits massively from a custom breadboard and opto-mechanics hardware that allows a rigid positioning of the optics, thermal stabilization and a very dense layout to avoid distortions due to beam propagation. The details on the hardware can be found in [59] figure 11.

Apart from mechanical rigidity, the quality of the CEP stable seed pulse is elaborated by exploiting some properties of the nonlinear interactions. After the initial splitting of the 800 nm Ti:Sapphire pulse and WLG via SPM in a plate of YAG, the WL continuum is amplified in a first OPA stage. The phase-matching is tuned to amplify the 1300 nm component, which is the zero dispersion wavelength of fused silica; therefore, the dispersion in optical components such as lenses and dichroic beam combiners is low. The time structure of the pulses and the thickness of the BBO crystals are choosen such that pump depletion occurs. In this regime, the amplification and therefore pulse energy of signal and idler is clamped to the intensity of the pump beam. Now, the energy fluctuations of signal and idler depend on the fluctuations of the pump beam that are usually lower compared to the fluctuations of the white light. Since idler and signal pulses are located left and right from the pump spectrum in frequency domain, the group velocity mismatch due to the frequency-dependent refractive index leading to a walk-off and separation of the pulses. Since the idle pulse exists only because of the interaction between the pump and the signal, the pulses still overlap because of the amplification process, even though they would be separated by the pulse splitting length because of the different group velocities. To maintain a long pump-seed interaction in a relatively thick BBO (4 mm), the 1.3 μm seed pulse is transmitted through a narrowband filter (12 nm) in order to ensure a longer pulse duration compared to the pump. The DFG process in the second BBO gives the idler at 2.08 μm that is passively CEP stable. For subsequent seeding of the other WLG stages in the OPAs at the right wavelength, the pulse is frequency doubled to 1.04 μm.

The measurement of the CEP in a f-2f configuration similarly relies on the conservation of the CEP in the nonlinear process of second harmonic generation (SHG). The phase information of the fundamental (F) in a (SHG) process is conserved such as

$$\begin{aligned} \omega_{SH} &= 2 \cdot \omega_F \\ \phi_{SH} &= \pi/2 + 2 \cdot \phi_F \end{aligned} \tag{2.4}$$

A portion of the CEP stable 1.04 μm pulse is split and guided to the f-2f measurement. A WL stage broadens the 1.04 μm pulse to an octave-spanning spectrum and a BBO allows for the second harmonic generation of the long wavelength part. The second harmonic of the long wavelength part beats with the short wavelength part. A spectral filter and polarizer are used to match the relative intensities and polarizations. The resulting interference and especially the phase of the fringes in frequency domain are sensitive to CEP changes. Extraction of the phase value at the position of the beating frequency gives quantitative measurements for the pulse-to-pulse CEP fluctuation.

The narrowband CEP stable pulse at 1.04 μm is the driver for the WLG stages which serve as the seed pulse in the OPA stages. For parallel amplification channels as in the PWS, the seed has to cover above two octaves of bandwidth. Figure 2.4, adapted from [43] shows a WLG in 3 mm YAG split by custom dichroic mirrors to the three subsequent channels for amplification. Intuitively, this approach is most straightforward to minimize any non-common WL fluctuations

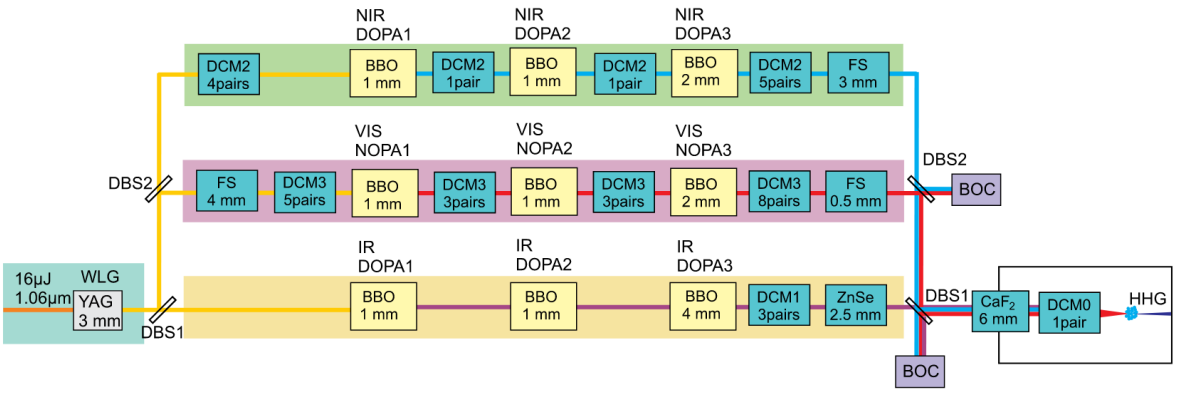

Figure 2.4: Scheme of dispersion and spectral management of the first-generation synthesizer. A CEP stable 1.06μm pulse drives an initial white light (WL) in 3 mm YAG. The WL is split and partially recompressed by intermediate double-chirped mirrors (DCMs). Three channels are shown with three amplification stages each. A final beam combination via dichroic mirror (DM) optics and synchronization via a balanced optical cross-correlator (BOC) is shown on the right side. The feedback signal is derived from DM leakage with the main beam ending at a vacuum chamber, indicating the intended application for HHG. From [43]

among the spectral channels. The drawback is the extreme bandwidth that the single WL needs to cover. The intensity required to drive a severe SPM is very close to the crystal's damage threshold. Any fluctuation in the driving laser or local hotspots in the beam profile would re-

quire a replacement of the WL crystal and realignment. On top of abrupt damage to the crystal, an octave-spanning WLG unavoidable leads to aging of the crystal and long-term performance degradation the harder the process is driven. Even for the moderately driven WL in the CEP stable seeding frontend, the WL crystal is shifted regularly to a new position every few months. R. E. Mainz *et al.* [23] have shown that splitting the seed pulse and driving two WLs in different crystals can fulfill the required stability constraints. The phase jitter between the WLs was measured to be well below 20 mrad at 550 nm. The phase jitter increases slightly once the WL crystals differ in material (YAG/Sapphire) and thickness, but the increase in long-term stability when matching the WL crystal for each spectral band pays off. The current scheme of the DFG OPA for CEP stable seed generation is shown on the left side of the figure 2.5, with a subsequent splitting of the seed pulse (sketched in green color) for separate WL generation in each spectral channel. One recognizes the interferometric layout of the beam path for the OPAs and beam transport. This ensures that any occurring geometrical drifts are mostly common drifts of the interacting beams.

The central part of figure 2.5 shows the OPAs. After completion of the NIR ($650-950$ nm) and the IR ($1200-2200$ nm) spectral channels and successful coherent synthesis, the systems's capabilities to generate IAPs and control the HHG properties were very promising, so the development of the attosecond beamline to fully exploit the PWS as a HHG driving source is focussed. The visible channel, as grayed out, is under construction but is not addressed in this work.

All OPAs are designed as three-stage amplification to ensure low superfluorescence and $>$ 100 μJ output energy. The spectral gap ($950-1200$ nm) results from the fact that the WL driver is located at 1040 nm and the spectral phase around that region is strongly modulated and difficult to compress. In addition, the phase-matching conditions of those broad bandwidths in BBO define the wavelength as such. The employed OPAs follow the concepts presented by C. Manzoni and G. Cerullo in [19]. The phase-matching conditions for efficient energy conservation from pump to signal pulses must be satisfied.

$$\Delta k = k_p - k_s - k_i \stackrel{!}{=} 0 \tag{2.5}$$

For narrowband pulses, the wavevector k can be treated as a single value, while for broadband pulses, the frequency dependence comes into play. The mismatch of the wavevector are expanded in a Taylor series where the first partial derivative describes the group velocity and the second partial derivation the group velocity dispersion.

$$\Delta k = \left(\frac{1}{v_{g_i}} - \frac{1}{v_{g_s}}\right)\Delta\omega - \frac{1}{2}(GVD_i + GVD_s)\Delta\omega^2 \stackrel{!}{=} 0 \tag{2.6}$$

The condition for phase-matching depends on the velocity of signal and idler pulse in the nonlinear medium. The velocity of signal and idler pulse can be matched by introducing an angle on one of the beams so that the projected velocity on the straight is reduced. This is referred

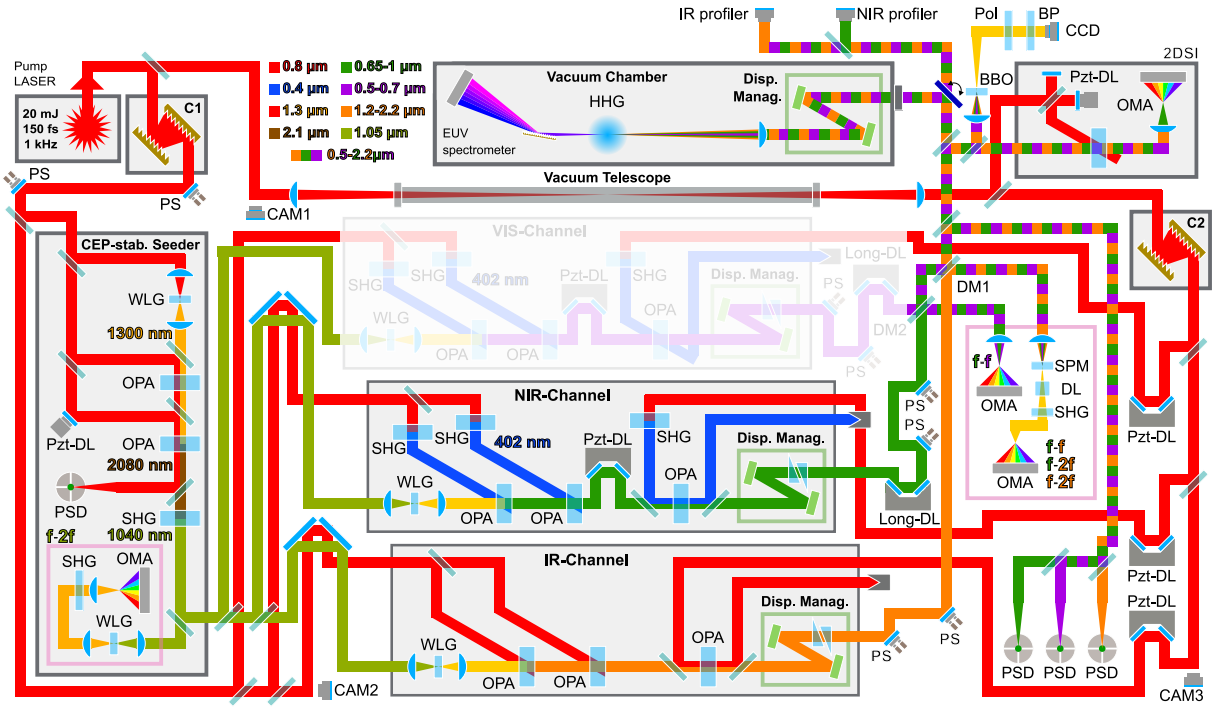

Figure 2.5: Scheme of the current implementation of the PWS adapted from [44]. The pump laser is shown on the top left with Compressor C1 located closely and compressor C2 located to the right side. The CEP-stab. seeder to the bottom left with the first f-2f characterization on the 1040 nm seed beam. Delay management of pump and seed prior to the OPA channels is located in the center. The VIS-Channel is grayed out as it is currently not integrated. Beam combination via dichroic mirrors (DM) and feedbacks are located on the right side. Pointing stabilization (PS), including position-sensitive detectors (PSD) for each spectral channel. Second f-2f and integrated f-f spectrometer and 2DSI setup for temporal and spectral phase control. Spatial f-2f setup with CCD camera and beam profile characterization right before the HHG chamber on top. The camera positions (CAM1-3) indicate the beam profile monitoring system.

to as a non-collinear OPA (NOPA). In a NOPA, the intersection of the beams under an angle usually leads to spatial chirp, as the beam profiles do not overlap in a constant manner while propagating through the crystal and additional optimizations such as pulse front tilt have to be implemented. A rather convinient way to match signal and idler group velocities is introduced with the degenerate OPA (DOPA). The signal and idler have the same frequencies with a pump pulse of twice the photon energy.

So far we have neglected the polarization of the constituent pulses. As a birefringent crystal, BBO has a different refractive index on the extraordinary axis than on the ordinary axis. In the case of a DOPA, the signal and idler pulses are polarized along the ordinary axis while the extraordinary axis is matched to satisfy the phase-matching condition with the pump pulse. By slightly detuning the perfect phase-matching angle, the phase-matching conditions on both sides of the spectrum are optimized and very broadband amplification is realized in a DOPA.

The combination of the Ti:Sapphire laser wavelength and the β-BBO crystal properties al-

lows to design the IR and NIR channel as a DOPA pumped with the Ti:Sapphire and its SH ($\approx$ 400 nm) in regard. The first amplification stage amplifies the WL from a few nJ to $\approx$ 1.5 μJ. Due to the small energy, the size of the focal spot in the first stage must be very small and requires perfect mechanical stability. The second stage amplifies to $\approx$ 15 μJ. The energy of the NIR and IR channels, including partially the losses due to compression and beam combinations, is measured to $\approx$ 100 μJ and $\approx$ 500 μJ, respectively after the third stage amplification. The energy stability is about 1 %. Due to the need for extended feedback signals and beam routing compared to a single channel source, the energy of the pulses that arrive in the HHG at the point of HHG is reduced to $\approx$ half of the initial OPA output energy.
The spectra for each stage and channel are shown in figure 2.6.

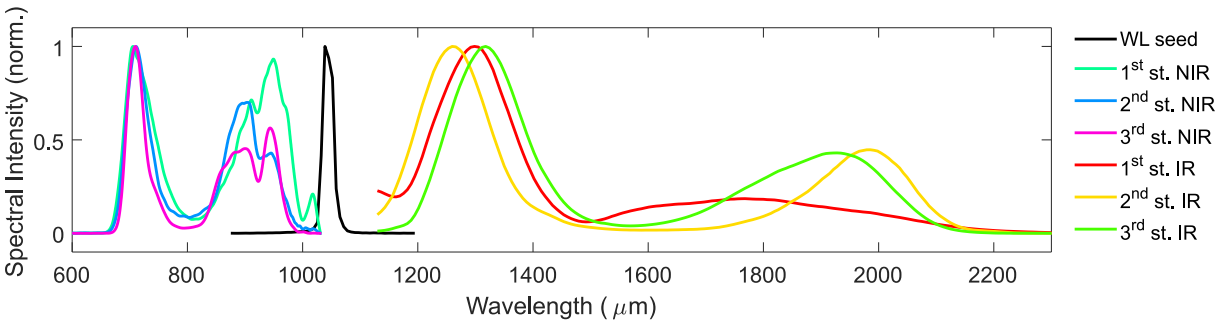

Figure 2.6: Spectra of the PWS. WL generated seed, first, second and third amplification stage for NIR and IR channel. Spectra taken with Ocean Optics Flame (Si detector) and Ocean Optics NirQuest (InGaAs detector). The first and second stage is measured via fiber coupling (FG105LCA, Thorlabs).

2.2.3 Spectral Phase Control and Characterization

The spectral phase defines the chirp and temporal duration of the pulse, which must be considered in each section of the PWS. Before we end at the final pulse compression to meet the shortest possible pulse duration at the point of the experiment, the peculiarities of the temporal structure in the whole PWS are discussed. In the previous sections, the importance of matching the pulses' time duration to fulfill stable and broadband amplification is explained, e.g. in the seeding frontend and amplification stages. A severe distortion by higher order phase components would result in temporary local intensity spikes in the pulse and a strong response to the nonlinear interactions.
The beam manipulation and nonlinear interactions require a minimum amount of transparent materials such as BBO and fused silica for lenses exhibiting a chromatic dispersion on the pulse. In the scheme of the parallel WS, additional optics are introduced for beam splitting and recombination. The larger the bandwidth, the harder is to find optical materials whose dispersion cancels and to design dispersive optics. Here, the parallel approach benefits from an independent handling of the dispersion in each spectral channel.
The spectral phase of the pulse, while propagating through the PWS, is kept well-shaped by

alternating normal and anomalous dispersing elements. A flip of the spectral phase due to uncontrolled anomalous dispersion between the amplification stages would be detrimental for a smooth spectral shape. Figure 2.7 plots the dispersion of common materials used in the PWS. While the transparent materials consistently exhibit normal (positive) dispersion for the band-

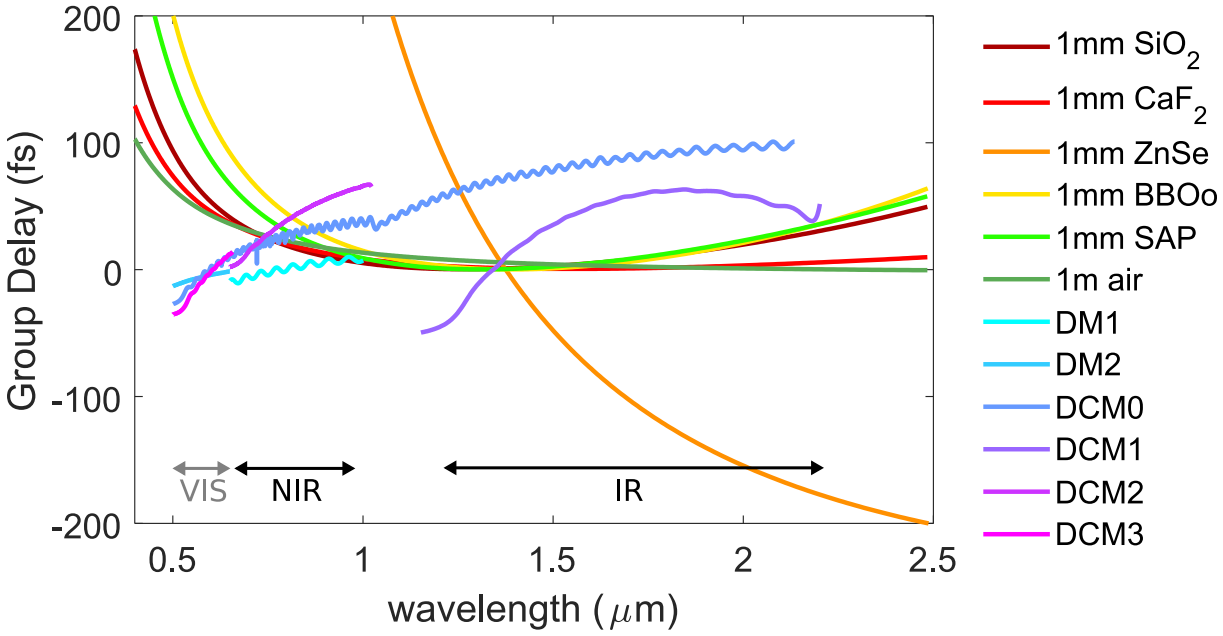

Figure 2.7: Group delay (GD) characteristics of optical elements as transmitted in the PWS (red-ish colors) and group delay of custom double-chirped mirror (DCM 1-3) and dichroic mirror (DM 1,2) (blue-ish colors). The DCM group delay is plotted as the average of a DCM pair. The GD of the DMs is given for the reflection. The transmission mainly exhibits a linear phase and is not plotted. The linear delay offset is removed for better overlap and visibility. The spectral location of the synthesizer channels are indicated. DCM and DM Data from [60], other data from [61] and references therein.

width of the NIR channel, that is accounted for by negative dispersion introduced by the DCM, the handling of the infrared wavelength for the IR channel is more complex. Most optical materials have their zero dispersion point at $1.2-1.5\ \mu$m, so that part of the IR channel undergoes positive dispersion while the long wavelength part sees a negative dispersion in a single material. The positive dispersion for the IR channel is introduced by zinc selenid (ZnSe) wedges. Since it is a rather soft material that is difficult to polish and detoxify (and toxic), the minimum thickness of the ZnSe wedges is limited. Together with high dispersion, the flexible placement of that material along the beam path is restricted. Reverse calculations from the final measured spectral phase and manual tuning based on the amplification characteristics of the OPA stages have led to the current placing of wedges and DCMs for dispersion control. Table 2.1 lists the current elements and thicknesses of optics in correct order as propagated by the NIR and IR channel and can be seen as an update to the proposed dispersion scheme from figure 2.4

The overall optimization of the dispersion is possible due to a custom design of the dielectric optics by former colleague Dr. Shih-Hsuan Chia [60]. In addition to DCMs and optical ma-

	NIR channel		IR channel	
location	materials	amount	material	amount
WLG	SAP	3mm	SAP	3mm
	FS	2mm		
1st OPA	BBO	1mm		2mm
	SDCM2	2+2		
2nd OPA	BBO	2mm		2mm
	SDCM2	2+2	SDCM1	3+3
	FS	1.5 mm	ZnSe	3.4 mm
BC pumped	FS	3.43 mm		3.43 mm
3rd OPA	BBO	2mm		3mm
BS pumped	FS	3.43 mm		3.43 mm
	FS	2.5 mm		
	SDCM2	8+8	SDCM1	3+3
	FS	1 mm	ZnSe	2.4 mm
BC	DM2	3.43 mm	DM1	3.43 mm
			FS	3 mm
	CaF_2	1.5 mm		1.5 mm
chamber window	CaF_2	3 mm		3 mm
	SDCM0	1+1		1+1
BS	CaF_2	5.2 mm		5.2 mm

Table 2.1: A listing of optical elements as propagated by NIR and IR channel starting from the white-light generation (WLG) to the point of HHG in the vacuum chamber. SAP:sapphire, FS: fused silica, SDCM#: custom double-chirped mirror, BBO: β-Bariumborat, BC: beam combiner, BS: beam splitter, DM#: custom dichroic mirror

terials whose dispersion is fixed once manufactured, a few publications show the use of pulse shapers (SLM, AOPDF) in a synthesizer concept [33], [47], [62], as discussed previously. Due to the high losses and low damage threshold, the use is usually limited to the seed pulse or low energy stages of the synthesizer upstream. As mentioned, the intermediate dispersion control between amplification stages downstream is crucial, here the deployment of DCMs, having a low loss per reflection (< 1 %) and high damage threshold, gives more flexibility in positioning them.

Since the DCM takes a central role in our and several published synthesizer concepts [39], [63], the physics will be explained in detail. Developed for the compression of visible to NIR pulses, DCMs are designed to raise anomalous dispersion, meaning that the longer wavelengths travel the structure for a longer time. The penetration depth of a specific wavelength is tuned based on thin layers with a tuned thickness of alternating dielectric coatings. The basic concept of Gires-Tournois interferometer (GTI) [64] leads to a group delay dispersion due to the interference between the partially reflecting front surface and reflecting back surface of such an interferometer. Adding multiple layers with an optical path equal to a quarter wavelength, a so-called Bragg stack increases the amount of interfering waves and thus the reflectivity. The

design criteria of a simple Bragg stack is given as

$$\lambda_B = 2(n_H d_H + n_L d_L) \tag{2.7}$$

with n the refractive index of high (H) and low (L) index material and d the corresponding thickness. A variation, the chirp, of the Bragg condition with thinner layers at the front surface reflecting short wavelengths and thicker layers in the back reflecting longer wavelengths only after a certain propagation in the mirror, generates the anomalous dispersion. In such a mirror, the GTI effect between the front and back surface is still present and generates an oscillation in the group delay for broadband pulses. As proposed by Kärtner *et al.* [30], [65] an additional chirp (the double in DCM) only on the high index material layers matches the impedance to free air and therefore minimizes the reflections leading to the GTI effect. Further reduction of GD oscillations is achieved by using pairs of DCMs. Either by adding $\lambda/4$ beam path thickness to one of the mirrors on the first layer [66] or by using pairs of chirped mirrors at a specific angle [67] leads to a 180° phase shift of the GD oscillations and thus to their cancellation.
Not only the pulse compression has been considered in the dispersion scheme, but also the beam splitting and combination is designed in [60]. Here, the dual-adiabatic-matching (DAM) structure introduces a second matching of the impedance towards the backside of the mirror on the side of the substrate again by varying the high index layer. This ensures a well-behaved group delay of the transmitted long wavelengths. The details on the layer design is given in figure 2.8. The overall dispersion scheme involves custom dielectric optics for (1) dichroic splitting

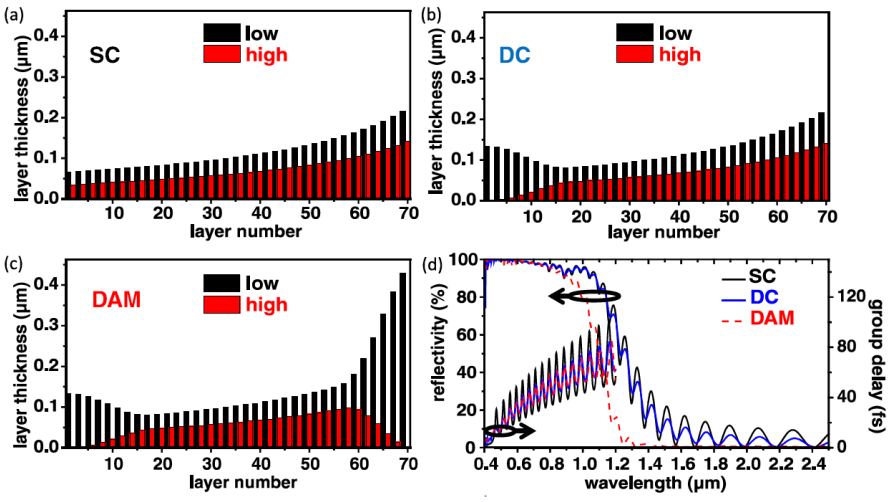

Figure 2.8: Comparison of dielectric chirped coating design for ultrabroadband optics. The newly developed DAM structure on the lower panel as used for the PWS. Adapted from [60]

and combination following the DAM approach, (2) DCM for each spectral channel with a bandwidth of nearly one octave and reflectivity $> 98\%$ and (3) DCM for the final compression in vacuum spanning above 2 octaves with a reflectivity $> 90\%$.

With a bandwidth covering almost two octaves and a precisely tuned dispersion scheme, the pulse duration is expected to read < 5 femtoseconds. State of the Art characterization of ultrashort laser pulses employs second or third-order nonlinear effects with a more recent addition of strong-field based techniques. Namely FROG [68], SPIDER [69], ptychography [70], D-scan [71], strong-field sampling methods [72] and a plethora of their variants have been developed in the last decades and a review is presented in [73].

As for PWS, an appropriate characterization technique must capture the fundamental spectrum and the spectrum of the generated signal of the nonlinear interaction, e.g. SFG or second harmonic. Common Si or InGaAs detectors cover either the NIR or IR spectral range. The method of Two-dimensional spectral shearing interferometry (2DSI) [74] that has been developed in the group is prooven to cover the bandwidth of both NIR and IR channel in a single setup and is chosen as a standard technique for measuring the spectral phase. Closely related to the interferometric technique of SPIDER, 2DSI relaxes the constraints of spectral resolution and calibration at the cost of single-shot capability. The idea of 2DSI is sketched in figure 2.9. The ancillae

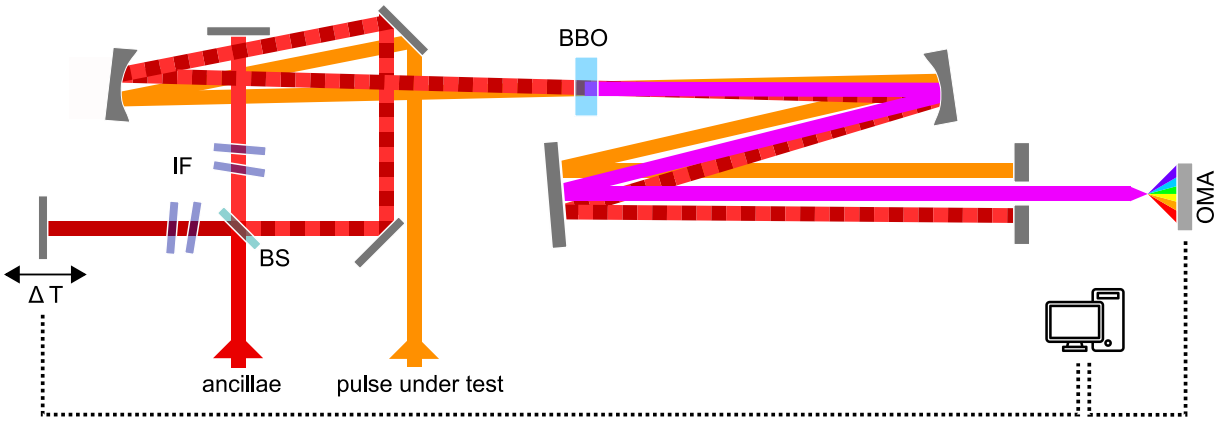

Figure 2.9: Scheme of a Two-dimensional spectral shearing interferometry (2DSI) setup for pulse characterization. The pulse under test is only reflected by silver mirrors before the focus in the BBO crystal exploits the $\chi^{(2)}$ nonlinearity. A second "ancillae" pulse pair is prepared in a Michelson interferometer equipped with two narrowband bandpass interference filters (IF) slightly sheared in frequency. The combination of narrowband IF allows for ≈ 1 nm bandwidth. The central wavelength of the ancillae are separated by ≈ 5 nm. One arm of the interferometer is modulated as indicated by the arrow to introduce a time delay. The signal from the 2DSI is collimated and focused in a spectrometer. The control of delay and synchronized recording of the spectra is computer controlled.

pulses are narrowband pulses, slightly sheared in frequency and in this implementation prepared with narrowband bandpass filters (LL01-808 and LL01-810, Semrock). A sum frequency with the pulse under test in a $\chi^{(2)}$ medium produces two broadband pulses with the upshifted bandwidth of the pulse under test. Due to the bandwidth, the upconverted pulses have a large overlap in frequency while being slightly sheared by the offset given from the sheared ancillae pulses. The collinear propagation allows for interference between the upconverted signal that carries the spectral phase information of the pulse under test as phase difference between neighboring

frequency components.

The optical setup of the 2DSI allows for rather independent preparation of the ancillae pulses that only have to be temporally linked to the pulse under test. A strong ancillae can enhance the SNR for a weak pulse under test. Furthermore, the SFG with a narrowband and broadband pulse allows a very large bandwidth in a phase-matched condition in BBO. Here, we utilize type II phase-matching with the broadband signal polarized along the ordinary axis and the ancillae along the extraordinary axis of the crystal.

The SFG process depends on the intensity of the electric field, and the 2DSI measurement is not sensitive to the carrier electric field i.e. CEP effects. The upconverted pulse under test with spectral amplitudes $A(\omega)$ and $A(\omega-\Omega)$ as slightly sheared. The measurable spectral intensity ($I(\omega,\phi_{delay})$) is described by the squarred amplitudes and the interference is modulated by the linear phase of delay τ.

$$\begin{aligned} I(\omega,\phi_{delay}) &= |A(\omega)+A(\omega-\Omega)e^{\phi_{delay}}|^2 \\ &= |A(\omega)|+|A(\omega-\Omega)|+2|A(\omega)A(\omega-\Omega)|\cos(\phi_{delay}+\Phi(\omega)-\Phi(\omega-\Omega)). \end{aligned} \tag{2.8}$$

Note that ω corresponds to the frequency range after upconversion and Ω usually reads a few nm in wavelength shift ($\approx$ 2 Thz). The phase delay ϕ_{delay} is introduced to one of the ancillae via a piezo actuator and corresponds to $\phi_{delay}=\omega\cdot\tau$. The spectral phase $\phi(\omega)$ information is captured in the argument of the cosine function. Deviding the argument of the cosine by the shear frequency Ω expresses by definition as the group delay:

$$T_g=\frac{d\phi(\omega)}{d\omega}\approx\frac{\Phi(\omega)-\Phi(\omega-\Omega)}{\Omega}. \tag{2.9}$$

The shear frequency defines the resolution of the measurement and, according to the Shannon Sampling Theorem, the maximum time window ΔT that can be captured correctly without aliasing effects with a 2DSI measurement.

$$\Delta T\leq\frac{2\pi}{\Omega} \tag{2.10}$$

Note that the temporal window needs to be much larger than a FWHM duration of the pulse. A time window that is too small aliases the remained energy excluded from the window into the calculation and leads to a false characterization [75].

For a reliable and convenient pulse measurement, the 2DSI setup is placed close to the vacuum chamber at the point of the experiment in order to pay attention to the dispersion of air in the measurement. The ancillae pulses are derived from a portion of the 150 fs Ti:Sapphire pump laser at 800 nm and 805 nm that is time delayed to match the timing at the output of the PWS. A copy of the synthesized pulse, which is directed to the experiment, is derived from a reflection on a thin glass plate. Optics that are added inside the vacuum chamber, including the entrance windows, are copied into the beam path of the pulse copy. Unavoidable discrepancies of the

beam path in air are numerically accounted for after the measurement.

Figure 2.10 (a1, b1) displays the measured spectrogram with the delay axis along the y-direction and the wavelength along the x-direction. Due to the upconversion, the spectrogram is measured at $350-450$ nm for the NIR channel and $480-590$ nm for the IR channel. Afterwards the spectrogram is shifted back to the fundamental wavelength numerically. The spectral intensity and phase are plotted in (a2, b2). The compression of both pulses is ideal, leaving only tiny oscillations within $[-\pi,\pi]$. Accordingly, the time domain intensity is close to the Fourier limit. The side lobes of such broadband M-shaped spectra are unavoidable, as can already be seen from the transform-limited pulses in the time domain.

The broad bandwidth of the 2DSI technique is exploited in a single measurement with both

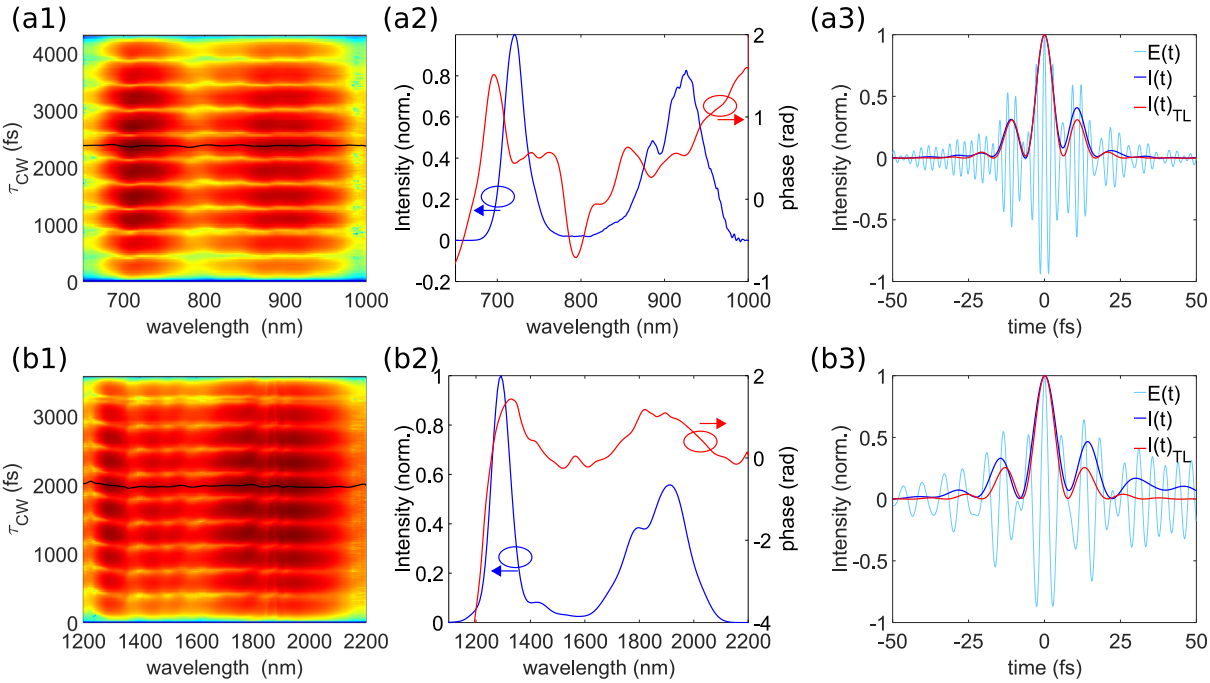

Figure 2.10: Characterization of the NIR and IR pulse by means of 2DSI. (a1,b1) shows the recorded spectrogram with the time delay between the ancillae pulses τ_{CW}. (a2,b2) displays the measured spectral phase and the spectrum. (a3,b3) shows the pulses in time domain measured to 6 fs FWHM (6 fs TL) for the NIR and 8.1 fs FWHM (7.2 fs TL) for the IR channel.

channels of the PWS, shown in figure 2.11. Since the 2DSI does not give an absolute arrival time of the pulses, the measurement with both pulses is not a complete characterization in itelf and merely serves as a demonstration of the bandwidth. An absolute characterization of the absolute electric field waveform is presented later in an attosecond streaking experiment, see chapter 3.5.

The independently measured traces can be synthesized numerically and a first look at the resulting waveforms is shown in figure 2.12. A numerical delay scan gives a glimpse of possible waveforms around time zero. The synthesis leads to partial suppression of the wings and an intense central cycle. Plotted is the electric field. The FHWM of the intensity is simulated

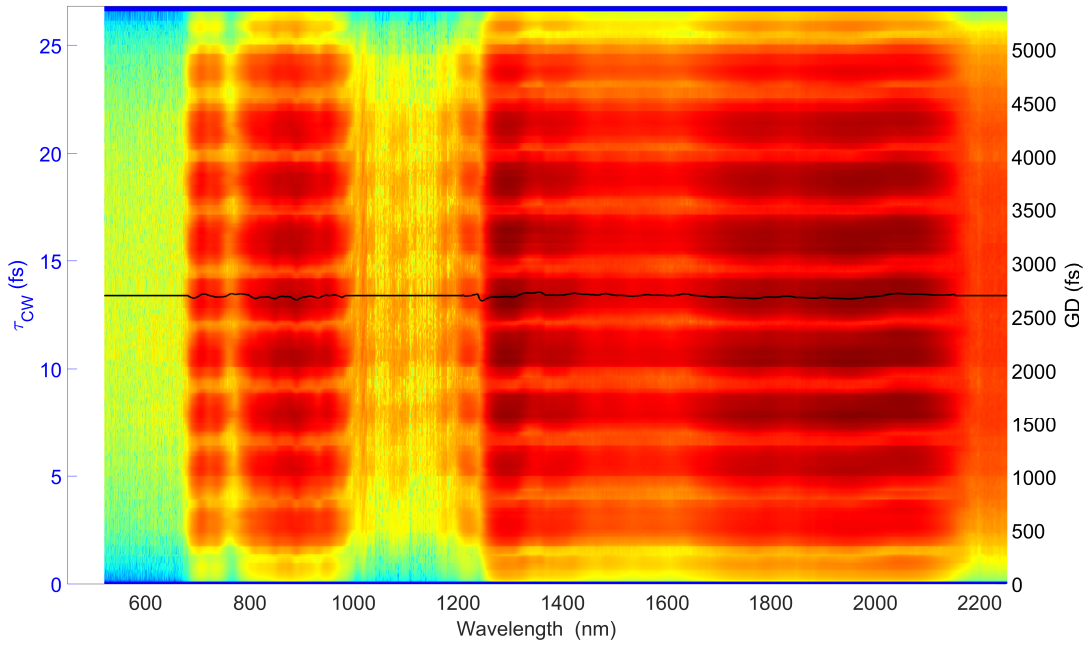

Figure 2.11: Characterization of the NIR and IR pulse simultaneously by 2DSI. The bandwidth in a single measurement spans from 670 nm to 2200 nm. The measurement is taken with the ancillae at 804 nm and 808 nm and a BBO of 10 μm in type II phase-matching.

down to 3.8 fs, corresponding to 0.6 cycles at a central wavelength of 1.4 μm. The CEP of the pulses is set to 0 since the $\chi^{(2)}$ based 2DSI is insensitive to CEP variations. The numeric modeling of the waveforms based on the measurements allows us to vary the CEP as shown for some cases in figure 2.12 (c). An insight of how much these waveforms differ from a sinusoidal waveform is given by the calculation of the first left- and right-sided intersection of the electric field with the abscissa at $E(t) = 0$ as given in panel (b). The time of the zero node is given as the distance between the central peak and the first left- and right-hand intersection points, with the mean value plotted as a continuous line. At the point of temporal overlap, the durations of left and right quarter cycles begin to vary up to a factor of ≈ 2. Taking the average cycle duration ($4\times$ average zero node time), the expected central wavelength in a classical definition is plotted on the top x-axes of panel (b). Out of time zero, the central wavelength of 1.6 μm corresponds to the single IR channel central wavelength. At time zero overlap, the waveform is compressed to a smaller cycle duration and accordingly lower central wavelength of $\approx 1\mu$m. Depending on the absolute electric field strength at the adjacent cycles, the dynamic structure of advancing long or advancing short half cycles gives a control over strong-field light-matter interaction. Furthermore, it is observed that the central wavelength, as we derive it from the temporal domain for these non-sinusoidal fields drops below the estimated central wavelength of 1.4 μm when only the center of mass and energy of the channels are considered. For our fields, it is demonstrated for the process of HHG in [45], figure 5, that depending on the non-

sinusoidal shape of left or right half-cycle, the ionization and excursion of the electron wave paket is influenced.

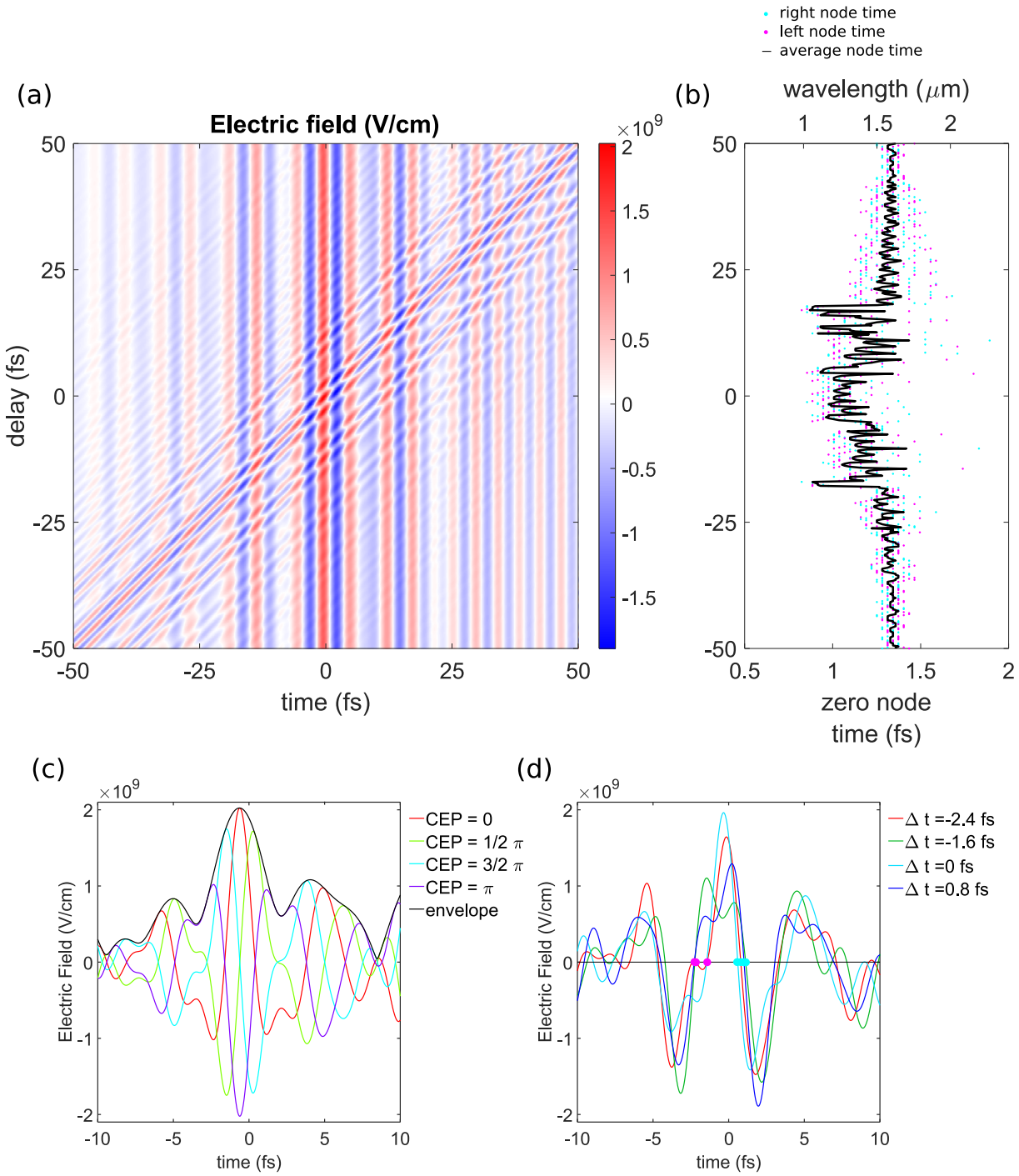

Figure 2.12: Numerical delay scan based on 2DSI measurements of NIR and IR channel. The electric fields of the synthesizer, depending on the delay are plotted as a colormap (a). The location of the zero nodes ($E(t) = 0$) with respect to the peak for left and right first node is indicated by cyan and magenta dots is plotted in panel (b) with the average in black. The average temporal distance of the first zero nodes (left to right zero crossing) is taken as a half-cycle duration and the wavelength scale is plotted accordingly to estimate the central wavelength locally for the central cycle. Out of time zero, the central wavelength corresponds to the single IR channel one (1.6 μm) whereas around time zero, the calculated half-cycle durations dynamically modulate the central wavelength of the synthesized pulse. CEP variation of the field at $t = 0$ shown in panel (c) and lineouts from the delay scan around time zero given in panel (d). In panel (d) the nodes are marked exemplarily.

2.2.4 Coherent Synthesis

The passive phase stability of individual generated WLs is proven in [76], stating an excellent temporal and spatial coherence. The PWS in this thesis demonstrates its capabilities of free space coherent combination, maintaining both sub-cycle temporal duration and high-energy in the mJ regime. The techniques enabling this performance are presented.
First principle interference between laser pulses sharing same frequencies contains the information whether the electric fields are spatially and temporally stable with respect to each other. However, the information about the temporal direction between the two pulses is only given within a single cycle. The frequency of the interference signal depends on the arrival time difference (ATD) but especially close to the overlap is only measurable with low resolution due to very low frequency. Moreover, the interferometric technique fails a priori if the pulses to be compared have different spectra. A versatile technique for the ATD of dissimilar pulses is the balanced optical cross-correlator (BOC) [77]. To determine the ATD between pulse A and B in a BOC setup, two pairs of a pulse copy are prepared. Each copy of pulse A and B is overlapped collinearly and undergoes a nonlinear interaction. A delay, e.g., via a chromatic dispersion element, is introduced before the nonlinear interaction for pair #1, while twice the inverse dispersion is introduced for pair #2. Due to the chromatic dispersion, the signal after nonlinear interaction is equal, but at negative or positive ATD, the convolution signal is time-shifted. The signals are detected with a photodiode and a subtraction of the signal represents the ATD.
A discussion starting from the conventional BOC is given in [78], testing the capabilities for the use in the PWS. In the first generation of the PWS, G. M. Rossi and R. E. Mainz investigated the use of a BOC for locking the ATD of the IR and VIS channels. Since the BOC utilizes the $\chi^{(2)}$ nonlinear polarization, it is inherently sensitive only to the pulse envelopes. A comparison of the BOC signal with an interference signal realized by overlapping a second harmonic of the IR with the VIS channel showed severe jitter of the interference fringes even the pulses are locked to the BOC signal. The definition and measurement of the ATD of a sub-cycle waveform via the pulse envelope evidently hides important information. The ATD measurement by the BOC has to be accompanied by individual CEP stabilization, e.g., by f-2f measurements for each spectral channel. The current implementation of the PWS does not employ the BOC and relies on interference to derive the feedback signals, as explained below.
Starting from the beginning of the experimental setup, the CEP stable seed generation contains a f-2f setup for the measurement of the CEP and a piezo actuator on the pump pulse of the second OPA, as sketched in figure 2.5 on the left side to control the CEP. During the parametric amplification in each spectral channel, pump and signal pulses are not actively stabilized in time. The relative phase (RP) between NIR and IR channel and the CEP of the final synthesized pulse is measured just before the experimental vacuum chamber. The multi-phase meter for the detection of RP and CEP is shown in figure 2.13, which is taken from [44]. As an interferometric method, the phase meter is sensitive to any changes of the electric field, i.e.,

RP and CEP. Stabilization of the electric field in this layout allows to drive field-dependent strong-field processes with long-term stabilized sub-cycle waveforms. The stabilization of the RP in an interferometric manner in the context of waveform synthesis was recently published in [79], where the authors called it relative timing (RT). However, they evaluate the f-2f trace in a different way. While the authors evaluate a change in frequency of the Fourier component and counting the number of interference fringes, our system evaluates the phase at the frequency of interference in the Fourier domain. Comparing the measured residual phase noise, the evaluation of the phase allows for the improvement of the RMS jitter by ≈ 2. Important for the measurement with the multi-phase meter is dynamic range of the piezo acting on the relative phase. A phase jump by 2π would result in the same RP when measured with the multi-phase meter, thus a good passive stability ob the setup must be ensured and the system of fast, short range and long range piezo must follow the phase change without latency to avoid undetected phase slips.

The predefined leakage of the dichroic mirror ($\approx 5\%$) serves as a signal for the multi-phase

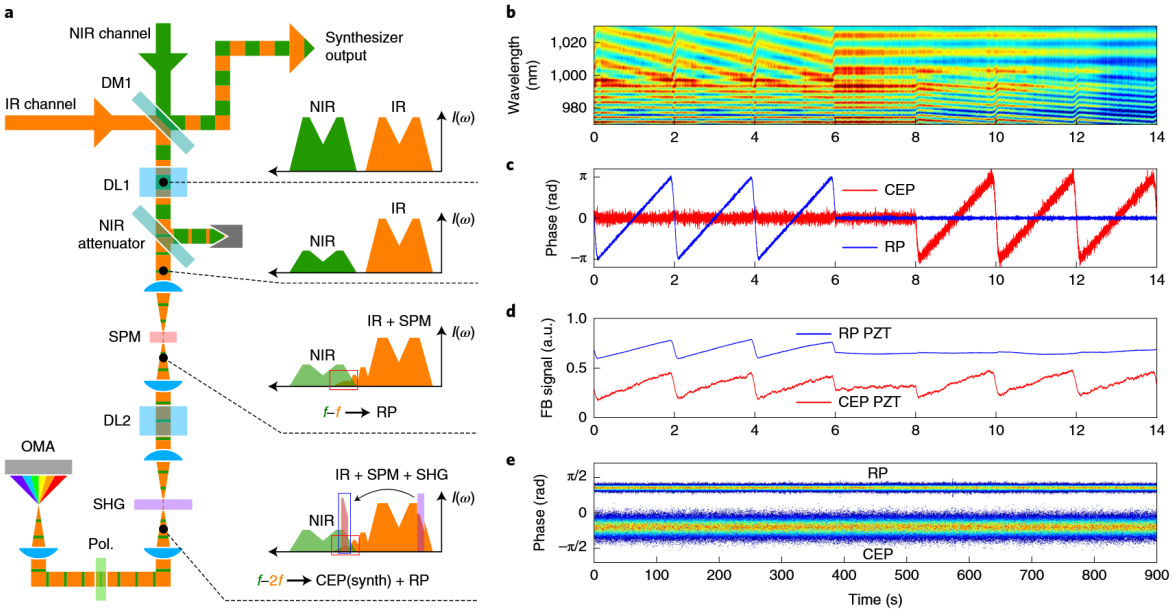

Figure 2.13: In-line multi-phase meter as developed for the measurement of relative phase (RP) and CEP in a PWS. The individual pulses are combined at the dichroic mirror (DM1) and a leakage of the mirrors drives the phase meter. A first delay (DL1) between the pulses via chromatic dispersion is introduced before the long wavelength pulse (IR) undergoes SPM in a bulk crystal. A second delay (DL1) rearranges the pulses in time before the SHG of the broadened IR channel. A polarizer (Pol.) projects the polarizations on the same plane. Panel (b) plots the measured signal of the optical multichannel analyzer (OMA) vs. time. The retrieved measured CEP and RP is plotted in (c) with the feedback signal controlling the piezo (PZT) delay stages in (d). The measured RMS noise (d) reads 70 mrad RMS for the RP and of 233 mrad RMS for the CEP (both single-shot every-shot, calculated over 900,000 consecutive pulses). From [44]

meter. In order to generate an interference signal between IR and NIR channel, the conceptual

spectral gap between the channels has to be closed. This is done via spectral broadening in a bulk SAP/YAG. To control the spectral broadening, the NIR channel is attenuated to allow SPM preferably on the IR pulse. A bulk of glass introduces some delay between the IR and NIR channel via chromatic dispersion in order to generate the interference fringes at a convenient frequency to detect. This signal contains information of the relative phase between the channels. The RP is stabilized by a fast but short-range piezo at the NIR channel location between the 2nd and 3rd amplification stage, see figure 2.5 "PZT-DL" and a long-range stick-slip piezo (N-565, PI) is located after the 3rd stage in the NIR channel. The second part of the multi-phase meter consists of a second bulk of glass to separate the fringe's frequency on the spectrogram and basically describes an f-2f setup where part of the long wavelength spectrum is frequency doubled and beats with the short wavelength component. The f-2f for the synthesized beam contains the f from NIR channel and the 2f from the IR channel. The raw f-2f signal contains the combination of CEP and RP while the RP is measured isolated via the f-f interference and can be subtracted in post-processing. A third signal on the spectrometer of the multi-phase meter originates from a second f-2f, where the f relates to the broadened IR channel short wavelength portion and the 2f from the frequency doubled IR channel long wavelength portion. When only the IR channel of the synthesizer is used for experiments, the multi-phase meter works just as a conventional f-2f and allows to stabilize the CEP of the IR channel. The performance of the system can be seen on the right panel of figure 2.13 with distinct control of the RP during the first six seconds, two seconds of stabilization and distinct cycling of the CEP starting from second eight. Long-term phase measurements on time scales of half an hour have given 70 mrad RMS for the RP noise and 233 mrad RMS for the CEP noise.

An out-of-loop measurement and evidence that the multi-phase meter is capable to stabilize sub-cycle synthesized waveforms is derived from a spatially resolved f-2f setup for a qualitative judgment of the synthesized beam stability, as shown in figure 2.14. A small portion of the synthesizer pulse is split from the main beam with a thin quartz window. The IR channel undergoes SHG in a phase-matched BBO crystal and the focus is imaged on a CCD camera. Here, the imaging spherical mirrors are chosen to provide a magnification at the same time to have a good resolution of the focus on the CCD chip. A wire grid polarizer adjusts the relative intensity of NIR and SH or IR channel. A bandpass filter enhances the contrast by selecting only the interfering wavelength components. The camera (ace acA640-750um, Basler) is triggered with the laser frequency and by selecting a region of interest, the camera is able to run at > 1000 frames per second (fps). The setup allows observing any shortcomings in spatial stability as well as in phase stability due to the f-2f nature of the signal. As mentioned ealier, the CEP is measured at the front end of the phase-stable seed pulse and a second time after amplification and synthesis of the final pulse. The feedback system can be freely programmed and can take either of the two CEP measurements as input source for the feedback to drive the piezo and stabilize the CEP. In all cases, the action on the CEP is happening with the piezo in the front end. Figure 2.15 plots the data of the RP and CEP measurement in conjunction with the stability of the spatial

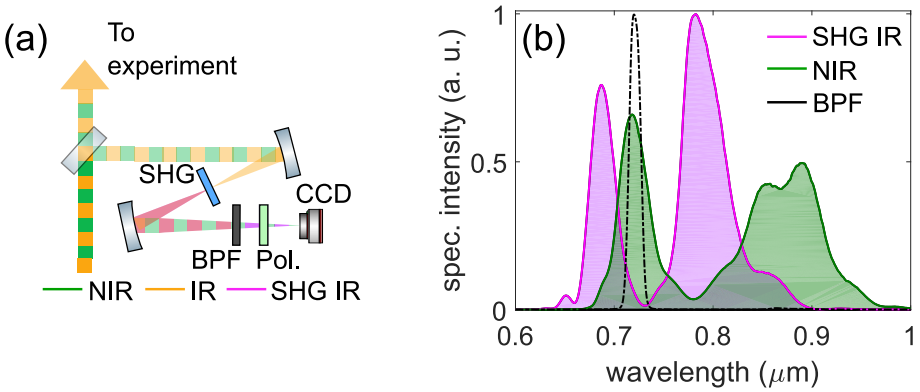

Figure 2.14: Experimental setup (a) of a spatially resolved f-2f measurement. A weak copy of the main beam is guided to a spherical mirror. The second harmonic generation (SHG) in BBO is tuned for the IR channel. The resulting spectra are shown in (b). A spectral overlap of fundamental NIR and second harmonic IR is selected by a bandpass filter and projected on the same polarization by a wire grid polarizer (Pol.) The second spherical mirror images the focus on a CCD camera.

fringe. The signal from the CCD is integrated to get a one-dimensional graph. A stable synthesis would result in stable interference and thus stable intensity on the CCD, optimized here for constructive interference. The destructive interference lowers the intensity as can be seen on the 1D trace as a drop of the signal. The insets in the left plot of figure 2.15 shows the CCD signal for constructive and destructive interference. The pulses are locked for $\approx 2.5 \times 10^5$shots $=$ half a minute, and the measured phases are stable, as confirmed by stable constructive interference of the spatial f-2f setup. The zoomed area of the plot shows a sinusoidal modulation of the CEP and two frequencies, followed by a modulation of the RP at two frequencies. The interference signal from the CCD is closely following the phase modulation of the waveform. Finally, the long-term stable synthesis is accomplished, the synthesis parameters in terms of RP and CEP can be tuned precisely and the out-of-loop single-shot CCD recording gives a good reference for the synthesized pulse at focus.

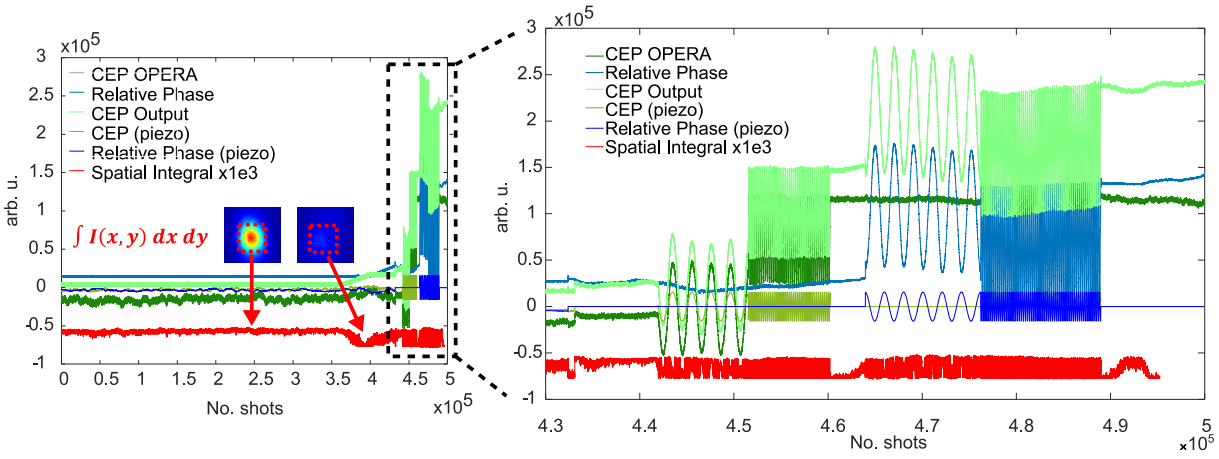

Figure 2.15: Measurement and control of CEP and RP parallel to the recording of the spatial interference between the NIR channel and second harmonic of the IR channel at focus. A measure of the interference is given as integral of a detector signal. The insets display the signal for constructive (left) and deconstructive (right) interference. First, the phases are stabilized and a constant constructive interference is observed. The zoomed region shows the modulated signal. First, the CEP is modulated at low and high frequencies and second, the RP is modulated at low and high frequencies. The interference signals follow the modulated phases.

2.2.5 Spatial Characterization and Stabilization

The previous section already anticipated the use of a CCD and the recording of beam profiles as part of the stability measurements. Here we will take a step back and guide through the rigorous measurements of the beam profiles in near and far field for both the NIR and IR channel. Starting from the seed pulse, the beam sizes in the OPAs are matched to the pump beam and the right intensity for parametric amplification. After the channels are output, the IR channel is subject to the constraint that the intensity in the ZnSe wedges must be minimized for pulse compression to avoid phase fluctuations due to the B-integral of ZnSe. After the last stage of amplification, both channels contain a mirror telescope to match the beam sizes. We follow the consideration from [43], [80]–[82] and match the beam sizes for a “constant waist width”. With a factor of two between the central wavelength of IR and NIR channel, the beam size of the IR channel is adjusted to match $\approx 2\times$ the NIR beam size. The beam profiles are displayed in 2.16. The profiles are measured with a silicon-based CCD detector (SP620, Spiricon, pixel pitch 4.4 μm) for the NIR and a pyroelectric detector array (Pyrocam 4, Spiricon, pixel pitch 80 μm) for the IR channel. The beam sizes differ slightly from time to time due to unavoidable realignments of the pump laser or the PWS. Nevertheless, the pulse profiles shown measure 4.7 mm for NIR and 10.9 mm for IR channel, measured in 4σ which is a typical average size. The quality of the focus is measured directly at the point of the experiment using a CCD PCB chip camera (daA1920-30um bare, Basler, pixel pitch 2.2 μm). A photo of the measurement setup is shown in figure 2.17. The stage of the HHG gas cell also scans the CCD camera through the focus. For the IR channel, the silicon-based CCD detects the two-photon absorp-

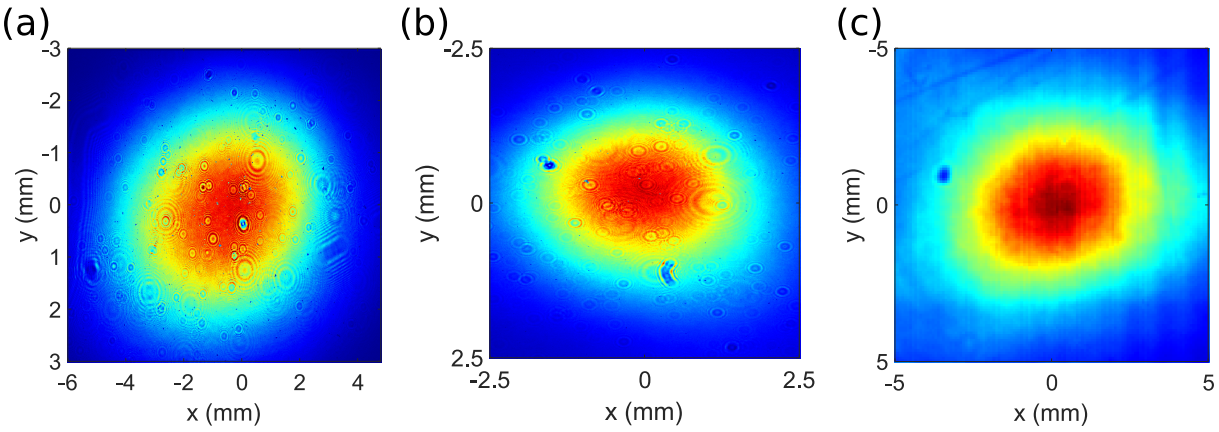

Figure 2.16: Beam profile of the seed beam (a) NIR channel (b) and IR channel (c). The diameters are measured to 5.8 mm for the seed, 4.7 mm for NIR and 10.9 mm for IR at 4σ $(1/e^2)$.

tion and the calculated beam sizes are corrected by $\sqrt{2}$. Due to the lack of high resolution, small pixel detectors, the two-photon absorption or an upconversion to wavelength < 1 μm are the only methods for near-field characterization. The upconversion, i.e. via SHG in BBO requires the nonlinear conversion. To get consistent measurements, the phase-matching angle of the crystal has to be optimized and ideally cross-checked with a spectrometer. The efficiency of the two-photon absorption is most likely not homogeneous across the full bandwidth of the IR channel but at least it stays constant with the fixed mounting and orientation of the PCB CCD. In addition, measuring both channels with the same referenced detector allows the precise point of caustics to be measured even in the z-direction along the beam. This is crucial to ensure a synthesized field with a defined intensity in the focus. Since the measurement is done with the same remote-controlled stage as the HHG gas cell is mounted on, the measurement also reveals at which position of the gas cell with respect to the focus, the HHG emission is maximized. The measurement routine automatically moves the stage at a predefined array of positions and adjusts the exposure time of the CCD at each posititon to ensure a good dynamic range while avoiding saturation. If necessary, the background is taken with exactly the same parameters once the beam is blocked.

An attempt to scan the focus with the pyroelectric detector that is used for the far field beam profile characterization (Pyrocam 3 and 4, Spiricon, pixel pitch 80 μm) is shown in figure 2.18 (b) and (c), as this is the only available beam camera specified at the IR channels wavelengths. At least an upper limit of the beam size of ≈ 2 times the pixel size can be ensured from that measurement. The solution to conveniently detect the IR channel at high resolution by the use of two-photon absorption in the silicon CCD is investigated also in [83], [84]. To estimate the beam size correctly, the square root scaling of the two-photon effect has to be taken into account. To verify the absolute accuracy of the two-photon based measurement, a knife edge measurement was performed systematically along the focus is recorded. The knife edge measurement was only taken along the horizontal dimension of the beam profile. The measured caustic is

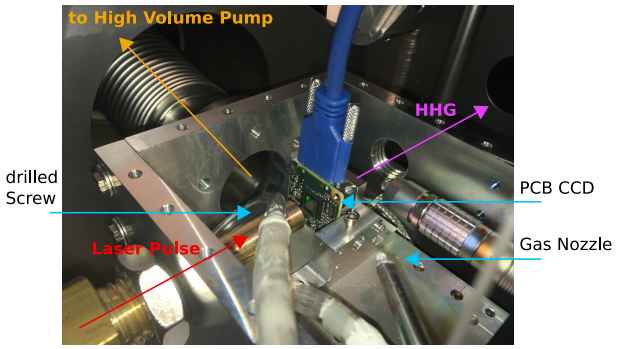

Figure 2.17: Analysis of the focus for NIR and IR channel with a PCB board CCD camera mounted on the stage of the HHG gas cell. The gas cell is removed from the focus positions and seen to the left. The beam profile characterization happens in-situ in the vacuum chamber but at atmospheric conditions.

shown on the right panel of figure 2.18 (a, violet and green curve) and the insets show the data quality at selected posititions. In comparison with the $\sqrt{2}$ corrected two-photon absorption data from the CCD, the measured beam diameter match fairly well. As shown in figure 2.18 (a), the measured beam waists at each position (black data points) and the Gaussian fits (red,blue,black curve) at positions close to the focus differ. The narrowing effect, as entitled in [84] close to the focus and fading intensity at distances far from focus results in a non-Gaussian beam caustic when characterized by two-photon absorption. The valid region for the fit has to be defined carefully to obtain an accurate result for the IR channel waist. Due to the good agreement and practicability, the in-situ two-photon absorption measurements with the PCB CCD chip camera is routinely used to optimize the beam profile after change of the focussing mirrors or realignment of the Laser/PWS.

A complete characterization of the focus is displayed in figure 2.19 for the NIR channel (left) and IR channel (right). The beam waist w at the focus reads on average 44 μm and 47 μm for NIR, respectively IR channel. The measurements are taken when an OAP with $f = 4$ inch was installed in the beamline under exactly the same conditions for NIR and IR measurements. The challenge is to optimize both beams simultaneously. Depending on the quality of the input beam, the alignment of the OAP to one channel, probably accounting for some abberations, usually does notmatch the best alignment for the other channel. Compared to a single source driven HHG beamline, the arguments on the spatial beam profile optimization visualize the complexity of the HHG generation with the PWS. A solid performance of the Laser and OPAs upstream has to be ensured in order to realize the desired effect of the synthesized waveform at the point of HHG and motivates the large efforts in tracking the beam profiles along the entire system. The resulting peak intensity are calculated based on the waist and pulse duration. When assuming a Gaussian pulse profile in time and space, the intensity reads

$$I(r,t) = I_{peak} e^{-2\left(\frac{r}{w}\right)^2} e^{-4\ln 2(\frac{t}{\tau})^2} \tag{2.11}$$

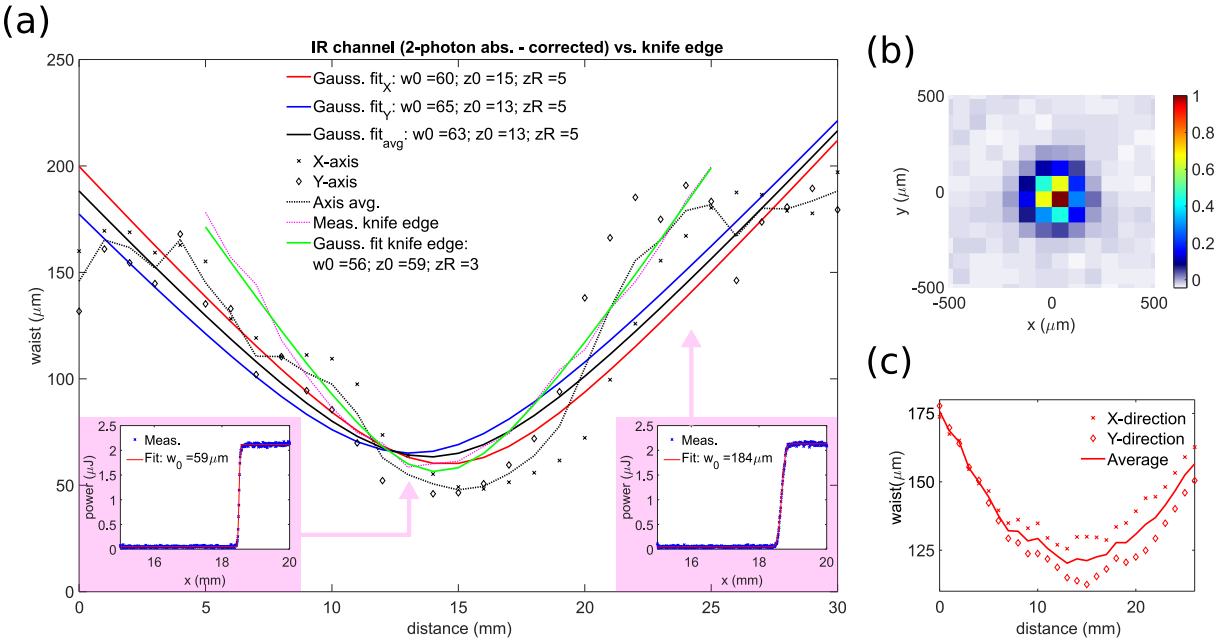

Figure 2.18: Comparison of focus measurements of the IR channel. Panel (a) plots the waist along the focus as measured by the two-photon CCD absorption $\sqrt{2}$ corrected compared to a knife edge measurements. The knife edge data at two positions are displayed by the insets. Gaussian fits are plotted for CCD and knife edge data. Panel (b) and (c) display a measurement of the focus with an pyroelectric-based detector (Pyrocam 4, Spiricon, pixel pitch 80 μm) which pixel pitch is too large for precise detection. At least an upper limit can be given.

Integrating along time and space using the solution $\int_{-\inf}^{\inf} e^{-ax^2} dx = \sqrt{\frac{\pi}{a}}$ yields the total pulse energy W

$$W = I_{peak} \frac{\pi\sqrt{\pi}}{4\sqrt{\ln 2}} \tau w^2 \tag{2.12}$$

Solving that for the I_{peak} allows for an estimation of the peak intensity based on beam waist, pulse duration and total pulse energy that is conveniently accessible with a energy meter.

$$I_{peak} = \frac{4\sqrt{\ln 2}}{\pi\sqrt{\pi}} \frac{W}{\tau w^2} \tag{2.13}$$

Typical beam parameters when characterized with $f = 6$ inch focusing are given in the following table including the extimated peak intensities. The measurements on HHG as presented in the following chapters are taken with changing focusing mirrors from $f = 6$ inch to $f = 500$ mm. The Rayleigh range z_R as defined for a Gaussian beam defines the distance from the point of focus along the laser propagation to which the cross section has doubled.

$$z_R = \frac{\pi w^2}{\lambda} \tag{2.14}$$

The confocal parameter $b = 2z_R$ defines the region symmetric around the focus where the intensity reaches $\geq$ half of the maximum intensity.

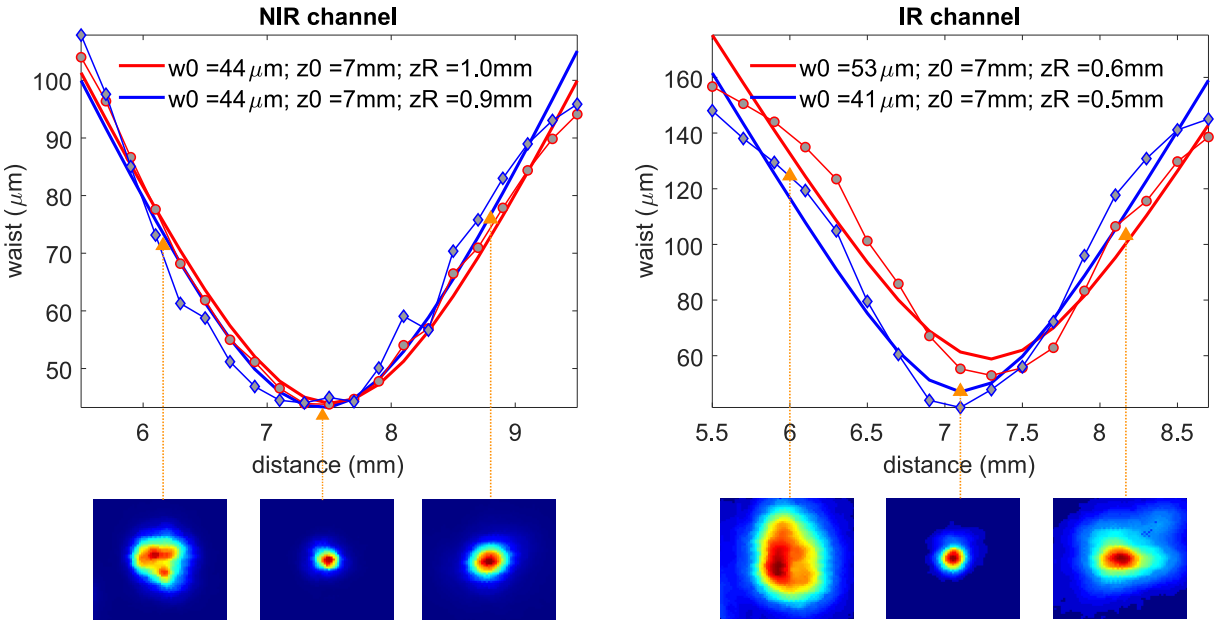

Figure 2.19: Beam profile scan along the laser focus for NIR channel (left) and IR channel (right). The waist at focus is measured to 44 μm and 47 μm, respectively defined at $4\sigma = 1/e^2$. The insets display the beam profiles at selected positions as marked by the arrows. The laser direction is from right to left, given by the positioning of the stage. The x axis "distance" are absolute positions.

	beam waist w (μm)	Energy W (μJ)	FWHM pulse duration τ (fs)	peak intensity I_{peak} (W/cm^2)	Rayleigh range z_R (mm)
NIR channel	44	50	6	2.5×10^{14}	7.6
IR channel	47	150	8	5.0×10^{14}	4.3
Synth	46	200	2.7	1.5×10^{15}	4.7

Table 2.2: Peak intensity and rayleigh range for NIR, IR channel and synthesized pulse as calculated for the focus measurements with a $f = 6$ inch off-axis parabola mirror.

At this point, the synthesized waveform is characterized and stabilized for its time duration, spatial beam profiles and temporal phases such as CE and relative phase. The following chapter introduces to the primary application of HHG and will show that the methods for characterizing and controlling the PWS waveform are capable to drive and control strong-field processes such as HHG.

3 High Harmonic Generation with Synthesized Infrared Fields

3.1 Introduction to High Harmonic Generation

High Harmonic Generation (HHG) as a somewhat generic term, is mostly interpreted as a technique to generate XUV to soft X-ray radiation from visible to IR laser pulses. At UV wavelengths and below, the spectral coverage of classical lasers, OPAs and nonlinear broadening schemes fade out. A strong-field light-matter interaction leads to the process of HHG and the emission of harmonics of the fundamental laser frequency up to an order of several hundreds and even up to the 5000th order when driven with IR wavelengths [85]. Early experimental results on the XUV radiation based on HHG can be found in [86], [87] documenting the observation of up to the seventeenth order (14.6nm) in neon from a UV laser.

HHG has been established as a major technique for observing ultrafast femto- to attosecond processes. Usually involving a noble gas and a laser pulse of $10^{14} - 10^{15}$ W/cm^2, this technique enables to generate XUV to soft X-ray (SXR) pulses with attosecond time scales. The process will be discussed in the following paragraphs.

The harmonics generated by HHG preserve the attributes of the laser, such as temporal and spatial coherence [88], [89] and a defined repetition rate and timing with respect to the fundamental laser. The timing and temporal duration of a single SXR pulse emitted via HHG is a peculiarity of HHG when compared to soft X-ray pulses as generated via Free Electron Lasers (FEL) [90], [91]. While the (seeded) FEL pulse jitter is on the order of a few femtoseconds [92], the jitter can be actively reduced to a few attoseconds in an attosecond pump-probe scheme using HHG [93]–[95]. In contrast, the conversion efficiency of HHG and thus the maximum pulse energy of the emitted harmonics is a major limitation, and pulse energies in the range of pJ are many orders of magnitude lower compared to FEL pulse energies above μJ.

But HHG is not only a source for attosecond soft X-ray pulses and enables the field of attosecond science, since the process of HHG is intrinsically sensitive to the light-matter interaction, the emitted radiation is itself a probe. HHG from small molecules is used as a probe in the field

of high harmonic spectroscopy and reveals electron/ion dynamics [96]–[98] and the imaging of orbitals [99], where the amplitude and phase of the emitted harmonics allow the tomographic reconstruction of the orbitals of nitrogen. The HHG spectra from solids reveal the phonon dynamics [100] and the band structure [101].

The limitations in the process of HHG with ordinary sinusoidal few-cycle laser pulses are a motivation to construct the PWS as a driver for HHG. A sub-cycle time duration allows to concentrate most of the pulse energy to a single HHG event. A single XUV/SXR pulse emission per laser pulse, called an isolated attosecond pulse (IAP), is desirable for attosecond resolved experiments to precisely define the pulse arrival time and duration of light-matter interaction. To date, the generation of IAPs has been based on the concept of gating, i.e. limiting the emission of the harmonics to a single-cycle of the laser pulse even though the pulse comprises multiple cycles. Apart from the unmatched time duration, the concept of synthesized waveforms produces electric fields other than sinusoidal-shaped, as shown previously in figure 2.12. This allows for the control of the HHG process, namely the tunnel ionization of the electron, acceleration and recombination. Numerous theoretical studies [102]–[104] predict an enhancement of yield and/or photon cut-off energy when using non-sinusoidal fields.

The work in this thesis exploits the capabilities of the PWS in HHG, and the following sections guide through the theoretical description of HHG, the generation of higher harmonics with the PWS at medium photon energies, the characterization in time domain by means of attosecond streaking experiments and the results from “Water Window” high harmonics at high photon energies.

3.1.1 Theory of High Harmonic Generation

The strong-field process of HHG is formulated in a quantum mechanical model by M. Lewenstein [105] and in a semi-classical model by P. Corkum [106]. The semi-classical model, also known as the three-step model, describes the process as (i) tunnel ionization of an electron from an atom (ii) acceleration of the freed electron in the electric field of the laser and (iii) recombination with the parent ion that leads to the emission of a high-energy photon.

The first step of ionization is crucial for the distribution of the ionized electrons in time. At the recombination, the temporal distribution of the electron wave packet defines the temporal shape of the emitted XUV/soft X-ray pulse. A model for the ionization rate of an atom under high intense optical pulses has been derived by Keldysh [107], [108]. For a laser field with photon energies $\hbar \cdot \omega_L$ small compared to the ionization potential I_P of the atom, the Keldysh parameter is given as

$$\gamma = \frac{\omega_L \sqrt{2 I_P}}{E} \tag{3.1}$$

with E the electric field amplitude. The Keldysh parameter sets the inverse tunneling time, as a frequency and the frequency of the (laser) field in relation. Involving the ponderomotive energy

of the optical field, that is the cycle averaged kinetic energy

$$\begin{aligned} U_p &= \left(\frac{E}{2\omega_L}\right)^2 \quad \text{(atomic units)} \\ U_p &= \frac{(eE)^2}{4m_e\omega_L^2} \quad \text{(SI units)} \end{aligned} \tag{3.2}$$

the Keldysh Parameter can be expressed as

$$\gamma = \sqrt{\frac{I_P}{2U_p}} \tag{3.3}$$

Depending on the laser wavelength and the electric field amplitude, the Keldysh parameter defines the regime of

$$\begin{aligned} \gamma &\gg 1 \quad \text{tunnel regime} \\ \gamma &\gg 1 \quad \text{multiphoton ionization} \end{aligned} \tag{3.4}$$

where in the tunneling regime, the strong electric field lowers the Coulomb barrier of the atom and the electron can tunnel from the parent ion as shown in figure 3.1 Typical values for the

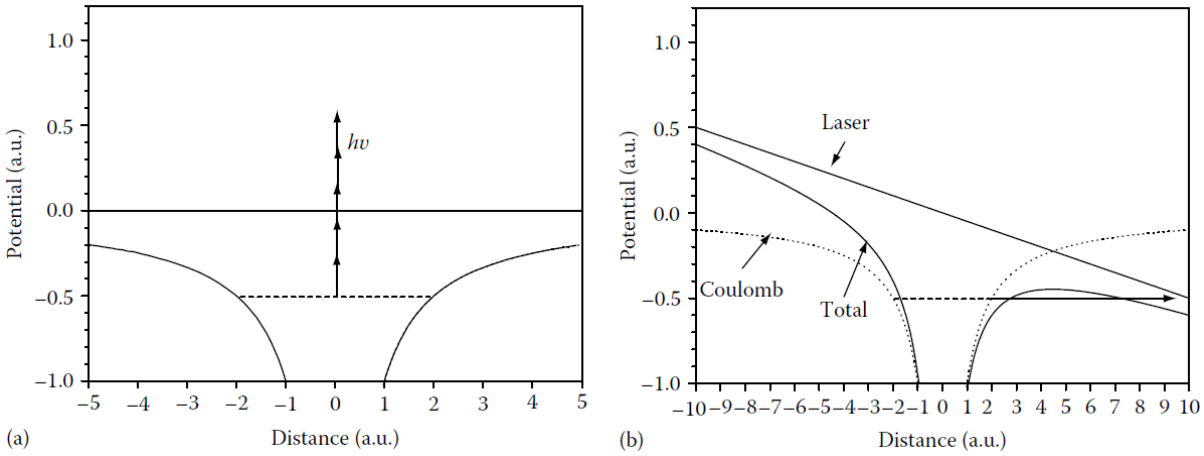

Figure 3.1: Multiphoton (left) vs. tunnel ionization (right). In multiphoton ionization, the potential is reached by absorbing several photons ob energy $h\nu$. Tunnel ionization describes the passage through the Coulomb barrier that is lowered in the field of an intense laser. from [109]

keldysh parameter are $\gamma \approx 0.8$, $\gamma \approx 0.3$, $\gamma \approx 0.2$ for NIR, IR and synthesized pulse. The time-dependent fraction of electrons from ionization are expressed as an ionization rate given by the PPT (Perelomov, Popov and Terent'ev [110]) model and the ADK (Ammosov, Delone and Krainov [111]) model. A comparison of these theories measured against experimental data is found in [112] and explains that the PPT model generally gives correct modeling at pulse intensities used for HHG. The ADK model diverges in the deep tunneling regime at lower peak intensities, especially for short wavelength driver pulses.

The second step (ii) of the semi-classical model is the propagation and acceleration of the tunneled electron in the field of the laser. Approximately, we can neglect the influence of the Coulomb force from the ion since the laser field becomes dominant once the electron is ionized. The equation of motion of the electron under pure influence of the electric field is

$$\begin{aligned} a(t) &= \frac{dx(t)^2}{d^2t} = E\cos\omega t \\ v(t) &= \frac{dx(t)}{dt} = \frac{E}{\omega}\sin\omega t - \frac{E}{\omega}\sin\omega t_0 \\ x(t) &= -\frac{E}{\omega^2}\cos\omega t - (t-t_0)\frac{E}{\omega}\sin\omega t_0 + \frac{E}{\omega^2}\cos\omega t_0 \end{aligned} \tag{3.5}$$

Figure 3.2 presents a couple of solutions to equation 3.5. The ionization probability is calculated quasi-static related to the field at that point in time and the electron are assumed to start from zero velocity after ionization. The electron trajectories are plotted for a laser wavelength of 800 nm and 1600 nm. Note that for the wavelength twice as long, the excursion of the electron

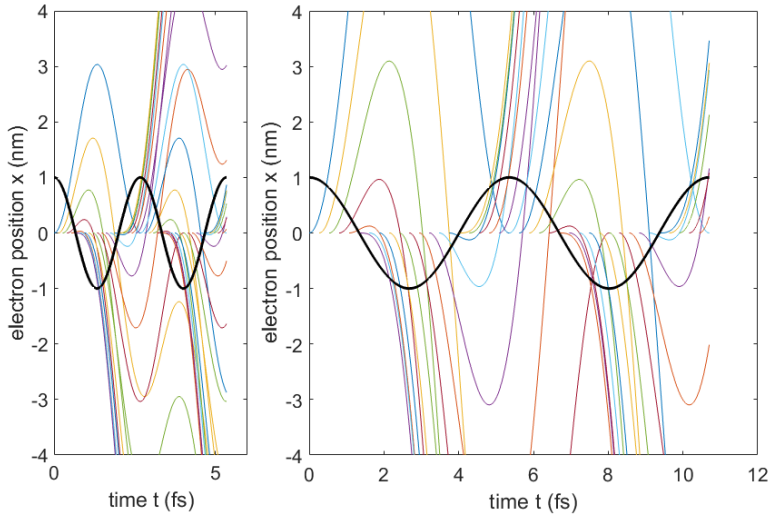

Figure 3.2: Electron trajectories for 800 nm driving laser (left) and 1600 nm driving laser (right). The driving field is plotted in black, and the electron trajectories in color. Note the drastically increased electron excursion for the 1600 nm driving laser.

increases drastically. It can be also seen that depending on the time of ionization with respect to the driving field, the excursion and the time of recombination (zero crossing) vary. Some electron trajectories do not return and will never generate HH. Calculating the kinetic energy of the returning electrons, as plotted in figure 3.3, each kinetic energy is generated from electrons starting at different ionization times. There are so-called short trajectories (shaded in green) and long trajectories (shaded in red) of the electrons giving rise to equivalent electron energies and thus photon energies at the point of recombination.

At the point of recombination, the emitted photon takes the kinetic energy of the electron and

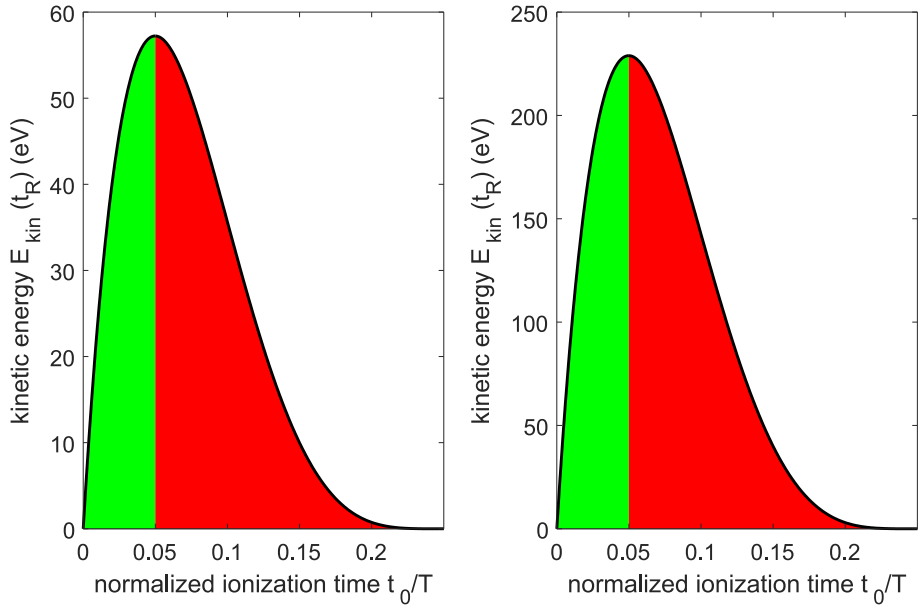

Figure 3.3: Kinetic energy of the returning electrons. Separated in short (green) and long (red) trajectories. Note the increased kinetic energy by almost an order of magnitude for a two-fold increase of the driving laser wavelength. Based on calculations for laser wavelength of 800 nm (left) and 1600 nm (right).

the potential energy from the ionization step.

$$\hbar\omega_{HHG}(t) = \frac{1}{2}mv^2(t) + I_P = 2U_p\left(\sin\omega t - \sin\omega t_0\right)^2 + I_P \tag{3.6}$$

Already from the classical picture, the trajectories and temporal structure in short and long trajectories can be understood and that the short trajectories come with a positive chirp while the long trajectories carry an increased negative chirp. Now, for the calculation of the photon energy, the time the electron spent in the laser field from ionization to recombination is important. A plot is given in figure 3.4 showing the recombination time vs. the time of ionization. An analytical solution is not given but fitting the curve in figure 3.4 to a function as followed from [109]

$$\omega t = \frac{\pi}{2} - 3\sin^{-1}\left(\frac{2}{\pi}\omega t_0 - 1\right) \tag{3.7}$$

allows to solve equation 3.6 by replacing ωt to

$$\frac{E_{kin}(\omega t_0)}{U_p} = 2\left(\cos\left(3\sin^{-1}\left(\frac{2}{\pi}\omega t_0 - 1\right)\right) - \sin\omega t_0\right)^2 \tag{3.8}$$

Linking the maximum energy to the emission time from plot in figure 3.3, the maximum kinetic energy at the recombination time t_r is

$$\hbar\omega_{HHG,max}(t_r) = I_P + 3.17U_p \tag{3.9}$$

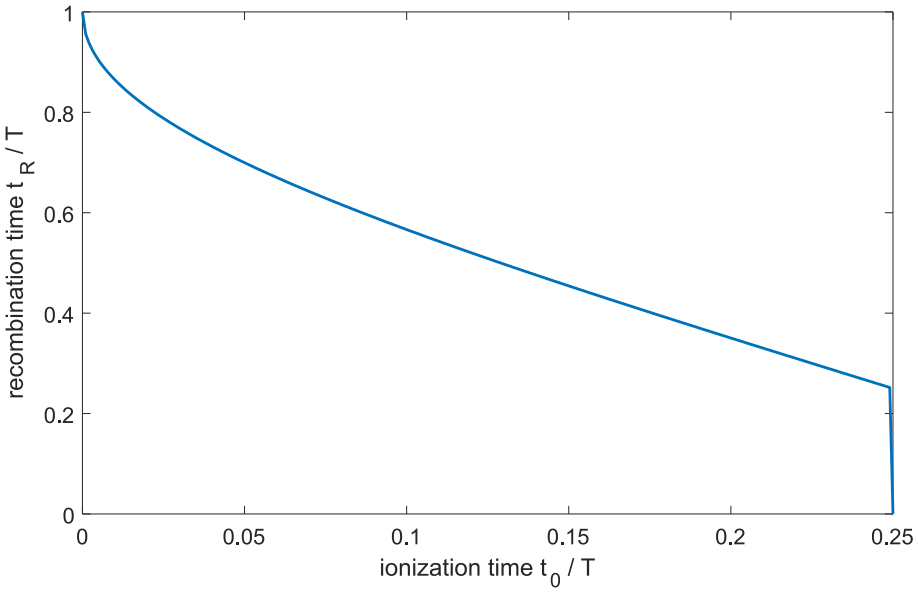

Figure 3.4: Ionization vs. recombination time of the tunnel ionized electrons in the classical trajectory picture of HHG.

This maximum energy of the emitted harmonics as linked to U_p is valid for the numerical solution as based on the sinusoidal field. A closer look at U_p

$$U_p = \frac{Ie^2\lambda^2}{2\pi\varepsilon_0 c^2 m_e} \propto \lambda^2 \propto I \tag{3.10}$$

allows stating the basic principles of HHG in the frame of a single atom. The cut-off energy of the harmonics increases quadratically with the driving lasers wavelength and scales linearly with increasing intensity of the laser pulse. Furthermore, a high ionization potential increases the energy of the recollision, too. In practice, the scaling is limited. First of all, the natural selection of noble gas atoms with given I_P, where an exception are experiments on multiply ionized atoms, thereby increasing the I_P [113]–[115]. Typical cut-off energies as calculated with the equation 3.9 from the values in table 2.2 are 70 eV (NIR), 400 eV (IR) and 900 eV (synth) with the I_P of helium. For the single NIR and IR channel, these cut-off energies are observed experimentally while the peak intensity of the synthesized beam $> 10^{15}$ W/cm^2 violates the macroscopic phase-matching constraint and a cut-off energy of 900 eV is not observed in the experiment. So far, the intensity of the laser pulse is limited by the maximum ionization fraction that allows to fulfill the macroscopic phase-matching condition, as will be discussed later. Increasing the driving laser wavelength is coupled not only to the increase of photon energy but more drastically to a decrease in efficiency of the HHG process scaling with $\propto \lambda^{-5\ldots-6}$. Speaking in the quantum mechanical picture, a longer excursion time and larger distance from the electron to the parent ion reduces the wave function overlap with the ground state [116], [117].

A quantum mechanical description of the HHG was presented in 1994 by M. Lewenstein *at*

al. [105] in the frame of a strong-field approximation (SFA) as a solution to the Schrödinger equation. The central approximation is the assumption that the laser's electric field is strong compared to the potential of the ion that can be neglected; therefore, the electron trajectory in the continuum is dominated by the intense laser pulse. Furthermore, the single active electron (SAE) approximation is included. Multiple reviews [119], comparisons and extensions [120] has been published.

So far, the description is limited to a single atom or even a single active electron in the atom. The typical light-matter interaction takes place in a gas jet of a certain diameter or even a geometrically shaped interaction region [121], [122], and therefore millions of atoms contribute to the emission of radiation and propagation properties. As introduced for nonlinear optics, *phase-matching* has to be considered in the macroscopic picture of the strong-field interaction as well to drive HHG efficiently. Most prominent are four factors that have to be taken into account to fulfill an efficient built up of HH along the longitudinal direction. Namely, there is the geometric phase of a focussed laser pulse described by the Gouy phase Δk_{Gouy}, the neutral dispersion of the medium/gas Δk_N, the dispersion of the ionized gas respectively electrons so-called plasma dispersion Δk_P and the dipole phase Δk_{dipole}originating directly from the single atom picture.

$$\Delta k = \Delta k_{Gouy} + \Delta k_N + \Delta k_p + \Delta k_{dipole} \tag{3.11}$$

The gouy phase [123], [124] describes a 180° flip of the geometrical phase of a gaussian beam compared to a plane wave when going through a focus. One explanation of the origin of this phase flip is a visualization of the differences in propagation between different points in the focussed gaussian beam caustic compared to a plane wave.

$$\Delta k_{Gouy} = q\frac{\partial}{\partial z}\left(-arctan\left(\frac{z}{z_0}\right)\right) \tag{3.12}$$

Here, z is the coordinate in the propagation direction.
The phase mismatch due to dispersion simply results from different group velocities for vastly separated frequencies of fundamental and generated HH.

$$\Delta k_{medium} = q\frac{2\pi}{\lambda_0}(n(\lambda_{HHG}) - n(\lambda_0)) \tag{3.13}$$

where λ_{HHG} is $q \cdot \lambda_0$ when speaking of precise harmonics of order q. The contribution of the neutral gas is:

$$\Delta k_N = q\frac{2\pi}{\lambda_0}\frac{P}{P_{atm}}\delta_n(1-\eta) \tag{3.14}$$

The refractive index $n(\lambda)$ is given as $\delta(\lambda) = n(\lambda) - 1$ and scaled from the atmospheric pressure P_{atm} from any pressure P. Since the laser pulse partially ionizes the neutral gas, the contribution is reduced by η, the ionized fraction of the gas atoms.

The contribution from the plasma is similarly derived starting from the refractive index defined from the plasma frequency.

$$n_p(t) = \sqrt{1 - \frac{\omega_p^2(t)}{\omega^2}} \approx 1 - \frac{\omega_p^2(t)}{2\omega^2} \text{ for } \omega^2 \gg \omega_p^2 \text{ with } \omega_p = \sqrt{\frac{N_e e^2}{\varepsilon_0 m}} \tag{3.15}$$

Inserting the plasma refractive index $n_p(t)$ in equation 3.13 yields the phase contribution of the ionized gas:

$$\Delta k_p = \eta \left(\frac{\lambda_0}{2\pi c}\right)^2 \frac{N_{atm}\, P\, e^2}{2\, P_{atm}\, \varepsilon\, m} \frac{1-q^2}{q} \tag{3.16}$$

where the free electron density $N_e(t)$ is given as an ionization fraction from the atmospheric number of atoms $N_e = \eta(t) N_{atm} P/P_{atm}$ with $\eta(t)$ the fraction of ionization. In general, the formation of the plasma happens dynamically according to the time-dependent intensity of the ultrashort laser pulse, therefore the phase-matching condition changes from cycle to cycle. Lastly, the contribution of the dipole phase [125], [126], that varies depending on the laser intensity, describes the phase accumulated during the excursion of the electron until recombination.

$$\Delta k_{dipole} = -\alpha \frac{\partial I}{\partial \beta} \tag{3.17}$$

For short trajectories, this accumulated phase is less pronounced compared to long trajectories and shows a negative contribution when the generation medium is placed before the focus of the laser and vice versa.

Summing the contributions of each component to the phase mismatch (equation 3.11), a phase-matched situation is usually achieved by balancing the positive contribution of the neutral gas against the negative contribution of the plasma and Gouy phase. Since the Gouy phase is less dynamic with increased distance from the focus, a macroscopic volume for stable optimal phase-matching is usually found shortly after the geometric focus.

In the single atom picture, the fixed relation between the recombination time and kinetic energy of the electron imprints a temporal structure on the attosecond pulse, the *attochirp*. [127] As can be seen from figure 3.5, the short trajectories show a positive chirp (low energies advance), while long trajectories show a negative chirp. From the slope (marked in blue, figure 3.5), the chirp of the attosecond pulse can be derived and it decreases with increasing intensity and drive laser wavelength in the case of short trajectories. The interest in chirp-compensated HHG accelerated with the possibility of generating isolated attosecond pulses [128]. The interaction of intense pulses and high-pressure gas media becomes very dynamic and especially the contribution of Δk_p changes upon propagation of the driving pulse through the generation medium. To counteract the decreasing efficiency for long-wavelength drivers, one attempt is to extend the interaction distance as proposed by T. Popmintchev *et al.* in a hollow fiber geometry [129]. The physics of filamentation as discussed in chapter 1.2 apply and pronounce as well in dense gas media and defocusing of the laser pulse by the plasma leads to lower peak intensities and

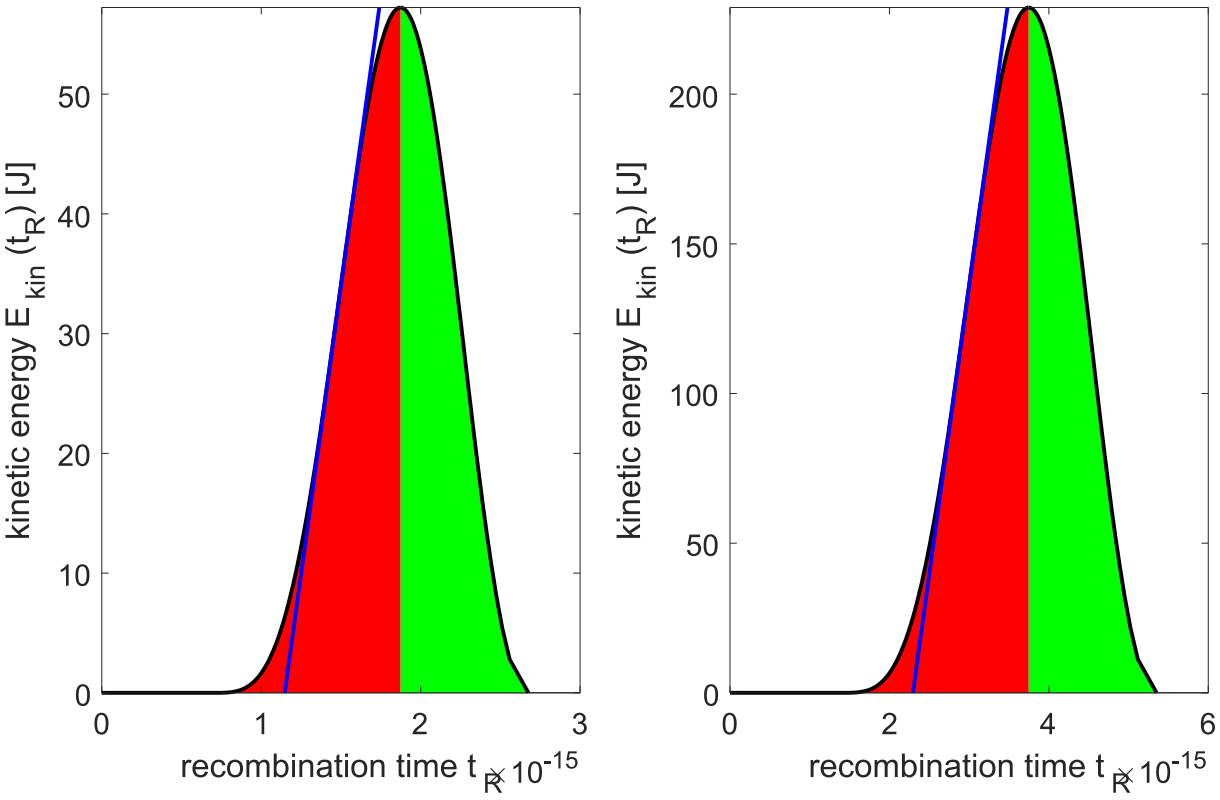

Figure 3.5: Kinetic energy of the electrons with respect to their recombination time. Short trajectories in red, long trajectories in green. Driving laser wavelength of 800 nm (left) and 1600 nm (right)

subsequent HHG with lower cut-off energies. This behavior is experimentally verified in [130] for multi-cycle driver pulses. A measure of the maximum distance over which HHG builds up constructively is the coherence length $l_{coh} = \pi/\Delta k$. A typical coherence length is on the order of sub- to a few millimeters, depending on greatly changing beamline and laser pulse parameters [130]–[132]. The limited coherence length indicates that increasing the laser pulse energy or generation medium volume and pressure can not overcome the efficiency limits of HHG. Lai *et al.* [133] have argued on the plasma defocusing as a major limitation, as it leads to a significant drop in peak intensity and reshaping of the pulse profile in time domain, that recursively changes the phase-matching parameters k_{Gouy} and k_{dipole}. The authors define an enhancement factor ξ that is proportional to the high harmonic pulse energy and comprises the propagation effects. The enhancement factor is plotted in figure 3.6 for the case of helium and neon. Already at modest pressures of > 50 mbar, the effect of plasma defocusing becomes severe and the high harmonic yield drops.

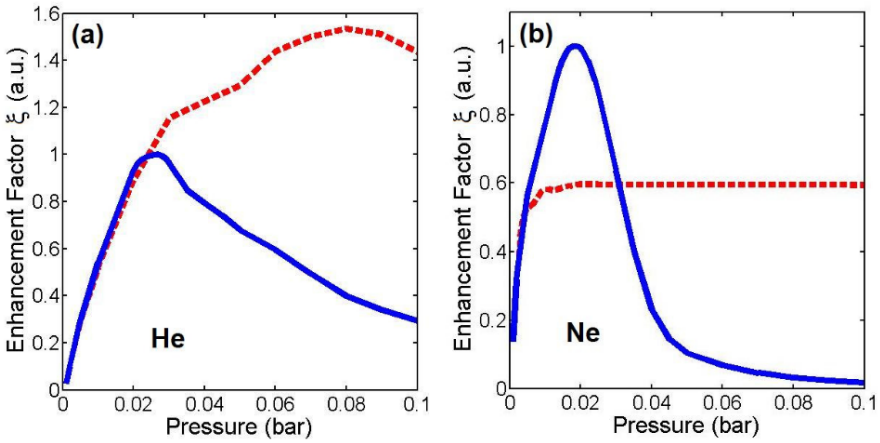

Figure 3.6: Effect of plasma defocusing on the HHG yield. Plotted is the enhancement factor that is proportional to the HH energy and comprises the propagation effects of HHG. The dotted line is calculated without propagation effects. The solid line includes propagation effects. From [133]

3.1.2 Multicolor driven HHG

Early ideas suggested that a combination of a primary laser pulse at central frequency ω with a (usually weaker) pulse at 2ω or 3ω can influence the trajectory of the electron with the aim to achieve (1) higher yield and/or cut-off energy [102] or (2) isolation of the harmonic emission to generate an IAP [134]–[136]. Several authors have doubted this technique as a "temporal gate" [137], [138] within a multi-cycle pulse. The relative ease of these experiments based on multi-cycle (tens of fs) pulses and their second or third harmonic have enabled many studies investigating the effect of multicolor fields on HHG. A couple of these experiments are summarized in the following. Due to the multi-cycle pulse duration and a limited precision in the control of the relative phase and CEP of such multicolor fields as shown in most of the experiments, a clear separation has to be made with respect to single to sub-cycle sources as the HCF WS [8] and the PWS [44] as featured in this thesis. Nevertheless, the inter-cycle shaping of the electric field as intended with synthesis of multi-cycle driver to control the electron trajectory holds for multi-cycle and sub-cycle pulses.

In general, it is hard to state a fair comparison between single-color-driven and multicolor-driven HHG results since the phase-matching parameters alter drastically between single and multichannel operation and also change depending on the temporal overlap. We will have a closer look into that comparison on later chapters containing the results of the PWS-driven HHG. For the case of multi-cycle, multicolor driven experiments, Schütte *et al.* [139] report on a cut-off extension from 100 eV to 150 eV in neon using a 800 nm and 1300 nm two-color laser field while the yield only drops by a factor of 2 up to the cut-off, whereas Siegel *et al.* [140] mainly report on the yield enhancement of factor $\times 4$ while observing similar cut-off energy. Experimentally it can be observed that the trade-off between cut-off extension or yield enhancement is associated with the ratio of adjacent pulse intensities. A weak perturbation by a

short wavelength field to a long wavelength field enhances the yield. The majority of multicolor driven HHG experiments show a continuous spectrum around the time overlap. As explained in [137], the multicolor field increases the effective periodicity to ≈ 2 times the laser frequency, that would limit the emission possibilities. A continuum of up to 200 eV was reported by Calegari *et al.* in [141] for the case of neon gas. T. Kroh *at al.* [142] report a yield enhancement of $\times 8$ at cut-off energies of ≈ 70 eV but only $\times 2$ at cut-off energies of ≈ 200 eV. Takahashi *at al.* [143] reported on the generation of an IAP by multicolor laser fields, as proven by the CEP dependence of the HH yield even for multi-cycle (≈ 10 cycle) pulses. An attosecond streaking experiment with a few-cycle (≈ 2) pulse consisting of a 800 nm pulse and its 2^{nd} harmonic shows the generation of an isolated attosecond pulse at 90 eV central photon energy [144] as measured via attosecond streaking.

3.1.3 The Isolated Attosecond Pulse

The quest for ever shorter pulses of light is motivated by the natural time scales of electrons and according processes, and have put HHG in a prominent position. Ultrabroadband sources in the optical regime are mostly limited to fs timescales since the bandwidth necessary to significantly surpass the cycle duration of an optical pulse is technologically very challenging. The evolution of historical pulse durations is presented in a recent review [145] by Orfanos *at al.*. Depending on the definition of a pulse duration, the HCF WS has reported sub fs optical pulses [39]. The HHG emission at short wavelength happening within an optical cycle is temporarily very defined by default but a repetition at every half-cycle leads to a train of XUV pulses for multi-cycle driving pulses. The availabilty of intense few-cycle pulses, mostly from HCF compressors has led to the development of techniques that limit the HH emission from a few-cycle to only a single-cycle, therefore transforming the attosecond pulse train as generated by a few-cycle driver pulse to an *isolated attosecond pulse (IAP)*. Such techniques, doubted *gating*, are (1) polarization gating [146]–[150], (2) double optical gating (DOG) [151], [152], (3) ionization gating [153], [154] and (4) the previously mentioned temporal gating. At high photon energies, several groups have reported on pulses below 100 as FWHM duration with the current record hold at 43 as [90], [155], [156].

In contrast to gating few-cycle pulses, the interest in high-energy waveform synthesis is driven by its sub-cycle temporal duration and the ability to generate IAP without the need of additional gating techniques. Numerical simulations based on an IR waveform synthesizer predicting 55 as SXR pulses are presented in [157]. Experimental evidence of IAP generated by the PWS is pioneered in this thesis for various bandwidth. The reader is referred to the experimental section 3.6 with a vast demonstration of SXR continua as generated directly with the PWS.

As mentioned, the attochirp becomes interesting for IAP [127], [158]–[160]. The positive chirp of an attosecond pulse, as generated by short trajectories, can be counteracted by material dispersion [161]–[163]. Metal filters, commonly used for spectral filtering and blocking of the

driving laser pulse, exhibit negative dispersion. The flexibility of a dispersion scheme at XUV and SXR photon energies is limited to the available metals, their spectral transmission properties and the technical possibility of fabricating thin films. An overview of the most common metal filters, including their transmission and dispersion, is given in the figure 3.7. The refractive index and resulting group delay as derived from the complex refractive index:

$$n(\omega) = 1 - \delta(\omega) + i\beta(\omega) \tag{3.18}$$

$$GD(\omega) = \frac{z}{v_g} \quad \text{with} \quad v_g = \frac{dk(\omega)}{d\omega} \quad \text{with} \quad k(\omega) = \frac{n(\omega)\omega}{c} \tag{3.19}$$

with ω the frequency of the XUV/SXR pulse and z the material thickness. The chirp of the IAP

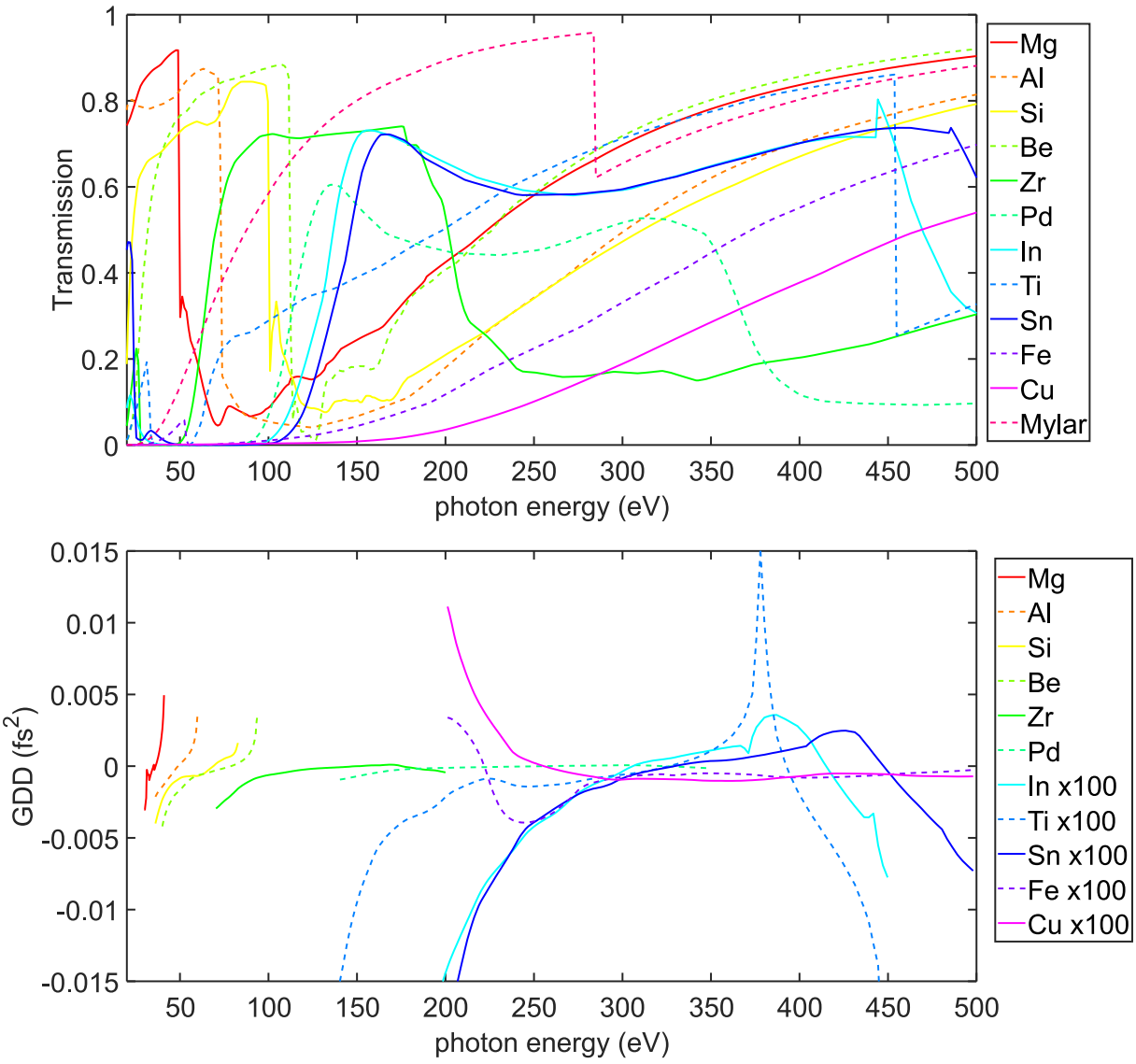

Figure 3.7: Transmission properties of metal filters (top) and GDD properties (bottom) with a thickness of 200 nm. For greater visibility, the low dispersion at high energies is multiplied by $\times 100$. The XUV/soft X-ray data is downloaded from [164]

scales inversely with the driver wavelength $\propto 1/\lambda$ and therefore high-energy continua inher-

ently show less chirp [165]. Contrary, the lack of metal foils with convenient transmission and negative dispersion for high-energy photons prevent IAPs with pulse durations close to their transform-limit. To raise negative dispersion in the water window range, Z. Chang *et al.* have proposed the use of gases and their linear refractive index [166] or of ionized hydrogen [167].
Coming back to a synthesized infrared driving field for the generation of IAP, the ability to control the electron trajectory can be used to not only optimize cut-off or yield, but can affect the chirp of the IAP. Simulations based on experimentally available sources [157], [168] have shown that with a control of ionization and recombination, the adjacent time window of recombination can be controlled and minimized to a certain extent. In a purely theoretical paper without the bound of experimental parameters, Kohler *et al.* [169] have shown the possibility for chirp-free IAP due to synthesized driving fields, where eight sinusoidal fields are synthesized to generate HHG in a He^{+} or Li^{2+} gas. Qualitatively similar fields approximating a DC field during the time of ionization is presented by Chipperfield *et al.* [102] with the goal to maximize the recollision energy but no further analysis on the temporal structure. The measured IAPs of this work are presented in the experimental section and show durations very close to the transform limit where only the propagation in the generation gas is assumed to help reducing the attochirp [45].

3.2 Waveform Dependent Strong-Field Control and Attosecond Science

The ability to generate ever shorter laser pulses goes along with a direct control of the electric field. While the control of pulse envelope to ever shorter temporal durations and control of the spectral phase has been subject for many decades, the transition to single-cycle optics can be seen as a transition from the envelope description to a direct electric field description. In the past, waveform control is mostly realized via two-color (multi-cycle) waveforms or the CEP control. HHG is a dominant application, as discussed in chapter 3.1.2, and shaping of the XUV continuum by CEP and polarization control is demonstrated in [170], [171]. Furthermore, waveform control enabled sub-fs timing of emission for short and long trajectory harmonics [172], dissociation dynamics in molecules [173] and charge migration in molecules [174]. Innercycle-resolved ionization dynamics of a laser pulse are measured in time domain with sub-cycle synthesized pulses as realized in an early version of the HCF WS [8].
A second version of the HCF WS [39] demonstrated the charge control by sub-cycle optical waveforms in SiO_2 [175]. The experiment disentangled the contribution of inter- and intraband currents leading to the emission of harmonics from the solid in the XUV. Inter- and intraband currents are controlled by the driving waveform and, moreover the characterization of the generated harmonics via attosecond streaking even allowed to disentangle a negative contribution to the chirp by intraband generated harmonics and vice versa for interband. A control of the

chirp from HH generated in a solid is found similar in theoretical work from Nourbakhsh *et al.* [176] modeling the emission of a MgO crystal pumped by two-color IR waveforms.

3.3 The Attosecond Beamline

The experimental realization of the science motivated in earlier chapters requires an elaborate infrastructure to generate, manipulate, detect and apply the XUV/SXR radiation. Vacuum chambers are required because of the absorption of the shortwave radiation in air. In addition, the guiding of SXR radiation solely by grazing incidence optics limits the flexibility and leads to rather extended experimental layouts. Parts of the beamline are inherited from the former Ph.D. student Y. Yang, see [177] for additional details. Ongoing modifications to the beamline for the experiments presented, has led to several changes that are covered in this chapter, starting from the initial setup. The details of the hardware are discussed first, and finally the procedures for data acquisition and calibration of XUV/SXR spectra are described.

3.3.1 Experimental Setup

The beamline consists of two large "main" chambers and smaller auxiliary chambers. The two main chambers are conveniently designed to provide sufficient space for all possible beam manipulation optics and remotely controllable stages, and have numerous ports for pumps, viewing windows, or feedthroughs. A computer-aided design (CAD) drawing of the full beamline is shown in figure 3.8. The first chamber takes the PWS as an input beam and contains the final pair of DCM, a beam-splitting assembly and the focusing optics to focus the PWS beam onto the HHG gas target. A mirror on a remote controlled stage serves as kick-out to inspect the beam through a viewport after transmission through the gas cell. The focusing optics are adapted to the experiments ranging from a $f = 4$ inch off-axis parabolic (OAP) to a $f = 375$, 400 or 500 mm spherical mirror. The gas inlet to the gas cell is controlled by a programmable electronic valve (El-Press, Bronkhorst) that covers sub 100 mbar to 10 bar of backing pressure. The second chamber contains the XUV optic, namely a toroidal mirror to image the generated harmonics, a motorized iris on a three-axis stage to mark the reference beam position, and a glass plate on a linear stage to block the XUV/SXR light when acquiring the background. As for the streaking experiment, the delay stage and beam recombination are positioned in the second chamber as well. The first two chambers are designed with an inner breadboard that is mounted on the floating optical table below the chambers, while the main chamber body rests on an aluminum frame. The geometric flexibility and vacuum-tight sealing is ensured by metal bellows. Superbly designed to isolate the heavy chambers and connected vibrating vacuum pumps from the optical setup, this concept has pros and cons as will be discussed. For historical reasons, the toroidal mirror has an imaging distance that hardly matches

the dimensions of the chambers and is applied differently from a 1 : 1 imaging while a second toroidal mirror was received at some point and is used in later experiments. The parameters of the toroidal mirrors used are given in table 3.1 From the curvatures of the toroidal mirror, the

Mirrors	R (mm)	r (mm)	S (mm)	α (°)
Toroidal Mirror # 1 (short)	8000	39	558.06	86
Toroidal Mirror # 2 (long)	10700	52.07	746.39	86

Table 3.1: Parameters of toroidal mirrors as used in the beamline

incident angle α and imaging distance S is calculated by

$$S = 2f_{sag} = 2f_{tag} \stackrel{!}{=} S' \tag{3.20}$$

$$\begin{aligned} f_{sag} &= \frac{r}{2\cos\alpha} \\ f_{tan} &= \frac{R\cos\alpha}{2} \end{aligned} \tag{3.21}$$

$$\alpha = \sqrt{\frac{r}{R}} \tag{3.22}$$

Placing the toroidal mirror with unequal incident arm length (S) and exit arm length (S') distance leads to aberrations since the focal lengths of saggital and tangential plane only overlaps at the designed imaging distance S of the toroidal mirror. The positioning of the toroidal mirror # 1 is realized with $S = 760$ mm and $S' = 440$ mm that minimizes the ratio S/S' as much as possible for the given geometry of the vacuum chambers. An electron time of flight (TOF) spectrometer is mounted closely to the second chamber resting on the frame and is not referenced to the optical table.

For the XUV HHG and attosecond streaking experiments (see section 3.5) the TOF spectrometer mounted on the small experimental cube chamber is located at the focus of the toroidal mirror. A motorized mount and a goniometer allow to optimize the imaging of the toroidal while the chambers are evacuated. The height of the toroidal mirror is fixed and aligned to the height of the driving laser beam. The focus of the NIR channel is imaged and captured on a CCD camera after the toroidal mirror via the kick-out mirror (dashed line in the figure 3.8) on a CCD camera. This configuration allows to fine-tune the angles of the toroidal mirror in vacuum. The optimization of the toroidal with the optical beam of the NIR channel is observed to be reliable with only minor optimization once the HHG beam is observed on the XUV CCD camera (Newton 940 CCD, Andor). The inset in figure 3.5 shows the imaged focus of the NIR channel exactly 3 mm in front of the TOF spectrometer. The grating spectrometer (251MX, McPherson) with an XUV CCD camera is located behind the TOF spectrometer. The spectrometer is resting on the optical table and therefore referenced with the optical and HHG beam.

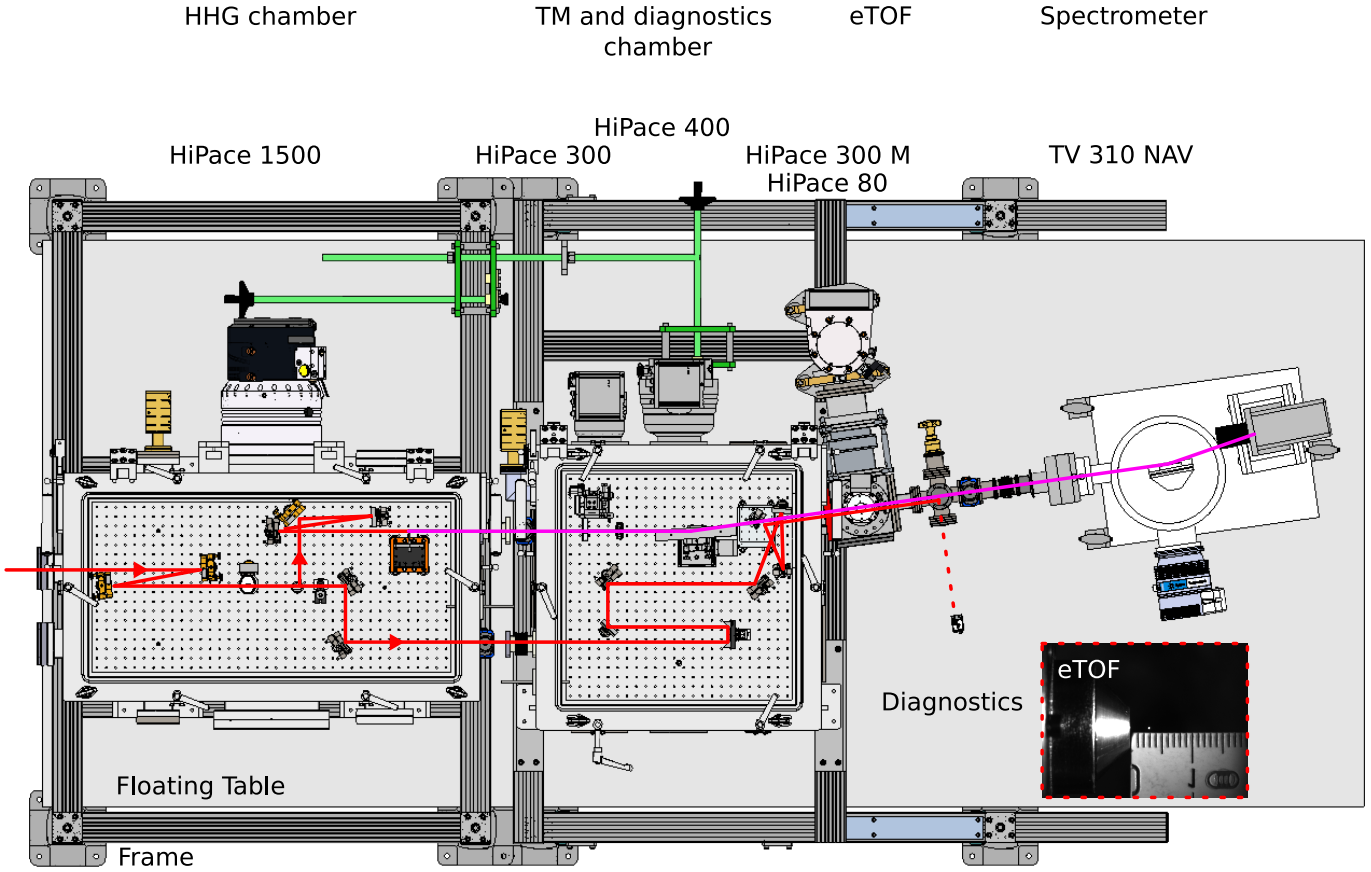

Figure 3.8: Attosecond beamline in the initial state as used for attosecond streaking measurements. The PWS pulse enters on the left and undergoes a final reflection on a pair of DCM (SDCM0) before the pulse is split in the vertically arranged CaF_2 splitting unit. The reflection of the CaF_2 window is guided to the second chamber while the transmission is focused with a spherical mirror ($f = 500/375$ mm) on the HHG gas target. The lower energy pulse copy, the "streaking field" is recombined with the HHG beam in the second chamber by means of a holey mirror and focussed at the TOF spectrometer while the harmonics are imaged with a toroidal mirror at the TOF. The driver beam is observed after passing through the beamline with a kick-out mirror as sketched by the dashed lines. The inset shows a camera image as used for geometrical alignment of the beams and TOF. To the right, a grating spectrometer (251MX, McPherson) with XUV CCD (Newton CCD, Andor, 13.5 μm pixel pitch) is placed. The frame and floating table is indicated with the breadboards in the first two big chambers connected to the floating table.

3.3.2 High-Pressure Gas Cell

The necessity to reach high pressures (couple of bars) in the gas cell to fulfill phase-matching conditions for the generation of high photon energies required an update of the generation condition in the first chamber. The concept of recent beamlines to employ a very compact generation chamber and to isolate the experimental chambers with several differential pumping stages [178], [179] stays in contrast to the concept of two central big chambers as in our beamline. In addition, the toroidal's fixed geometry does not allow separating the chambers arbitrarily to insert differential pumping stages. The working solution is a chamber-in-chamber design as shown in figure 3.10, basically a single-stage differential pumping concept. A direct connection to a vacuum pump allows to pump most of the gas load before it reaches the turbo pump of the main chamber. The high-pressure gas cell is designed with big exchangeable screws as in- and outlet hole for the laser, they are pictured in figure 3.9 (e) made out of brass and the nuts hold them in position. Towards the tip, the outer diameter is machined as well to fit the stage below. The Screws allow for a flexible exchange of the hole diameter and hole-to-focus distance without the need to remanufacture the full chamber. The screws have a central stepped conical hole with 1 mm diameter at the tip. The adjustment of the screws as far from gas cell as the laser transmission allows, optimizes the efficiency of differential pumping to the big chamber. The larger the distance between screw tip and gas needle, the less gas transmits to the surrounding chamber and the more gas turbulently disperses in the high-pressure gas chamber. This design allows the backing pressure to be increased from $\approx$ 500 mbar with a free-standing gas nozzle to $\approx$ 10 bar. Still, the pumps of the beamline are working at their limits and the pressure in the first big chamber around the high-pressure gas cell reaches up to 0.1 mbar. The pressure at the high-pressure gas cell is measured in the tens of mbar regime. In this regime, the available turbo pumps are inefficient because the pressure is too high and the available scroll pumps are inefficient because the pressure is too low. A solution yet to be tested is presented in section 4 with larger roots and multistage roots pump directly attached to the high-pressure gas cell.
The most efficient way to limit the complexity of high-power vacuum pumps is a precise machining of the gas nozzle itself. The smallest possible diameter in the gas nozzle that still ensures the laser transmission allows (1) high backing pressure and (2) limits the consumption of noble gases. The gas nozzle preparation is done in-house with the typical lab tools in an empirical manner. With laser micromachining and printing becoming more popular and cheaper, this is probably a good try in the future. The nozzles used throughout this thesis are semi-infinite designs in glass and metal. A few photographs are given in figure 3.9.

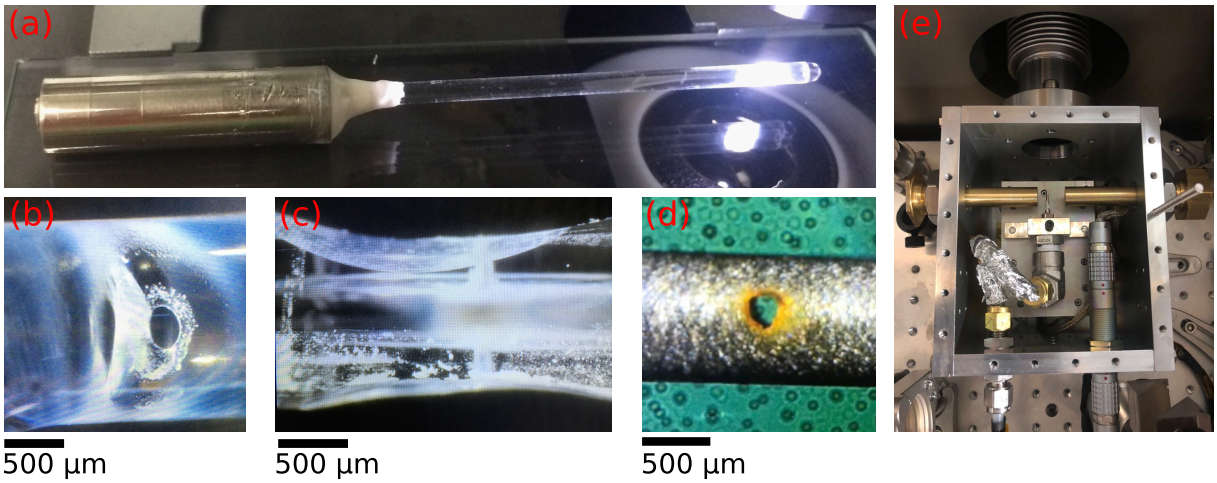

Figure 3.9: Semi-infinite gas nozzles for the generation of HHG. Glass capillaries from hollow core fibers are glued to metallic tubes (a). Tapering of the thick walls (c) allowed for well-shaped conical holes. A metal gas cell (d) is shown in detail and mounted with the Luer-lock system in the high-pressure gas cell (e).

3.3.3 Beamline Modification

The experimental setup, as shown in the previous sections, has been optimized throughout of this thesis which led to minor, detailed and major structural changes. Following the description of the beamline, this section introduces to the modifications made while transferring from attosecond streaking measurements to purely SXR generation and characterization. The CAD drawing including the modifications is shown in figure 3.10.

The toroidal mirror #2 with $S = 746.39$ mm allows to place the gas needle and the input slit of the spectrometer close to an ideal $1:1$ imaging condition. With the aim to detect the high-energy photons that unavoidably come with lower flux, the entrance slit of the spectrometer should be located close to the toroidal imaging. In this way, the spectrometer slit does not need to be reduced and the spectra can be taken with maximum flux and resolution. Furthermore, the beam dimensions are covered by the XUV CCD camera, and it is possible to record the spatial beam profile of the XUV/SXR via the zero-order reflection from the grating.

The transition to high backing pressures makes the precise machining of the gas nozzle important. The gas nozzles are displayed in figure 3.9, with the transition from glass to metal nozzles for the following reason. The homemade glass nozzles are laser drilled with ≈ 4 mJ of a Ti:sapphire laser, with the benefit that they are robust against the PWS pulse and survive any misalignments or beam-pointing deviations. At high backing pressures, the exact (smallest) hole size becomes most important and it became clear that the hole drilled by another laser never fits perfectly to the PWS focus. Metallic gas cells, on the other hand, can be drilled in the focus with the PWS in the exact position of the HHG. That makes a perfect fit but any vibration on the beamline or beam-pointing makes it necessary to replace the gas cell. To operate the beamline efficiently, a day-to-day long-term geometric stability between the vacuum chamber

and the gas needle monted therein with the PWS beam of less than a few μm is desirable.
The optical setup is based on large connected floating optical tables, that extend to the vacuum beamline and the breadboards inside the vacuum chambers are linked to the big optical tables. Flexible metal bellows isolate the vacuum. It was already observed during the streak measurements that the evacuated and vented vacuum chambers lead to an irreversible height change with respect to the PWS beam. To quantify this motion, a small laser diode (LD) is fixed to the TOF that is resting on the frame and pointing on a CCD camera that is mounted on the optical table close to the PWS beam combination optics, as sketched in 3.12. The CCD camera data is recorded at 1 fps while the vacuum chambers are being evacuated, resulting in a shift of the laser diode beam profile on the CCD camera (inset of figure 3.11). As each CCD image is analyzed, the center of the beam profile is determined, and a plot of the X-Y coordinates is shown in figure 3.11. The CCD camera (ace acA640-750um, Basler) has a pixel size of 4.8 μm. The left panel of the figure 3.11 shows some manual excitation of the table. The position in vertical and horizontal directions does not recover. The right panel shows the measurement while the vacuum chambers are evacuated (pumped) repeatedly two times. Again, especially the vertical positions stays with an offset and the corresponding linear fits do not suggest a recovery of the position in an acceptable time span. The pressure-controlled floating of the optical tables is realized with a lever-actuated valve that shows a limited precision with a measured hysteresis of ≈ 100 μm.
An imaging system based on kick-out mirrors, vacuum apertures and CCD cameras is installed to make a full beam alignment in the vacuum chambers possible even under evacuated conditions. That is helpful and enables a precise alignment but is time consuming. Finally, the optical table of the vacuum beamline is detached from the optical table of the PWS setup, and the floating behavior of the beamline breadboards is currently prevented by fixing the floating table to the stable, ground-referenced frame. A sketch of the table and vacuum infrastructure is given in figure 3.12 with the initial situation (left) and the current situation (right). In this way, the beamline is operated much more efficiently and the passive stability is sufficient to operate the precise metal gas nozzle for several weeks without damage (proper beam point stabilization for the PWS provided). Furthermore, the detachment between the laser/PWS setup and vacuum beamline increased the long-term stability of the OPAs as part of the synthesizer because the ”T” connected table does not act as a big lever anymore (sketched as angle α in figure 3.12). It has to be investigated if fixing the optical setup in the beamline to the frame and therefore coupling the vibrations of the vacuum pumps tighter to the optics might be disadvantageous once time resolved, attosecond measurements will be continue. The turbopumps that are connected directly to the sensitive TOF and experimental chamber are magnetic levitation pumps (HiPace 300 M, Pfeiffer) and should limit any mechanical vibration to the minimum possible.

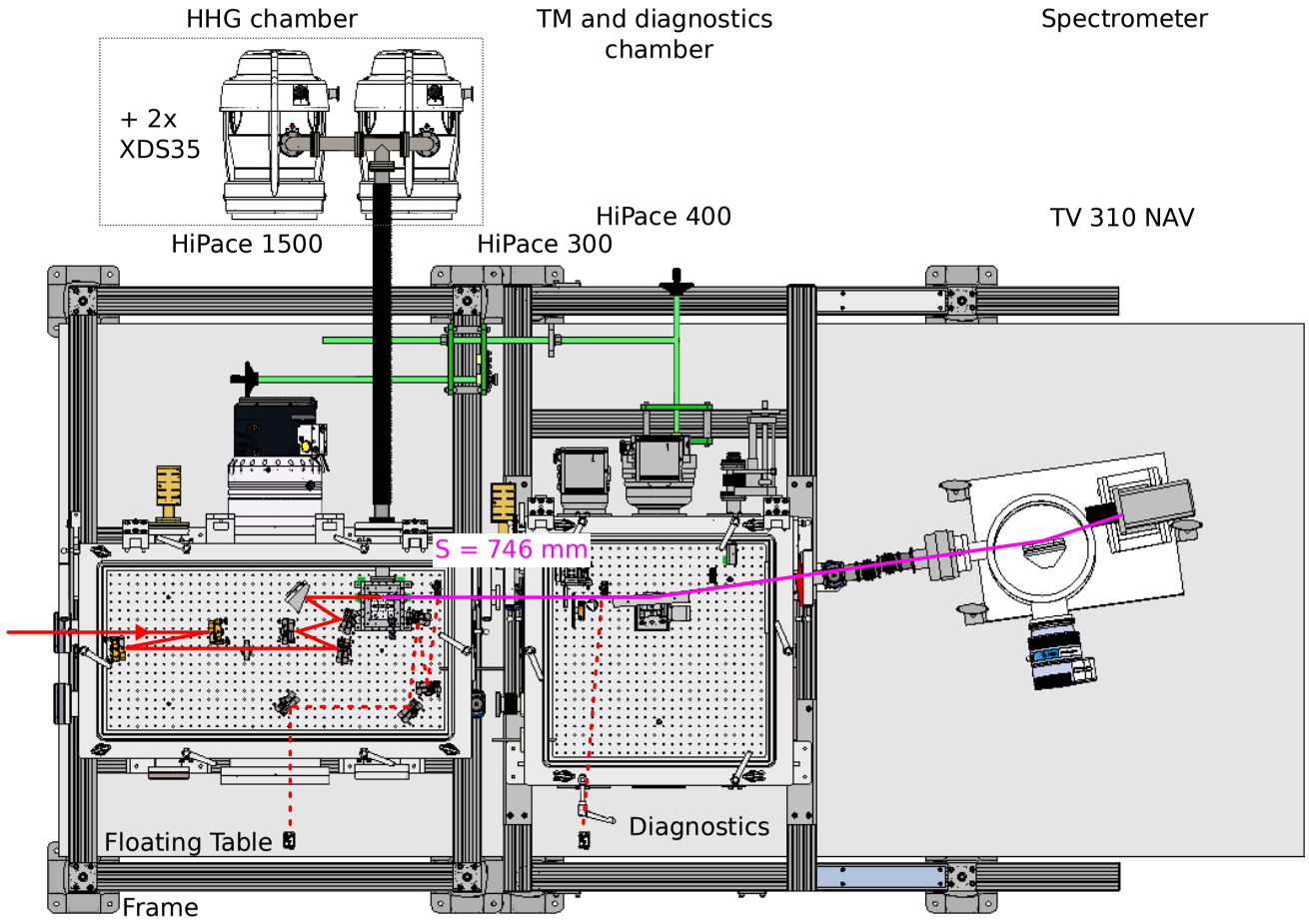

Figure 3.10: Attosecond beamline modified for the generation and efficient detection of SXR harmonics. After final compression on a pair of DCM (SDCM0), the PWS pulse is focussed with an $f = 4$ inch 45° degree OAP mirror on the HHG gas target. An additional motorized wheel to hold SXR metal filter foils and the XUV photodiode is mounted in the second chamber. The toroidal mirror installed is specified with an imaging distance of $S = 746.39$mm. The input slit of the XUV spectrometer is placed as close as possible to the image point of the toroidal mirror.

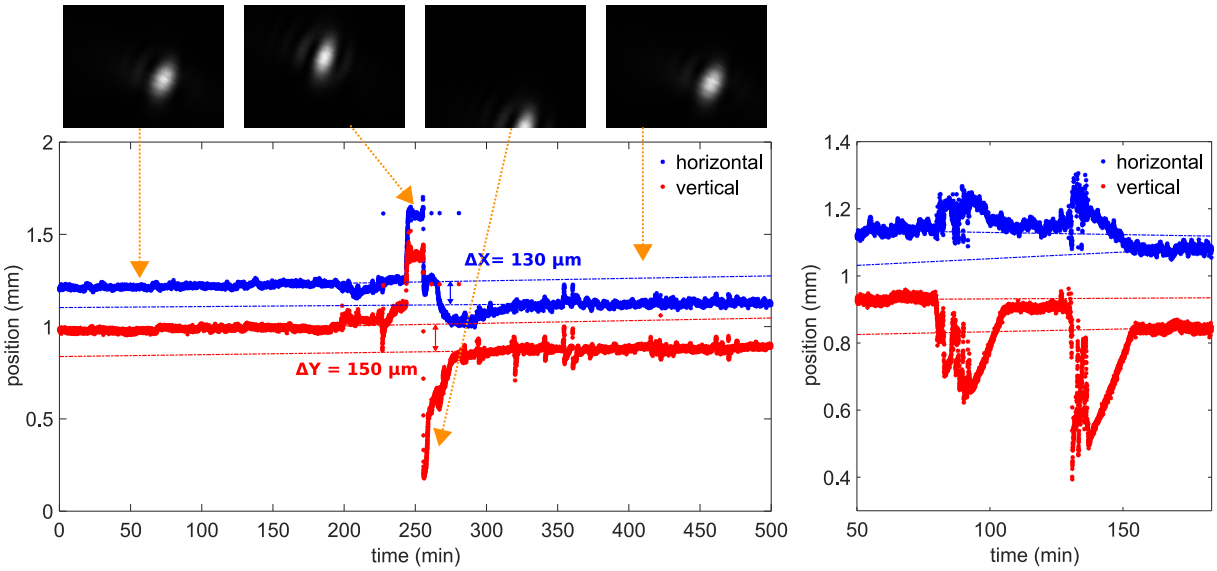

Figure 3.11: Measurements of the movement between TOF spectrometer as mounted on a solid frame and the floating optical table. Data retrieved by analyzing the beam position on a CCD camera with a temporal resolution of 1 s. The positioning of laser diode and CCD camera is shown in figure 3.12. The left plot shows some manual excitation of the table. The position in vertical and horizontal direction does not recover. Four exemplary frames of the CCD camera recorded beam profile at characteristic times. The right panel shows the measurement while the vacuum chambers are evacuated (pumped) repeatedly two times. Again, especially the vertical positions stay with an offset.

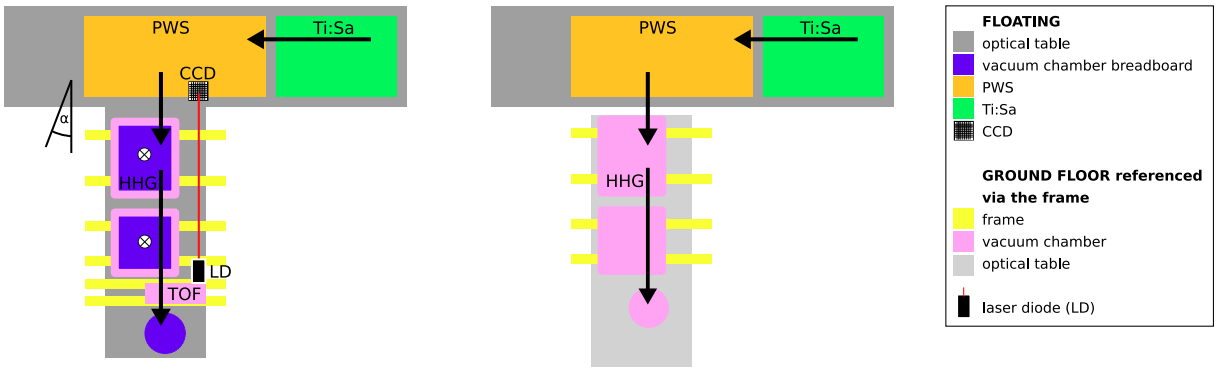

Figure 3.12: Infrastructure of the laser system and attosecond beamline with a special focus between ground floor referenced and floating optical tables referenced setups as marked by the colors (see legend) Left panel displays the initial setup with the "T" connected optical tables and floating breadboards. The force raised by the vacuum leads to a vertical tilting (indicated by α). The right setup shows the disconnected tables and the optical table of the beamline fixed to the frame.

3.3.4 Experimental Data Recording and Processing

Having covered the extensive beamline infrastructure in the previous sections, the following sections address the characterization of the generated XUV/SXR pulses. The spectrum of the HH signal is recorded with a grating spectrometer (251MX, McPherson) and a cooled XUV CCD (Newton 940, Andor) camera. Three different gratings are available, two of which can be installed simultaneously in the vacuum chamber and adjusted for a suitable shift in spectral acquisition bandwidth. The details of the gratings are summarized in the table 3.2.

The geometry of the grating spectrometer is sketched in figure 3.13 based on the details given

Grating selection (grooves/mm)	300	1200	2400
Angle of incidence (degrees)	87	87	88.65
Deviation angle degrees	170	170	174.4
Focal plane width (mm)	25	25	20
Spectral range (eV)	15-65	62-248	248-1240
image distance r to input (mm)	237	237	237

Table 3.2: Details of XUV/SXR gratings as used with the McPherson 251MX spectrometer. The gratings are blazed aberration-corrected concave gratings for a flat-field image plane. See figure 7.3 in appendix.

in figure 7.3, see appendix. All dimensions are in mm. The 2400 gr/mm grating, designated "high-energy" grating, requires a different angle of the internal mounting and tuning of the entire spectrometer angle to the beam with respect to the "low-" and "mid energy" gratings. In the plane of the detector, the dimensions are given that the CCD detector has to cover respectively to be positioned at. The photons are spectrally dispersed in the shaded area while the dashed line indicates the zero-order reflections. The displacement of ≈ 40 mm is realized with a linear micrometer stage and a flexible bellow connects the CCD camera to the grating chamber. The energy calibration of the HHG spectra is done in two different ways depending on the energy range. Usually for the photon energies < 100 eV, the NIR channel is used to generate a harmonic comb. From the distinct harmonic peaks, the 1^{st} and 2^{nd} diffraction order of the grating can be identified. With the following grating equations and the known geometry of the grating (figure 3.13), an absolute spacing of the harmonics in the plane of the detector is calculated. The relation between incident angle α and wavelength-dependent diffraction angle β for a given order m depends on the groove spacing Λ

$$m\lambda_q = \Lambda\left(\sin\alpha + \sin\beta_q^m\right) \tag{3.23}$$

indicating the q-th harmonic wavelength and diffraction angle. Setting up the relation between 1^{st} and 2^{nd} order for the q-th harmonic

$$2\left(\sin\alpha + \sin\beta_q^{m=1}\right) = \frac{2}{\Lambda}\lambda_q = \left(\sin\alpha + \sin\beta_q^{m=2}\right) \tag{3.24}$$

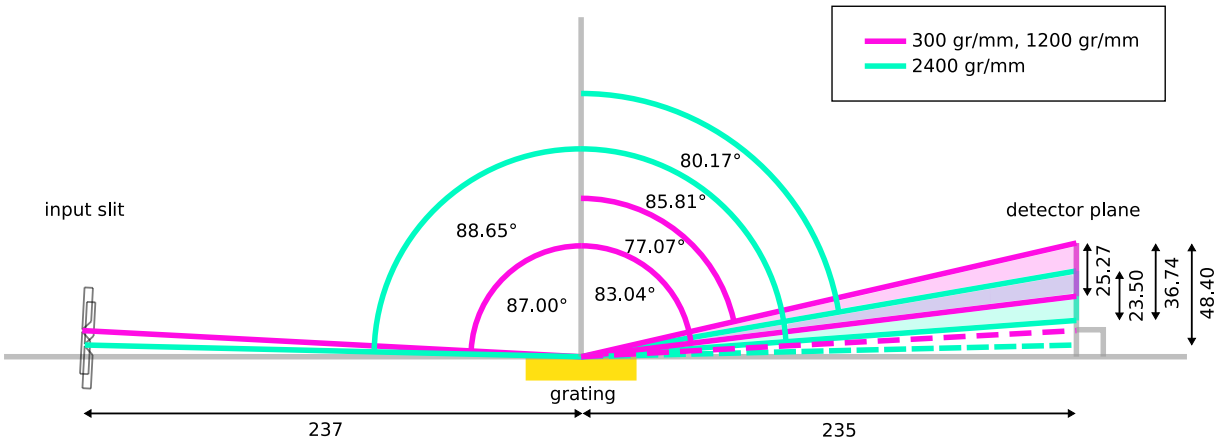

Figure 3.13: Geometry of the gratings as used in the grating spectrometer. The high photon energy grating (2400 gr/mm) requires different angles compared to the low photon energy gratings (300 gr/mm, 1200 gr/mm)

yields

$$\sin\alpha + 2\sin\beta_q^{m=1} = \sin\beta_q^{m=2} \tag{3.25}$$

The distance on the detector plane from the horizontal plane to the transverse position is given by

$$y_q^m = R_0 \cot\beta_q^m \tag{3.26}$$

with R_0 defined as horizontal grating to detector distance as defined by the manufacturer to be $R_0 = 235$ mm. The distance y_q^m is calculated for at least two harmonics and their 1^{st} and 2^{nd} diffraction order. The distance on the detector plane is then compared to the measured distance as can be measured absolutely by converting the pixel location of the harmonics via the pixel size (pixel $= 13.5\mu$m for Andor Newton). Due to imperfections on the precise adjustment of the spectrometer apparatus to the incident angle of the XUV/SXR beam, the calculated distances for harmonic q and $q+1$ may not match the measured distances on the detector. A slight modification of the incident angle α in the calculation allows to minimize the error between calculated and measured distance. Finally, the conversion from the linear wavelength array to linear energy array need to take into account the Jacobian factor [180] so that for the signal S, the integration $S(E)dE = S(\lambda)d\lambda$ are equal. The result of the calibration is shown in figure 3.14 for a spectrum generated with the NIR channel only in argon. After the background subtraction, a pair of corresponding harmonics in 1^{st} and 2^{nd} order are selected as indicated by the dashed lines in figure 3.14 (b) and the resulting pixel to energy (in eV) curve is calculated. The calibrated spectrum is shown on the right. The harmonics are generated with the single NIR channel in argon at a backing pressure of 250 mbar focusing with a spherical mirror $f = 375$ mm. The spectra in this energy range are taken with grating # 1 of 300 gr/mm The residual NIR light is blocked

with a 300 nm Al filter. Due to the pulse parameters of the synthesizer, only the NIR channel

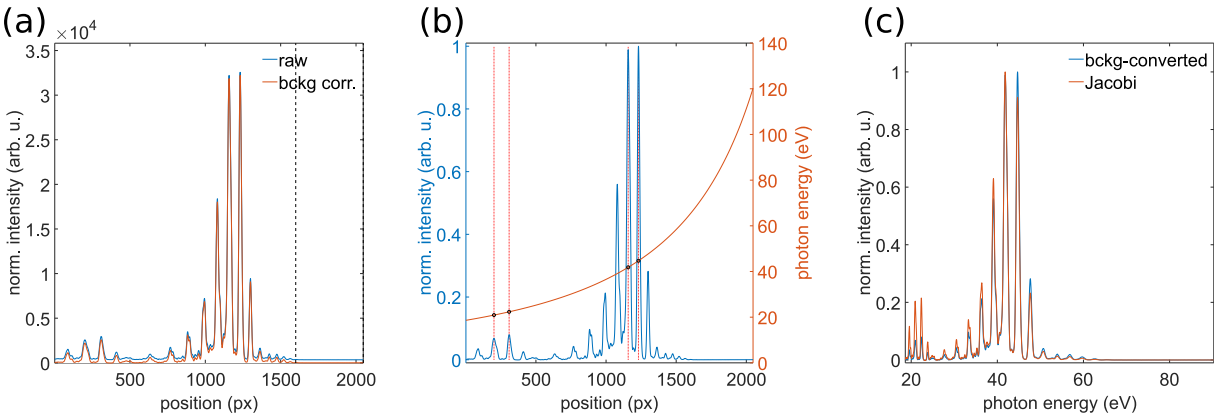

Figure 3.14: Calibration procedure of HHG spectra based on harmonic peaks. The raw data are background corrected (a) and a pair of neighboring harmonic peaks in first and second diffraction order are manually selected as indicated by dashed lines (b). Based on the grating equation and known grating geometry, the calibrating spectra including the Jacobi correction is plotted in (c).

generates distinct harmonic combs that do not extend beyond ≈ 100 eV. An extrapolation of the calibrated energy axis well beyond the calibrated range would lead to significant error due to the exponential dependency between pixel position and photon energy. At higher photon energy, such as those produced by the IR channel or synthetic pulses, the continuous spectra are calibrated using the known absorption edges of thin metal foils. In this case, the photon energies corresponding to the absorption edges are known from literature [164]. A calculation of the expected distance of the edges on the detector plane based on the diffraction angles β is compared to the measured distance based on the pixel size. Similar to the previous calibration method, a slight variation of the incident angle α allows to optimize the calibration procedure. Analog to figure 3.14, the calibration procedure for XUV/SXR continua is shown in figure 3.15. The continua are generated with the single IR channel in helium at a backing pressure of 10 bar focusing with an OAP of $f = 4$ inch. The spectra in this energy range are taken with grating # 3 of 2400 gr/mm. A 200 nm titanium filter blocks the residual IR light and a 500 nm mylar filter is used to exhibit the Carbon edge (284 eV) and a 400 nm Boron filter cuts the spectrum at 188 eV.

The calibration along the spectral intensity axes involves the transfer functions of the XUV optics and the quantum efficiency of the XUV CCD camera as supplied by the manufacturer. The measured spectrum defined as S_{meas} and the generated spectrum at the source as S_{source} are related by the transfer functions h.

$$\mathrm{S_{meas}} = \mathrm{h_{filter}} \times \mathrm{h_{toroidal}} \times \mathrm{h_{grating}} \times \mathrm{h_{QE,CCD}} \times \mathrm{h_{eh,CCD}} \times \mathrm{S_{source}} \tag{3.27}$$

The filter transmission h_{filter} is given in figure 3.7. The reflection of a (as in our case) gold-coated toroidal mirror at an incident angle of 4° is given from the X-Ray database [164] for

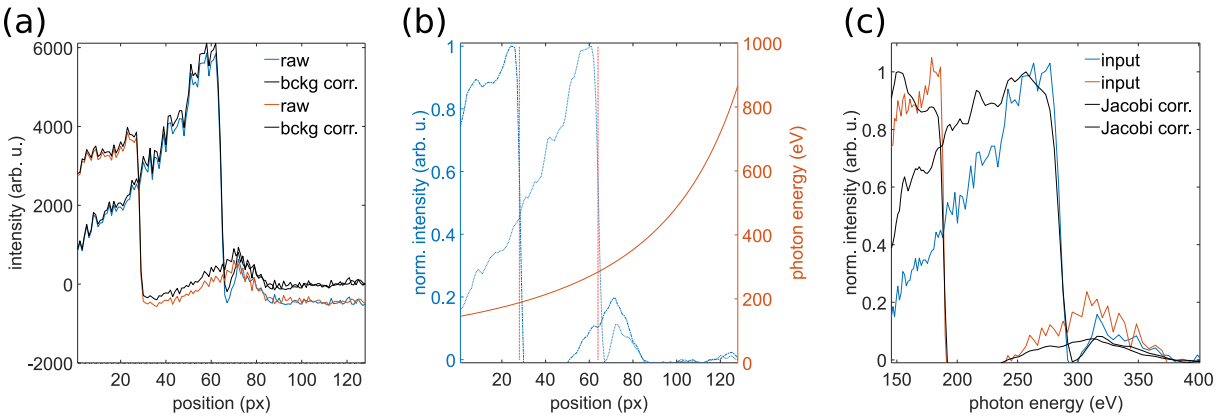

Figure 3.15: Calibration procedure for HHG spectra based on absorption edges of metallic filters for broadband continuous spectra. The raw data are background corrected (a) and two spectra transmitted through different metallic filters are overlayed. The absorption edges are identified as indicated by dashed lines (b). Based on the known energy from literature of the absorption edges, the calibrating spectra, including the Jacobian correction, is plotted in (c). Filters used in this calibration are Boron (188 eV) and Mylar (C-edge, 284 eV).

$h_{toroidal}$. The manufacturer-specified grating transfer function $h_{grating}$ as given by the manufacturer and quantum efficiency QE of the XUV CCD $h_{QE,CCD}$ is plotted in figure 3.16. On top of the QE, the number of generated electron-hole pairs in the CCD scales linearly with the photon energy and is accounted for by $h_{eh,CCD}$. The photon energy required to generate an electron-hole pair is 3.65 eV, e.g. a 10 eV photon generates $\frac{10}{3.65} \approx 2.73$ photoelectrons per XUV photon [181], [182] In addition to the XUV/SXR characterization, this thesis will investigate

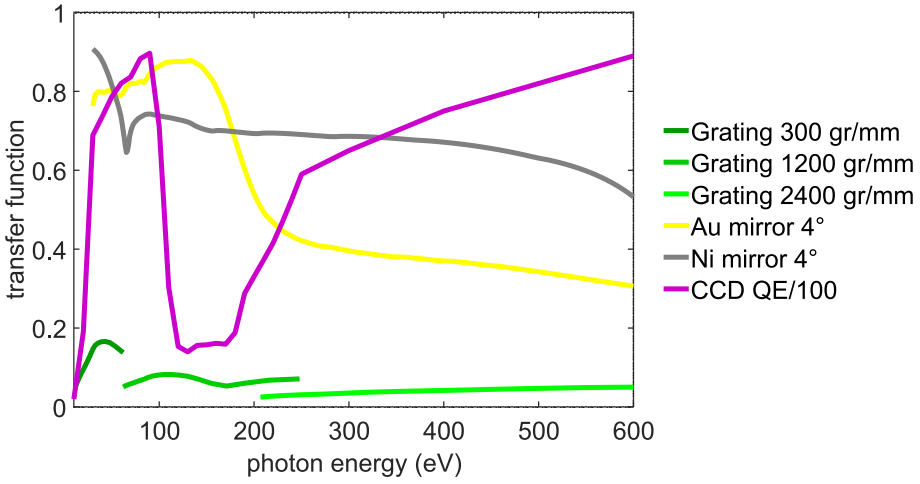

Figure 3.16: The reflectivity of XUV optics and quantum efficiency (QE) of XUV CCD camera as used in the beamline and applied for intensity calibrations. The reflectivity of the gratings is plotted for the 1^{st} diffraction order. The reflectivity of gold (Au) at given incident angle of 4° degree is taken for the toroidal mirror. The reflectivity of Nickel (Ni) plotted for comparison.

the tight dependence between PWS waveform and the generated harmonics. Once the macroscopic parameters such as pulse energy, spatial beam overlap and focusing conditions are fixed,

the waveform at the point of HHG is controlled by the RP and CEP of the PWS. A synchronous recording of the relative and carrier envelope phase values that arrive at the laser repetition rate (1 kHz) from the PWS feedback system and recording of the XUV CCD data is necessary to link the generated XUV/SXR to the phase settings of the PWS. The XUV CCD camera is operated with $0.2 - 0.5$ s integration time at lower photon energies and $1 - 2$ s at higher photon energies around der C-edge. Historically, the PWS feedback control and the HHG data processing ran on separate PCs. Therefore, early measurements presented in section 3.4 and 3.5 are synchronized using short flashes of an LED as a timestamp. The LED is triggered by the feedback system at defined times and positioned at a viewport of the XUV spectrometer. The LED flashes saturate the detector for a single integration period that marks as time stamp. At low integration times, the synchronization is sufficient and the loss of HHG spectral data due to the saturation of the detector is negligible. With an update of the PC hardware, it is now possible to run the data streaming from the feedback system and from the XUV CCD camera on the same machine, giving both measurements the same time reference for rough synchronization. In order to precisely time align both processes, which are run in different scripts, the "fire" output of the XUV CCD camera is used. The fire output provides a signal in a TTL format for the time that the CCD detector is recording. The signal from the fire output is recorded by the feedback system synchronously with the RP and CEP values. This ensures a tight lock between the phase data from the PWS and the recorded XUV/SXR spectra. A synchronized set of data from the phase lock system and XUV spectrometer is presented in figure 3.17. The CEP and RP as measured by the feedback system are plotted synchronized with the HHG spectra. The phases are modulated in random sequences with a sawtooth-like modulation. The synchronized data show a tight dependence on the recorded phase values. Already here, various spectral shapes are observed that will be presented in greater detail in section 3.4. More Details on the synchronization and another set of data is given in figure 7.1 of the appendix.

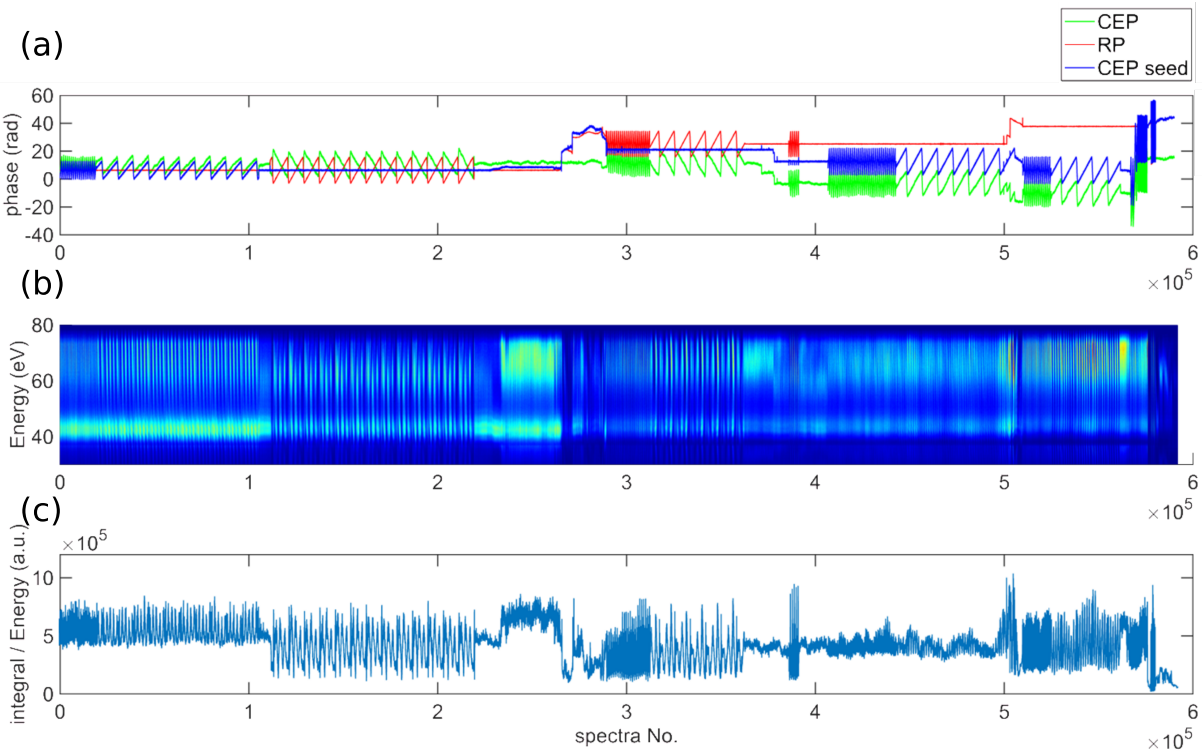

Figure 3.17: The representation of a synchronized RP-CEP scan. The top panel (a) plots the measured RP and CEP data. The two curves for the CEP correspond to the measured CEP at the CEP stable front-end "CEP seed" (blue) and to the CEP measured with the multi-phase meter at the PWS output (green). The central panel (b) shows the spectrogram of the recorded HHG spectra in argon and the bottom panel (c) plots the integral of the spectra in arb. units. The plots show several sections of CEP and/or RP sawtooth like modulation and short sections of stabilized conditions. A tight dependence of the HH spectra on the phase values is observed.

3.3.5 XUV Photodiode

One of the motivations to drive HHG with complex non-sinusoidal waveforms are the theoretical predictions on yield enhancement [102]–[104], as discussed previously. The question of what is a fair comparison between synthesized driven HHG and single-color-driven HHG at which energies and central wavelength shifts to the following chapters, while the details on the measurement routine of the absolute photon flux are presented here. The measurements are acquired with a calibrated XUV photodiode and finally compared to the calculated photon numbers as retrieved from the XUV CCD camera measurements. The photodiode measurements are taken as reference and the XUV spectrometer data, which usually underestimates the photon number by a factor 2-3, are upscaled to match the reading of the photo diode. From the side of the photodiode, the main difficulty is the suppression of the background light, primarily the residual optical laser that propagates collinearly. The photodiode is sensitive to wavelength < 1 μm and thus sensitive to the NIR channel. Metal filters are supposed to block the residual laser light, but possible tiny holes in the thin foils permit the laser light to transmit. High quality

filters (Luxel corp.) are visibly hole-free, but still do not solve the background issue in our case. When the NIR channel is added to the IR channel, a significant signal on the photodiode is measured. An estimation of the photon numbers based on data from [61] gives a transmission of $10^{-11} - 10^{-13}$ for a 200 nm metal foil at visible wavelengths. The number of photons per second in the NIR channel of 20 μJ calculates to $\approx 8 \times 10^{16}$ ph/s. Applying the transmission of a metal filter, the photon number after a 200 nm metal filter still reads 10^5 ph/s, which is on the order of the expected HHG photon flux in the water window. Furthermore, a very dynamic visible change in the visible light emitted from the plasma in the HHG gas cell is observed when the RP between NIR and IR is modified. This means that there is no constant background to subtract when performing scans of the RP.

On the other hand, the uncertainties of the XUV CCD camera are manifold, with possible errors in the transfer functions due to oxidation or carbon contamination of the filter and surfaces, "lost" photons due to scattering from imperfect surfaces or simply due to the tight apertures such as the slit of the grating spectrometer.

The XUV photodiode (SXUV100, Opto Diode) is mounted in a ceramic PCB with a transimpedance amplifier 10 GΩ directly in the vacuum. The voltage is measured with an oscilloscope or digital-to-analog converter (DAC). The response of the XUV photodiode is confirmed in a beamtime at P04, PETRA3. The XUV beamline P04 allows for relatively low photon energies that match the range of typical HHG spectra and a small bandpass of the beamline ensures a precise tuning of different photon energies to take spectrally resolved reference measurements. The benchmark for our photodiode (denoted UFOX-PD) is the measured flux of the beamline hard- and software. The beamline photodiode (denoted P04-PD) is regularly calibrated at the Physikalisch-Technische Bundesanstalt (PTB), Braunschweig and the photo current is measured with an electrometer (6517A, Keithley). The measurement spans from $100 - 600$ eV while the data from $100 - 250$ eV might contain contributions of other than the specified wavelength since the undulator had to be detuned drastically to reach such low photon energies. For each photon energy, the P04-PD and the UFOX-PD are positioned alternately in the beam including a background measurement for every data point. Furthermore, the P04 beamline delivers 10^{12} photons per second, that is well above the expected photon flux from a HHG source. The photon flux of the beamline is reduced by several filters in order to establish similar conditions compared to the HHG beamline. The absolute voltage measured from the transimpedance amplifier reads a few volts, that is still an order of magnitude higher compared to the measurements at the HHG beamline but sufficiently lower than the saturation voltage of the transimpedance amplifier at ≈ 15 V. The raw data are given in amperes for the P04-PD from the electrometer and in volts for the UFOX-PD from the transimpedance amplifier. The voltage-to-current translation is calculated via the 10 $G\Omega$ resistor.

The power [W] is calculated from the PD current [A] via the response curve given by the manufacturer

$$P[\mathrm{W}] = \frac{PD\ current[\mathrm{A}]}{responsitivity[\mathrm{A/W}]} \tag{3.28}$$

The resulting photon flux (1/s) is calculated to

$$N_{Ph}\,[1/\mathrm{s}] = \frac{P[\mathrm{W}]}{E[\mathrm{eV}]} \cdot 1.6 \cdot 10^{-19} \tag{3.29}$$

Figure 3.18 displays in (a) the responsitivity and in (b) the XUV photodiode with an active surface of 10×10 mm (b). The measured currents and calculated power and photon numbers vs. the photon energy is plotted in panels (c-e). For the P04-PD, the beamline software outputs

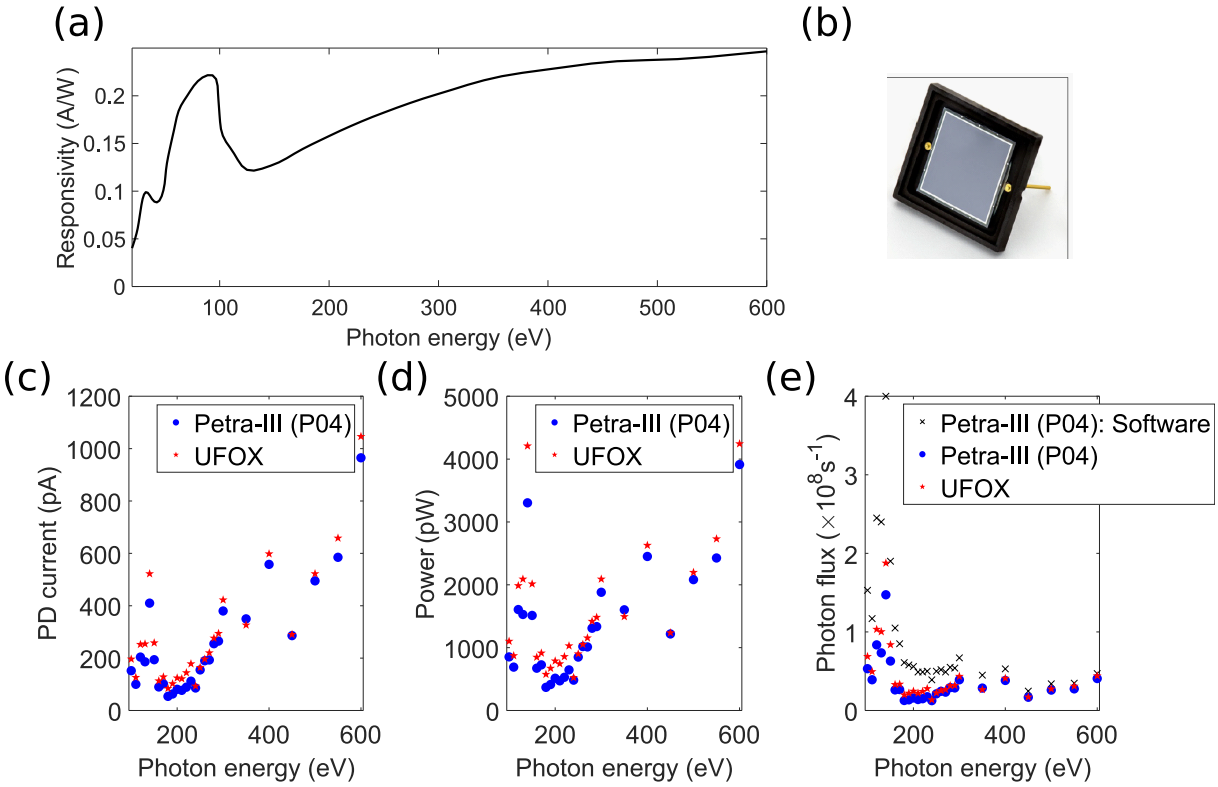

Figure 3.18: Calibration measurements of an XUV photodiode (SXUV100, Opto Diode) at P04, PETRA III beamline. The responsitivity curve (a) as provided by the manufacturer for the photodiode of 10×10 mm active area. The measurements of our photodiode "UFOX" compared to the calibrated photodiode from P04 beamline ón the undulator beam (c) and calculated power (d). The resulting photon flux (e) is plotted including the photon flux as displayed by the beamline software.

the raw PD current and the photon flux. How the conversion is done was not accessible. Based on the raw data, the photon flux is calculated via equation 3.29 and plotted in panel (e) of figure 3.18 together with the photon flux of the beamline software. The calculation seem to differ with a linearly increasing offset to smaller photon energies but from 250 eV onwards, where the beam should only contain the specified wavelength, the raw PD current and power are in good agreement with ≈ 6 % error.

3.3.6 Electron Time-of-Flight Spectrometer

The streaking spectrograms are measured with an electron time-of-flight spectrometer (eTOF). Since only this single electron TOF, no ion TOF etc. is used throughout this thesis, it is refered as TOF. As a rather simple instrument with a single detector, it allows electron spectra to be measured over a large bandwidth with high efficiency because of the collection of all electron energies on a single detector. The energy resolution is obtained by high-speed read out electronics detecting the electrons on a microchannel plate (MCP). The TOF used throughout the experiments (ETF11, Kaesdorff) consists of an electrostatic lens, a μ-metal shielded drift tube of $L = 294$mm, an acceleration or deceleration stage and the MCP. The distance between entrance aperture and the electrons to be measured (= focus of the laser in a streaking experiment) is designed to be 3 mm. An MCP detector follows the design of the chevron geometry with two MCP plates and slightly oppositely angled channels of 5 μm diameter. The overall diameter is given to 40 mm. A high voltage applied to the MCP allows an impinging electron to generate an avalanche of secondary electrons that is measured as current at the anode. The electrostatic lens allows to increase the acceptance angle but increases the spectral selectivity and is not used for the measurements in this thesis. The minimum electron energy is given to 20 eV The energy of electrons is measured via the time-of-flight according to

$$E = \frac{m_e}{2}\left(\frac{L}{T}\right)^2 \tag{3.30}$$

with m_e the electron mass, T the time-of-flight and L the drift length.
The MCP is read out with a fast oscilloscope (WaveRunner 640Zi, Teledyne LeCroy) specified with a bandwidth of 4 GHz and 20 GS/s. The oscilloscope is triggered by the laser pulse with a fast photodiode (ET4000, EOT). With the triggered time windows set correctly, a couple of hundred sweeps are summed until a defined spectrum is obtained.
The photoelectrons measured for the streaking spectrograms are measured down to 10eV due to the large bandwidth of the generated HHG continuum. Optimization of the collection efficiencies while keeping up a minimum resolution, especially for low energy electrons, is done qualitatively with electrons generated via static above threshold ionization (ATI) spectra.
Finally, a calibration of the TOF spectra is done by comparing the TOF spectrum to corresponding calibrated spectrum from the grating spectrometer. To conserve the integral, the spectral intensity $I(E)$ in photo energy domain is corrected according to:

$$I(E) = I(t)\frac{dt}{dE} \tag{3.31}$$

3.4 Waveform-Controlled HHG in Argon and Neon

The previous chapters were devoted to the realization of a phase-stable, synthesized sub-cycle IR waveform with long-term stability and the preparation of the infrastructure for HHG and its characterization. This chapter is the onset of an endeavor to fully exploit the tunability of synthesized waveforms in the application of HHG.

The first observed HHG signal as generated with the PWS was from an argon gas jet. The beamline was previously used with a Ti:sapphire driven HCF pulse as the driver for HHG [177] and it was straightforward to test the single NIR channel for first HHG experiences because of the matching spectral regime and pulse duration compared to the HCF pulse. The harmonics are generated at 200 mbar backing pressure of argon with a focusing geometry of $f = 375$ mm spherical mirror. The NIR channel as a few-cycle driver generates clearly distinguishable harmonics as plotted in figure 3.19. At low backing pressures in argon, the NIR channel is the primary driver of the harmonics and the macroscopic parameters such as focusing and backing pressure are adjusted for an optimized HHG signal from the NIR channel. The IR channel on its own does not show a HH signal under these conditions. Launching both, the NIR and IR channel, a variety of XUV continua are observed once the temporal and spatial overlap is ensured. As is displayed in figure 3.19, the spectra can be tuned from narrowband to broadband continua spanning almost an octave.

To exploit the full landscape of possible waveforms, the "tuning knobs" of the waveform are

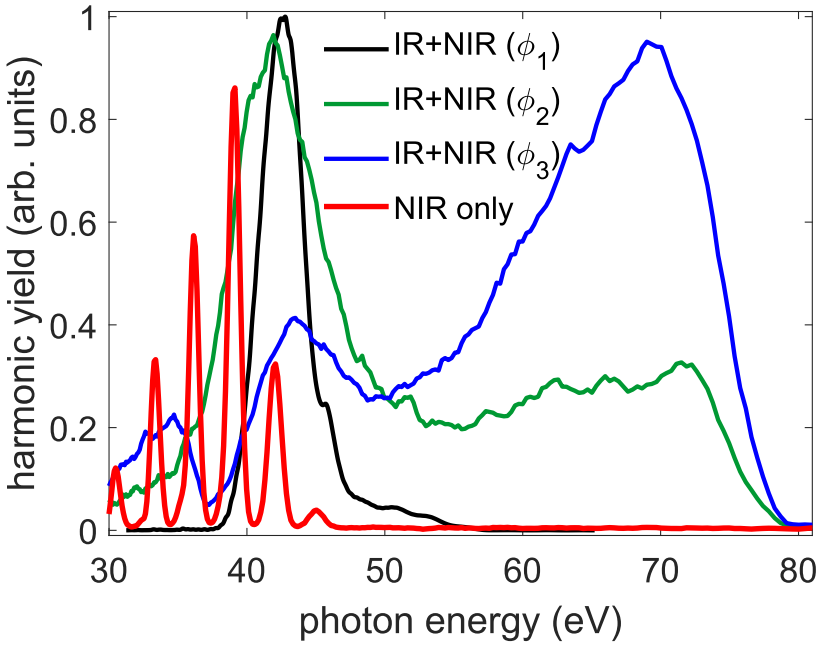

Figure 3.19: HHG spectra generated with the PWS. Signal generated with the NIR channel only (red) and XUV continua as generated with NIR and IR channel at different phase settings. All spectra generated with argon.

systematically scanned. A typical scan routine consists of a slow scan (ramp) of the relative

phase while the CEP is repeatedly cycled by at least 3π. The scanning routine is referred to as "RP-CEP" scan while a one-dimensional scan of the delay between NIR and IR channel would correspond to an "RP" scan. The resulting HHG spectra are recorded synchronously in order to relate an RP and CEP value to each single XUV spectrum as plotted in figure 3.20. The phases as plotted are not absolute phases, i.e. RP = 0 does not necessarily correspond to the absolute time zero overlap between the channels. The position of time zero between the two channels is judged by their maximum nonlinear interaction. Likewise, the CEP is measured via the f-2f phase meter as described previously and represents no absolute CEP. Nevertheless, the phase lock is maintained during the entire phase scan to relate the phases precisely for all CEP and RP values. Since RP and CEP are modulated simultaneously during the experimental scan, a resorting of the HHG data is necessary to plot the data for a single RP or CEP value as done for selected phase values in figure 3.20. The measurement is done in argon at 300 mbar backing pressure with a $f = 375$ mm spherical mirror and the driving laser beam is separated from the XUV with a 500 nm beryllium metallic filter (LeBow). The pulse energies are measured to 70 μJ (NIR) and 170 μJ (IR) at the point of HHG that results in a peak intensity of $2-3\times10^{15}$ W/cm^2 at perfect time overlap. The resolution of the RP step is defined to 0.8 rad at 940 nm. The gas target is a ≈ 2 mm thick semi-infinite gas nozzle.

The HH yield at photon energies < 100 eV allows for short integration times (200 ms) of the XUV spectrometer resulting in a total measurement time of ≈ 40 minutes for a full RP-CEP scan. The data from argon demonstrate the capability of the sub-cycle synthesized waveform to control the process of HHG. Spectra of sub-10 eV bandwidth to over octave-spanning bandwidth are generated. Interestingly, all spectra appear to be continuous from low energy, narrowband cases to broadband spectra. These spectra seem to deviate significantly from the traditional HHG spectra with a single defined cut-off energy. The top rows of figure 3.20 (a,b) display a scan of the RP at a single CEP. This would correspond to a delay scan with fixed CEP as familiar from previous two-color experiments summarized in section 3.1.2, where negative delay/RP means that the IR channel is advancing. The Scan is repeated twice to observe the low-energy content (left panels of figure 3.20) with the 300 gr/mm grating installed in the spectrometer and with the 1200 gr/mm grating to cover the high-energy part of the spectrum (right panels of figure 3.20). Plots (c,e) display a section of the RP scan for CEP shifted by $\pi/2$ with respect to the CEP of plots (a,b). Since the data set consists of HHG photon energy, spectral intensity, RP and CEP, it is plotted either for fixed CEP or fixed RP. The plots along the CEP (d,f-j) represent the familiar CEP scan. The CEP dependency is clearly visible, even at low photon energies. The tilt angle of the fringes and the contrast changes among the CEP scans giving rise to the ability to generate broadband and narrowband continua by dialing in the corresponding phase settings.

The interaction lasts for ≈ 50 fs that, regarding the FWHM duration of ≈ 8 fs for NIR and IR pulse, seems to be a rather long time window. Taking into account the wings of the NIR and IR pulses in time domain as plotted in 2.12, which are unavoidable for complex spectral shapes,

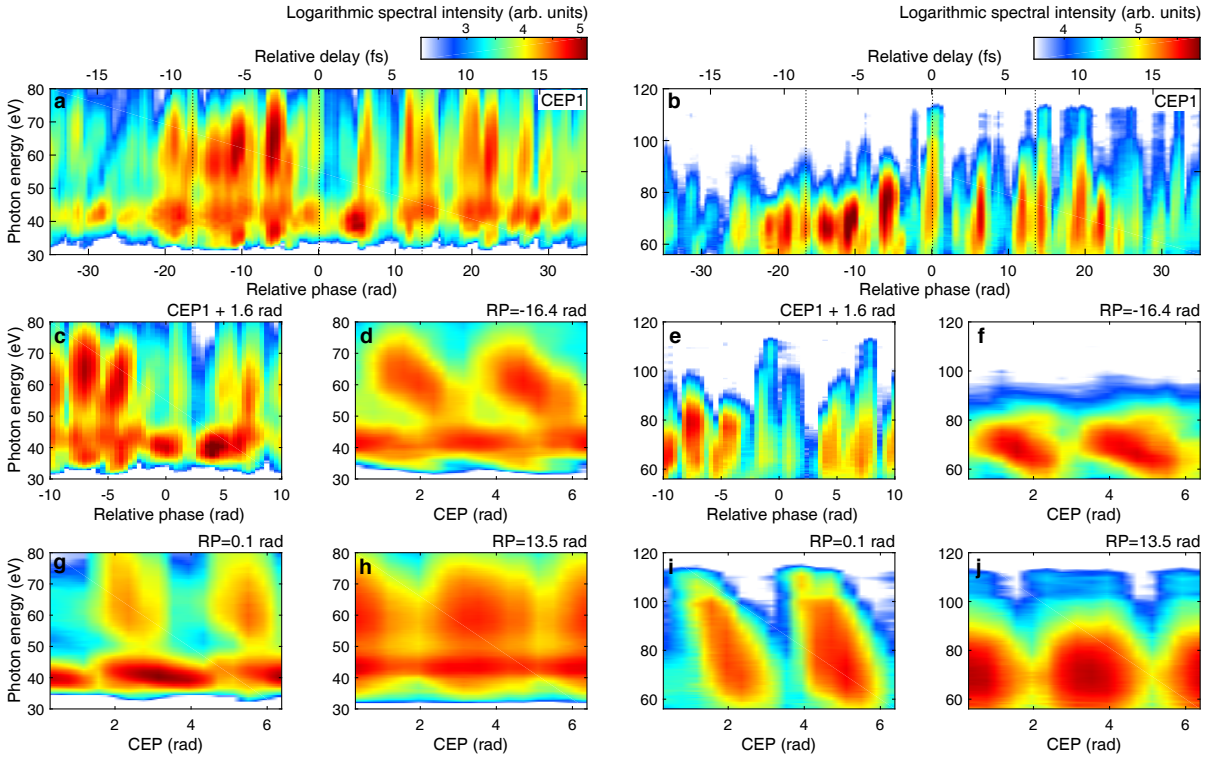

Figure 3.20: Generation of HH continua in argon with the PWS as function of the RP and CEP. The spectra are recorded in the low energy range with the 300 gr/mm grating (a,c,d,g,h) and in the higher energy range with the 1200 gr/mm grating. The top panels (a,b) display a RP scan at a fixed CEP showing the formation of various broadband spectra. The higher energy spectra indicate an increase of yield and cut-off energy around the time zero interaction region. The direction of the RP is given with the IR channel advancing towards negative RP values. A $\pi/2$ CEP shift changes the spectra across the RP axis (c,e). The RP-CEP maps are plotted as a function of the CEP in (d,f,g,h,i,j) for fixed RP values as indicated at the plots. All continua show a CEP dependence with an increased contrast close to RP ≈ 0 and a moderate slope outside the time overlap. The spectra are recorded with 200 ms integration time and a 500 nm Beryllium filter is applied to block the driving laser beam. Taken from [45]

it is most likely that an overlap of the central portion from the IR channel with the wings of the NIR channel and vice versa can lead to HH emission. Especially in argon, the necessary peak intensity for HHG can easily be generated by other cycle then the central one at time zero. With the argument similar to the ones of the publications summarized in section 3.1.2, the non-sinusoidal shapes for several of the waveform cycles during the scan allow the emission of continua and IAP. A confirmation for the IAP will be given in a later section via attosecond streaking measurements.

The systematic scan is repeated for neon while resolving the HHG with the mid-energy grating (1200 gr/mm) to observe higher photon energies. To optimize the generation of higher photon energies, a higher peak intensity is reached by moving the gas cell closer to the focus in order to optimize the HHG yield. All other parameters (300 mbar backing pressure, $f = 375$ mm) are

kept the same as for previous argon and neon scans. The RP scan for neon is plotted in figure 3.21.

In neon, the temporal window of delay in which HH continua are observed is much more

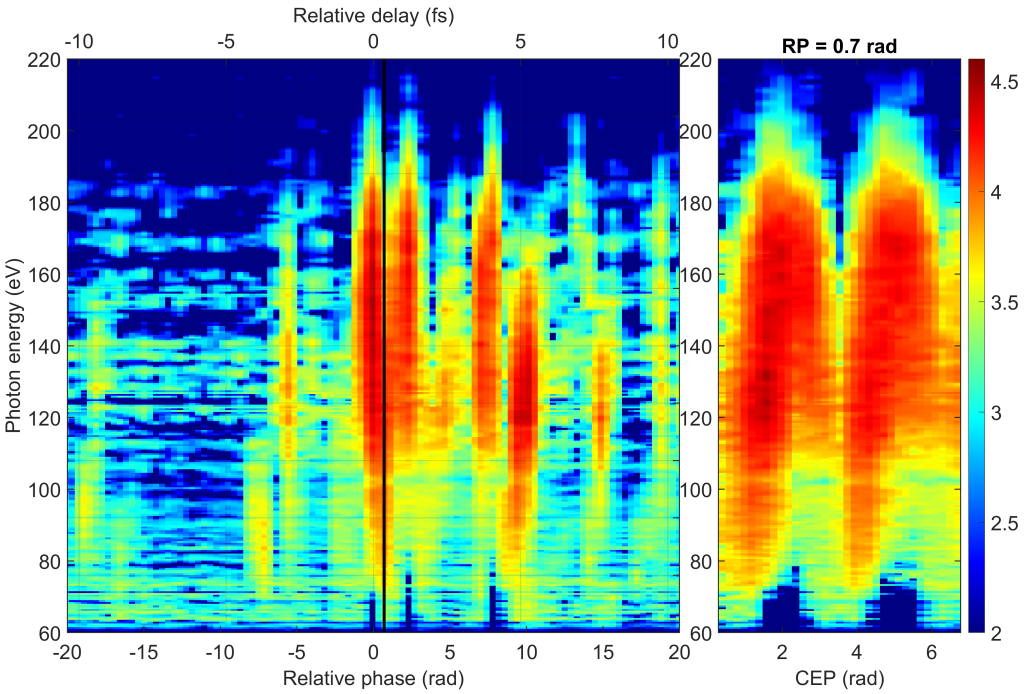

Figure 3.21: Record of the HHG spectra for a RP-CEP scan in neon. The PWS waveform is focused by an $f = 375$ mm spherical mirrors on a 300 mbar backing pressure neon gas nozzle of 2 mm length. The spectra are resolved with the mid-energy (1200 gr/mm) grating. According to an RP $= 0.7$ rad, the CEP scan is plotted on the right panel.

defined. Only at specific delays, a waveform is formed that ionizes the neon atoms. The bandwidth of the continua are remarkable, with almost 2 octaves reaching from 50 eV to 200 eV feet-to-feet with an almost flat intensity distribution. The CEP scan shown in the right panel of figure 3.21 at the given RP, as indicated by the black marker line in the left panel of figure 3.21, states a CEP dependency across the full XUV spectrum. Despite a very small signal at low energies, no harmonics are observed out of the temporal overlap region, meaning that neither the IR nor the NIR channel are generating harmonics on their own under the given macroscopic conditions. Interestingly, the spectra taken at high photon energies (figure 3.21) are recorded with the same integration times as the spectra in argon (200 ms). The RP scans for argon and especially for neon indicate an increased yield at time overlap based on the comparison to the spectra generated with the single channels. The claim of "yield enhancement" yet is not proven with this single RP-CEP scan, which is measured in first place to explore shaping possibilities and stability of the emitted harmonic continua. Due to the vastly changing peak intensities for synthesized pulses compared to the single channels, a parameter scan of the macroscopic conditions like gas pressure, overall peak intensity e.g. via change of focal length and the ratio of pulse energy has to be covered. Nevertheless, the photon numbers are measured to

$\approx 10^8$ ph/pulse for narrowband continua in argon and about an order of magnitude lower for broadband spectra in argon. The continua in neon at ≈ 70 eV are measured to $\approx 10^6$ ph/pulse. Due to the sensitivity of the XUV PD to the NIR channel, as explained in section 3.3.5, the photon numbers are derived from the XUV CCD camera that are referenced with a comparison measurement of the single IR channel on the XUV PD. The photon flux of the single IR channel generating broadband spectra at photon energies of ≈ 60 eV at 200 mbar backing pressure is measured to $\approx 5 \times 10^4$ ph/pulse. Now one could anticipate an enhancement of 3-4 orders of magnitude, but that misses some interpretation. Regarding the HHG photon energies, one would probably not choose a $\lambda_c = 1.6\ \mu$m pulse to generate these photon energies. A measurement of the single NIR channel is not reliable due to the strong background contribution in the current beamline configuration. Nevertheless, a comparison with published photon fluxes [90], [154], [183], [184] shows that the stated photon numbers are at least in good company with recently stated high-performance sources. A global optimization of the macroscopic for the generation in argon and neon at lower backing pressures is not done.

On top of the well-reproducible and periodic CEP scans, a continuous recording of the HHG signal for a stabilized waveform proves the stability of the PWS. Figure 3.22 displays four different XUV continua recorded over a time span of 20-30 minutes for four different phase settings RP and CEP of the PWS. Long-term operation of the PWS on the order of months is possible when no active components fail. Nevertheless, drifts as seen partially in figure 3.22 are due to passive drifts, which are mainly identified as temperature changes that the PWS feedback system is not designed to account for. As one of the last components that is not actively stabilized, the external compressor, which is not permanently irradiated due to laser shutter/lab safety, drifts continuously during the day. Only an extended warm-up time of ≈ 8 hours ensured very stable conditions. The temperature of the grating compressor, due to energy deposition from the laser, changes the distances and mostly affects the delay of the third stage OPA pump pulses. This again slowly changes the spectra of the OPAs and usually results in a shift of central wavelength of the amplified pulses. An active feedback control integrating delay stages and a controlled stage for the grating compressor using reference spectra as setpoint is under construction.

In the spatial domain, the synthesized waveform has been shown to be identical to a single pulse driving the HHG. Future experiments depend not only on a suitable spectrum and flux, but also on consistent behavior of the HHG pulse in the spatial domain. Since the spatial characterization, as discussed in section 2.2.5, is technically limited to the resolution of the detectors and a wavefront measurement is not done, the HHG driven from the IR and NIR portion of the synthesized beam could very well point slightly differently. The spatial domain i.e., the beam profile of the HHG, is measured with the XUV CCD camera. In the configuration of the grating chamber, the zero-order reflection of the grating allows to capture the beam profile without major changes on the beamline. A second way observe the spectro-spatial evolution of the XUV beam is to use the spectrally resolving 1^{st} order of the grating and making use of the vertical

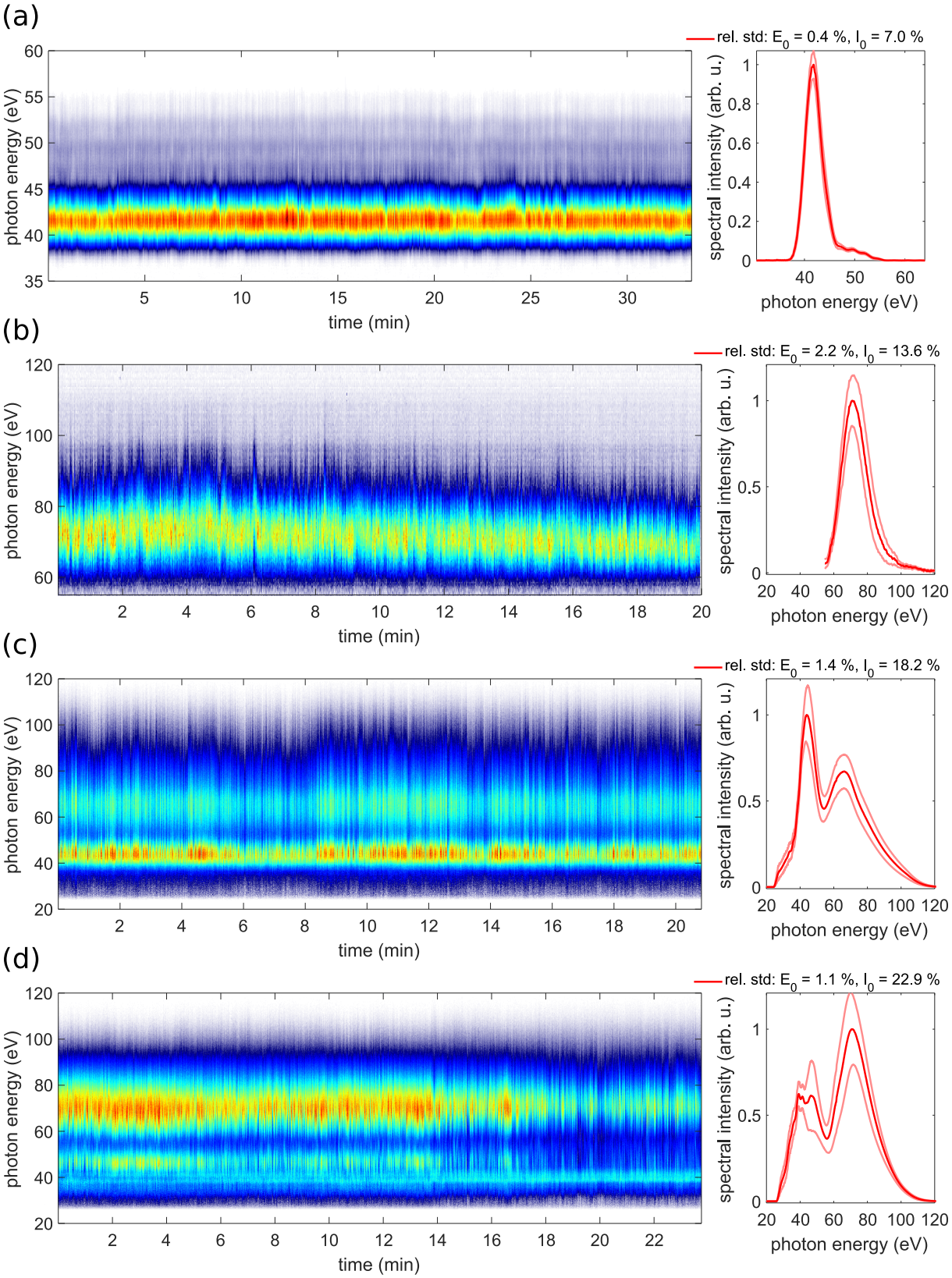

Figure 3.22: Long-term stability measurements of generated HHG continua by the PWS waveform. From top to bottom: Plots (a)-(c) show HHG generated in argon at 300 mbar backing pressure and plot (d) showing HHG generated in neon at 550 mbar backing pressure, all with $f = 375$ mm focusing.

resolution of the XUV CCD camera. The vertical binning of the XUV CCD camera is usually integrated to take single spectra at best SNR. The beam profiles are taken with the XUV CCD camera at its current position and do not correspond to the beams right at the toroidal mirror imaging point. Furthermore, during the change from toroidal mirror # 1 to # 2, a flat gold mirror was installed to guide the beam towards the XUV CCD camera without distortion. The HHG spatial profiles in figure 3.23 (c,d) correspond to measurements with the flat gold mirror (Thorlabs, PFSQ20-03-M03) and a distance of ≈ 1.7 m from the point of generation. An estimation based on the driving laser waist gives a source size of ≈ 100 μm in diamater resulting in a divergence of 1.8 ± 0.15mrad. The beam profile on the XUV CCD camera is measured to 4.3 mm $(1/e^2)$ The divergence angle Θ is defined as

$$\Theta = 2 \arctan\left(\frac{D_z - D_i}{2L}\right) \tag{3.32}$$

with D_i the beam diameter (4σ) at some initial position of the beam and D_z the diameter at a later position of distance L. The measurements in figure 3.23 resemble the photon energies as shown in previous spectra. The macroscopic conditions are given with 90 mbar backing pressure for the single NIR channel and 600 mbar for the PWS pulse driven HHG, both with $f = 375$ mm spherical focusing mirror and ≈ 2 mm gas target. Remarkable is the formation of a single XUV pulse also in the spatial domain. Once the pressure is tuned for ideal phase-matching, the XUV continuum quality in spatial domain is close to the single channel-driven HHG. The PWS-driven continuum appears qualitatively to be brighter on the image recorded from zero-order reflection. A little offset in center position is on the order of the single channel driven HHG pointing. The beam profile of the PWS-driven HHG is measured while locking the CEP and RP. A series of images similar to the ones shown are recorded and show a similar stability in shape, position and spectrum compared to the single channel driven HHG.

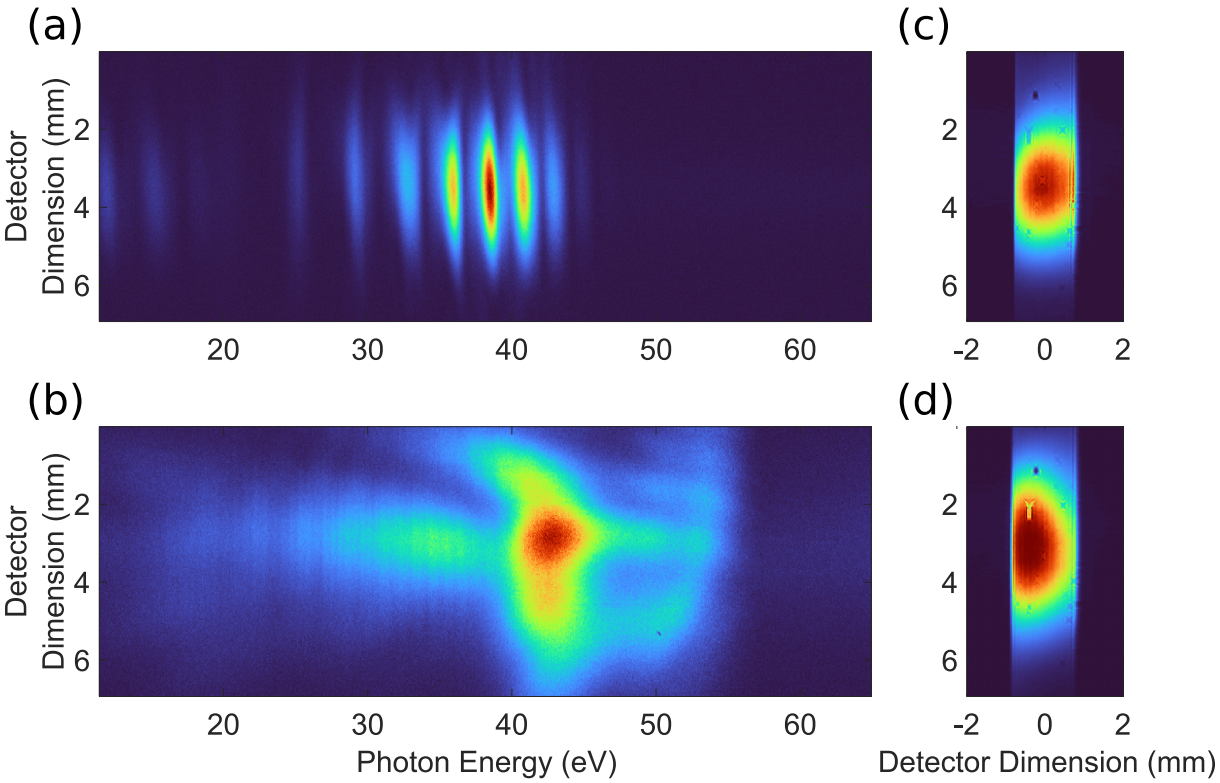

Figure 3.23: HHG spatial profiles recorded with the XUV CCD camera. Panel (a,b) is measured spectrally resolved from the 1^{st} diffraction order and vertically resolved in spatial dimension. (a) shows distinct harmonics when driven with the single NIR channel, while (b) shows a continuous spectrum when driven with the synthesized PWS as input pulse. The XUV continuum conserves a single coherent profile of the HHG continuum. On the path from the source to the spectrometer apparatus, the HHG beam is deflected from a flat gold mirror at 4° grazing incidence. Panel (c,d) show the adjacent zero-order reflection from the grating, therefore imaging the x and y spatial dimension on the XUV CCD camera for single NIR channel (c) and synthesized PWS (d). The hard cuts on the imaging is the limitation by the entrance slit opening, that the HHG at the given distance of 1.7 m from the source is clipping. Measurements are taken at 0.2 s and with the 300 gr/mm grating installed.

3.5 Attosecond Streaking

The principle of the “streak camera” [185] and initial experiments [186] utilize the sub-cycle duration of the HHG XUV pulse with respect to the NIR laser field to characterize the attosecond pulse in duration. Tight temporal synchronization of the laser pulse and attosecond XUV pulse on a sub-cycle time scale allows to ”dress” or “streak” the photoelectron emission by the laser field. The photoelectron spectra recorded as a function of time delay τ between laser and attosecond pulse essentially transfers the laser pulses’ vector potential to a measurable shift in the photoelectron energies. The vector potential $A(\tau)$ is defined as the integrated electric field starting at time τ, which in the case of attosecond streaking is equivalent to the time at which

the XUV pulses ionizes the electron with respect to the lasers electric field.

$$\vec{A}(\tau) = \int_{\tau}^{\text{inf}} dt\ \vec{E}_{laser}(\tau) \tag{3.33}$$

The observed momentum $\vec{p}$, as measured with the TOF apparatus, consists of the initial momentum $\vec{p}_i$ of the electron given by XUV photon energy, reduced by the ionization potential I_P, that depends on the atomic species being ionized. With linear polarization of the laser and attosecond pulse, the vectors turn to scalar values as measured by the one dimensional MCP detector of the TOF apparatus. Noble gases are commonly used for attosecond experiments to characterize the laser and attosecond pulse with the I_P given as: But not only are attosec-

	I_P (eV)
Xenon	12.13
Argon	15.76
Neon	21.56
Helium	24.59

Table 3.3: Ionization potential I_P of noble gases

ond streaking experiments applied for pulse characterization. The attosecond resolution allows measuring relative time delays of photoionization processes. The delays are measured as phase shifts of the streaked laser vector potential. The relative delay in ionization between 2p and 2s states in neon e.g. can be measured down to 21 as [187]. The experimental scheme of a generic streaking measurement is shown in figure 3.24 for two distinct time delays τ.

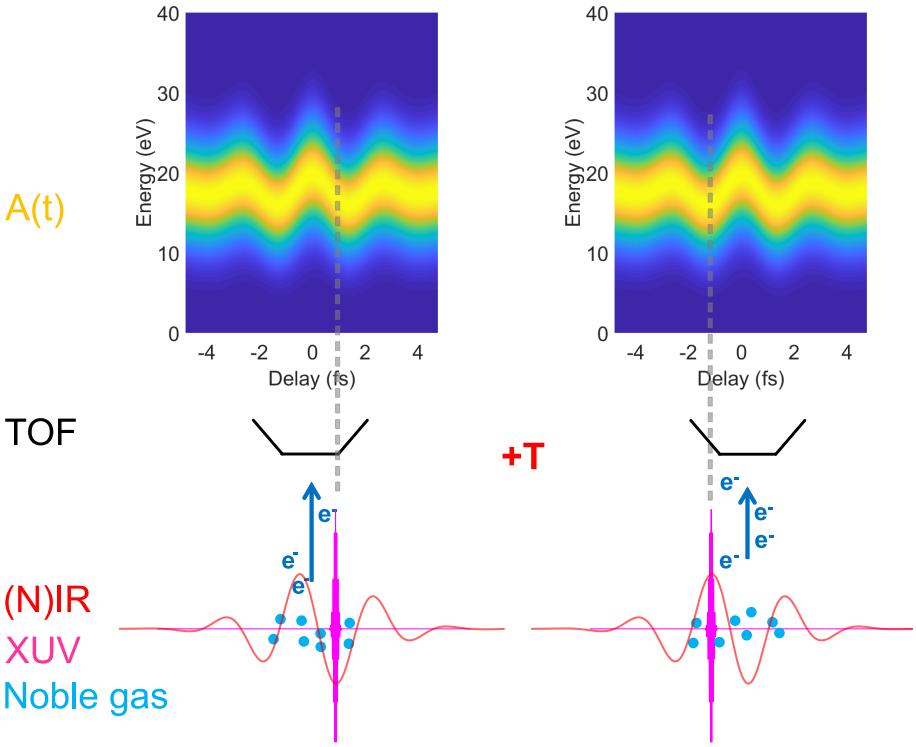

Figure 3.24: Schematic of an attosecond streaking experiment. The laser ((N)IR) overlaps with the attosecond pulse (XUV) in a noble gas. The photoionized electrons are streaked by the laser field and recorded by a time-of-flight (TOF) spectrometer. The modulated electron momenta as shown in the simulated streaking spectrograms resemble the vector potential $A(t)$ of the laser pulse recorded as a function of τ (+T). The polarization of the laser field in the simple case is linear, so that the electric field and the TOF apparatus are in plane.

3.5.1 The Attosecond Streaking Experiment

The synchronized data from RP-CEP scans and HHG spectra show a tight dependence of the HHG continua and the phase parameters of the PWS. A CEP dependence of the generated continua can be seen as a good hint for IAP. To measure the temporal structure of the IAP quantitatively, attosecond streaking measurements are presented in this chapter. The interest in an attosecond streaking experiment is not only motivated by the IAP, since the streaking apparatus can reveal both the IAP and the streaking field, which in this case is a copy of the synthesized waveform generating the IAP. Ideally, the streaking experiment gives a direct link between the driving waveform as adjusted by the phase control and the generated IAP. Furthermore, the experiment relies on a stable streaking field and a successful measurement proves the long-term stability of the PWS. The experimental setup, the retrieval algorithm and finally, the results of different IAPs as generated in argon and neon are presented.

The experimental setup is part of figure 3.8 on the right side of the toroidal mirror. The XUV/SXR pulse is refocused by the toroidal mirror. Collinearly, the streaking field derived from the synthesized waveform is overlapped and focused on the same spot. At the focal point,

a gas jet injects a noble gas at moderate pressure. The XUV/soft X-ray pulse ionizes the gas atoms and the released electron is accelerated in the streaking field. Depending on the temporal overlap between XUV and streaking field, the electron is released at different times within the frame of the streaking field that results in a varying electron momentum. The electron momentum is recorded using the TOF spectrometer.

The preparation of the streaking field as a weak replica of the synthesized waveform should ideally be dispersion-free in order to measure the exact waveform that generates the IAP. Since the dispersion scheme of the PWS is rather defined, it was chosen to reduce the 6 mm thick CaF_2 input window to the vacuum chamber to 3 mm and use a second CaF_2 plate as beam splitter to conserve the dispersion. A 2 inch CaF_2 plate is mounted with an angle of 55° in S-Polarization to derive ≈ 12 % of the input energy as pulse copy. The Fresnel reflection shows an almost flat wavelength response across the bandwidth of the PWS. Experimental setup and reflectivity is shown in figure 3.25. After a delay line (SLC stage, Smaract), the streaking field is recombined with the XUV/soft X-ray by means of a holey mirror.

The TOF spectra as function of delay are recorded with an oscilloscope (Waverunner 640Zi,

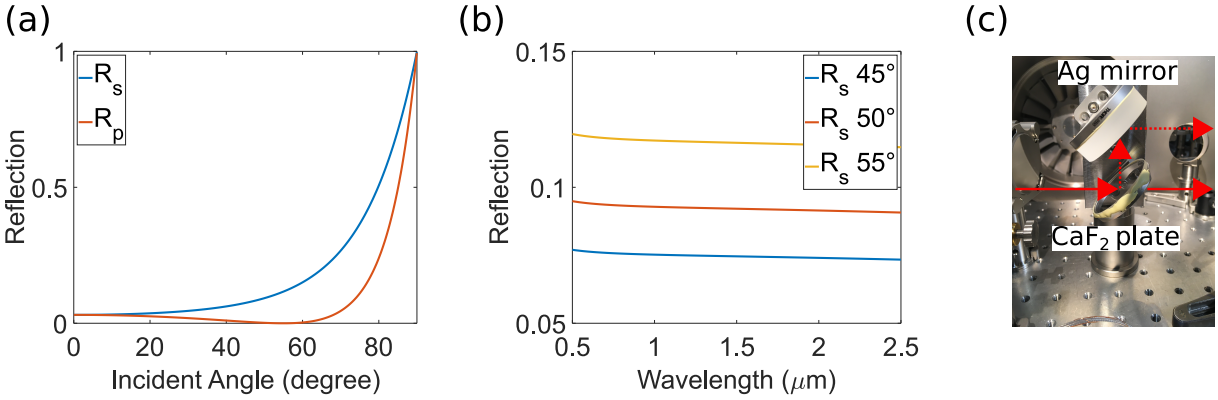

Figure 3.25: Reflectivity of a CaF_2 plate as function of incident angle for S- and P-polarization for the central wavelength of 1.4 μm (a) and reflectivity as function of wavelength for incident angles as given in the legend (a). The beam splitting assembly is shown in (s) with the dotted line being the reflection for the pulse copy.

LeCroy) and result in the spectrogram as plotted in figure 3.27 top panel.

The evaluation of the spectrogram includes the calibration before the data is hand over to an iterative algorithm to retrieve the attosecond pulse and the streaked waveform. The energy calibration is inferred from a simultaneous taken XUV CCD spectrum. With the single NIR channel driven HHG, an XUV comb is generated and measured via the TOF and the XUV CCD camera. By shifting the TOF spectrum by the ionization potential of the generation gas and matching of the harmonic combs, the energy axis for the TOF data is generated. The broad bandwidth of the XUV continua at relatively low photon energy leads to a deviation of the spectral intensity between TOF and XUV CCD camera. Background subtraction and the Jacobi factor are applied when calibrating the spectrogram on an energy axis, but an intensity transfer function to fit the TOF spectral shape to the XUV CCD data is not applied for most measurements. Figure 3.26

shows the basic step of energy calibration starting from a calibrated XUV CCD spectrum (left) and the final calibrated spectrogram (right).

Comparable to pulse retrieval algorithms in the optical domain, a variety are available for

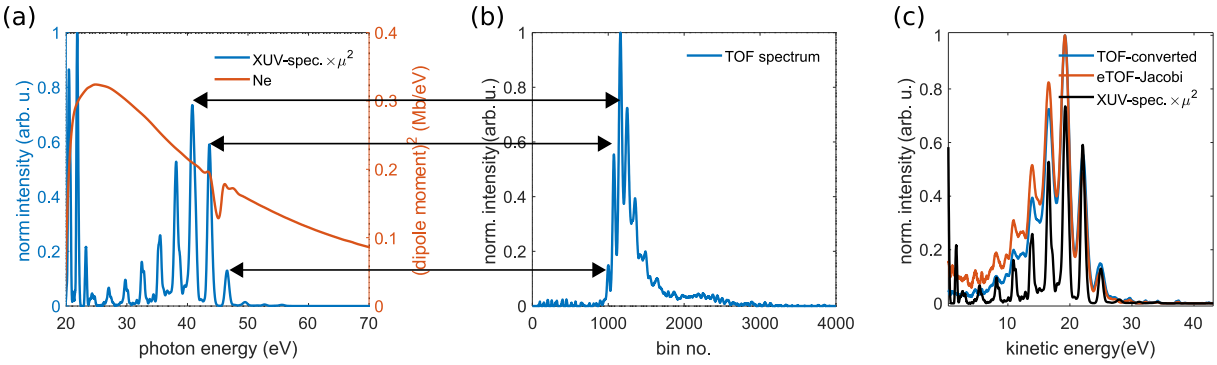

Figure 3.26: Energy calibration of the TOF apparatus. The TOF data is calibrated by matching the XUV comb peaks (b) to a calibrated spectrum from the XUV CCD camera(a). The dipole moment of the streaking gas (neon) is given in the right scale of (a). Cross sections taken from [188]. The energy calibrated spectra is compared in (c) with the XUV spectrum shifted by the ionization potential and corrected by the dipole moment.

streaking experiments. The following paragraph briefly summarizes the available methods with an emphasis on the Volkov transform generalized projection algorithm (VTGPA) [189] as used to retrieve the streaking traces measured in the course of this thesis.

An extension to the well-established frequency-resolved optical gating (FROG) algorithm from the optical regime includes the strong-field description of the ionization process by the optical/IR field to FROG for complete retrieval of attosecond bursts (FROG-CRAB). [190], [191]. FROG-CRAB uses the phase modulation of the ionized electrons by the dressing optical field. The essential gate of the FROG method is represented as a phase gate defined by the time of ionization by the attosecond pulse. The iterative algorithm is capable to retrieve both, IAP and attosecond pulse trains. The temporal resolution for the attosecond burst is given by the maximum momentum transfer on the streaked electrons and therefore the FROG-CRAB method usually works with rather strong IR fields. To achieve the time resolution down to 10s of as, the streaking field would need to be increased into the multiphoton regime and interfere with the streaking spectrogram. Another limitation is the Fourier Transform as part of the iterative algorithm to calculate the spectrogram relies on the central momentum approximation (CMA) for the electrons, that for broadband attosecond pulses is a major limitation. As for the HHG continua shown in the following chapters, the CMA cannot be fulfilled when the bandwidth of the continuum exceeds their central energy.

A retrieval for high temporal resolution was developed in the group of Z. Zhang with a method called phase retrieval by omega oscillation filtering (PROOF) [192]. The PROOF method is experimentally very similar to the FROG-CRAB with a delay scan between IR streaking field and XUV/soft X-ray pulse in a gas jet while measuring the electron kinetic energy. The spectral

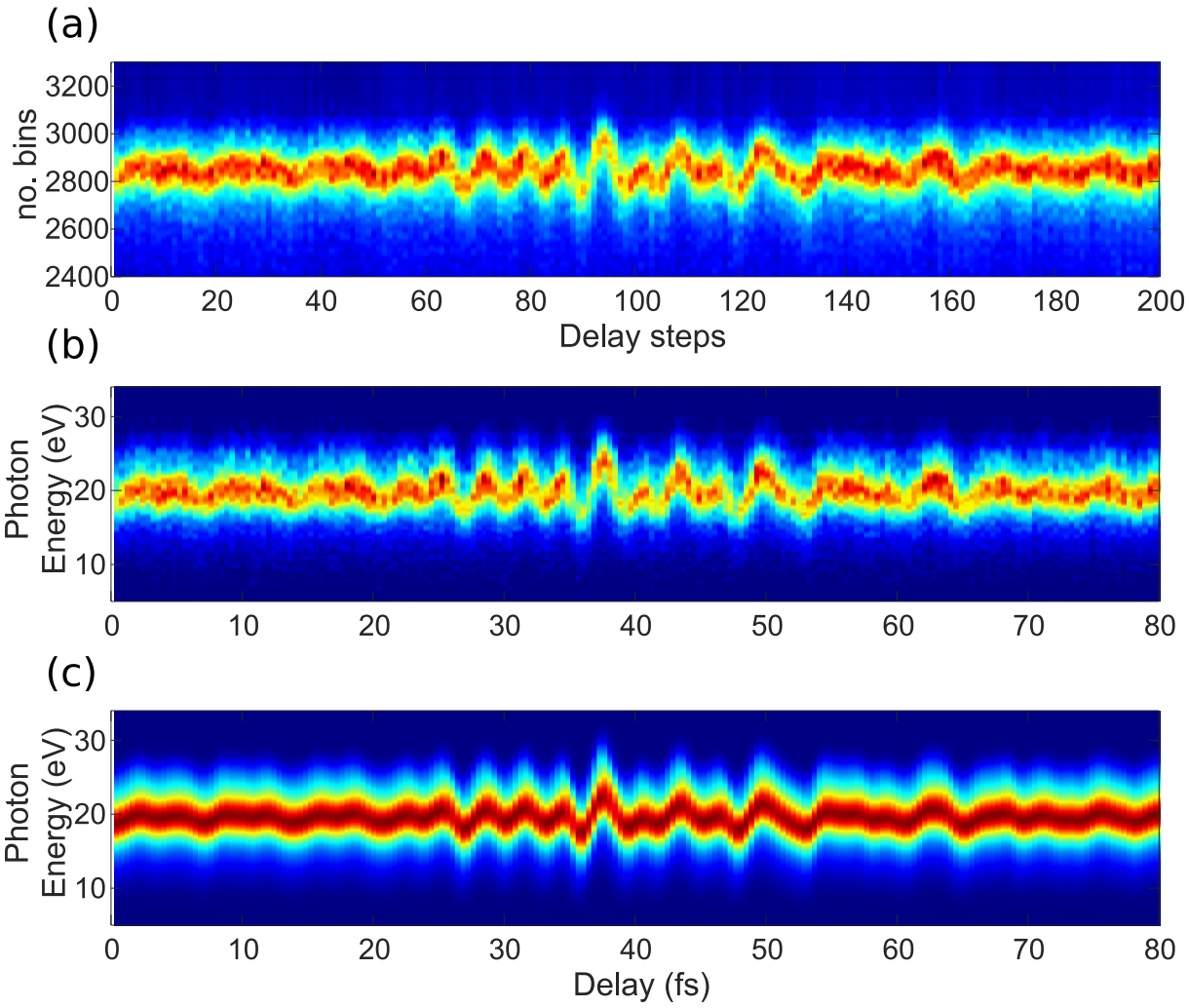

Figure 3.27: First attosecond streaking measurement with a PWS. Measured (a) and calibrated (b) streaking spectrogram and retrieved, calculated spectrogram as with VTGPA (c).

phase information for the XUV field (ω_{HHG}) nevertheless is obtained from interference. Similar to the first interferometric characterization technique, as was introduced with RABBITT (= reconstruction of attosecond beating by interference of two-photon transitions) [193], [194] where the photoelectrons are generated from a gas jet with an harmonic comb dressed by an IR laser field that results in beating sidebands at the frequencies of even harmonics depending on the delay between XUV train and IR pulse, PROOF retrieves the spectral phase information from interference. A beating signal of the dressed states ($\omega_{HHG} + \omega_L$ and $\omega_{HHG} - \omega_L$) is filtered from the spectrogram by the frequency of the streaking field (ω_L). At a given photoelectron energy, the interference pattern is filtered by the frequency of the streaking field and the phase difference of neighboring frequency components is given as a function of delay between XUV and IR pulse. The dressing requires only a single photon of the streaking field, therefore the streaking field intensities are reported to be around 10^{11} W/cm^2 [192]. Furthermore, the phase retrieval from interference mitigates the CMA and much broader, non-Gaussian like con-

tinua can be retrieved from the streaking spectrogram. An extension to RABITT and PROOF is presented with improved PROOF (iPROOF), adressing the capabilities for arbitrary spectra and taking into acount atomic physics for the ionization process [195]. However, the definition of the dressing laser frequency limits the retrievals to IR pulses satisfying the slowly varying envelope approximation (SVEA) and inaccurately describes the situation with sub-cycle non-sinusoidal streaking fields. Also, the retrieval of PROOF only targets the SXR pulse and does not retrieve the streaking field.

The streaking measurements presented in this thesis are retrieved with the method of Volkov transform generalized projections algorithm (VTGPA) [189]. The methodology is more related to the FROG-CRAB procedure than to the interferometric methods. Therefore, the inherent limitations of PROOF, the SVEA and first-order perturbation intensity of the streaking field, do not apply for VTGPA. The bottleneck of the FROG-CRAB algorithm, i.e., the switching between time and frequency domain using the FFT to fit the constraints, is mitigated in VTGPA by a figure of merit soleley in the frequency domain that is minimized in a least squares (LS) approach. As taken from [189], the figure of merit for LS minimization is defined as:

$$M = \sum_{l=0}^{N_W-1} \Delta W l \sum_{m=0}^{N_\tau-1} \Delta\tau |\tilde{a}[l,m] - \tilde{a}'[l,m]|^2 \tag{3.34}$$

The matrix $\tilde{a}[l,m]$ describes the probability of the ground state to continuum transition in the frame of SFA, including the action by the vector potential of the streaking field. The measured signal is represented in $\tilde{a}'[l,m]$ incorporating the measured photoelectron spectrum and the calculated phase $arg(\tilde{a}[l,m])$. The figure of merit numerically integrates over the delay step $\Delta\tau$ and the energy resolution $\Delta W[l]$. The VTGPA contains the description of the vector potential as an envelope with cubic spline of J points and the carrier field parameterized by coefficients $\alpha\ cos(\alpha_0 + \alpha_1 t + \ldots + \alpha_{K-1} t^{K-1})$ instead of an array. It has been seen during the retrieval of our complex synthesized waveform from the streaking trace, that the amount of J points have to be increased significantly in order to describe the non-sinusoidal waveform adequately and successful conversion of the retrieval. Thus, the retrieval process for waveforms with large bandwidth generating a very dynamic spectrogram with a rather large total time window takes a multiple of the originally stated 1.5 hours of CPU time. Nevertheless, all of the streaking measurements are successfully retrieved with the method of VTGPA judging the similarity between calculated and measured spectrogram. For completeness, the work of Gaumnitz *et al.* [156] should be mentioned as an extension to the VTGPA by including multiple photoelectron bands. Very broadband SXR pulses cover the ionization energies of various electronic shells, whose photoelectrons end up at the same measured energy due to the large SXR bandwidth.

For the streaking experiment, an XUV continuum is generated in argon at modest backing pressures of $\approx$ 300 mbar and a central photon energy of 42 eV. The streaking gas is neon with an (I_P) of 21.56 eV. The streaking measurement from figure 3.27 is fully retrieved with the VTGPA method and the result is shown with the retrieved spectrogram on the lower panel. It can

be observed that the spectrogram shows major deviations compared to a sinusoidal modulation as can be found for example in [196], [197]. Referring to the temporal delay axes in figure 3.27, the maximum of the vector potential occures at ≈ 38 fs during the central main cycle of the field, with strongly varying electric field amplitudes to the right side as well as kind of a sawtooth-like cycle at ≈ 52 fs that correspond to a rather long local oscillation period.
As the synthesized stabilized IR waveform is the first of its kind, a primary interest of the streaking measurement is the waveform of the synthesized IR waveform itself, plotted in figure 3.28. The FWHM duration of the pulse as indicated by the arrows read $\tau_{FWHM}(A) = 3.5$ fs measured from the intensity envelope $A(t)$ and $\tau_{FWHM}(I) = 2.3$ fs for the instantaneous intensity $I(t)$. The right panel of figure 3.28 represents the spectral composition as calculated from the retrieved time domain electric field via FFT that serves as a good sanity check and feedback for the interaction of streaking and XUV field in front of the TOF. The complete spectral bandwidth of the PWS is preserved in this measurement; nevertheless, a lower intensity of the IR channel than expected is observed. Most probably, the focusing and geometrical beam synthesis at the focus in front of the TOF may have lowered the peak intensity of the IR channel component. The retrieved attosecond pulse is displayed in figure 3.29 with a FWHM pulse

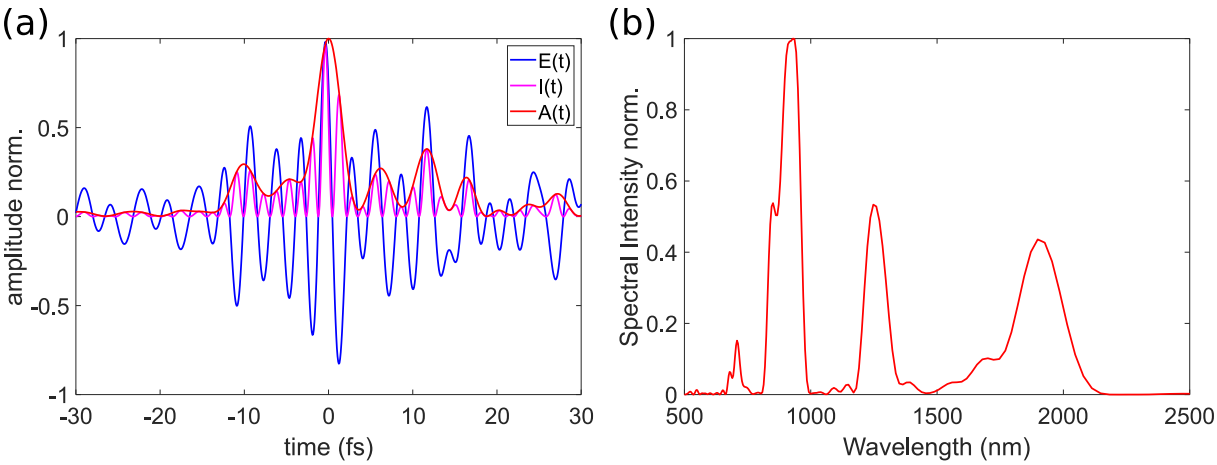

Figure 3.28: Retrieved streaking field E(t) and corresponding instantaneous intensity I(t) and intensity envelope A(t) (left panel). Spectral intensity of the retrieved streaking field (right panel) as calculated directly from E(t) via FFT.

duration of $\tau_{FWHM} = 240$ as. The stability of the PWS waveform and the streaking apparatus is proven in consecutive streaking measurements. The phase lock of the feedback system was maintained for > 2 hours, guaranteeing a stable waveform and HHG continua. Four streaking measurements are plotted in figure 3.30 in the first two rows. All fields are retrieved to very similar electric fields, as shown in the lower right plot. The lower left plot shows a streaking trace with the CEP flip of the PWS waveform as controlled by the interactive phase control. The PWS waveform is evaluated from the streaking traces by means of the center of mass (COM) [198] of the photoelectron spectra along the delay axis.

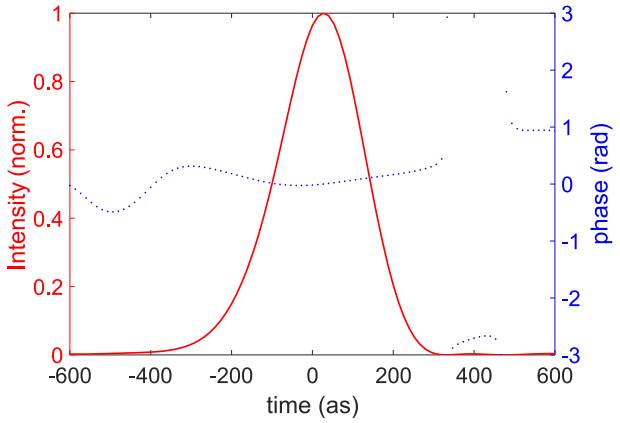

Figure 3.29: Retrieved attosecond pulse from streaking measurement (figure 3.27). Plotted is the intensity and phase in time domain. The FWHM duration is measured as $\tau_{FWHM} = 240$as

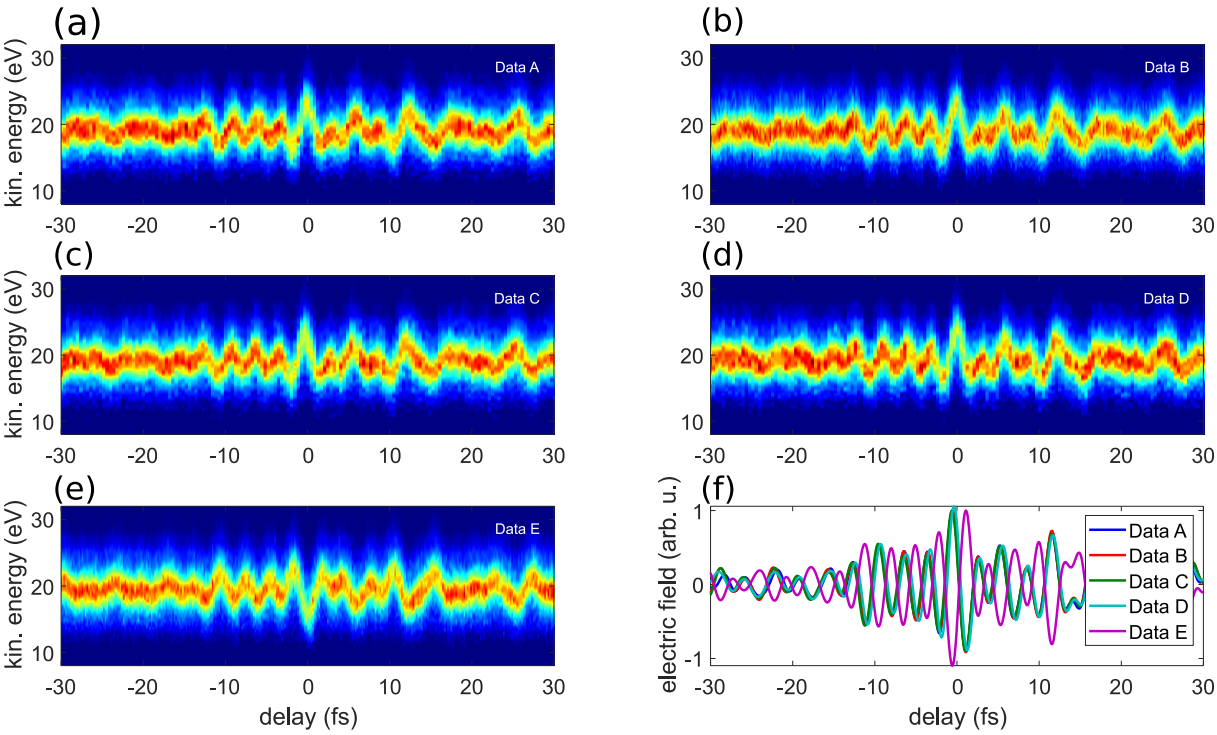

Figure 3.30: Consecutive streaking measurements over a time span of ≈ 2 hours to demonstrate a long-term stable operation of the synthesizer phase-locked waveform and HHG beamline. First two rows show streaking traces at constant phase settings of the waveform. Bottom left plot shows the CEP flipped waveform and bottom right panel plots the evaluated electric field of the IR waveform.

3.5.2 Shaping the Attosecond Pulse

A variety of XUV continua are already shown in chapter 3.4, whereas in the following a selection of continua are characterized via attosecond streaking to show the isolated nature of the XUV pulses and gain insight into the temporal structure of these pulses. The measurements are displayed in figure 3.31 for four different waveforms. The continua are generated

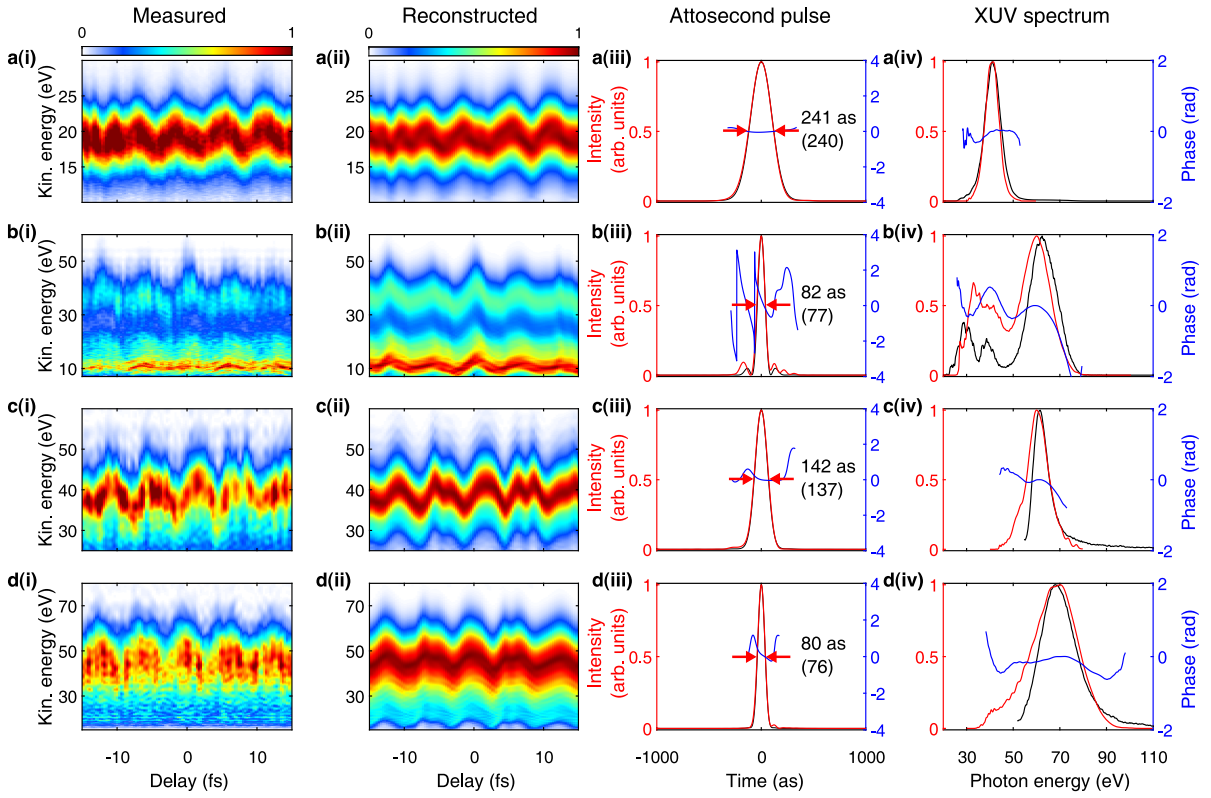

Figure 3.31: Attosecond streaking measurements of various HH continua as generated with the PWS. The XUV continua are tuned in bandwidth and central photon energy. XUV continua are generated from argon (a,b) and neon (c,d). The measured photoelectron spectra as measured (i) and reconstructed (ii) with the retrieved attosecond pulse in time (iii) and photon energy (iv) domain. The transform-limited pulse envelope and FWHM duration is given in black. The XUV spectrum is measured independently from the XUV CCD camera and plotted in black for comparison. from [45]

by focusing the PWS pulse with a $f = 375$ mm spherical mirror into the gas target of ≈ 2 mm length. Rows (a) and (b) represent an XUV pulse as generated in argon with a backing pressure of ≈ 300 mbar. The waveform is tuned for a narrowband continuum (figure 3.31 (a)) and a broadband continuum (figure 3.31 (b)). The retrieved spectrograms in column (ii) resemble the measured spectrograms in column (i) and testify a solid reconstruction. Only the experimental data at low kinetic energy of the electrons appears to be noisy and the detection of very broadband XUV spectra in argon is limited by the TOF capabilities to > 10 eV. The XUV pulse in the time domain is plotted in column (iii) and shows FWHM time durations close to the Fourier limit with 241 as FWHM for narrowband and 82 as FWHM for broadband continua. The XUV continua are plotted in column (iv) where the calibrated spectra, as recorded with the XUV CCD camera, are compared to the spectra as recorded via the photoelectrons with the TOF. Especially for broadband spectra, a deviation at lower energies is observed. The spectra recorded by the XUV CCD camera are corrected back to the point of the TOF, meaning that the transfer function of the XUV CCD camera, grating and transmitted metal filters are accounted

for. Those transfer functions can add up and contribute to the error between XUV CCD and TOF spectral data. But, more likely is a lower collection efficiency of low kinetic energy electrons in the TOF. In order to collect the full bandwidth, the TOF was operated without applying a lens voltage. The lower two rows of 3.31 present the XUV pulses as generated in neon at ≈ 500 mbar of backing pressure. The focusing geometry is kept fix and the switch between all the presented spectra can be dialed in within minutes. In neon, the pulses appear to be close to the Fourier limit again with the shortest pulse of $\tau = 80$ as.
Including the streaking spectrogram shown in the previous section, it can be observed that the intensity of the streaking trace in the rising and falling half cycles is visually very similar. As discussed in detail by L. Gagnon *et al.* in [198], the width and contrast of the photoelectron spectrogram is related to the chirp of the attosecond pulse. In our case, the results of the VTGPA reconstronstruction with low chirp match the appearance of the spectrograms. Furthermore, single atom simulations as presented in [45] including the dispersion of the ≈ 2 mm long gas jet, confirm the integrity of the streaking measurements and show similar low-chirp IAPs.

3.6 Waveform Controlled HHG in Neon and Helium

The application of the PWS waveform to HHG with high photon energies (> 200 eV) is the topic of the following sections. The general strategy to take a single channel of the PWS for initial alignment and phase-matching optimization, which is later optimized in RP-CEP scans for synthesized waveforms, has shown good reproducibility and is a deterministic way to characterize the advantage of synthesized waveforms. In contrast to previous chapters where the NIR channel was used as primary beam, for the generation of high photon energies the IR channel is the primary pulse. A high-pressure generation gas cell to obtain phase-matching is a central prerequisite to achieve high photon energies. In order to prepare the beamline for convenient operation at high photon energies, some modifications were made from the experimental setup in previous chapters, where the focus was on the streaking apparatus and TOF spectrometer. The technical drawing in figure 3.10 shows the current state of the beamline. The TOF spectrometer is removed for the benefit to move the spectrometer closer to the imaging point of the toroidal mirror. The technical details on the beamline modifications are covered in section 3.3.3.

3.6.1 Generation of "Water Window" Soft X-Rays

The IR channel at its wavelength of $\lambda_0 = 1.6$ μm is used to find a regime of macroscopic paramaters for the generation of high-energy photons. In order to exploit the full energy of the PWS, the peak intensity is varied by changing the focusing mirror. Experimental data for a $f = 4$ inch OAP, $f = 400$ mm and $f = 500$ mm spherical mirror are shown. Each case involves an optimization of the gas pressure and gas cell position. Once, the ideal parameters are found

for the IR channel, several RP-CEP scans are repeated in order to fine-tune the macroscopic parameters to the ever-changing waveforms depending on the RP and CEP.
A pressure scan displayed in figure 3.32 shows photon energies up to the carbon edge, while higher energy photons got absorbed by carbon contamination of the XUV optics. The carbon contamination is reduced in future measurements by cleaning the chambers with UV lamps. The measurements are taken with a pixel binning of 4, resulting in an energy resolution of

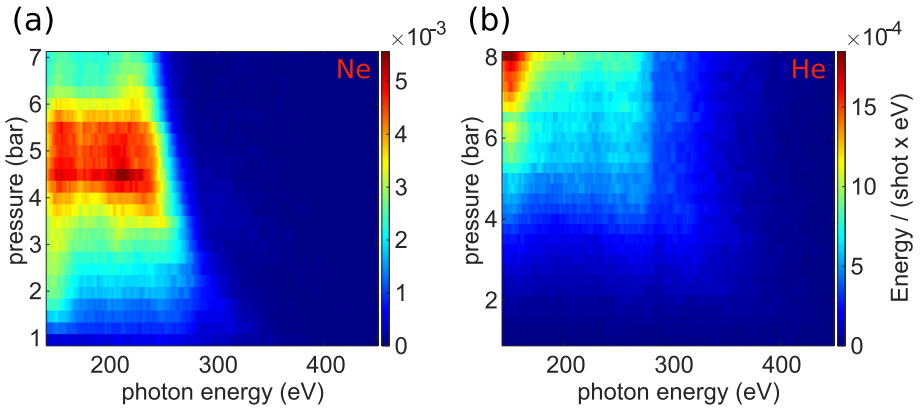

Figure 3.32: Backing pressure scan for neon (a) and helium (b) gas target. The spectra are generated in a metallic gas nozzle with ≈ 0.5 mm inner diameter and the single IR channel. The position of the nozzle is optimized with a difference of 250 μm between the neon and helium measurements. A 200 nm Ti filter blocks the IR light. The beams are focussed with $f = 6$ inch leading to a peak intensity of $I_{peak} \approx 2.5 \times 10^{14}$ for the IR channel.

≈ 0.7 eV at ≈ 200 eV photon energies. Firstly, it is seen that the single IR channel presumably can generate broadband continua on its own. This would be explained due to the short ≈ 1.5-cycle duration and the assistance of ionization gating arguments. In neon, the flux optimizes at 4.5 bar with a cut-off at 250 eV. The measurements are taken with a focal length of 6 inch that, especially for neon increased the ionization above the critical level, therefore the input iris to the HHG chamber is used to lower the peak intensity. For helium, the optimum pressure is not yet reached and the capabilities of the vacuum pumps are the limiting factor.
A scan of the gas nozzle at fixed pressure is given in figure 3.33. With the input iris partially closed, the HHG cut-off seems to show some linear behavior on the gas nozzle position. This is not observed when the input iris is fully opened. The gas nozzle scan in helium shows a significant portion of the spectrum above the C-edge. The spectra are intensity calibrated with the transfer function. The gas cell position z is the absolute position of the motorized stage but not referenced to the laser focus. The harmonic yield optimizes at positions ≈ 1 mm apart from each other. The scan of pressure and gas nozzle position is done at a defined and stabilized CEP of the IR channel and optimized for flux and cut-off to serve as a reference.

Next, the synthesized waveform is exploited in helium and neon at similar conditions as we optimized for with the single IR channel. The possibility to scan the RP and CEP at mrad resolution enlarges the data space significantly. A scan of the RP usually consists of 150 steps with

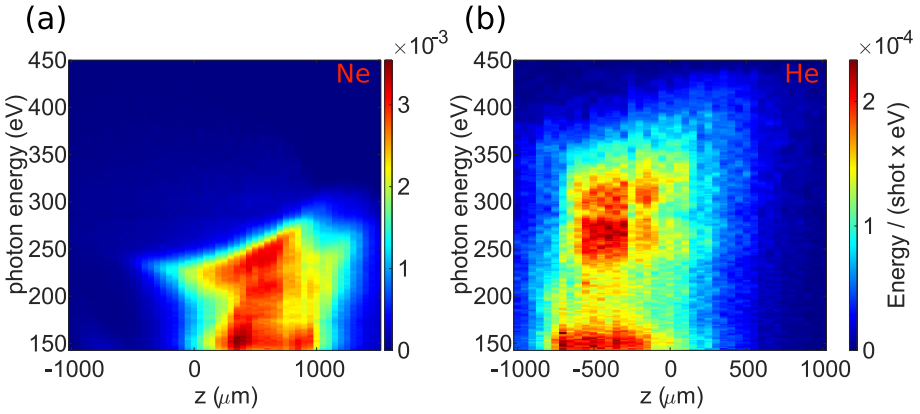

Figure 3.33: Gas nozzle scan for neon (left) and helium (right) gas target. The spectra are generated in a metallic gas nozzle with ≈ 0.5 mm inner diameter and the single IR channel as driving pulse. A 200nm Ti filter blocks the IR light. Both measurements are taken with a backing pressure of 4 bar. The beams are focussed with $f = 6$ inch leading to a peak intensity of $I_{peak} \approx 2.5 \times 10^{14}$ W/cm^2 for the IR channel.

400 mrad resolution to observe a full passage between NIR and IR channel. An additional CEP scan for each RP step with a resolution of 200 mrad results in $150 \times 30 = 4500$ samples, which in turn results in ≈ 2.5 hours with an integration time of 2 s for each spectrum. The technical details on the synchronization of a CEP-RP scan with the XUV spectra is given in figure 7.1 in the appendix. Here, a comparison is given for RP scans at a single stabilized CEP recorded as a function of the gas nozzle position. This aims to optimize the generation condition for every possible waveform of the PWS. The yield of the single IR channel can be estimated from positions far from time overlap qualitatively. The scans of the phase and the gas cell positions show that the yield and shape of the generated continuum strongly depends on the CEP and RP properties, but less on the macroscopic conditions, when comparing the patterns from figure 3.34 (b) to (c). On top of the single IR channel pressure and gas nozzle scans, a CEP scan is presented in figure 3.35 (a) to identify the maximum possible flux and cut-off for the single IR channel. For this measurement, the gas cell position is again optimized for the single IR channel, but instead of estimating the photon flux for a single or averaged CEP, the value is given CEP-dependent. For better visibility of the cut-off region, the spectra are plotted without the transfer function on the colormap. The adjacent lineouts represent in dotted lines the spectra from the spectrogram and in solid lines the transfer function corrected spectra. The total input pulse energies for these scans are ≈ 180 μJ of the IR channel and ≈ 20 μJ of the NIR channel, that makes an increase of ≈ 10 % for the synthesized waveform against the single IR channel. To account for an increase of the peak intensity, which is affected more by shortening of the pulse duration than by the increase of pulse energy, RP scans at different gas nozzle positions are repeated in order to optimize the phase-matching for different waveforms. Throughout the scans of the PWS-driven HHG, an enhancement of the overall yield can be observed. The enhancement can be judged by comparing the photon numbers given in figures 3.34 and 3.35. From these numbers one could

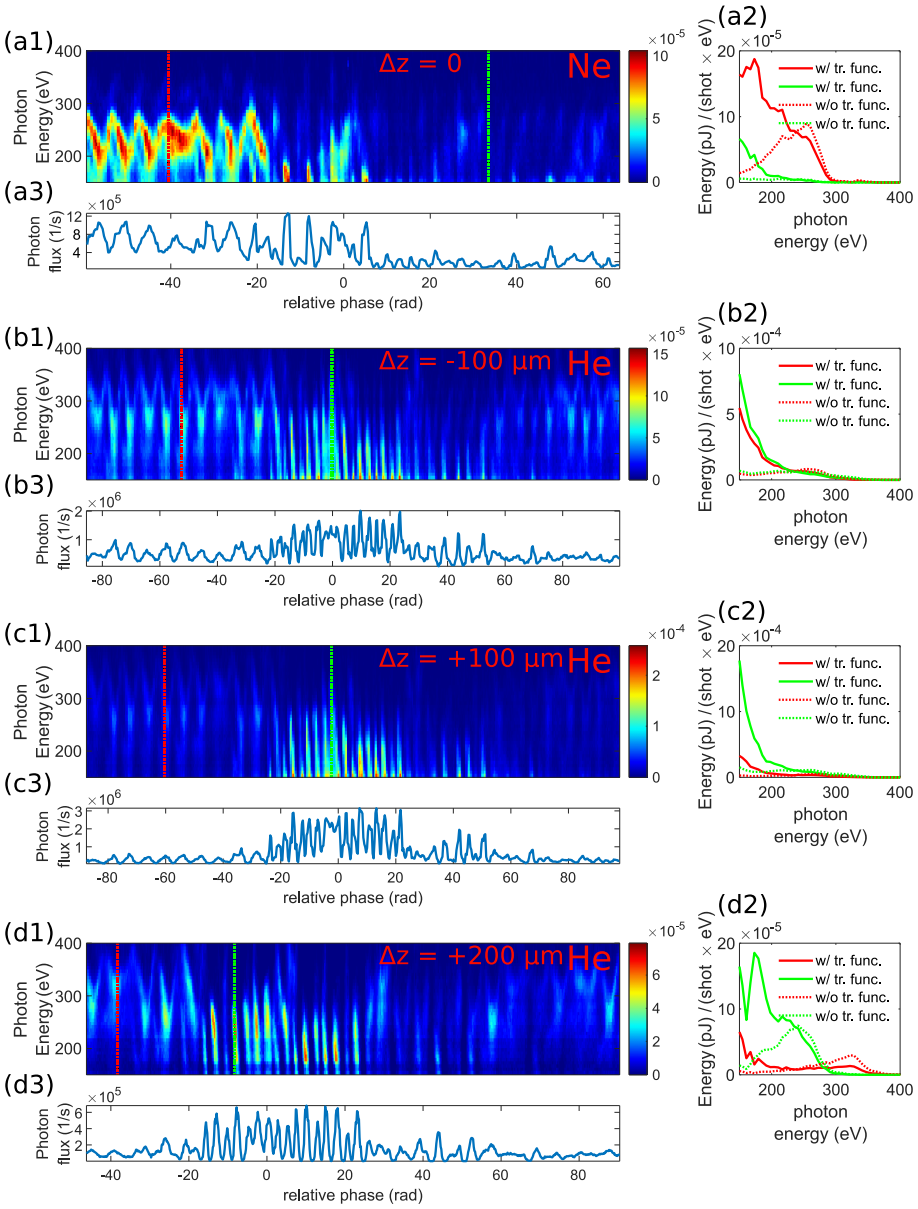

Figure 3.34: HHG results of RP scans of the PWS waveform in neon and helium. The CEP is optimized qualitatively for highest cut-off HHG for the spectra around time zero and stabilized during a scan. The IR channel is advancing to the left side of the x-axis. Scan (a) is recorded with neon at 4 bar backing pressure. Due du ionization at time zero and onwards, the harmonic emission is suppressed. Panels (b-d) are recorded with helium as generation gas at a backing pressure of 10 bar. To the right, the adjacent lineouts are plotted for two spectra from the scan and for case with transfer function (W/ tr. func.) including XUV CCD QE, grating response, filter transmission and for the case without transfer function (w/o tr. func.). Mainly due to the high slope of the XUV CCD in the range from $100-200$ eV, the spectra are heavily altered. The colormap plots show the spectra without transfer function. The scans in helium are taken at various positions of the gas nozzle as indicated by Δz. A 300 μm Ti filter is used to block the residual IR light with exception to panel (d) where 2×100 μm Al is used.

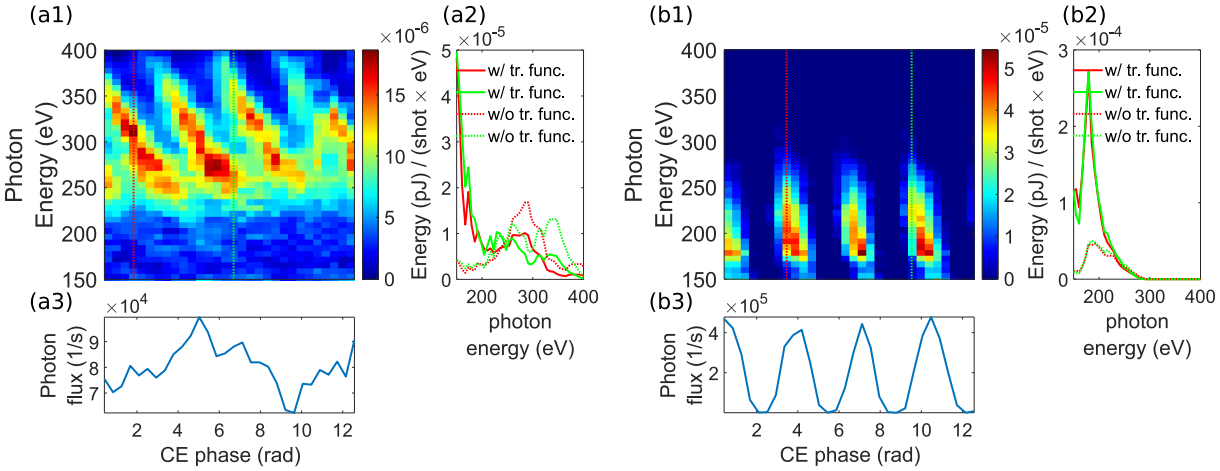

Figure 3.35: HHG dependency on the CEP of single IR channel (a) and PWS waveform (b). The RP of the PWS is fixed around time zero. The measurements are taken with helium at 10 bar backing pressure and the residual IR light is blocked by 2×100 nm Al filter.

state roughly a factor of 5 higher photon flux compared to the single IR channel driven case. On the other hand, the photon flux is integrated along the full spectrum that the 2400 gr/mm grating allows to observe. From the spectral lineouts, it becomes obvious that the cut-off downshifts for the PWS-driven HHG, so the comparison purely on photon numbers lacks this import detail. Nevertheless, for measurements around the C-edge and below, the enhancement as observed is beneficial. The arguments are valid for the case of helium as generation gas. The parameter scans in neon at the same focusing conditions plotted in figure 3.34 (a) reveal a counteracting signature of the PWS waveform. The decrease of the signal around time zero is assumed to result from a peak intensity well above the critical ionization that suppresses most of the emission. To the left of plot (a) in figure 3.34, the IR channel is advances and gives rise to HHG continua that are slightly modulated by the wings of the NIR channel and therefore represent close to single IR channel driven HHG but at time overlap and beyond, the signal disappears.
The CEP scans in figure 3.35 state a comparison for maximum possible photon yield for single IR channel driven HHG (a) and PWS-driven HHG (b) with the total flux increased by a factor of 5, as given by (a3,b3). Furthermore, the contrast of the CEP scan improves greatly with the PWS driven continua. But again, similar as observed in the RP scans, the continua downshift and barely reach the C-edge.
The recorded spectrograms give a complete picture of the phase-sensitive generation of harmonic continua, all collected in a single focusing geometry ($f = 6$ inch). The strong ionization in neon and the non-optimal signature of yield enhancement in helium motivates to repeat similar scans in helium and neon at a lower peak intensity. Since a reduction of the single channels pulse energy is not straightforward, as mentioned, due to the dependency of feedbacks i.e. phase meter and pointing stabilizer, the measurements are repeated with a spherical mirror of longer focal length ($f = 400$ mm).

The reference measurements of the single IR channel are presented in figure 3.36 for helium (a) and neon (b). The spectrograms are displayed without transfer function while the corrected spectra are given at the lineout (solid lines in (a2,b2)). An analysis of the photon flux in 1% bandwidth around the given photon energies is plotted in panel (a3,b3). The peak intensity at $f = 400$ mm is characterized to 1.2×10^{14} W/cm^2 and 0.2×10^{14} W/cm^2 for IR and NIR channel, respectively. The gas nozzle maps show the emission of harmonics at similar positions for the cases of helium and neon as generation gas. The total photon flux maximizes at 3×10^6 ph/s and 5×10^6 ph/s photons for helium respectively neon. At the given focal length,

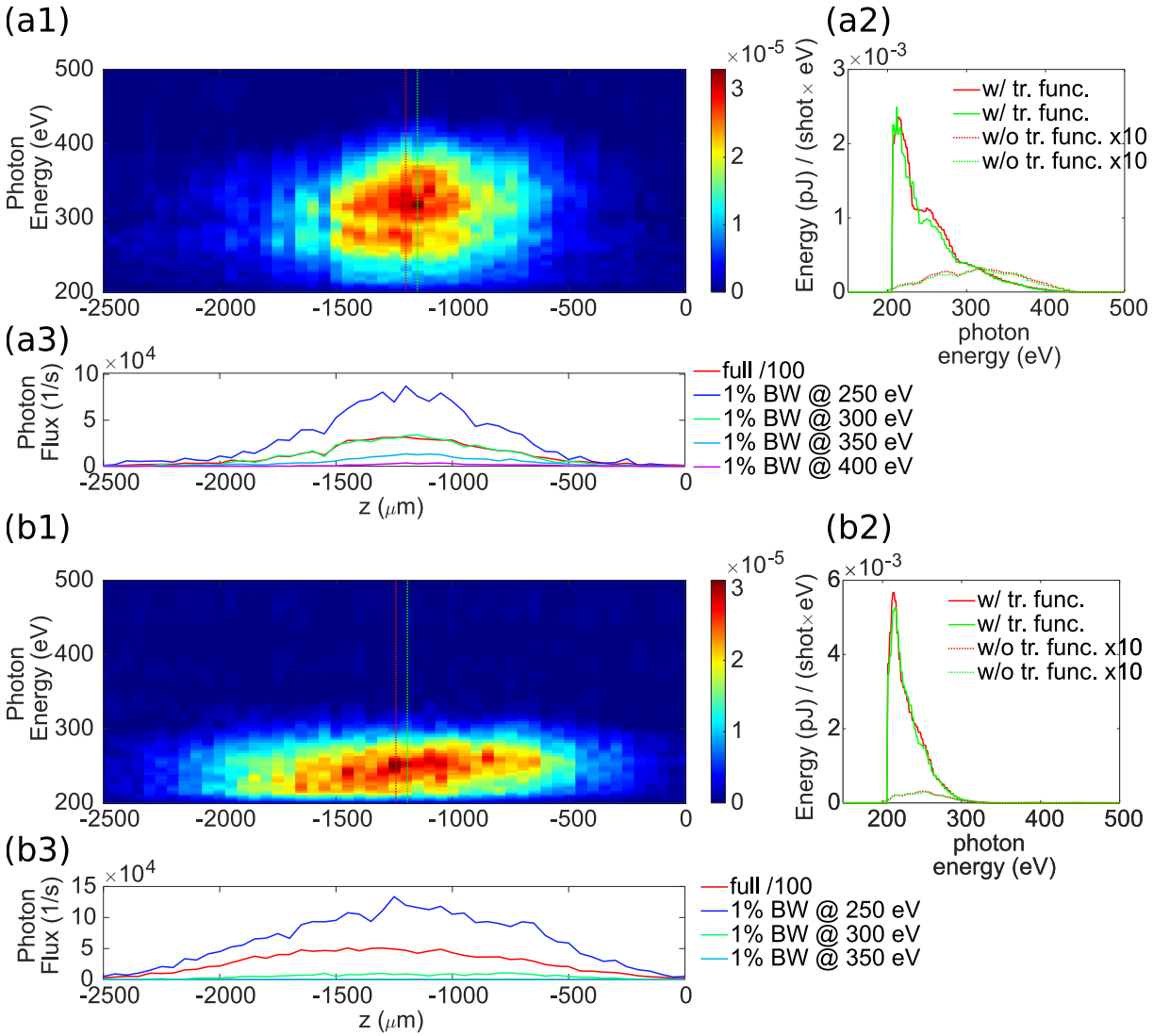

Figure 3.36: Optimization of the gas cell position for the single IR driven HHG in helium at 8 bar (a) and neon at 2 bar (b) backing pressure. The spectrogram displays the data without transfer function. Panel (a2,b2) plot the lineouts in dotted lines and the transfer function corrected spectra in solid lines. The residual IR light is filtered by 100 nm Al and 100 nm Cu filter.

the HHG yield is optimal with the input iris fully open and the gas nozzle scans appear to be almost symmetric. For the case of helium, the C-edge is clearly visible.

The results of the PWS-generated HHG in helium are given in figure 3.37 as RP-CEP scan. All data shown in this figure were recorded at a gas nozzle position of $z = -1200$ μm that corresponds to the optimum position as derived from figure 3.36, and this time is referenced to the focus of the laser pulse. Since the stage is encoded oposite to the laser propagation direction, $z = -1200$ μm corresponds to the gas nozzle position after the focus of the beam. Panel (a) corresponds to an RP scan at a single CEP. The solid markers indicate the RPs for which the CEP scans are plotted in panels (b,c). Due to the large data space, only two CEP scans are plotted. Panel (d) correspond to a CEP scan of the single IR channel. The total photo flux read up to 1.5×10^7 ph/s for the PWS-driven HHG that is again a factor 5 increase compared to single IR channel in terms of overall yield. Different to the last scan that was measured with $f = 6$ inch, this scan does not show a significant downshift in photon energies. A cut-off up to 400 eV is observed, also for synthesized driver fields. At the RP positions -10rad, -1rad and $+10$rad, one can observe the shaping of the XUV continua towards higher and lower photon energies and redistribution of the spectral yield. The analysis given in panel (a3) shows an increase in the photon energy band around 250 eV, while the yellow curve shows a decrease at 300 eV and vice versa, demonstrating that the PWS waveform can control the spectral yield. The dotted markers indicate the lineouts plotted in panel (e). Again, the spectrograms are plotted without transfer function but the pulse energy and photon flux include all transfer function and represent numbers at the source. The cyan and magenta curves in panel (e) show the increased flux around the C-edge of $\times 4$ compared to the single IR channel (red curve). The RP-CEP scan is plotted with an extended RP axis in figure 7.2 of the appendix. From the measurements presented and many more that were conducted during the course of this thesis, the possibility to shape the XUV continua are observed for photon energies below the cut-off energy as given by the longer wavelength IR channel. As the structure of the thesis is basically split into two regimes, the generation of lower photon energy continua with the NIR channel as guiding pulse and the generation of higher photon energy continua with the IR channel as guiding pulse, it can be stated that the ease to generate a large variety of continua seems to be given much more for the lower photon energy continua. An extension of the cut-off is barely observed when the shorter wavelength NIR channel is added to the IR channel. Chipperfield *et al.* have observed similar trends in [102] and figure 2 therein. The two-color field simulation ($800 + 1600$ nm) shows a decrease of cut-off energy by ≈ 20 % and yield enhancement of $\times 5 - 10$ around the reduced cut-off. Their simulation are performed for neon as generation gas. We observe the same trend for neon and helium as shown for the case of helium in figure 3.37. The decrease in the cut-off follows the scaling law from single atom calculation as was also confirmed experimentally in [199], [200]. Assuming an increase of the peak intensity by a factor of 2, mainly due to the shortening of the temporal duration, exceeding the linear dependency of HHG yield and driving laser intensity regarding the observed factor of $\times 5$ yield increase. An explanation involves the single atom picture and macroscopic phase-matching considerations. The "perfect" design of a waveform allows to increase the electric field at times of ionization and recombi-

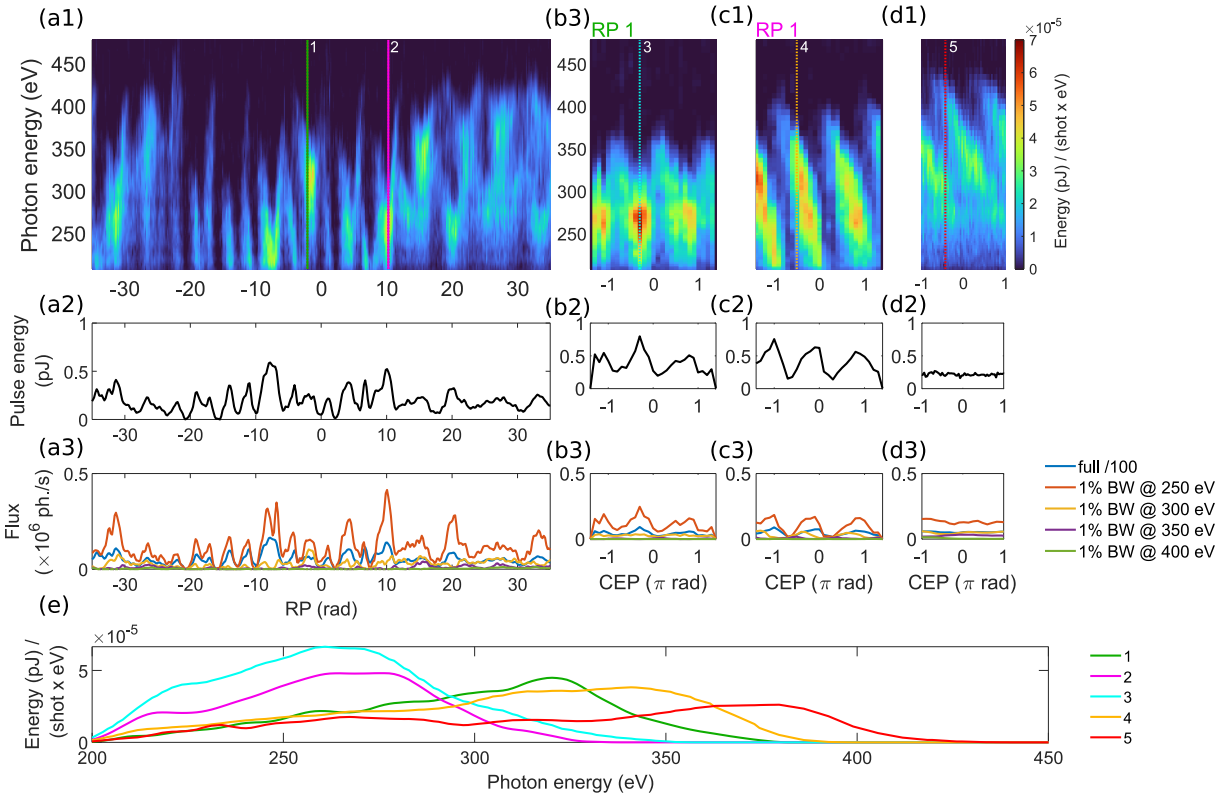

Figure 3.37: Presentation of the RP-CEP scan in helium at 8 bar backing pressure and a focusing condition of $f = 400$ mm. The recorded XUV spectra are presented as a function of the RP (a1) and a single CEP. (b,c) correspond to CEP scans at a specific RP indicated by the solid markers in (a1). (d) corresponds to a CEP scan measurement of the single IR channel. All measurements are taken with the same position of the gas nozzle. The spectrograms do not contain the transfer function while the pulse energies and photon flux given in rows 2 and 3 include the transfer function and correspond to photon numbers at the source. The photon flux is given in a 1% bandwidth (BW) given by the legend. The lineouts indicated by the dotted lines and marked (1-4) are plotted in (e), showcasing various continua as generated with the PWS compared to the single IR channel in red color (5).

nation compared to a sinusoidal field, see [104] and figure 1 therein. Considering the time the electron spends in the continuum as a measure of the HHG efficiency [201], the "perfect" waveform would allow higher recollision energies at same traveling times. If the traveling time is not fixed, the "perfect" waveform would allow higher recollision energies at the same traveling times, therefore increasing the single atom yield.

An extension to the description of macroscopic phase-matching, as given in section 3.1, is discussed by I. P. Christov *et al.* [202] for the case of short laser pulses. For pulse durations on the order of the classical tunneling times, the response of the atomic dipole becomes nonadiabatic and at high peak intensities the ionization becomes dependent on the pulse duration of the driving laser. As a consequence, a higher field can be applied that still fulfills the phase-matching condition. A comparison with the experiment confirms the yield increase with decreasing pulse durations down to a pulse duration of 25 fs as, it was available at the times of that publication.

As a summary, the photon numbers as measured for various macroscopic conditions are given in table 3.4. The first section of the table contains the numbers for driving conditions at low phase-matching pressures and photon energies at a central energy of $40-70$ eV. The IR channel flux measurement is taken to calibrate the absolute numbers of the XUV CCD based calculation and do not correspond to optimized HHG in the given energy regime. Here, the maximum pulse energy of the XUV continuum of 585 pJ is comparable to the stated pulse energy of 0.5nJ as published in [183] for the HCF WS. Nevertheless, the central wavelength of the synthesized driver pulses differ by a factor of 2, limiting a direct comparisson of these sources
The photon numbers given for high-pressure phase-matching represent a valid comparison between the single IR channel driven HHG and the PWS-driven HHG. For each given focal length, the total flux is increased by a factor of $2-5$. The comparison of single bands (1 % BW) can also show greater enhancements. Nevertheless, a comparison of the case of neon gas and $f = 400/500$ nm disclose that the relative enhancement is advantageous for $f = 500$ nm but the absolute yield is higher for $f = 400$ nm where the enhancement is lower ($\times 2$) but still observable. This is an important fact since we aim for a global optimization of the absolute yield and not only for a local comparisson at a single macroscopic phase-matching condition. In order to place the given photon numbers for the WW in relation with other laboratories, the photon flux of the beamline at Imperial College [54] is given with 4.0×10^6 ph/s across the WW for helium and 4.0×10^7 for neon. Their source is described to drive HHG in the "overdriven" regime where the generated plasma spatiotemporally reshapes the driving laser beneficially and optimizes the HH yield. Their input pulse energy of the IR driver ($\lambda_0 = 1.8\ \mu m$) is given as 550 μJ that is $\approx \times 2$ our energy. In addition, published measurements of the HH yield from the Biegert lab [203], Kapteyn-Murnane lab [204] and Leone lab [205] are given in table 3.4. A comparison of the fluxes show, that the total yield in the WW is higher for sources with a $1.8-2$ μm driving laser, where the cut-off reaches to higher photon energies. The 1.3 μm driving laser of the Leone lab has the most similar central wavelength compared to the PWS and is reportet with 2.5×10^4 ph/s/1 % BW @ 300 eV for a 1 mm long gas cell. At similar conditions, the flux with the PWS can be scaled by almost an order of magnitude to 1.6×10^5 ph/s/1 % BW @ 300 eV at only a fifth of the driver pulse energy as stated in [205]. For completeness, the authors report on a study of the gas cell where a different macroscopic generation condition with 7.5 cm long cells improved the flux by almost two orders of magnitude. The use of geometrically extended gas cells is in preparation but still has to be investigated with the PWS driven HHG.

	focal length f (mm)	gas type	nozzle diam. (mm)	pulse energy E (pJ)	total ph. # (ph/s)	WW ph. # (ph/s)	1 % BW @ 250 eV (ph/s)	1 % BW @ 300 eV (ph/s)	1 % BW @ 350 eV (ph/s)	1 % BW @ 400 eV (ph/s)	comments
IR	375	Ar 0.2 bar	2	0.62	8.7×10^7						at 50 eV
Synth	375	Ar 0.3 bar	2	585	9.0×10^{10}						at 40 eV
Synth	375	Ne 0.3 bar	2	16	1.4×10^9						at 70 eV
IR	250	Ne 4 bar	0.5	0.19	5.2×10^6	1.7×10^5	1.8×10^5	2.3×10^4	1.5×10^3	1.2×10^2	
Synth	250	Ne 4 bar	0.5	0.19	5.1×10^6	2.5×10^5	1.8×10^5	2.9×10^4	4.8×10^3	7.4×10^2	
IR	250	He 10 bar	0.5	0.09	2.2×10^6	3.7×10^5	7.0×10^4	2.0×10^4	1.8×10^4	7.6×10^2	
Synth	250	He 10 bar	0.5	0.34	9.3×10^6	4.6×10^5	2.5×10^5	5.5×10^4	1.3×10^4	3.1×10^3	
IR	400	Ne 2 bar	1.0	0.52	1.4×10^7	4.4×10^5	4.8×10^5	4.9×10^4	1.3×10^3	8.2×10^2	
Synth	400	Ne 2 bar	1.0	0.8	2.2×10^7	7.1×10^5	6.0×10^5	1.0×10^5	6.8×10^3	1.2×10^3	
IR	400	He 8 bar	1.0	0.3	7.7×10^6	1.1×10^6	2.0×10^5	9.3×10^4	4.4×10^3	1.5×10^4	
Synth	400	He 8 bar	1.0	0.78	2.1×10^7	1.9×10^6	5.2×10^5	1.6×10^5	5.3×10^4	7.5×10^3	
IR	500	Ne 3 bar	1.0	0.16	4.5×10^6	7.6×10^4	1.0×10^5	3.4×10^3	1.9×10^3	7.8×10^2	
Synth	500	Ne 3 bar	1.0	0.47	1.3×10^7	1.4×10^5	2.2×10^5	1.1×10^4	1.7×10^3	1.1×10^3	
[203]		He 12.5 bar	1	0.9	1.8×10^6 ph/s/10 % BW @ 284 eV						0.4 mJ, 1.85 μm
[204]		He 3-15 bar	10		6×10^7 ph/s in WW						2.4 mJ, 2 μm
[54]		He 5 bar	0.8	0.2	4×10^6 ph/s in WW						0.55 mJ, 1.8 μm
[54]		Ne 2 bar	0.8	2	4×10^7 ph/s in WW						0.55 mJ, 1.8 μm
[205]		He 3 bar	1		2.5×10^4 ph/s/1 % BW @ 300 eV						1 mJ, 1.3 μm

Table 3.4: Summary of the photon numbers at source for the single IR channel and synthesized waveform (Synth) driven conditions. The macroscopic parameters such as focal length, gas type and nozzle diameter are given. The HH yield is given in pulse energy (pJ) and flux (photons/s). For high photon energy HHG, the flux is given in the water window (WW) spectrum and at 1 % bandwidth (BW). A couple of published sources with flux measurements in the WW regime are added for reference. The pulse energy and central wavelength of the driver pulse are given in the comments.

4 A Beamline for Future Pump-Probe Experiments

The PWS synthesizer is proven as a reliable source for HHG. The large spectrum of photon energies and the possibility to generate IAP right from the source is hard to beat with conventional sources. The observation of strong field control of the generated XUV and SXR continua, including a first sign of yield enhancement, motivates to extend the PWS by an additional channel to increase the bandwidth and the possibility for a wealth of additional sub-cycle waveforms. The HHG yield is expected to further increase while the cut-off stays constant when a third field is added [104]. The dispersion scheme and pump laser energy are designed to support a third visible (VIS) channel as sketched in figure 2.5. The spectrum of the visible channel is located around the 3^{rd} harmonic of the IR channel, which is reported as an ideal composition for yield enhancement [104], [142].

From the point of applications, the set of methods developed in this work to routinely generate sub-cycle waveforms and characterize the PWS and the generated XUV continua prepares for future experiments. A redesign of the vacuum apparatus serves both a new chamber to host experiments in liquid-, solid- or gas-phase and to remove existing limitations in the generation of harmonics that we encountered during the course of this thesis. It is mostly the tight design of XUV imaging optics, that prevented a convenient installation of additional hardware for beam characterization. Furthermore, the installation of the high-pressure gas cell allowed for "water window" HHG generation, but the background pressure in the surrounding chamber as high as 10^{-1} mbar is incompatible with pump-probe experiments. The technical drawing of the beamline as planned and partially set up is given in figure 4.1. The differential pumping of the gas jet chamber is updated with a combination of roots pump (booster pump) and multistage roots pump (Ruvac WH700 and ecodry 65 plus, Leybold). Compared to the previously used scroll pumps (xds35i, Edwards), the pumping capabilities should increase by two orders of magnitude.

A toroidal mirror with an imaging distance $S = 1000$ mm and nickel coating is planned to place

the focus of the HHG beam right in the center of the experimental chamber. The recombination chamber between the second and experimental chamber allows to vary the focus of the IR pump beam in order to adjust the peak intensity. All reflecting XUV optics are designed with an incidence angle of 3°.

The newly designed spectrometer obeys an arm length of 650 mm and is planned to host curved aberration-corrected gratings or reflecting zone plates (RZP) that image the point of the experiment on the detector. This configuration avoids the use of an input slit that would lower the throughput, and avoid the use of a second toroidal mirror that is often used to refocus the light from the experiment to the spectrometer. RZP have gained increasing interest in recent years [206], [207]. The matured technology of electron and ion etching allows for a flexible design of the structure and the possibility for two-dimensional variation of the periodic line spacing. Customized zone plates have shown great improvements concerning the efficiency while keeping the bandwidth and energy resolution comparable to gratings (at least for gratings that are available of the shelf). The offer to fabricate custom RZPs at reasonable costs compared to custom SXR gratings gives the possibility to implement experiment-specific RZPs. Currently, we are investigating the option for broadband ($200-600$ nm) RZPs at a resolving power of $E/\Delta E \approx 600$ and RZP with $E/\Delta E > 1000$ for specific absorption edges and smaller total bandwidth.

The experimental chamber itself is designed to host the existing TOF, but likewise is designed to mount various samples. A central port in the bottom allows to mount a catcher and pump for experiments in liquid phase. The outgoing ports in addition to the central port in direction of the laser are arranged for $45° \pm 4°$ and $30° \pm 8°$ to allow reflection measurements on solids.

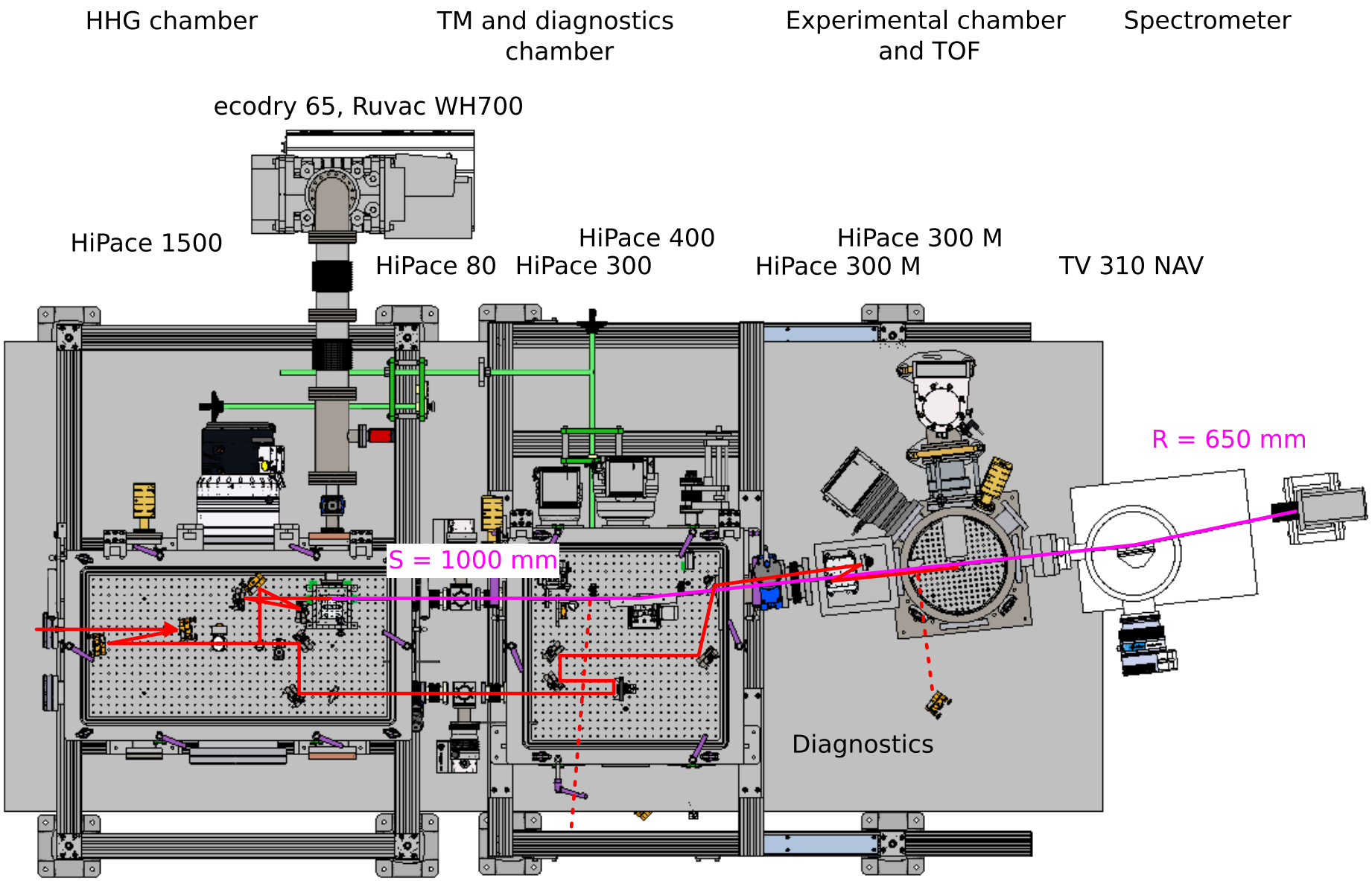

Figure 4.1: Extension of the beamline for attosecond transient absorption experiments and photo electron measurements. A powerful pumping system is added for the high-pressure gas cell. XUV optics with longer imaging distances allows for additional differential pumping. The newly designed experimental chamber is located between the toroidal mirror (TM) chamber and spectrometer.

5 Summary

The concept of parametric waveform synthesis (PWS) for the generation of sub-cycle IR pulses is proven as key technology to break the barrier for multi-octave spanning, highly intense pulses. A phase jitter of < 70 mrad relative phase and < 250 mrad carrier-envelope phase presents the synthesized pulses no different to conventional phase stabilized single channel sources. The synthesis in spatial domain is pioneered and shown to result in stable wavefronts as observed via spatially resolved interference. For the first time, synthesized IR waveforms with a central wavelength of $\lambda_0 = 1.4$ μm and sub-cycle durations at an energy of ≈ 200 μJ are applied extensively to the generation of high harmonics in gases. Due to the sub-cycle nature (3.8 fs$, 0.6$ cycles) of the driving waveform, XUV and soft X-ray spectra are observed almost exclusively as continous spectra. The spatial profile of the continua appears as Gaussian as the single source driven HHG. The generated continua in argon, neon and helium show a tight correlation with the driving waveform that is parametrized via the relative and CE phase. Waveform control is shown to shape the XUV and soft X-ray continua in bandwidth up to a factor of 3 and the central photon energy by a factor of 2 in a single macroscopic condition. The stability of the source allowed long-term parameter scans involving the relative and CE phase and macroscopic phase-matching on a time scale of several hours.

The experiment of attosecond streaking and evaluation with the Volkov transform generalized projection algorithm proved the consistency of waveform control and stability. Consecutive streaking measurements revealed isolated attosecond pulses down to 80 as at 70 eV central photon energy with very low attochirp. The low attochirp is observed for narrow- and broadband continua.

An expansion of the vacuum apparatus involving a high-pressure gas cell, new toroidal mirror and update of the vacuum pumps allowed to establish the high-pressure phase-matching condition for HHG in the “Water Window”. Photon energies of up to 450 eV are observed with PWS driven HHG. Within the error bars of slightly changing beam parameters from the PWS channels on the long term, the yield of generated harmonics by the synthesized waveform increases by a factor of $2-5$ depending on the observed photon energy range compared to the single IR channel driven HHG. The addition of the NIR channel with only 10 % of the IR chan-

nel energy and an optimization of RP and CEP multiplies the yield. At optimized macroscopic conditions, the yield increases for specific stabilized phases and is explained to originate from the overall reduction in pulse duration and increase of peak intensity ones the pulses are synthesized, together with the control of the electric field waveform to optimize for the ionization and recombination of the electron wave packet.
The final design of the attosecond beamline includes an experimental chamber for transient absorption experiments in gas, liquid and solid phase to prepare for future attosecond pump probe experiments.

Bibliography

[1] S. Mukamel, *Principles of Nonlinear Optical Spectroscopy*. Oxford University Press on Demand, 1999.

[2] U. Morgner, F. X. Kärtner, S. H. Cho, Y. Chen, H. A. Haus, J. G. Fujimoto, E. P. Ippen, V. Scheuer, G. Angelow, and T. Tschudi, "Sub-two-cycle pulses from a Kerr-lens mode-locked Ti:sapphire laser," *Optics Letters*, vol. 24, no. 6, pp. 411–413, Mar. 1999, ISSN: 1539-4794. DOI: 10.1364/OL.24.000411.

[3] P. Agostini, F. Fabre, G. Mainfray, G. Petite, and N. K. Rahman, "Free-Free Transitions Following Six-Photon Ionization of Xenon Atoms," *Phys. Rev. Lett.*, vol. 42, no. 17, pp. 1127–1130, Apr. 1979. DOI: 10.1103/PhysRevLett.42.1127.

[4] G. G. Paulus, F. Grasbon, H. Walther, P. Villoresi, M. Nisoli, S. Stagira, E. Priori, and S. De Silvestri, "Absolute-phase phenomena in photoionization with few-cycle laser pulses," *Nature*, vol. 414, no. 6860, pp. 182–184, Nov. 2001, ISSN: 1476-4687. DOI: 10.1038/35102520.

[5] F. Kelkensberg, W. Siu, J. F. Pérez-Torres, F. Morales, G. Gademann, A. Rouzée, P. Johnsson, M. Lucchini, F. Calegari, J. L. Sanz-Vicario, F. Martín, and M. J. J. Vrakking, "Attosecond Control in Photoionization of Hydrogen Molecules," *Phys. Rev. Lett.*, vol. 107, no. 4, p. 043 002, Jul. 2011. DOI: 10.1103/PhysRevLett.107.043002.

[6] M. Drescher, M. Hentschel, R. Kienberger, M. Uiberacker, V. Yakovlev, A. Scrinzi, T. Westerwalbesloh, U. Kleineberg, U. Heinzmann, and F. Krausz, "Time-resolved atomic inner-shell spectroscopy," *Nature*, vol. 419, no. 6909, pp. 803–807, Oct. 2002, ISSN: 1476-4687. DOI: 10.1038/nature01143.

[7] F. Calegari, D. Ayuso, A. Trabattoni, L. Belshaw, S. D. Camillis, S. Anumula, F. Frassetto, L. Poletto, A. Palacios, P. Decleva, J. B. Greenwood, F. Martín, and M. Nisoli, "Ultrafast electron dynamics in phenylalanine initiated by attosecond pulses," *Science*, vol. 346, no. 6207, pp. 336–339, 2014. DOI: 10.1126/science.1254061.

[8] A. Wirth, M. T. Hassan, I. Grguraš, J. Gagnon, A. Moulet, T. T. Luu, S. Pabst, R. Santra, Z. A. Alahmed, A. M. Azzeer, V. S. Yakovlev, V. Pervak, F. Krausz, and E. Goulielmakis, "Synthesized Light Transients," *Science*, vol. 334, no. 6053, pp. 195–200, 2011. DOI: 10.1126/science.1210268.

[9] A. Baltuška, T. Udem, M. Uiberacker, M. Hentschel, E. Goulielmakis, C. Gohle, R. Holzwarth, V. S. Yakovlev, A. Scrinzi, T. W. Hänsch, and F. Krausz, "Attosecond control of electronic processes by intense light fields," *Nature*, vol. 421, no. 6923, pp. 611–615, Feb. 2003, ISSN: 1476-4687. DOI: 10.1038/nature01414.

[10] A. Moulet, J. B. Bertrand, T. Klostermann, A. Guggenmos, N. Karpowicz, and E. Goulielmakis, "Soft x-ray excitonics," *Science*, vol. 357, no. 6356, pp. 1134–1138, 2017. DOI: 10.1126/science.aan4737.

[11] M. Chini, B. Zhao, H. Wang, Y. Cheng, S. X. Hu, and Z. Chang, "Subcycle ac Stark Shift of Helium Excited States Probed with Isolated Attosecond Pulses," *Phys. Rev.*

Lett., vol. 109, no. 7, p. 073 601, Aug. 2012. DOI: 10.1103/PhysRevLett.109.073601.

[12] M. Sabbar, H. Timmers, Y.-J. Chen, A. K. Pymer, Z.-H. Loh, S. G. Sayres, S. Pabst, R. Santra, and S. R. Leone, "State-resolved attosecond reversible and irreversible dynamics in strong optical fields," *Nature Physics*, vol. 13, no. 5, pp. 472–478, May 2017, ISSN: 1745-2481. DOI: 10.1038/nphys4027.

[13] T. H. Maiman, "Optical and Microwave-Optical Experiments in Ruby," *Phys. Rev. Lett.*, vol. 4, no. 11, pp. 564–566, Jun. 1960. DOI: 10.1103/PhysRevLett.4.564.

[14] J. Hecht, "Short history of laser development," *Optical Engineering*, vol. 49, no. 9, p. 091 002, 2010. DOI: 10.1117/1.3483597.

[15] P. F. Moulton, "Spectroscopic and laser characteristics of Ti:Al2O3," *J. Opt. Soc. Am. B*, vol. 3, no. 1, pp. 125–133, Jan. 1986. DOI: 10.1364/JOSAB.3.000125.

[16] A. Stingl, M. Lenzner, C. Spielmann, F. Krausz, and R. Szipöcs, "Sub-10-fs mirror-dispersion-controlled Ti:sapphire laser," *Opt. Lett.*, vol. 20, no. 6, pp. 602–604, Mar. 1995. DOI: 10.1364/OL.20.000602.

[17] R. Ell, U. Morgner, F. X. Kärtner, J. G. Fujimoto, E. P. Ippen, V. Scheuer, G. Angelow, T. Tschudi, M. J. Lederer, A. Boiko, and B. Luther-Davies, "Generation of 5-fs pulses and octave-spanning spectra directly from a Ti:sapphire laser," *Opt. Lett.*, vol. 26, no. 6, pp. 373–375, Mar. 2001. DOI: 10.1364/OL.26.000373.

[18] G. Cerullo and S. De Silvestri, "Ultrafast optical parametric amplifiers," *Review of Scientific Instruments*, vol. 74, no. 1, pp. 1–18, 2003. DOI: 10.1063/1.1523642.

[19] C. Manzoni and G. Cerullo, "Design criteria for ultrafast optical parametric amplifiers," *Journal of Optics*, vol. 18, no. 10, p. 103 501, Oct. 2016. DOI: 10.1088/2040-8978/18/10/103501.

[20] J. Zhang, K. Fai Mak, N. Nagl, M. Seidel, D. Bauer, D. Sutter, V. Pervak, F. Krausz, and O. Pronin, "Multi-mW, few-cycle mid-infrared continuum spanning from 500 to 2250 cm-1," *Light: Science & Applications*, vol. 7, no. 2, pp. 17 180–17 180, Feb. 2018, ISSN: 2047-7538. DOI: 10.1038/lsa.2017.180.

[21] A. Couairon and A. Mysyrowicz, "Femtosecond filamentation in transparent media," *Physics Reports*, vol. 441, no. 2, pp. 47–189, 2007, ISSN: 0370-1573. DOI: 10.1016/j.physrep.2006.12.005.

[22] J. Darginavičius, D. Majus, V. Jukna, N. Garejev, G. Valiulis, A. Couairon, and A. Dubietis, "Ultrabroadband supercontinuum and third-harmonic generation in bulk solids with two optical-cycle carrier-envelope phase-stable pulses at 2 *M*m," *Optics Express*, vol. 21, no. 21, pp. 25 210–25 220, Oct. 2013, ISSN: 1094-4087. DOI: 10.1364/OE.21.025210.

[23] R. E. Mainz, G. M. Rossi, G. Cirmi, Y. Yang, S.-H. Chia, E. J. Takahashi, O. D. Mücke, and F. X. Kärtner, "Can sub-optical-cycle parametric waveform synthesizers be seeded by separate bulk white-light supercontinua?" In *2016 Conference on Lasers and Electro-Optics (CLEO)*, Jun. 2016, pp. 1–2.

[24] G. M. Rossi, L. Wang, R. E. Mainz, H. Çankaya, F. X. Kärtner, and G. Cirmi, "CEP dependence of signal and idler upon pump-seed synchronization in optical parametric amplifiers," *Optics Letters*, vol. 43, no. 2, pp. 178–181, Jan. 2018, ISSN: 1539-4794. DOI: 10.1364/OL.43.000178.

[25] M. Nisoli, S. D. Silvestri, O. Svelto, R. Szipöcs, K. Ferencz, C. Spielmann, S. Sartania, and F. Krausz, "Compression of high-energy laser pulses below 5 fs," *Opt. Lett.*, vol. 22, no. 8, pp. 522–524, Apr. 1997. DOI: 10.1364/OL.22.000522.

[26] T. Nagy, S. Hädrich, P. Simon, A. Blumenstein, N. Walther, R. Klas, J. Buldt, H. Stark, S. Breitkopf, P. Jójárt, I. Seres, Z. Várallyay, T. Eidam, and J. Limpert, "Generation of three-cycle multi-millijoule laser pulses at 318 W average power," *Optica*, vol. 6, no. 11, pp. 1423–1424, Nov. 2019. DOI: 10.1364/OPTICA.6.001423.

[27] T. Nagy, P. Simon, and L. Veisz, "High-energy few-cycle pulses: Post-compression techniques," *Advances in Physics: X*, vol. 6, no. 1, p. 1 845 795, 2021. DOI: 10.1080/23746149.2020.1845795.

[28] R. Budriūnas, D. Kučinskas, and A. Varanavičius, "High-energy continuum generation in an array of thin plates pumped by tunable femtosecond IR pulses," *Applied Physics B*, vol. 123, no. 7, p. 212, Jul. 2017, ISSN: 1432-0649. DOI: 10.1007/s00340-017-6785-9.

[29] M. Kaumanns, V. Pervak, D. Kormin, V. Leshchenko, A. Kessel, M. Ueffing, Y. Chen, and T. Nubbemeyer, "Multipass spectral broadening of 18 mJ pulses compressible from 1.3 ps to 41 fs," *Opt. Lett.*, vol. 43, no. 23, pp. 5877–5880, Dec. 2018. DOI: 10.1364/OL.43.005877.

[30] F. X. Kärtner, N. Matuschek, T. Schibli, U. Keller, H. A. Haus, C. Heine, R. Morf, V. Scheuer, M. Tilsch, and T. Tschudi, "Design and fabrication of double-chirped mirrors," *Optics Letters*, vol. 22, no. 11, pp. 831–833, Jun. 1997, ISSN: 1539-4794. DOI: 10.1364/OL.22.000831.

[31] S. Rausch, T. Binhammer, A. Harth, F. X. Kärtner, and U. Morgner, "Few-cycle femtosecond field synthesizer," *Optics Express*, vol. 16, no. 22, p. 17 410, Oct. 2008, ISSN: 1094-4087. DOI: 10.1364/OE.16.017410.

[32] H. Telle, G. Steinmeyer, A. Dunlop, J. Stenger, D. Sutter, and U. Keller, "Carrier-envelope offset phase control: A novel concept for absolute optical frequency measurement and ultrashort pulse generation," *Applied Physics B*, vol. 69, no. 4, pp. 327–332, Oct. 1999, ISSN: 1432-0649. DOI: 10.1007/s003400050813.

[33] Y.-C. Lin, K. Midorikawa, and Y. Nabekawa, "Carrier-envelope phase control of synthesized waveforms with two acousto-optic programmable dispersive filters," *Optics Express*, vol. 30, no. 7, pp. 10 818–10 832, Mar. 2022, ISSN: 1094-4087. DOI: 10.1364/OE.447820.

[34] S. Kerbstadt, D. Timmer, L. Englert, T. Bayer, and M. Wollenhaupt, "Ultrashort polarization-tailored bichromatic fields from a CEP-stable white light supercontinuum," *Optics Express*, vol. 25, no. 11, pp. 12 518–12 530, May 2017, ISSN: 1094-4087. DOI: 10.1364/OE.25.012518.

[35] O. Kfir, P. Grychtol, E. Turgut, R. Knut, D. Zusin, D. Popmintchev, T. Popmintchev, H. Nembach, J. M. Shaw, A. Fleischer, H. Kapteyn, M. Murnane, and O. Cohen, "Generation of bright phase-matched circularly-polarized extreme ultraviolet high harmonics," *Nature Photonics*, vol. 9, no. 2, pp. 99–105, Feb. 2015, ISSN: 1749-4893. DOI: 10.1038/nphoton.2014.293.

[36] M. Müller, C. Aleshire, A. Klenke, A. Klenke, E. Haddad, F. Légaré, A. Tünnermann, A. Tünnermann, A. Tünnermann, J. Limpert, J. Limpert, and J. Limpert, "10.4 kW coherently combined ultrafast fiber laser," *Optics Letters*, vol. 45, no. 11, pp. 3083–3086, Jun. 2020, ISSN: 1539-4794. DOI: 10.1364/OL.392843.

[37] F. Wellmann, F. Wellmann, F. Wellmann, F. Wellmann, N. Bode, N. Bode, N. Bode, N. Bode, P. Wessels, P. Wessels, L. Overmeyer, L. Overmeyer, L. Overmeyer, J. Neumann, B. Willke, B. Willke, D. Kracht, and D. Kracht, "Low noise 400 W coherently combined single frequency laser beam for next generation gravitational wave detectors," *Optics*

Express, vol. 29, no. 7, pp. 10 140–10 149, Mar. 2021, ISSN: 1094-4087. DOI: 10.1364/OE.420350.

[38] N. Singh, M. Xin, N. Li, D. Vermeulen, A. Ruocco, E. S. Magden, K. Shtyrkova, E. Ippen, F. X. Kärtner, and M. R. Watts, "Silicon Photonics Optical Frequency Synthesizer," *Laser & Photonics Reviews*, vol. 14, no. 7, p. 1 900 449, 2020, ISSN: 1863-8899. DOI: 10.1002/lpor.201900449.

[39] M. T. Hassan, T. T. Luu, A. Moulet, O. Raskazovskaya, P. Zhokhov, M. Garg, N. Karpowicz, A. M. Zheltikov, V. Pervak, F. Krausz, and E. Goulielmakis, "Optical attosecond pulses and tracking the nonlinear response of bound electrons," *Nature*, vol. 530, no. 7588, pp. 66–70, Feb. 2016, ISSN: 1476-4687. DOI: 10.1038/nature16528.

[40] E. Ridente, M. Mamaikin, N. Altwaijry, D. Zimin, M. F. Kling, V. Pervak, M. Weidman, F. Krausz, and N. Karpowicz, "Electro-optic characterization of synthesized infrared-visible light fields," *Nature Communications*, vol. 13, no. 1, p. 1111, Mar. 2022, ISSN: 2041-1723. DOI: 10.1038/s41467-022-28699-6.

[41] S.-W. Huang, G. Cirmi, J. Moses, K.-H. Hong, S. Bhardwaj, J. R. Birge, L.-J. Chen, E. Li, B. J. Eggleton, G. Cerullo, and F. X. Kärtner, "High-energy pulse synthesis with sub-cycle waveform control for strong-field physics," *Nature Photonics*, vol. 5, no. 8, pp. 475–479, Aug. 2011, ISSN: 1749-4893. DOI: 10.1038/nphoton.2011.140.

[42] C. Manzoni, O. D. Mücke, G. Cirmi, S. Fang, J. Moses, S.-W. Huang, K.-H. Hong, G. Cerullo, and F. X. Kärtner, "Coherent pulse synthesis: Towards sub-cycle optical waveforms," *Laser & Photonics Reviews*, vol. 9, no. 2, pp. 129–171, 2015. DOI: 10.1002/lpor.201400181.

[43] O. D. Mücke, S. Fang, G. Cirmi, G. M. Rossi, S.-H. Chia, H. Ye, Y. Yang, R. Mainz, C. Manzoni, P. Farinello, G. Cerullo, and F. X. Kärtner, "Toward Waveform Nonlinear Optics Using Multimillijoule Sub-Cycle Waveform Synthesizers," *IEEE Journal of Selected Topics in Quantum Electronics*, vol. 21, no. 5, pp. 1–12, Sep. 2015, ISSN: 1558-4542. DOI: 10.1109/JSTQE.2015.2426653.

[44] G. M. Rossi, R. E. Mainz, Y. Yang, F. Scheiba, M. A. Silva-Toledo, S.-H. Chia, P. D. Keathley, S. Fang, O. D. Mücke, C. Manzoni, G. Cerullo, G. Cirmi, and F. X. Kärtner, "Sub-cycle millijoule-level parametric waveform synthesizer for attosecond science," *Nature Photonics*, vol. 14, no. 10, pp. 629–635, Oct. 2020, ISSN: 1749-4893. DOI: 10.1038/s41566-020-0659-0.

[45] Y. Yang, R. E. Mainz, G. M. Rossi, F. Scheiba, M. A. Silva-Toledo, P. D. Keathley, G. Cirmi, and F. X. Kärtner, "Strong-field coherent control of isolated attosecond pulse generation," *Nature Communications*, vol. 12, no. 1, p. 6641, Nov. 2021, ISSN: 2041-1723. DOI: 10.1038/s41467-021-26772-0.

[46] B. Xue, Y. Tamaru, Y. Fu, H. Yuan, P. Lan, O. D. Mücke, A. Suda, K. Midorikawa, and E. J. Takahashi, "Fully stabilized multi-TW optical waveform synthesizer: Toward gigawatt isolated attosecond pulses," *Science Advances*, vol. 6, no. 16, eaay2802, Apr. 2020. DOI: 10.1126/sciadv.aay2802.

[47] Y.-C. Lin, Y. Nabekawa, and K. Midorikawa, "Optical parametric amplification of sub-cycle shortwave infrared pulses," *Nature Communications*, vol. 11, no. 1, p. 3413, Jul. 2020, ISSN: 2041-1723. DOI: 10.1038/s41467-020-17247-9.

[48] A. Harth, M. Schultze, T. Lang, T. Binhammer, S. Rausch, and U. Morgner, "Two-color pumped OPCPA system emitting spectra spanning 1.5 octaves from VIS to NIR," *Optics Express*, vol. 20, no. 3, pp. 3076–3081, Jan. 2012, ISSN: 1094-4087. DOI: 10.1364/OE.20.003076.

[49] D. E. Rivas, A. Borot, D. E. Cardenas, G. Marcus, X. Gu, D. Herrmann, J. Xu, J. Tan, D. Kormin, G. Ma, W. Dallari, G. D. Tsakiris, I. B. Földes, S.-w Chou, M. Weidman, B. Bergues, T. Wittmann, H. Schröder, P. Tzallas, D. Charalambidis, O. Razskazovskaya, V. Pervak, F. Krausz, and L. Veisz, "Next Generation Driver for Attosecond and Laser-plasma Physics," *Scientific Reports*, vol. 7, no. 1, p. 5224, Jul. 2017, ISSN: 2045-2322. DOI: 10.1038/s41598-017-05082-w.

[50] H. Çankaya, A.-L. Calendron, C. Zhou, S.-H. Chia, O. D. Mücke, G. Cirmi, and F. X. Kärtner, "40-µJ passively CEP-stable seed source for ytterbium-based high-energy optical waveform synthesizers," *Opt. Express*, vol. 24, no. 22, pp. 25 169–25 180, Oct. 2016. DOI: 10.1364/OE.24.025169.

[51] A. Alismail, H. Wang, G. Barbiero, N. Altwaijry, S. A. Hussain, V. Pervak, W. Schweinberger, A. M. Azzeer, F. Krausz, and H. Fattahi, "Multi-octave, CEP-stable source for high-energy field synthesis," *Science Advances*, vol. 6, no. 7, eaax3408, 2020. DOI: 10.1126/sciadv.aax3408.

[52] C. M. Heyl, C. L. Arnold, A. Couairon, and A. L'Huillier, "Introduction to macroscopic power scaling principles for high-order harmonic generation," *Journal of Physics B: Atomic, Molecular and Optical Physics*, vol. 50, no. 1, p. 013 001, Dec. 2016, ISSN: 0953-4075. DOI: 10.1088/1361-6455/50/1/013001.

[53] S. L. Cousin, F. Silva, S. Teichmann, M. Hemmer, B. Buades, and J. Biegert, "High-flux table-top soft x-ray source driven by sub-2-cycle, CEP stable, 1.85-μm 1-kHz pulses for carbon K-edge spectroscopy," *Opt. Lett.*, vol. 39, no. 18, pp. 5383–5386, Sep. 2014. DOI: 10.1364/OL.39.005383.

[54] A. S. Johnson, D. R. Austin, D. A. Wood, C. Brahms, A. Gregory, K. B. Holzner, S. Jarosch, E. W. Larsen, S. Parker, C. S. Strüber, P. Ye, J. W. G. Tisch, and J. P. Marangos, "High-flux soft x-ray harmonic generation from ionization-shaped few-cycle laser pulses," *Science Advances*, vol. 4, no. 5, eaar3761, 2018. DOI: 10.1126/sciadv.aar3761.

[55] C. Kleine, M. Ekimova, G. Goldsztejn, S. Raabe, C. Strüber, J. Ludwig, S. Yarlagadda, S. Eisebitt, M. J. J. Vrakking, T. Elsaesser, E. T. J. Nibbering, and A. Rouzée, "Soft X-ray Absorption Spectroscopy of Aqueous Solutions Using a Table-Top Femtosecond Soft X-ray Source," *The Journal of Physical Chemistry Letters*, vol. 10, no. 1, pp. 52–58, Jan. 2019. DOI: 10.1021/acs.jpclett.8b03420.

[56] R. Mainz, F. Kärtner, and W. Wurth, "Sub-Cycle Light Field Synthesizer for Attosecond Science," Ph.D. dissertation, Verlag Deutsches Elektronen-Synchrotron, 2018.

[57] G. M. Rossi, F. Kärtner, and M. Drescher, "Parametric Waveform Synthesis," Ph.D. dissertation, Verlag Deutsches Elektronen-Synchrotron, 2019.

[58] A. Baltuška, T. Fuji, and T. Kobayashi, "Controlling the Carrier-Envelope Phase of Ultrashort Light Pulses with Optical Parametric Amplifiers," *Physical Review Letters*, vol. 88, no. 13, p. 133 901, Mar. 2002. DOI: 10.1103/PhysRevLett.88.133901.

[60] S.-H. Chia, G. Cirmi, S. Fang, G. M. Rossi, O. D. Mücke, and F. X. Kärtner, "Two-octave-spanning dispersion-controlled precision optics for sub-optical-cycle waveform synthesizers," *Optica*, vol. 1, no. 5, p. 315, Nov. 2014, ISSN: 2334-2536. DOI: 10.1364/OPTICA.1.000315.

[61] M. N. Polyanskiy, *Refractive index database*.

[62] Y. Deng, A. Schwarz, H. Fattahi, M. Ueffing, X. Gu, M. Ossiander, T. Metzger, V. Pervak, H. Ishizuki, T. Taira, T. Kobayashi, G. Marcus, F. Krausz, R. Kienberger, and N. Karpowicz, "Carrier-envelope-phase-stable, 12 mJ, 15 cycle laser pulses at 21 um,"

Optics Letters, vol. 37, no. 23, p. 4973, Dec. 2012, ISSN: 0146-9592, 1539-4794. DOI: 10.1364/OL.37.004973.

[63] H. Wang, A. Alismail, G. Barbiero, R. N. Ahmad, and H. Fattahi, "High Energy, Sub-Cycle, Field Synthesizers," *IEEE Journal of Selected Topics in Quantum Electronics*, vol. 25, no. 4, pp. 1–12, Jul. 2019, ISSN: 1558-4542. DOI: 10.1109/JSTQE.2019.2924151.

[64] P. T. F. Gires, "Interferometre utilisable pour la compression d impulsions lumineuses modulees en frequence," no. 258, pp. 6112–6115, 1964.

[65] N. Matuschek, F. Kartner, and U. Keller, "Theory of double-chirped mirrors," *IEEE Journal of Selected Topics in Quantum Electronics*, vol. 4, no. 2, pp. 197–208, Mar. 1998, ISSN: 1558-4542. DOI: 10.1109/2944.686724.

[66] F. X. Kärtner, U. Morgner, R. Ell, T. Schibli, J. G. Fujimoto, E. P. Ippen, V. Scheuer, G. Angelow, and T. Tschudi, "Ultrabroadband double-chirped mirror pairs for generation of octave spectra," *JOSA B*, vol. 18, no. 6, pp. 882–885, Jun. 2001, ISSN: 1520-8540. DOI: 10.1364/JOSAB.18.000882.

[67] V. Pervak, I. Ahmad, M. K. Trubetskov, A. V. Tikhonravov, and F. Krausz, "Double-angle multilayer mirrors with smooth dispersion characteristics," *Optics Express*, vol. 17, no. 10, p. 7943, May 2009, ISSN: 1094-4087. DOI: 10.1364/OE.17.007943.

[68] D. J. Kane and R. Trebino, "Characterization of arbitrary femtosecond pulses using frequency-resolved optical gating," *IEEE Journal of Quantum Electronics (Institute of Electrical and Electronics Engineers); (United States)*, vol. 29:2, Feb. 1993, ISSN: 0018-9197. DOI: 10.1109/3.199311.

[69] C. Iaconis and I. A. Walmsley, "Spectral phase interferometry for direct electric-field reconstruction of ultrashort optical pulses," *Optics Letters*, vol. 23, no. 10, pp. 792–794, May 1998, ISSN: 1539-4794. DOI: 10.1364/OL.23.000792.

[70] D. J. Kane and A. B. Vakhtin, "A review of ptychographic techniques for ultrashort pulse measurement," *Progress in Quantum Electronics*, Special Issue in Honor of Professor J. Gary Eden on the Occasion of His 60th Birthday, vol. 81, p. 100 364, Jan. 2022, ISSN: 0079-6727. DOI: 10.1016/j.pquantelec.2021.100364.

[71] M. Miranda, C. L. Arnold, T. Fordell, F. Silva, B. Alonso, R. Weigand, A. L'Huillier, and H. Crespo, "Characterization of broadband few-cycle laser pulses with the d-scan technique," *Optics Express*, vol. 20, no. 17, pp. 18 732–18 743, Aug. 2012, ISSN: 1094-4087. DOI: 10.1364/OE.20.018732.

[72] S. Sederberg, D. Zimin, S. Keiber, F. Siegrist, M. S. Wismer, V. S. Yakovlev, I. Floss, C. Lemell, J. Burgdörfer, M. Schultze, F. Krausz, and N. Karpowicz, "Attosecond optoelectronic field measurement in solids," *Nature Communications*, vol. 11, no. 1, p. 430, Jan. 2020, ISSN: 2041-1723. DOI: 10.1038/s41467-019-14268-x.

[73] I. A. Walmsley and C. Dorrer, "Characterization of ultrashort electromagnetic pulses," *Advances in Optics and Photonics*, vol. 1, no. 2, pp. 308–437, Apr. 2009, ISSN: 1943-8206. DOI: 10.1364/AOP.1.000308.

[74] J. R. Birge, R. Ell, and F. X. Kärtner, "Two-dimensional spectral shearing interferometry for few-cycle pulse characterization," *Optics Letters*, vol. 31, no. 13, pp. 2063–2065, Jul. 2006, ISSN: 1539-4794. DOI: 10.1364/OL.31.002063.

[75] J. R. Birge, H. M. Crespo, and F. X. Kärtner, "Theory and design of two-dimensional spectral shearing interferometry for few-cycle pulse measurement," *JOSA B*, vol. 27, no. 6, pp. 1165–1173, Jun. 2010, ISSN: 1520-8540. DOI: 10.1364/JOSAB.27.001165.

[76] M. Bellini and T. W. Hänsch, "Phase-locked white-light continuum pulses: Toward a universal optical frequency-comb synthesizer," *Optics Letters*, vol. 25, no. 14, pp. 1049–1051, Jul. 2000, ISSN: 1539-4794. DOI: 10.1364/OL.25.001049.

[77] T. R. Schibli, J. Kim, O. Kuzucu, J. T. Gopinath, S. N. Tandon, G. S. Petrich, L. A. Kolodziejski, J. G. Fujimoto, E. P. Ippen, and F. X. Kaertner, "Attosecond active synchronization of passively mode-locked lasers by balanced cross correlation," *Optics Letters*, vol. 28, no. 11, pp. 947–949, Jun. 2003, ISSN: 1539-4794. DOI: 10.1364/OL.28.000947.

[78] R. E. Mainz, G. M. Rossi, G. Cirmi, Y. Yang, O. D. Mücke, and F. X. Kärtner, "High-dynamic-range arrival time control for flexible, accurate and precise parametric sub-cycle waveform synthesis," *Optics Express*, vol. 25, no. 4, pp. 3052–3068, Feb. 2017, ISSN: 1094-4087. DOI: 10.1364/OE.25.003052.

[79] P. Huang, S. Fang, Y. Gao, K. Zhao, X. Hou, and Z. Wei, "Simple method for simultaneous long-term stabilization of relative timing and carrier-envelope phase in waveform synthesis," *Applied Physics Letters*, vol. 115, no. 3, p. 031 102, Jul. 2019, ISSN: 0003-6951. DOI: 10.1063/1.5083239.

[80] Q. Zou and B. Lü, "Propagation properties of ultrashort pulsed beams with constant waist width in free space," *Optics & Laser Technology*, vol. 39, no. 3, pp. 619–625, Apr. 2007, ISSN: 0030-3992. DOI: 10.1016/j.optlastec.2005.09.004.

[81] S.-W. Huang, G. Cirmi, J. Moses, K.-H. Hong, S. Bhardwaj, J. R. Birge, L.-J. Chen, E. Li, B. J. Eggleton, G. Cerullo, and F. X. Kärtner, "High-energy pulse synthesis with sub-cycle waveform control for strong-field physics," *Nature Photonics*, vol. 5, no. 8, pp. 475–479, Aug. 2011, ISSN: 1749-4893. DOI: 10.1038/nphoton.2011.140.

[82] S.-W. Huang, G. Cirmi, J. Moses, K.-H. Hong, S. Bhardwaj, J. R. Birge, L.-J. Chen, I. V. Kabakova, E. Li, B. J. Eggleton, G. Cerullo, and F. X. Kärtner, "Optical waveform synthesizer and its application to high-harmonic generation," *Journal of Physics B: Atomic, Molecular and Optical Physics*, vol. 45, no. 7, p. 074 009, Mar. 2012, ISSN: 0953-4075. DOI: 10.1088/0953-4075/45/7/074009.

[83] P. G. Chua, Y. Tanaka, M. Takeda, and T. Kurokawa, "Infra-red image detection with a Si-CCD image sensor due to the two-photon absorption process," in *Technical Digest. CLEO/Pacific Rim 2001. 4th Pacific Rim Conference on Lasers and Electro-Optics (Cat. No.01TH8557)*, vol. 1, Jul. 2001, pp. I–I. DOI: 10.1109/CLEOPR.2001.967934.

[84] W. Liu, D. Shen, G. Zhao, H. Yan, Z. Zhou, and W. Wan, "Spatial Narrowing of Two-Photon Imaging in a Silicon CCD Camera," *IEEE Photonics Technology Letters*, vol. 34, no. 9, pp. 459–462, May 2022, ISSN: 1941-0174. DOI: 10.1109/LPT.2022.3164462.

[85] T. Popmintchev, M.-C. Chen, D. Popmintchev, P. Arpin, S. Brown, S. Ališauskas, G. Andriukaitis, T. Balčiunas, O. D. Mücke, A. Pugzlys, A. Baltuška, B. Shim, S. E. Schrauth, A. Gaeta, C. Hernández-García, L. Plaja, A. Becker, A. Jaron-Becker, M. M. Murnane, and H. C. Kapteyn, "Bright Coherent Ultrahigh Harmonics in the keV X-ray Regime from Mid-Infrared Femtosecond Lasers," *Science*, vol. 336, no. 6086, pp. 1287–1291, Jun. 2012. DOI: 10.1126/science.1218497.

[86] A. McPherson, G. Gibson, H. Jara, U. Johann, T. S. Luk, I. A. McIntyre, K. Boyer, and C. K. Rhodes, "Studies of multiphoton production of vacuum-ultraviolet radiation in the rare gases," *JOSA B*, vol. 4, no. 4, pp. 595–601, Apr. 1987, ISSN: 1520-8540. DOI: 10.1364/JOSAB.4.000595.

[87] M. Ferray, A. L'Huillier, X. F. Li, L. A. Lompre, G. Mainfray, and C. Manus, "Multiple-harmonic conversion of 1064 nm radiation in rare gases," *Journal of Physics B: Atomic,*

Molecular and Optical Physics, vol. 21, no. 3, pp. L31–L35, Feb. 1988, ISSN: 0953-4075. DOI: 10.1088/0953-4075/21/3/001.

[88] M. Bellini, C. Lyngå, A. Tozzi, M. B. Gaarde, T. W. Hänsch, A. L'Huillier, and C.-G. Wahlström, "Temporal Coherence of Ultrashort High-Order Harmonic Pulses," *Physical Review Letters*, vol. 81, no. 2, pp. 297–300, Jul. 1998. DOI: 10.1103/PhysRevLett.81.297.

[89] P. Salières, A. L'Huillier, P. Antoine, and M. Lewenstein, "Study of The Spatial and Temporal Coherence of High-Order Harmonics," in *Advances In Atomic, Molecular, and Optical Physics*, B. Bederson and H. Walther, Eds., vol. 41, Academic Press, Jan. 1999, pp. 83–142. DOI: 10.1016/S1049-250X(08)60219-0.

[90] J. Li, X. Ren, Y. Yin, K. Zhao, A. Chew, Y. Cheng, E. Cunningham, Y. Wang, S. Hu, Y. Wu, M. Chini, and Z. Chang, "53-attosecond X-ray pulses reach the carbon K-edge," *Nature Communications*, vol. 8, no. 1, p. 186, Aug. 2017, ISSN: 2041-1723. DOI: 10.1038/s41467-017-00321-0.

[91] M. B. Danailov, F. Bencivenga, F. Capotondi, F. Casolari, P. Cinquegrana, A. Demidovich, E. Giangrisostomi, M. P. Kiskinova, G. Kurdi, M. Manfredda, C. Masciovecchio, R. Mincigrucci, I. P. Nikolov, E. Pedersoli, E. Principi, and P. Sigalotti, "Towards jitter-free pump-probe measurements at seeded free electron laser facilities," *Optics Express*, vol. 22, no. 11, pp. 12 869–12 879, Jun. 2014, ISSN: 1094-4087. DOI: 10.1364/OE.22.012869.

[92] E. Savelyev, R. Boll, C. Bomme, N. Schirmel, H. Redlin, B. Erk, S. Düsterer, E. Müller, H. Höppner, S. Toleikis, J. Müller, M. Kristin Czwalinna, R. Treusch, T. Kierspel, T. Mullins, S. Trippel, J. Wiese, J. Küpper, F. Brauβe, F. Krecinic, A. Rouzée, P. Rudawski, P. Johnsson, K. Amini, A. Lauer, M. Burt, M. Brouard, L. Christensen, J. Thøgersen, H. Stapelfeldt, N. Berrah, M. Müller, A. Ulmer, S. Techert, A. Rudenko, and D. Rolles, "Jitter-correction for IR/UV-XUV pump-probe experiments at the FLASH free-electron laser," *New Journal of Physics*, vol. 19, no. 4, p. 043 009, Apr. 2017, ISSN: 1367-2630. DOI: 10.1088/1367-2630/aa652d.

[93] M. Chini, H. Mashiko, H. Wang, S. Chen, C. Yun, S. Scott, S. Gilbertson, and Z. Chang, "Delay control in attosecond pump-probe experiments," *Optics Express*, vol. 17, no. 24, pp. 21 459–21 464, Nov. 2009, ISSN: 1094-4087. DOI: 10.1364/OE.17.021459.

[94] J. Vaughan, J. Bahder, B. Unzicker, D. Arthur, M. Tatum, T. Hart, G. Harrison, S. Burrows, P. Stringer, and G. M. Laurent, "Design of an optically-locked interferometer for attosecond pump-probe setups," *Optics Express*, vol. 27, no. 21, pp. 30 989–31 000, Oct. 2019, ISSN: 1094-4087. DOI: 10.1364/OE.27.030989.

[95] T. Khurelbaatar, A. Gliserin, J.-H. Mun, J. Heo, Y. Lee, and D.-E. Kim, "Realization of a Continuously Phase-Locked Few-Cycle Deep-UV/XUV Pump-Probe Beamline with Attosecond Precision for Ultrafast Spectroscopy," *Applied Sciences*, vol. 11, no. 15, p. 6840, Jan. 2021, ISSN: 2076-3417. DOI: 10.3390/app11156840.

[96] M. Lein, "Molecular imaging using recolliding electrons," *Journal of Physics B: Atomic, Molecular and Optical Physics*, vol. 40, no. 16, R135–R173, Aug. 2007, ISSN: 0953-4075. DOI: 10.1088/0953-4075/40/16/R01.

[97] H. Niikura, F. Légaré, R. Hasbani, A. D. Bandrauk, M. Y. Ivanov, D. M. Villeneuve, and P. B. Corkum, "Sub-laser-cycle electron pulses for probing molecular dynamics," *Nature*, vol. 417, no. 6892, pp. 917–922, Jun. 2002, ISSN: 1476-4687. DOI: 10.1038/nature00787.

[98] S. Baker, J. S. Robinson, C. A. Haworth, H. Teng, R. A. Smith, C. C. Chirilă, M. Lein, J. W. G. Tisch, and J. P. Marangos, "Probing Proton Dynamics in Molecules on an

Attosecond Time Scale," *Science*, vol. 312, no. 5772, pp. 424–427, Apr. 2006. DOI: 10.1126/science.1123904.

[99] S. Haessler, J. Caillat, W. Boutu, C. Giovanetti-Teixeira, T. Ruchon, T. Auguste, Z. Diveki, P. Breger, A. Maquet, B. Carré, R. Taïeb, and P. Salières, "Attosecond imaging of molecular electronic wavepackets," *Nature Physics*, vol. 6, no. 3, pp. 200–206, Mar. 2010, ISSN: 1745-2481. DOI: 10.1038/nphys1511.

[100] O. Neufeld, J. Zhang, U. De Giovannini, H. Hübener, and A. Rubio, "Probing phonon dynamics with multidimensional high harmonic carrier-envelope-phase spectroscopy," *Proceedings of the National Academy of Sciences*, vol. 119, no. 25, e2204219119, Jun. 2022, ISSN: 0027-8424, 1091-6490. DOI: 10.1073/pnas.2204219119.

[101] G. Vampa, T. J. Hammond, N. Thiré, B. E. Schmidt, F. Légaré, C. R. McDonald, T. Brabec, D. D. Klug, and P. B. Corkum, "All-Optical Reconstruction of Crystal Band Structure," *Physical Review Letters*, vol. 115, no. 19, p. 193 603, Nov. 2015. DOI: 10.1103/PhysRevLett.115.193603.

[102] L. E. Chipperfield, J. S. Robinson, J. W. G. Tisch, and J. P. Marangos, "Ideal Waveform to Generate the Maximum Possible Electron Recollision Energy for Any Given Oscillation Period," *Physical Review Letters*, vol. 102, no. 6, p. 063 003, Feb. 2009. DOI: 10.1103/PhysRevLett.102.063003.

[103] S. Haessler, T. Balčiunas, G. Fan, G. Andriukaitis, A. Pugžlys, A. Baltuška, T. Witting, R. Squibb, A. Zaïr, J. W. G. Tisch, J. P. Marangos, and L. E. Chipperfield, "Optimization of Quantum Trajectories Driven by Strong-Field Waveforms," *Physical Review X*, vol. 4, no. 2, p. 021 028, May 2014. DOI: 10.1103/PhysRevX.4.021028.

[104] C. Jin, G. Wang, H. Wei, A.-T. Le, and C. D. Lin, "Waveforms for optimal sub-keV high-order harmonics with synthesized two- or three-colour laser fields," *Nature Communications*, vol. 5, no. 1, p. 4003, May 2014, ISSN: 2041-1723. DOI: 10.1038/ncomms5003.

[105] M. Lewenstein, P. Balcou, M. Y. Ivanov, A. L'Huillier, and P. B. Corkum, "Theory of high-harmonic generation by low-frequency laser fields," *Physical Review A*, vol. 49, no. 3, pp. 2117–2132, Mar. 1994. DOI: 10.1103/PhysRevA.49.2117.

[106] P. B. Corkum, "Plasma perspective on strong field multiphoton ionization," *Physical Review Letters*, vol. 71, no. 13, pp. 1994–1997, Sep. 1993. DOI: 10.1103/PhysRevLett.71.1994.

[107] L. V. Keldysh, "Ionization in the Field of a Strong Electromagnetic Wave," *J. Exp. Theor. Phys.*, vol. 20, no. 5, pp. 1307–1314, 1965.

[108] M. V. Fedorov, "L. V. Keldysh's "Ionization in the Field of a Strong Electromagnetic Wave" and modern physics of atomic interaction with a strong laser field," *Journal of Experimental and Theoretical Physics*, vol. 122, no. 3, pp. 449–455, Mar. 2016, ISSN: 1090-6509. DOI: 10.1134/S1063776116030043.

[109] Z. Chang, *Fundamentals of Attosecond Optics*. Boca Raton: CRC Press, Feb. 2011, ISBN: 978-0-429-19302-6. DOI: 10.1201/b10402.

[110] A. M. Perelomov, V. S. Popov, and M. V. Terent'ev, "Ionization of Atoms in an Alternating Electric Field," *Soviet Journal of Experimental and Theoretical Physics*, vol. 23, p. 924, Nov. 1966, ISSN: 1063-7761.

[111] M. V. Ammosov, N. B. Delone, and V. P. Krainov, "Tunnel Ionization Of Complex Atoms And Atomic Ions In Electromagnetic Field," in *High Intensity Laser Processes*, vol. 0664, SPIE, Oct. 1986, pp. 138–141. DOI: 10.1117/12.938695.

[112] Y. H. Lai, J. Xu, U. B. Szafruga, B. K. Talbert, X. Gong, K. Zhang, H. Fuest, M. F. Kling, C. I. Blaga, P. Agostini, and L. F. DiMauro, "Experimental investigation of strong-field-

ionization theories for laser fields from visible to midinfrared frequencies," *Physical Review A*, vol. 96, no. 6, p. 063 417, Dec. 2017, ISSN: 2469-9926, 2469-9934. DOI: 10.1103/PhysRevA.96.063417.

[113] J. L. Krause, K. J. Schafer, and K. C. Kulander, "High-order harmonic generation from atoms and ions in the high intensity regime," *Physical Review Letters*, vol. 68, no. 24, pp. 3535–3538, Jun. 1992. DOI: 10.1103/PhysRevLett.68.3535.

[114] P. Arpin, T. Popmintchev, N. Wagner, A. Lytle, O. Cohen, H. C. Kapteyn, and M. M. Murnane, "High Harmonic Generation from Multiply Ionized Argon Extending Beyond 500 eV," in *Conference on Lasers and Electro-Optics/International Quantum Electronics Conference (2009), Paper JThG5*, Optica Publishing Group, May 2009, JThG5. DOI: 10.1364/CLEO.2009.JThG5.

[115] O. Finke, J. Vábek, M. Nevrkla, N. Bobrova, O. Hort, M. Jurkovič, M. Albrecht, A. Jančárek, F. Catoire, S. Skupin, and J. Nejdl, "Phase-matched high-order harmonic generation in pre-ionized noble gases," *Scientific Reports*, vol. 12, no. 1, p. 7715, May 2022, ISSN: 2045-2322. DOI: 10.1038/s41598-022-11313-6.

[116] A. D. Shiner, C. Trallero-Herrero, N. Kajumba, H.-C. Bandulet, D. Comtois, F. Légaré, M. Giguère, J.-C. Kieffer, P. B. Corkum, and D. M. Villeneuve, "Wavelength Scaling of High Harmonic Generation Efficiency," *Physical Review Letters*, vol. 103, no. 7, p. 073 902, Aug. 2009. DOI: 10.1103/PhysRevLett.103.073902.

[117] E. L. Falcão-Filho, V. M. Gkortsas, A. Gordon, and F. X. Kärtner, "Analytic scaling analysis of high harmonic generation conversion efficiency," *Optics Express*, vol. 17, no. 13, pp. 11 217–11 229, Jun. 2009, ISSN: 1094-4087. DOI: 10.1364/OE.17.011217.

[118] M. Lewenstein, P. Balcou, M. Y. Ivanov, A. L'Huillier, and P. B. Corkum, "Theory of high-harmonic generation by low-frequency laser fields," *Physical Review A*, vol. 49, no. 3, pp. 2117–2132, Mar. 1994, ISSN: 1050-2947, 1094-1622. DOI: 10.1103/PhysRevA.49.2117.

[119] K. Amini, J. Biegert, F. Calegari, A. Chac, M. F. Ciappina, A. Dauphin, and D. K. Efimov, "Symphony on strong field approximation," *Rep. Prog. Phys.*, p. 43, 2019.

[120] A.-T. Le, H. Wei, C. Jin, and C. D. Lin, "Strong-field approximation and its extension for high-order harmonic generation with mid-infrared lasers," *Journal of Physics B: Atomic, Molecular and Optical Physics*, vol. 49, no. 5, p. 053 001, Mar. 2016, ISSN: 0953-4075, 1361-6455. DOI: 10.1088/0953-4075/49/5/053001.

[121] D. D. Hickstein, D. R. Carlson, A. Kowligy, M. Kirchner, S. R. Domingue, N. Nader, H. Timmers, A. Lind, G. G. Ycas, M. M. Murnane, H. C. Kapteyn, S. B. Papp, and S. A. Diddams, "High-harmonic generation in periodically poled waveguides," *Optica*, vol. 4, no. 12, pp. 1538–1544, Dec. 2017, ISSN: 2334-2536. DOI: 10.1364/OPTICA.4.001538.

[122] A. G. Ciriolo, R. M. Vázquez, V. Tosa, A. Frezzotti, G. Crippa, M. Devetta, D. Faccialá, F. Frassetto, L. Poletto, A. Pusala, C. Vozzi, R. Osellame, and S. Stagira, "High-order harmonic generation in a microfluidic glass device," *Journal of Physics: Photonics*, vol. 2, no. 2, p. 024 005, Apr. 2020, ISSN: 2515-7647. DOI: 10.1088/2515-7647/ab7d81.

[123] L. G. Gouy, *Sur une propriété nouvelle des ondes lumineuses* (Mélanges scientifiques). Paris: Gauthier-Villars, 1890.

[124] R. W. Boyd, "Intuitive explanation of the phase anomaly of focused light beams," *JOSA*, vol. 70, no. 7, pp. 877–880, Jul. 1980. DOI: 10.1364/JOSA.70.000877.

[125] M. Lewenstein, P. Salières, and A. L'Huillier, "Phase of the atomic polarization in high-order harmonic generation," *Physical Review A*, vol. 52, no. 6, pp. 4747–4754, Dec. 1995. DOI: 10.1103/PhysRevA.52.4747.

[126] C. M. Heyl, J. Güdde, A. L'Huillier, and U. Höfer, "High-order harmonic generation with uJ laser pulses at high repetition rates," *Journal of Physics B: Atomic, Molecular and Optical Physics*, vol. 45, no. 7, p. 074 020, Mar. 2012, ISSN: 0953-4075. DOI: 10.1088/0953-4075/45/7/074020.

[127] K. Varjú, Y. Mairesse, B. Carré, M. B. Gaarde, P. Johnsson, S. Kazamias, R. López-Martens, J. Mauritsson, K. J. Schafer, P. Balcou, A. L'huillier, and P. Salières, "Frequency chirp of harmonic and attosecond pulses," *Journal of Modern Optics*, vol. 52, no. 2-3, pp. 379–394, Jan. 2005, ISSN: 0950-0340, 1362-3044. DOI: 10.1080/09500340412331300

[128] M. Hentschel, R. Kienberger, C. Spielmann, G. A. Reider, N. Milosevic, T. Brabec, P. Corkum, U. Heinzmann, M. Drescher, and F. Krausz, "Attosecond metrology," *Nature*, vol. 414, no. 6863, pp. 509–513, Nov. 2001, ISSN: 1476-4687. DOI: 10.1038/35107000.

[129] T. Popmintchev, M.-C. Chen, A. Bahabad, M. Gerrity, P. Sidorenko, O. Cohen, I. P. Christov, M. M. Murnane, and H. C. Kapteyn, "Phase matching of high harmonic generation in the soft and hard X-ray regions of the spectrum," *Proceedings of the National Academy of Sciences*, vol. 106, no. 26, pp. 10 516–10 521, Jun. 2009. DOI: 10.1073/pnas.0903748106.

[130] H. Dachraoui, T. Auguste, A. Helmstedt, P. Bartz, M. Michelswirth, N. Mueller, W. Pfeiffer, P. Salieres, and U. Heinzmann, "Interplay between absorption, dispersion and refraction in high order harmonic generation," *Journal of Physics B: Atomic, Molecular and Optical Physics*, vol. 42, no. 17, p. 175 402, Aug. 2009, ISSN: 0953-4075. DOI: 10.1088/0953-4075/42/17/175402.

[131] S. Kazamias, D. Douillet, F. Weihe, C. Valentin, A. Rousse, S. Sebban, G. Grillon, F. Augé, D. Hulin, and P. Balcou, "Global Optimization of High Harmonic Generation," *Physical Review Letters*, vol. 90, no. 19, p. 193 901, May 2003. DOI: 10.1103/PhysRevLett.90.193901.

[132] S. Kazamias, S. Daboussi, O. Guilbaud, K. Cassou, D. Ros, B. Cros, and G. Maynard, "Pressure-induced phase matching in high-order harmonic generation," *Physical Review A*, vol. 83, no. 6, p. 063 405, Jun. 2011. DOI: 10.1103/PhysRevA.83.063405.

[133] C.-J. Lai and F. X. Kärtner, "The influence of plasma defocusing in high harmonic generation," *Optics Express*, vol. 19, no. 23, pp. 22 377–22 387, Nov. 2011, ISSN: 1094-4087. DOI: 10.1364/OE.19.022377.

[134] M. Ivanov, P. B. Corkum, T. Zuo, and A. Bandrauk, "Routes to Control of Intense-Field Atomic Polarizability," *Physical Review Letters*, vol. 74, no. 15, pp. 2933–2936, Apr. 1995. DOI: 10.1103/PhysRevLett.74.2933.

[135] T. Pfeifer, L. Gallmann, M. J. Abel, D. M. Neumark, and S. R. Leone, "Single attosecond pulse generation in the multicycle-driver regime by adding a weak second-harmonic field," *Optics Letters*, vol. 31, no. 7, pp. 975–977, Apr. 2006, ISSN: 1539-4794. DOI: 10.1364/OL.31.000975.

[136] C. Chen, C. Hernández-García, Z. Tao, W. You, Y. Zhang, D. Zusin, C. Gentry, P. Tengdin, A. Becker, A. Jaron-Becker, H. Kapteyn, and M. Murnane, "Influence of microscopic and macroscopic effects on attosecond pulse generation using two-color laser fields," *Optics Express*, vol. 25, no. 23, pp. 28 684–28 696, Nov. 2017, ISSN: 1094-4087. DOI: 10.1364/OE.25.028684.

[137] B. Major, E. Balogh, K. Kovács, S. Han, B. Schütte, P. Weber, M. J. J. Vrakking, V. Tosa, A. Rouzée, and K. Varjú, "Spectral shifts and asymmetries in mid-infrared assisted high-order harmonic generation," *JOSA B*, vol. 35, no. 4, A32–A38, Apr. 2018, ISSN: 1520-8540. DOI: 10.1364/JOSAB.35.000A32.

[138] L. He, G. Yuan, K. Wang, W. Hua, C. Yu, and C. Jin, "Optimization of temporal gate by two-color chirped lasers for the generation of isolated attosecond pulse in soft X rays," *Photonics Research*, vol. 7, no. 12, pp. 1407–1415, Dec. 2019, ISSN: 2327-9125. DOI: 10.1364/PRJ.7.001407.

[139] B. Schütte, P. Weber, K. Kovács, E. Balogh, B. Major, V. Tosa, S. Han, M. J. J. Vrakking, K. Varjú, and A. Rouzée, "Bright attosecond soft X-ray pulse trains by transient phase-matching in two-color high-order harmonic generation," *Optics Express*, vol. 23, no. 26, pp. 33 947–33 955, Dec. 2015, ISSN: 1094-4087. DOI: 10.1364/OE.23.033947.

[140] T. Siegel, R. Torres, D. J. Hoffmann, L. Brugnera, I. Procino, A. Zaïr, J. G. Underwood, E. Springate, I. C. E. Turcu, L. E. Chipperfield, and J. P. Marangos, "High harmonic emission from a superposition of multiple unrelated frequency fields," *Optics Express*, vol. 18, no. 7, pp. 6853–6862, Mar. 2010, ISSN: 1094-4087. DOI: 10.1364/OE.18.006853.

[141] F. Calegari, C. Vozzi, M. Negro, G. Sansone, F. Frassetto, L. Poletto, P. Villoresi, M. Nisoli, S. D. Silvestri, and S. Stagira, "Efficient continuum generation exceeding 200 eV by intense ultrashort two-color driver," *Optics Letters*, vol. 34, no. 20, pp. 3125–3127, Oct. 2009, ISSN: 1539-4794. DOI: 10.1364/OL.34.003125.

[142] T. Kroh, C. Jin, P. Krogen, P. D. Keathley, A.-L. Calendron, J. P. Siqueira, H. Liang, E. L. Falcão-Filho, C. D. Lin, F. X. Kärtner, and K.-H. Hong, "Enhanced high-harmonic generation up to the soft X-ray region driven by mid-infrared pulses mixed with their third harmonic," *Optics Express*, vol. 26, no. 13, pp. 16 955–16 969, Jun. 2018, ISSN: 1094-4087. DOI: 10.1364/OE.26.016955.

[143] E. J. Takahashi, P. Lan, O. D. Mücke, Y. Nabekawa, and K. Midorikawa, "Infrared Two-Color Multicycle Laser Field Synthesis for Generating an Intense Attosecond Pulse," *Physical Review Letters*, vol. 104, no. 23, p. 233 901, Jun. 2010. DOI: 10.1103/PhysRevLett.104.233901.

[144] D. Greening, B. Weaver, A. J. Pettipher, D. J. Walke, E. W. Larsen, J. P. Marangos, and J. W. G. Tisch, "Generation and measurement of isolated attosecond pulses with enhanced flux using a two colour synthesized laser field," *Optics Express*, vol. 28, no. 16, pp. 23 329–23 337, Aug. 2020, ISSN: 1094-4087. DOI: 10.1364/OE.396927.

[145] I. Orfanos, I. Makos, I. Liontos, E. Skantzakis, B. Förg, D. Charalambidis, and P. Tzallas, "Attosecond pulse metrology," *APL Photonics*, vol. 4, no. 8, p. 080 901, Aug. 2019, ISSN: 2378-0967. DOI: 10.1063/1.5086773.

[146] P. B. Corkum, N. H. Burnett, and M. Y. Ivanov, "Subfemtosecond pulses," *Optics Letters*, vol. 19, no. 22, pp. 1870–1872, Nov. 1994, ISSN: 1539-4794. DOI: 10.1364/OL.19.001870.

[147] Z. Chang, "Single attosecond pulse and xuv supercontinuum in the high-order harmonic plateau," *Physical Review A*, vol. 70, no. 4, p. 043 802, Oct. 2004. DOI: 10.1103/PhysRevA.70.043802.

[148] B. Shan, S. Ghimire, and Z. Chang, "Generation of the attosecond extreme ultraviolet supercontinuum by a polarization gating," *Journal of Modern Optics*, vol. 52, no. 2-3, pp. 277–283, Jan. 2005, ISSN: 0950-0340. DOI: 10.1080/09500340410001729573.

[149] I. J. Sola, E. Mével, L. Elouga, E. Constant, V. Strelkov, L. Poletto, P. Villoresi, E. Benedetti, J.-P. Caumes, S. Stagira, C. Vozzi, G. Sansone, and M. Nisoli, "Controlling

attosecond electron dynamics by phase-stabilized polarization gating," *Nature Physics*, vol. 2, no. 5, pp. 319–322, May 2006, ISSN: 1745-2481. DOI: 10.1038/nphys281.

[150] G. Sansone, E. Benedetti, F. Calegari, C. Vozzi, L. Avaldi, R. Flammini, L. Poletto, P. Villoresi, C. Altucci, R. Velotta, S. Stagira, S. De Silvestri, and M. Nisoli, "Isolated Single-Cycle Attosecond Pulses," *Science*, vol. 314, no. 5798, pp. 443–446, Oct. 2006. DOI: 10.1126/science.1132838.

[151] H. Mashiko, S. Gilbertson, M. Chini, X. Feng, C. Yun, H. Wang, S. D. Khan, S. Chen, and Z. Chang, "Extreme ultraviolet supercontinua supporting pulse durations of less than one atomic unit of time," *Optics Letters*, vol. 34, no. 21, pp. 3337–3339, Nov. 2009, ISSN: 1539-4794. DOI: 10.1364/OL.34.003337.

[152] K. Zhao, Q. Zhang, M. Chini, Y. Wu, X. Wang, and Z. Chang, "Tailoring a 67 attosecond pulse through advantageous phase-mismatch," *Optics Letters*, vol. 37, no. 18, pp. 3891–3893, Sep. 2012, ISSN: 1539-4794. DOI: 10.1364/OL.37.003891.

[153] M. J. Abel, T. Pfeifer, P. M. Nagel, W. Boutu, M. J. Bell, C. P. Steiner, D. M. Neumark, and S. R. Leone, "Isolated attosecond pulses from ionization gating of high-harmonic emission," *Chemical Physics*, Attosecond Molecular Dynamics, vol. 366, no. 1, pp. 9–14, Dec. 2009, ISSN: 0301-0104. DOI: 10.1016/j.chemphys.2009.09.016.

[154] F. Ferrari, F. Calegari, M. Lucchini, C. Vozzi, S. Stagira, G. Sansone, and M. Nisoli, "High-energy isolated attosecond pulses generated by above-saturation few-cycle fields," *Nature Photonics*, vol. 4, no. 12, pp. 875–879, Dec. 2010, ISSN: 1749-4893. DOI: 10.1038/nphoton.2010.250.

[155] S. L. Cousin, N. Di Palo, B. Buades, S. M. Teichmann, M. Reduzzi, M. Devetta, A. Kheifets, G. Sansone, and J. Biegert, "Attosecond Streaking in the Water Window: A New Regime of Attosecond Pulse Characterization," *Physical Review X*, vol. 7, no. 4, p. 041 030, Nov. 2017. DOI: 10.1103/PhysRevX.7.041030.

[156] T. Gaumnitz, A. Jain, Y. Pertot, M. Huppert, I. Jordan, F. Ardana-Lamas, and H. J. Wörner, "Streaking of 43-attosecond soft-X-ray pulses generated by a passively CEP-stable mid-infrared driver," *Optics Express*, vol. 25, no. 22, pp. 27 506–27 518, Oct. 2017, ISSN: 1094-4087. DOI: 10.1364/OE.25.027506.

[157] Y. Fu, H. Yuan, K. Midorikawa, P. Lan, and E. J. Takahashi, "Towards GW-Scale Isolated Attosecond Pulse Far beyond Carbon K-Edge Driven by Mid-Infrared Waveform Synthesizer," *Applied Sciences*, vol. 8, no. 12, p. 2451, Dec. 2018, ISSN: 2076-3417. DOI: 10.3390/app8122451.

[158] S. Kazamias and P. Balcou, "Intrinsic chirp of attosecond pulses: Single-atom model versus experiment," *Physical Review A*, vol. 69, no. 6, p. 063 416, Jun. 2004. DOI: 10.1103/PhysRevA.69.063416.

[159] M. Mero, F. Frassetto, P. Villoresi, L. Poletto, and K. Varjú, "Compression methods for XUV attosecond pulses," *Optics Express*, vol. 19, no. 23, pp. 23 420–23 428, Nov. 2011, ISSN: 1094-4087. DOI: 10.1364/OE.19.023420.

[160] M. Chini, K. Zhao, and Z. Chang, "The generation, characterization and applications of broadband isolated attosecond pulses," *Nature Photonics*, vol. 8, no. 3, pp. 178–186, Mar. 2014, ISSN: 1749-4893. DOI: 10.1038/nphoton.2013.362.

[161] K. T. Kim, C. M. Kim, M.-G. Baik, G. Umesh, and C. H. Nam, "Single sub - 50 - attosecond pulse generation from chirp-compensated harmonic radiation using material dispersion," *Physical Review A*, vol. 69, no. 5, p. 051 805, May 2004, ISSN: 1050-2947, 1094-1622. DOI: 10.1103/PhysRevA.69.051805.

[162] R. López-Martens, K. Varjú, P. Johnsson, J. Mauritsson, Y. Mairesse, P. Salières, M. B. Gaarde, K. J. Schafer, A. Persson, S. Svanberg, C.-G. Wahlström, and A. L'Huillier,

"Amplitude and Phase Control of Attosecond Light Pulses," *Physical Review Letters*, vol. 94, no. 3, p. 033 001, Jan. 2005, ISSN: 0031-9007, 1079-7114. DOI: 10.1103/PhysRevLett.94.033001.

[163] D. H. Ko, K. T. Kim, and C. H. Nam, "Attosecond-chirp compensation with material dispersion to produce near transform-limited attosecond pulses," *Journal of Physics B: Atomic, Molecular and Optical Physics*, vol. 45, no. 7, p. 074 015, Mar. 2012, ISSN: 0953-4075. DOI: 10.1088/0953-4075/45/7/074015.

[164] B. L. Henke, E. M. Gullikson, and J. C. Davis, "X-Ray Interactions: Photoabsorption, Scattering, Transmission, and Reflection at E = 50-30,000 eV, Z = 1-92," *Atomic Data and Nuclear Data Tables*, vol. 54, no. 2, pp. 181–342, Jul. 1993, ISSN: 0092-640X. DOI: 10.1006/adnd.1993.1013.

[165] G. Doumy, J. Wheeler, C. Roedig, R. Chirla, P. Agostini, and L. F. DiMauro, "Attosecond Synchronization of High-Order Harmonics from Midinfrared Drivers," *Physical Review Letters*, vol. 102, no. 9, p. 093 002, Mar. 2009, ISSN: 0031-9007, 1079-7114. DOI: 10.1103/PhysRevLett.102.093002.

[166] Z. Chang, "Compensating chirp of attosecond X-ray pulses by a neutral hydrogen gas," *OSA Continuum*, vol. 2, no. 2, pp. 314–319, Feb. 2019, ISSN: 2578-7519. DOI: 10.1364/OSAC.2.000314.

[167] Z. Chang, "Attosecond chirp compensation in water window by plasma dispersion," *Optics Express*, vol. 26, no. 25, pp. 33 238–33 244, Dec. 2018, ISSN: 1094-4087. DOI: 10.1364/OE.26.033238.

[168] Y. Zheng, Z. Zeng, P. Zou, L. Zhang, X. Li, P. Liu, R. Li, and Z. Xu, "Dynamic Chirp Control and Pulse Compression for Attosecond High-Order Harmonic Emission," *Physical Review Letters*, vol. 103, no. 4, p. 043 904, Jul. 2009. DOI: 10.1103/PhysRevLett.103.043904.

[169] M. C. Kohler, C. H. Keitel, and K. Z. Hatsagortsyan, "Attochirp-free high-order harmonic generation," *Optics Express*, vol. 19, no. 5, pp. 4411–4420, Feb. 2011, ISSN: 1094-4087. DOI: 10.1364/OE.19.004411.

[170] G. Sansone, E. Benedetti, J. P. Caumes, S. Stagira, C. Vozzi, M. Nisoli, L. Poletto, P. Villoresi, V. Strelkov, I. Sola, L. B. Elouga, A. Zaïr, E. Mével, and E. Constant, "Shaping of attosecond pulses by phase-stabilized polarization gating," *Physical Review A*, vol. 80, no. 6, p. 063 837, Dec. 2009. DOI: 10.1103/PhysRevA.80.063837.

[171] H. Timmers, M. Sabbar, J. Hellwagner, Y. Kobayashi, D. M. Neumark, and S. R. Leone, "Polarization-assisted amplitude gating as a route to tunable, high-contrast attosecond pulses," *Optica*, vol. 3, no. 7, pp. 707–710, Jul. 2016, ISSN: 2334-2536. DOI: 10.1364/OPTICA.3.000707.

[172] N. Dudovich, O. Smirnova, J. Levesque, Y. Mairesse, M. Y. Ivanov, D. M. Villeneuve, and P. B. Corkum, "Measuring and controlling the birth of attosecond XUV pulses," *Nature Physics*, vol. 2, no. 11, pp. 781–786, Nov. 2006, ISSN: 1745-2481. DOI: 10.1038/nphys434.

[173] M. F. Kling, C. Siedschlag, A. J. Verhoef, J. I. Khan, M. Schultze, T. Uphues, Y. Ni, M. Uiberacker, M. Drescher, F. Krausz, and M. J. J. Vrakking, "Control of Electron Localization in Molecular Dissociation," *Science*, vol. 312, no. 5771, pp. 246–248, Apr. 2006. DOI: 10.1126/science.1126259.

[174] N. V. Golubev and A. I. Kuleff, "Control of charge migration in molecules by ultrashort laser pulses," *Physical Review A*, vol. 91, no. 5, p. 051 401, May 2015, ISSN: 1050-2947, 1094-1622. DOI: 10.1103/PhysRevA.91.051401.

[175] D. Hui, H. Alqattan, S. Yamada, V. Pervak, K. Yabana, and M. T. Hassan, "Attosecond electron motion control in dielectric," *Nature Photonics*, vol. 16, no. 1, pp. 33–37, Jan. 2022, ISSN: 1749-4893. DOI: 10.1038/s41566-021-00918-4.

[176] Z. Nourbakhsh, N. Tancogne-Dejean, H. Merdji, and A. Rubio, "High Harmonics and Isolated Attosecond Pulses from Mg O," *Physical Review Applied*, vol. 15, no. 1, p. 014 013, Jan. 2021, ISSN: 2331-7019. DOI: 10.1103/PhysRevApplied.15.014013.

[177] Y. Yang, "A novel optical tool for controlling and probing ultrafast surface dynamics," doctoralThesis, Staats- und Universitätsbibliothek Hamburg Carl von Ossietzky, 2017.

[178] M. Huppert, I. Jordan, and H. J. Wörner, "Attosecond beamline with actively stabilized and spatially separated beam paths," *Review of Scientific Instruments*, vol. 86, no. 12, p. 123 106, Dec. 2015, ISSN: 0034-6748. DOI: 10.1063/1.4937623.

[179] A. S. Johnson, D. Wood, D. R. Austin, C. Brahms, A. Gregory, K. B. Holzner, S. Jarosch, E. W. Larsen, S. Parker, C. Strüber, P. Ye, J. W. G. Tisch, and J. P. Marangos, "Apparatus for soft x-ray table-top high harmonic generation," *Review of Scientific Instruments*, vol. 89, no. 8, p. 083 110, Aug. 2018, ISSN: 0034-6748. DOI: 10.1063/1.5041498.

[180] J. Mooney and P. Kambhampati, "Get the Basics Right: Jacobian Conversion of Wavelength and Energy Scales for Quantitative Analysis of Emission Spectra," *The Journal of Physical Chemistry Letters*, vol. 4, no. 19, pp. 3316–3318, Oct. 2013, ISSN: 1948-7185, 1948-7185. DOI: 10.1021/jz401508t.

[181] F. Scholze, H. Henneken, P. Kuschnerus, H. Rabus, M. Richter, and G. Ulm, "Determination of the electron–hole pair creation energy for semiconductors from the spectral responsivity of photodiodes," *Nuclear Instruments and Methods in Physics Research Section A: Accelerators, Spectrometers, Detectors and Associated Equipment*, vol. 439, no. 2, pp. 208–215, Jan. 2000, ISSN: 0168-9002. DOI: 10.1016/S0168-9002(99)00937-7.

[182] *Understanding direct X-ray detection in scientific cameras*, https://andor.oxinst.com/learning/view/article/direct-detection.

[183] E. Goulielmakis, M. Schultze, M. Hofstetter, V. S. Yakovlev, J. Gagnon, M. Uiberacker, A. L. Aquila, E. M. Gullikson, D. T. Attwood, R. Kienberger, F. Krausz, and U. Kleineberg, "Single-Cycle Nonlinear Optics," *Science*, vol. 320, no. 5883, pp. 1614–1617, Jun. 2008. DOI: 10.1126/science.1157846.

[184] M. Ossiander, F. Siegrist, V. Shirvanyan, R. Pazourek, A. Sommer, T. Latka, A. Guggenmos, S. Nagele, J. Feist, J. Burgdörfer, R. Kienberger, and M. Schultze, "Attosecond correlation dynamics," *Nature Physics*, vol. 13, no. 3, pp. 280–285, Mar. 2017, ISSN: 1745-2481. DOI: 10.1038/nphys3941.

[185] J. Itatani, F. Quéré, G. L. Yudin, M. Y. Ivanov, F. Krausz, and P. B. Corkum, "Attosecond Streak Camera," *Physical Review Letters*, vol. 88, no. 17, p. 173 903, Apr. 2002. DOI: 10.1103/PhysRevLett.88.173903.

[186] M. Drescher, M. Hentschel, R. Kienberger, G. Tempea, C. Spielmann, G. A. Reider, P. B. Corkum, and F. Krausz, "X-ray Pulses Approaching the Attosecond Frontier," *Science*, vol. 291, no. 5510, pp. 1923–1927, Mar. 2001. DOI: 10.1126/science.1058561.

[187] M. Schultze, M. Fieß, N. Karpowicz, J. Gagnon, M. Korbman, M. Hofstetter, S. Neppl, A. L. Cavalieri, Y. Komninos, T. Mercouris, C. A. Nicolaides, R. Pazourek, S. Nagele, J. Feist, J. Burgdörfer, A. M. Azzeer, R. Ernstorfer, R. Kienberger, U. Kleineberg, E. Goulielmakis, F. Krausz, and V. S. Yakovlev, "Delay in Photoemission," *Science*, vol. 328, no. 5986, pp. 1658–1662, Jun. 2010. DOI: 10.1126/science.1189401.

[188] J. A. R. Samson and W. C. Stolte, "Precision measurements of the total photoionization cross-sections of He, Ne, Ar, Kr, and Xe," *Journal of Electron Spectroscopy and Related Phenomena*, Determination of Cross-Sections and Momentum Profiles of Atoms, Molecules and Condensed Matter, vol. 123, no. 2, pp. 265–276, May 2002, ISSN: 0368-2048. DOI: 10.1016/S0368-2048(02)00026-9.

[189] P. D. Keathley, S Bhardwaj, J Moses, G Laurent, and F. X. Kärtner, "Volkov transform generalized projection algorithm for attosecond pulse characterization," *New Journal of Physics*, vol. 18, no. 7, p. 073 009, Jul. 2016, ISSN: 1367-2630. DOI: 10.1088/1367-2630/18/7/073009.

[190] Y. Mairesse and F. Quéré, "Frequency-resolved optical gating for complete reconstruction of attosecond bursts," *Physical Review A*, vol. 71, no. 1, p. 011 401, Jan. 2005. DOI: 10.1103/PhysRevA.71.011401.

[191] J. Gagnon, E. Goulielmakis, and V. Yakovlev, "The accurate FROG characterization of attosecond pulses from streaking measurements," *Applied Physics B*, vol. 92, no. 1, pp. 25–32, Jul. 2008, ISSN: 1432-0649. DOI: 10.1007/s00340-008-3063-x.

[192] M. Chini, S. Gilbertson, S. D. Khan, and Z. Chang, "Characterizing ultrabroadband attosecond lasers," *Optics Express*, vol. 18, no. 12, pp. 13 006–13 016, Jun. 2010, ISSN: 1094-4087. DOI: 10.1364/OE.18.013006.

[193] P. M. Paul, E. S. Toma, P. Breger, G. Mullot, F. Augé, P. Balcou, H. G. Muller, and P. Agostini, "Observation of a Train of Attosecond Pulses from High Harmonic Generation," *Science*, vol. 292, no. 5522, pp. 1689–1692, Jun. 2001. DOI: 10.1126/science.1059413.

[194] L. Cattaneo, J. Vos, M. Lucchini, L. Gallmann, C. Cirelli, and U. Keller, "Comparison of attosecond streaking and RABBITT," *Optics Express*, vol. 24, no. 25, pp. 29 060–29 076, Dec. 2016, ISSN: 1094-4087. DOI: 10.1364/OE.24.029060.

[195] G. Laurent, W. Cao, I. Ben-Itzhak, and C. L. Cocke, "Attosecond pulse characterization," *Optics Express*, vol. 21, no. 14, p. 16 914, Jul. 2013, ISSN: 1094-4087. DOI: 10.1364/OE.21.016914.

[196] F. Krausz and M. Ivanov, "Attosecond physics," *Reviews of Modern Physics*, vol. 81, no. 1, pp. 163–234, Feb. 2009. DOI: 10.1103/RevModPhys.81.163.

[197] N. Saito, N. Ishii, T. Kanai, S. Watanabe, and J. Itatani, "Attosecond streaking measurement of extreme ultraviolet pulses using a long-wavelength electric field," *Scientific Reports*, vol. 6, no. 1, p. 35 594, Oct. 2016, ISSN: 2045-2322. DOI: 10.1038/srep35594.

[198] J. Gagnon and V. S. Yakovlev, "The direct evaluation of attosecond chirp from a streaking measurement," *Applied Physics B*, vol. 103, no. 2, pp. 303–309, May 2011, ISSN: 1432-0649. DOI: 10.1007/s00340-010-4358-2.

[199] G. Cirmi, C.-J. Lai, E. Granados, S.-W. Huang, A. Sell, K.-H. Hong, J. Moses, P. Keathley, and F. X. Kärtner, "Cut-off scaling of high-harmonic generation driven by a femtosecond visible optical parametric amplifier," *Journal of Physics B: Atomic, Molecular and Optical Physics*, vol. 45, no. 20, p. 205 601, Oct. 2012, ISSN: 0953-4075, 1361-6455. DOI: 10.1088/0953-4075/45/20/205601.

[200] M. V. Frolov, N. L. Manakov, W.-H. Xiong, L.-Y. Peng, J. Burgdörfer, and A. F. Starace, "Scaling laws for high-order-harmonic generation with midinfrared laser pulses," *Physical Review A*, vol. 92, no. 2, p. 023 409, Aug. 2015, ISSN: 1050-2947, 1094-1622. DOI: 10.1103/PhysRevA.92.023409.

[201] J. Tate, T. Auguste, H. G. Muller, P. Salières, P. Agostini, and L. F. DiMauro, "Scaling of Wave-Packet Dynamics in an Intense Midinfrared Field," *Physical Review Letters*, vol. 98, no. 1, p. 013 901, Jan. 2007. DOI: 10.1103/PhysRevLett.98.013901.

[202] I. P. Christov, J. Zhou, J. Peatross, A. Rundquist, M. M. Murnane, and H. C. Kapteyn, "Nonadiabatic Effects in High-Harmonic Generation with Ultrashort Pulses," *Physical Review Letters*, vol. 77, no. 9, pp. 1743–1746, Aug. 1996, ISSN: 0031-9007, 1079-7114. DOI: 10.1103/PhysRevLett.77.1743.

[203] S. M. Teichmann, F. Silva, S. L. Cousin, M. Hemmer, and J. Biegert, "0.5-keV Soft X-ray attosecond continua," *Nature Communications*, vol. 7, no. 1, p. 11 493, May 2016, ISSN: 2041-1723. DOI: 10.1038/ncomms11493.

[204] M.-C. Chen, P. Arpin, T. Popmintchev, M. Gerrity, B. Zhang, M. Seaberg, D. Popmintchev, M. M. Murnane, and H. C. Kapteyn, "Bright, Coherent, Ultrafast Soft X-Ray Harmonics Spanning the Water Window from a Tabletop Light Source," *Physical Review Letters*, vol. 105, no. 17, p. 173 901, Oct. 2010, ISSN: 0031-9007, 1079-7114. DOI: 10.1103/PhysRevLett.105.173901.

[205] L. Barreau, A. D. Ross, S. Garg, P. M. Kraus, D. M. Neumark, and S. R. Leone, "Efficient table-top dual-wavelength beamline for ultrafast transient absorption spectroscopy in the soft X-ray region," *Scientific Reports*, vol. 10, no. 1, p. 5773, Apr. 2020, ISSN: 2045-2322. DOI: 10.1038/s41598-020-62461-6.

[206] C. Braig, H. Löchel, R. Mitzner, W. Quevedo, P. Loukas, M. Kubin, C. Weniger, A. Firsov, J. Rehanek, M. Brzhezinskaya, P. Wernet, A. Föhlisch, and A. Erko, "Design and optimization of a parallel spectrometer for ultra-fast X-ray science," *Optics Express*, vol. 22, no. 10, p. 12 583, May 2014, ISSN: 1094-4087. DOI: 10.1364/OE.22.012583.

[207] C. Kleine, M. Ekimova, M.-O. Winghart, S. Eckert, O. Reichel, H. Löchel, J. Probst, C. Braig, C. Seifert, A. Erko, A. Sokolov, M. J. J. Vrakking, E. T. J. Nibbering, and A. Rouzée, "Highly efficient soft x-ray spectrometer for transient absorption spectroscopy with broadband table-top high harmonic sources," *Structural Dynamics*, vol. 8, no. 3, p. 034 302, May 2021. DOI: 10.1063/4.0000096.

Eidesstattliche Versicherung / Declaration on oath

Hiermit versichere ich an Eides statt, die vorliegende Dissertationsschrift selbst verfasst und keine anderen als die angegebenen Hilfsmittel und Quellen benutzt zu haben.

Hamburg, den 02-05-2023

Unterschrift der Doktorandin / des Doktoranden

6 List of Publications

Journal Publications and Conference Proceedings

G. M. Rossi, R. E. Mainz, Y. Yang, F. Scheiba, M. A. Silva-Toledo, S.-H. Chia, P. D. Keathley, S. Fang, O. D. Mücke, C. Manzoni, G. Cerullo, G. Cirmi, and F. X. Kärtner, "Sub-cycle millijoule-level parametric waveform synthesizer for attosecond science," *Nature Photonics*, vol. 14, no. 10, pp. 629–635, Oct. 2020, ISSN: 1749-4893. DOI: 10.1038/s41566-020-0659-0.

Y. Yang, R. E. Mainz, G. M. Rossi, F. Scheiba, M. A. Silva-Toledo, P. D. Keathley, G. Cirmi, and F. X. Kärtner, "Strong-field coherent control of isolated attosecond pulse generation," *Nature Communications*, vol. 12, no. 1, p. 6641, Nov. 2021, ISSN: 2041-1723. DOI: 10.1038/s41467-021-26772-0.

R. E. Mainz, G. M. Rossi, F. Scheiba, M. A. Silva-Toledo, G. Cirmi, and F. X. Kärtner, *Parametric Waveform Synthesis: A scalable approach to generate sub-cycle optical transients*, Aug. 2022. arXiv: 2208.00899 [physics].

F. Scheiba, G. M. Rossi, R. E. Mainz, Y. Yang, G. Cirmi, and F. X. Kärtner, "Millijoule-level sub-cycle pulses from two channels of a parallel parametric waveform synthesizer," *EPJ Web of Conferences*, vol. 205, p. 01 011, 2019, ISSN: 2100-014X. DOI: 10.1051/epjconf/201920501011.

F. Scheiba, N. Klemke, N. Tancogne-Dejean, G. M. Rossi, A. Rubio, O. D. Mücke, and F. X. Kärtner, "Time-domain vectorial field reconstruction of a circularly polarized harmonic from silicon using 2D spectral shearing interferometry," in *Conference on Lasers and Electro-Optics (2019), Paper SW3E.7*, Optica Publishing Group, May 2019, SW3E.7. DOI: 10.1364/CLEO_SI.2019.SW3E.7.

N. Klemke, N. Tancogne-Dejean, G. M. Rossi, Y. Yang, F. Scheiba, R. E. Mainz, G. Di Sciacca, A. Rubio, F. X. Kärtner, and O. D. Mücke, "Polarization-state-resolved high-harmonic spectroscopy of solids," *Nature Communications*, vol. 10, no. 1, p. 1319, Mar. 2019, ISSN: 2041-1723. DOI: 10.1038/s41467-019-09328-1.

F. Scheiba, Y. Yang, G. M. Rossi, R. E. Mainz, M. A. Silva-Toledo, P. D. Keathley, G. Cirmi, and F. X. Kärtner, "Attosecond streaking of parametrically amplified and synthesized waveforms.," in *Conference on Lasers and Electro-Optics (2020), Paper FW3D.6*, Optica Publishing Group, May 2020, FW3D.6. DOI: 10.1364/CLEO_QELS.2020.FW3D.6.

G. Cirmi, R. E. Mainz, M. A. Silva-Toledo, F. Scheiba, H. Cankaya, M. Kubullek, G. M. Rossi, and F. X. Kärtner, "Optical waveform synthesis and its applications," *Laser & Photonics Reviews (accepted)*,

7 Appendix

7.1 Feedback Synchronization

An additional plot to demonstrate the concept and precision of the synchronization between HHG spectra and phase parameters of the PWS is presented in figure 7.1. The Data originates from a RP-CEP scan where both, the RP and CEP are scanned. The spectra and phases are already synchronized and plotted on an index as counted by the FPGA based feedback (FB) system. The system is triggered from the laser and each index corresponds to a laser shot. With a repetition rate of 1 kHz and $\approx 1 \times 10^7$ samples, the measurements corresponds to 2 hours and 40 minutes.

To synchronize the data sets with high resolution, the method does not rely on any absolute time or CPU time. The synchronization happens on different layers for coarse and fine alignment of the phase axes. To establich an absolute link free of misinterpretation, the LED flashes are triggered by the FPGA based feedback system. The flashes ensure the coarse alignment as can be seen in plot (d) with the status of the LED as amplitude 1 or 0. The zoomed area (a1) shows the signal on the XUV CCD where all pixels are equally exposed. The LED is simply mounted on a viewport at the grating chamber. The duration and frequency of the flashes are randomized to give a unique pattern. One can see how the XUV CCD follows the duration of the flashes exactly.

The phase values of RP and CEP are saved at 1 kHz and they are saved to a .csv file with the start of the XUV CCD cameras integration time. The communication between different PC and/or processes that record the phase values and the spectra is established via a local network and the User Datagram Protocol (UDP). This ensures that each spectrum is tagged with a single phase vaule for RP and CEP, so-called UDP stream. These low resolution phase data are plotted in red. As can be seen on the zoomed areas (a2,a3,a4), we are finally able to perfectly match the low resolution data with the high resolution data as plotted with the blue markers, so-called FB data. Plotted is the RP in first row and CEP in second row. Also visually resolved is the standard routine of the scans. The RP is changed continously in one directed in steps. For each step, the CEP is cycled repeatedly.

In this way, each spectrum gets assigned a CEP and RP. The assigend CEP and RP values are averaged from the high resolution data for the integration time of each spectrum. In addition, the time of expose is recorded from the Andor XUV CCD via the “fire” output. The time of the CEP downramp (steep edge in the sawtooth-like CEP modulation) is indicated by the FB system itself and spectra falling into these index are not considered in post processing.
The data as presented are fully synchronized but plotted ”unsorted” just along the index. Already here, one can identify certain islands corresponding to a range of RP where the HHG yield is higher. The spectra are not calibrated and just plotted as raw data with pixel no., but nevertheless, a change in cut-off is observed when comparing (a2) with (a4).

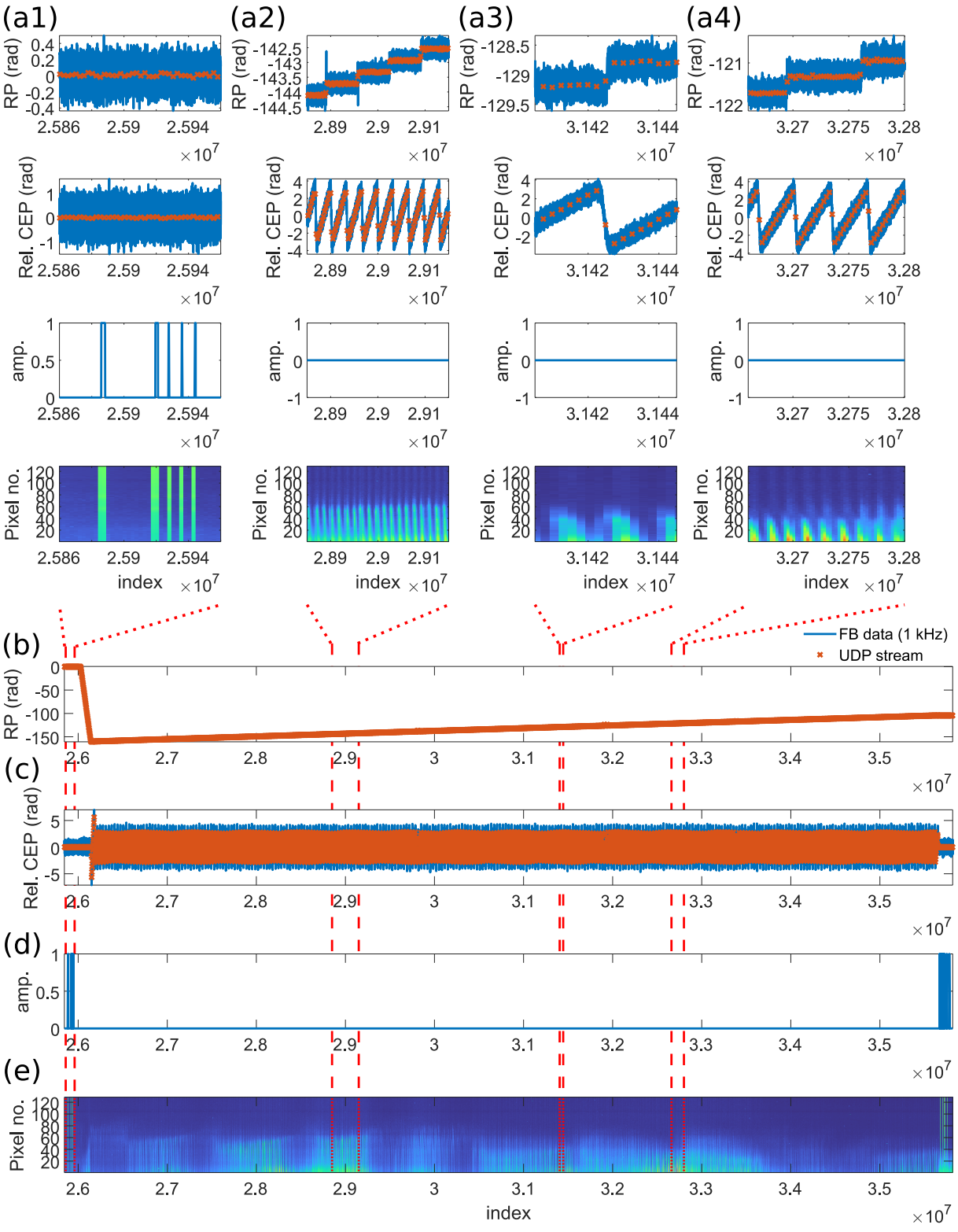

Figure 7.1: Procedure in synching the RP and CEP as stabilized and recorded with the feedback system at 1 kHz (FB data) with the HHG spectra. The lower resolution data (UDP stream) are exchanged between FB system process and XUV CCD recording by means of the User Datagram Protocol (UDP). For details, see main text.

7.2 RP-CEP Scan for f=400 mm

For better visibility, the large range RP-CEP scan from figure 3.37 is plotted on its full RP axes for the same CEP. Out of time zero ($RP = 0$ rad) the continua is still modulated for an extended range. To the right at $RP > 60$ rad, the modulated decreaes and the harmonic continuum originates mainly from the single IR channel. At $RP = -60$ rad, one can observe a small cut-off extension by 25 eV

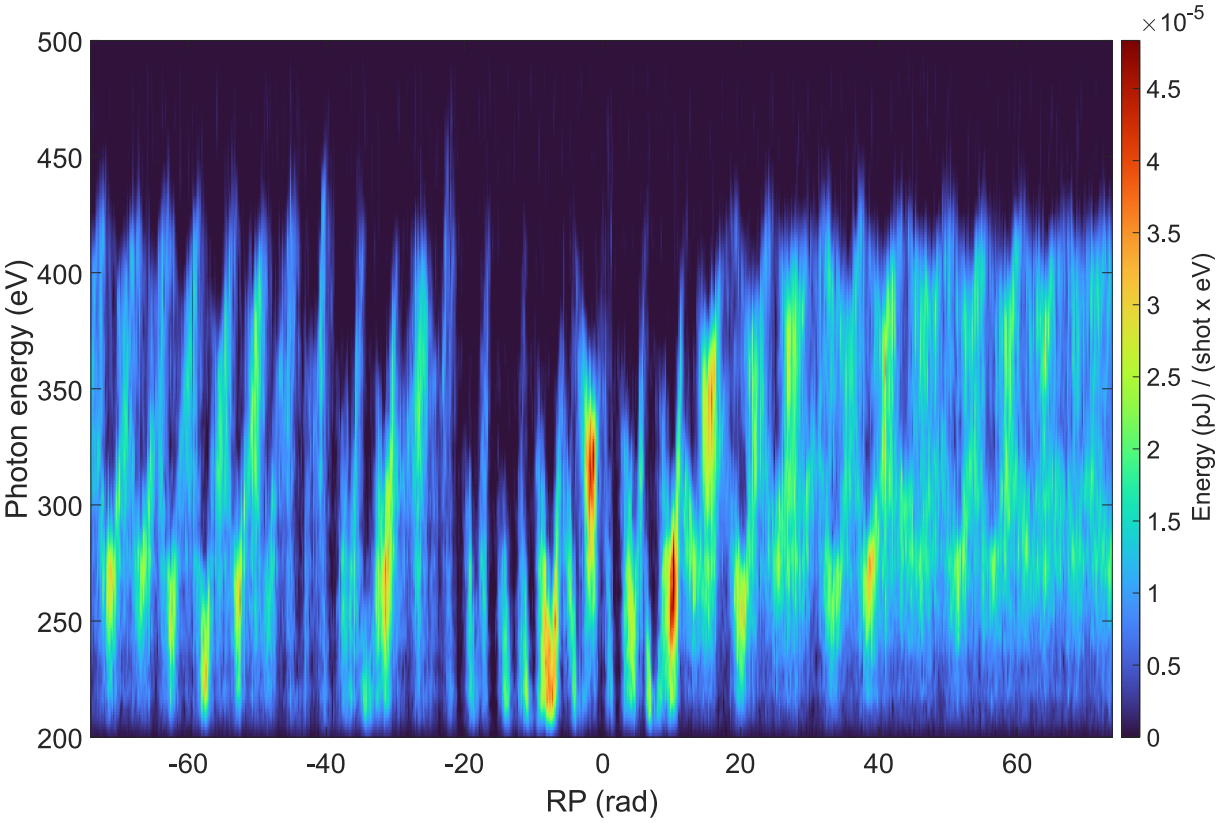

Figure 7.2: Data of figure 3.37 plotted with an extended RP axes. Out of time zero, the single IR channel contribution becomes visible.

7.3 XUV grating

Hitachi Aberration-Corrected Concave Gratings for Flat-Field Spectrographs

Grazing-Incidence Type

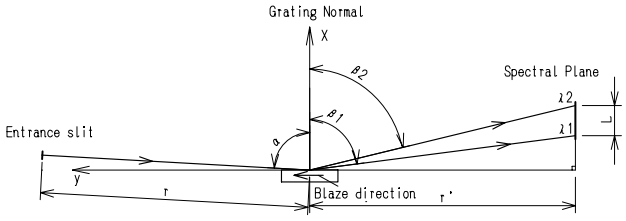

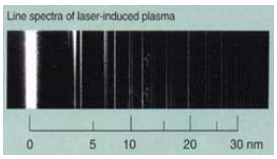

Grazing-incidence soft X-ray spectrograph with flat-field image focusing

The spectra of the soft X-ray region can be observed on a flat photographic plate when the grating is mounted at an incidence angle of 87°(001-0437, 001-0266).

Part No.	Grooves per mm	Radius of curvature (mm)	Blaze WL (nm)	Blank size H×W×T (mm)	Blaze angle (degree)	α (degree)	r (mm)	β1 (degree)	β2 (degree)	r' (mm)	WL Rang λ1 to λ2 (nm)	L (mm)	Material
001-0437 *1,2	1200	5649	10	30×50×10	3.2	87	237	-83.04	-77.07	235.3	5~20	25.3	Pyrex
001-0266 *1,2	1200	5649	10	30×50×10	3.2	87	237	-83.04	-77.07	235.3	5~20	25.3	Zero Dur
001-0450 *2	2400	15920	1.5	30×50×10	1.9	88.7	237	-85.81	-81.01	235.3	1~5	19.99	Pyrex
001-0471 *2	2400	15920	1.5	30×50×10	1.9	88.7	237	-85.81	-81.01	235.3	1~5	19.99	Zero Dur
001-0639	600	5649	31	30×50×10	3.7	85.3	350	-79.56	-67.26	469	22~124	110.16	Pyrex
001-0640	1200	5649	16	30×50×10	3.7	85.3	350	-79.56	-67.26	469	11~62	110.16	Pyrex
001-0659 *3	2400	57680	3	40×70×12	3	89	564	-85.91	-80.21	563.2	1~6	56.83	BK7
001-0660 *3	1200	13450	9	40×70×12	3	87	564	-83.04	-75.61	563.2	5~25	75.73	BK7

References

1. T. Kita, T. Harada , N. Nakano and H. Kuroda, "Mechanically ruled aberration-corrected concave gratings for a flat-field grazing-incidence spectrograph", Appl. Opt. 22, 512-513（1983）
2. N. Nakano, H. Kuroda, T. Kita and T. Harada, "Development of a flat-field grazing-incidence XUV spectrometer and its application in picosecond XUV spectroscopy", Appl. Opt. 23, 2386-2392（1984）
3. T. Harada, K. Takahashi, H. Sakuma and A. Osyczka, "Optimum design of a grazing-incidence flat-field spectrograph with a spherical varied-line-space grating", Appl. Opt. 38, 2743-2748(1999)

Hitachi High Technologies America, Inc.
phone: 800-548-9001 (toll free) email: Sales-LS@hitachi-hta.com
web site: www.hitachi-hta.com/LSHome

Figure 7.3: Specification of XUV to SXR gratings as mounted in the grating spectrometer (251MX, McPherson).

7.4 Toroidal Mirror

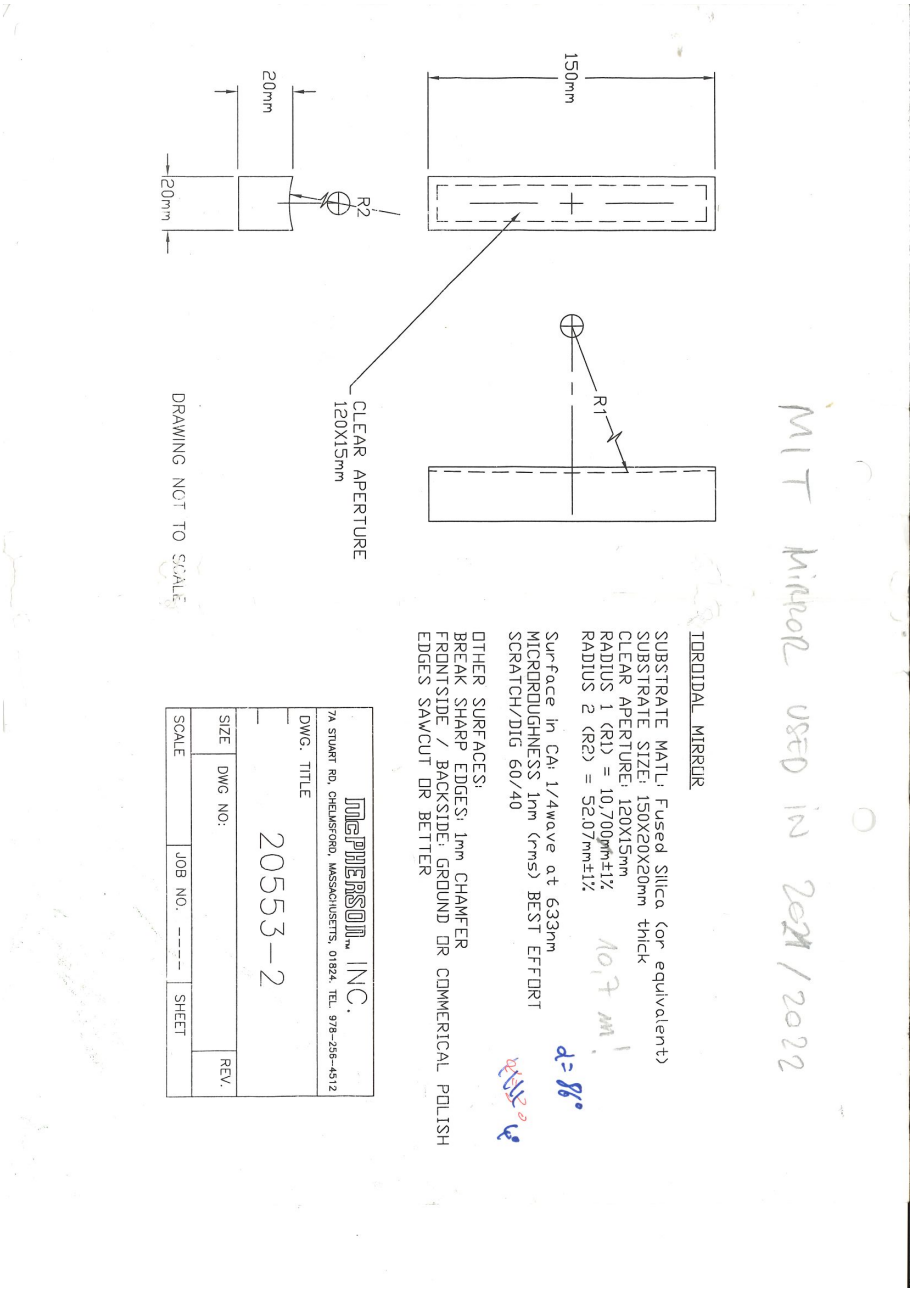

Figure 7.4: Specification of the toroidal mirror #2 with $S = 746$ mm.